

# Active Dynamics in Filament-Motor Mixtures

Inaugural-Dissertation

zur

Erlangung des Doktorgrads

der Mathematisch-Naturwissenschaftlichen Fakultät

der Universität zu Köln

Arvind Ravichandran

aus Mumbai, India

Berichterstatter: **Prof. Dr. Gerhard Gompper**

**Prof. Dr. Tobias Bollenbach**

Tag der mündlichen Prüfung: 15 Jan 2018

*For my mother.*



*The looking itself is a trace of what we are looking for.*  
RUMI



## Abstract

Molecular motors facilitate force generation in the cytoskeletal network necessary for the distribution of organelles and the restructuring of the cytoskeleton within eukaryotic cells. The polymers, such as actin and microtubules, that compose this network are under constant flux due to motors, such as myosin and kinesin. In most cases, many of these motors work together cooperatively to mediate activity at the micron-scale from the nano-scale. As a result, the cytoskeletal network is continually broken down, rebuilt, and redistributed to adapt to the cell's needs. Although mesoscopic structure and dynamics of such networks have been studied *in vitro* and *in vivo*, their connection to nanoscopic, motor-mediated force generation is not well understood. Here, we use two computational modelling approaches to gain insights into the role of nano-scale forces on cellular-scale cytoskeletal structure and dynamics.

In the first approach, we use two-dimensional Brownian dynamics simulations to study a dense, confined mixture of rigid microtubules (MTs) and motors. The motors are modelled as active springs, with two arms that can crosslink neighbouring MTs. Each arm walks unidirectionally on their respective attached MT, in the direction of the MT's polar orientation. The motors can either be tetrameric, with two active arms, or dimeric, with one active arm and one anchored arm. In both cases, motors walk on the crosslinked MTs, causing the springs to stretch. The MTs respond to this force by sliding on each other. MTs also interact with each other through a capped interaction potential, with an independently adjustable attractive component that mimics depletion interactions found in experiments. The confining wall is also attractive, which causes a layer of stabilised MTs to be trapped at the boundary.

We show that polarity sorting via dimeric motors produces large polar-aligned MT clusters. This process is slower than the sorting that occurs due to tetrameric motors, which produces polar-aligned bundles. MTs at high surface fractions in dimeric motor systems give multiple dynamic topological defects. This is absent in systems with tetrameric motors. In general, we show that the velocity is strongly dependent on the MT's local polar order, and dimeric motors cause significantly more dynamic MT networks than tetrameric motors. By decomposing MT velocities based on their polar order, we pinpoint why the asymmetric, dimeric motors are more effective in sliding MTs. Our results, where MTs move faster near the confining wall, are consistent with experimental observations in *Drosophila* oocytes, where enhanced MT activity is found close to the confining plasma membrane.

In the second approach, we develop a two-dimensional, Langevin dynamics model with an effective motor potential, under periodic boundary conditions. The effective motor model, coarse-grains the effect of individual motors and reduces substantially the computational overhead that was previously faced. Since in the first approach we found that MTs are most active when they are antialigned, in this method we construct the MT polarity-dependent potential, such that only antialigned MTs are propelled by the effective motor potential. We control the activity in the system using an antialigned motor probability, and the MT surface fraction by adjusting the simulation box size.

---

We find that the polarity sorting in this model gives large polar-aligned domains, similar to that observed in the confined, dimeric motor systems. The domain size increases with increasing surface fraction, and decreases with increasing motor probability. Also, multiple MTs form coherent streams over long length and time-scales at intermediate surface fractions. The coherence and persistence of streams increases with increasing activity. By separating the parallel velocity distribution into three categories of MT environment polarity, we find that the displacement distribution is skewed largely due to the active antialigned MTs. We also extract an active time-scale at which the skew of the displacement distribution is maximal. Furthermore, we predict that photobleaching experiments of active MT mixtures at intermediate surface fractions will show MT streaming. The circularly-bleached area of MTs will evolve to give elongated shadows. By calculating the collective effects of MTs, and the time-scales at which displacement correlations have their maxima and minima, we find a chronologically-sequenced cascade that leads to MT streaming and advection.

## Abstract

Molekulare Motoren erzeugen Kräfte im Zellskelett, die für die Verteilung von Organellen und die Restrukturierung des Zellskeletts in eukariotischen Zellen notwendig sind. Die Filamente, aus denen das Netzwerk besteht, z. B. Aktin und Mikrotubuli, befinden sich aufgrund der Motoren, z. B. Myosin und Kinesin, im konstanten Fluss. In den meisten Fällen arbeiten mehrere Motoren auf der Nanometerskala zusammen um auf der Mikrometerskala Aktivität zu erzeugen. Gemäß den Bedürfnissen der Zelle werden somit kontinuierlich Filamente transportiert und das Zellskelett wird umgebaut. Obwohl die mesoskopische Struktur und Dynamik der Netzwerke sowohl *in vitro* als auch *in vivo* untersucht wurde, sind viele Aspekte der molekularen Krafterzeugung noch nicht komplett verstanden. In dieser Arbeit wird mit Hilfe zweier verschiedener Simulationsmodelle die Rolle der Kräfte auf der molekularen Skala für die Struktur und Dynamik auf der Zellskala in Motor-Filament-Systemen untersucht.

Mit Hilfe des ersten Modells werden dichte Systeme steifer Mikrotubuli unter Verwendung von Brown'scher Dynamik simuliert. Motoren werden als aktive Federn modelliert, die mit ihren zwei Armen benachbarte MT verbinden. Jeder Arm wandert auf einem der polaren MT in einer definierten Richtung. Bei den Motoren kann es sich um tetramere Motoren mit zwei aktiven Armen oder um dimere Motoren mit einem aktiven Arm und einem verankerten Arm handeln. In beiden Fällen führt die Wanderung der Motoren auf den MT zur Elongierung der Federn und MT werden durch die entstehenden Kräfte gegeneinander verschoben. Desweiteren besitzt das Wechselwirkungspotential zwischen MT einen attraktiven Anteil, der die Veramungswechselwirkung in den experimentellen Systemen modelliert. Auch die Wechselwirkung mit der Wand ist attraktiv, was zu einer Schicht an der Wand stabilisierter MT führt.

Wir zeigen, daß-getrieben durch das Bestreben die Filamente lokal nach Polarität zu sortieren-sich in Systemen mit dimeren Motoren große polare MT-Domänen ausbilden. Dieser Sortierprozess ist langsamer als in Systemen mit tetrameren Motoren, in denen sich polare MT-Bündel bilden. Desweiteren finden sich-im Gegensatz zu tetrameren Motoren-in Systemen mit dimeren Motoren bei hohen MT-Konzentrationen dynamische, topologische Defekte. Die Geschwindigkeit der MT ist stark von der lokalen polaren Ordnung bestimmt und die Dynamik in Systemen mit dimeren Motoren ist signifikant stärker als in Systemen mit tetrameren Motoren. Durch eine Analyse der MT-Geschwindigkeiten in Abhängigkeit der polaren Ordnung zeigen wir, wie die asymmetrischen dimeren Motoren Filamente effektiver gegeneinander verschieben als tetramere Motoren. Desweiteren steigt die MT-Geschwindigkeit in der Nähe einer Wand an, was konsistent mit experimentellen Beobachtungen in *Drosophila*-Eizellen ist, in denen die MT-Aktivität in der Nähe der Plasmamembran zunimmt.

Mit Hilfe des zweiten Modells werden Systeme mit periodischen Randbedingungen und einem effektiven Motormodell unter Verwendung von zweidimensionalen Langevindynamik-Simulationen untersucht. Dieses effektive Motormodell basiert auf der Vergrößerung der Kräfte einzelner Motoren und reduziert somit den Simulationsaufwand signifikant. Mit Hilfe von Simulationen von Systemen mit expliziten Motoren konnte gezeigt werden, dass antiparallele MT aktiver sind. Daher wird für die effektiven Motoren eine polaritätsabhängige MT-Wechselwirkung verwendet, die nur antiparallele MT antreibt. Die Aktivität der Systeme kann hier über die Bindungswahrscheinlichkeit der Motoren kontrolliert und die MT-Oberflächendichte kann bei konstanter Filamentanzahl über die Systemgröße reguliert werden.

Der Mechanismus der Polaritäts-Sortierung von MT führt zur Bildung großer polarer Domänen, ähnlich den Systemen mit dimeren Motoren. Die Domänengröße nimmt mit zunehmender MT-Oberflächendichte zu und mit zunehmender Bindungswahrscheinlichkeit der Motoren ab. Bei mittleren MT-Oberflächendichten bilden sich sowohl langlebige als auch lange kohärente MT-Ströme

---

aus; Kohärenz und Persistenz der Ströme nehmen mit steigender Aktivität zu. Die Analyse der Schiefe der Verteilung der sogenannten parallelen MT-Geschwindigkeit zeigt, dass diese Asymmetrie in erster Linie durch antiparallele MT erzeugt wird. Die maximale Schiefe der Verteilung definiert eine charakteristische Zeit für die Aktivität. In Simulationen von FRAP-Experimenten werden kreisförmige, nicht fluoreszierende Bereiche in elongierte Bereiche deformiert. Mit Hilfe der Berechnung kollektiver MT-Effekte mit maximaler und minimaler Bewegung der MT sagen die Simulationen eine zeitliche Ordnung der verschiedenen Prozesse rund um die Ausbildung von lokalisierten Strömen und advektiver Strömung im System voraus.

# Contents

<b>1</b>	<b>Introduction</b>	<b>1</b>
1.1	Microtubules . . . . .	2
1.1.1	Structure . . . . .	2
1.1.2	Polymerisation dynamics . . . . .	3
1.1.3	Filament polarity . . . . .	4
1.2	Molecular motors . . . . .	5
1.2.1	Kinesins . . . . .	5
1.2.2	Molecular motors obey equilibrium laws . . . . .	6
1.2.3	Two-state motor model . . . . .	8
1.2.4	Dimeric vs. tetrameric motors . . . . .	10
1.3	Cytoplasmic streaming . . . . .	11
1.3.1	Flows due to microtubule sliding . . . . .	12
1.3.2	Streaming in cells . . . . .	13
1.4	Theoretical Descriptions . . . . .	15
1.4.1	Phase transitions in confinement . . . . .	15
1.4.2	Continuum theories of active nematics . . . . .	16
1.4.3	Large-scale motion in active nematics . . . . .	17
1.5	Outline . . . . .	17
<b>2</b>	<b>Multiscale model of microtubules and motors</b>	<b>19</b>
2.1	Langevin dynamics for active rods . . . . .	20
2.1.1	Fluctuation-dissipation theorem . . . . .	20
2.1.2	Rotational diffusion . . . . .	21
2.1.3	Translational diffusion . . . . .	22
2.1.4	Active fluctuations . . . . .	23
2.2	Explicit motor system . . . . .	24
2.2.1	Volume exclusion and depletion interactions . . . . .	24
2.2.2	Wall interactions . . . . .	28
2.2.3	Simplified motor walking . . . . .	29
2.2.4	Simulation schematic . . . . .	31
2.2.5	System parameters . . . . .	32
2.3	Effective motor system . . . . .	34
2.3.1	Phenomenological model . . . . .	35
2.3.2	Volume exclusion and internal forces . . . . .	36
2.3.3	Effective motor potential . . . . .	38

# CONTENTS

---

2.3.4	System parameters . . . . .	40
2.4	Explicit vs. effective motor system . . . . .	40
<b>3</b>	<b>Motor-induced microtubule structures within confinement</b>	<b>42</b>
3.1	Depletion forces and tetrameric motors give microtubule bundles . . . . .	43
3.2	Effect of microtubule packing fraction . . . . .	45
3.3	Domain sizes are conserved with confinement size . . . . .	46
3.4	Polarity sorting can occur at low motor concentrations . . . . .	46
3.5	Effects of other parameters on structure . . . . .	47
3.5.1	Motor spring constant . . . . .	47
3.5.2	Motor velocity . . . . .	47
3.6	Local polar order parameter . . . . .	48
3.7	Reaching steady-state structure . . . . .	52
3.8	Conclusions . . . . .	53
3.8.1	Steric effect and depletion forces . . . . .	53
3.8.2	Filament-motor mixtures . . . . .	54
<b>4</b>	<b>Motor-induced microtubule dynamics within confinement</b>	<b>55</b>
4.1	Motor-mediated microtubule motion . . . . .	55
4.1.1	Time scales for diffusion and activity . . . . .	55
4.1.2	Effect of confinement diameter . . . . .	57
4.1.3	Effect of motor stiffness . . . . .	58
4.1.4	Effect of motor velocity . . . . .	59
4.1.5	Effect of microtubule area fraction . . . . .	60
4.2	Motor propulsion and local order . . . . .	61
4.2.1	Antiparallel microtubules induce maximum motor propulsion . . . . .	61
4.2.2	Decomposed histogram of microtubule propulsion . . . . .	63
4.3	Collective rotation at the boundary . . . . .	63
4.3.1	Boundary microtubules are fastest . . . . .	63
4.3.2	Non-attractive confinement gives slower microtubules . . . . .	64
4.4	Life cycle of a motor . . . . .	65
4.4.1	Dimeric motors are more processive . . . . .	65
4.4.2	Effect of motor velocity on processivity . . . . .	67
4.5	Conclusions . . . . .	68
4.5.1	Effect of attractive confinement . . . . .	68
4.5.2	Role of motor-arm asymmetry . . . . .	69
4.5.3	Dependence of dynamics on local order . . . . .	69
4.5.4	Relevance of results to <i>in vitro</i> experiments . . . . .	70
<b>5</b>	<b>Microtubule streaming in effective motor systems</b>	<b>71</b>
5.1	Polar-aligned domain structures . . . . .	72
5.1.1	Domains from antialigned motor potentials . . . . .	72
5.1.2	Effect of aligned motor potentials . . . . .	74
5.2	Local polar order . . . . .	76
5.3	Microtubule Streaming . . . . .	79

5.4	Polarity-driven active motion . . . . .	83
5.4.1	Mean-squared displacement . . . . .	83
5.4.2	Active diffusion . . . . .	84
5.4.3	Parallel velocity and rotational diffusion . . . . .	85
5.5	Asymmetries in parallel velocity distributions . . . . .	90
5.5.1	Time-scale of maximum skew . . . . .	90
5.5.2	Microtubule dynamics at active timescale . . . . .	91
5.5.3	Microtubule dynamics in different regions . . . . .	93
5.6	Time-scale of microtubule streaming . . . . .	98
5.7	Time-scale of collective effects . . . . .	99
5.7.1	Neighbour displacement correlation function . . . . .	100
5.7.2	Predictions of photobleaching microtubule mixtures . . . . .	102
5.8	Conclusions . . . . .	102
5.8.1	Summary of time-scales . . . . .	102
5.8.2	Dynamics . . . . .	105
5.8.3	Effective motor models . . . . .	105
5.8.4	Polar ordering with antialigned motor potential . . . . .	106
5.8.5	Asymmetric displacements in polar particles . . . . .	107
5.8.6	Cytoplasmic streaming in <i>Drosophila</i> . . . . .	107
5.8.7	Collective effects . . . . .	108
<b>6</b>	<b>Conclusions</b>	<b>109</b>
6.1	Confined filaments driven by explicit motors . . . . .	109
6.1.1	Microtubule structures in confinements . . . . .	110
6.1.2	Confined microtubules driven by explicit motors . . . . .	110
6.2	Bulk microtubules driven by effective motors . . . . .	111
6.3	Outlook . . . . .	112
<b>A</b>	<b>Supplementary Figures</b>	<b>114</b>
<b>B</b>	<b>Time correlation algorithms</b>	<b>117</b>
B.1	Final output method . . . . .	117
B.2	On the fly method . . . . .	118
<b>C</b>	<b>Non-equilibrium as a violation of detailed balance</b>	<b>120</b>
<b>D</b>	<b>Benchmarking of effective motor system</b>	<b>121</b>



# Chapter 1

## Introduction

Non-equilibrium thermodynamics is a study of change. It describes the flux of energy that makes physical processes ephemeral. When this energy manifests in motion, it can drive dynamics that make life. This narrative of energy quanta's journey through the building blocks of life was not well understood until recently. In the mid 20th century, the chemiosmotic hypothesis; the basis of oxidative phosphorylation in mitochondria, was formulated [1]. This is the biological process by which cells orchestrate enzymes and substrates to come together and release stored energy from carbohydrates, proteins and fat in the form of Adenosine Triphosphate (ATP): the molecular energy currency. Food consumed by organisms needs to be converted to ATP before cellular processes necessary for life can be carried out. Cellular activity typically involves a host of active processes that consume ATP, often carried out by a dizzying variety of proteins. Being the functional basic unit of life, the cell can be considered to be a composite factory that generates and consumes ATP [2].

The interior of the cell is a mixture of carefully organised material, suspended in a water-based, gel-like environment, called the cytoplasm. The cytoskeleton is a dynamic network, which serves as scaffolding that criss-crosses the cytoplasm. In eukaryotic cells, this network is made up of long, thin protein fibres, which can help maintain cell shape, hold organelles in place, take part in cell division and enable cell movement [3]. The polymers that compose this network within the cell are also used as highways for the transport of vesicles and organelles. As the cytoskeleton can be remodelled, it is continually broken down and rebuilt by the cell to adapt to its needs. This versatile structure is composed of three main categories of cytoskeletal filaments: microtubules (MTs), actin, and intermediate filaments. Motor proteins are smaller, nanometric, components of the cytoskeleton. They are molecular machines that convert ATP into mechanical work used to power cytoskeletal dynamics. Such motors typically fall into one of two categories: (1) motors that act on MTs, such as dynein and kinesin, or (2) motors that act on actin, such as myosin [2].

The field of biological active matter studies entities that are actively transported because they gain energy from their environment, usually through ATP. Although computational models need not necessarily take into account each ATP molecule in the solution, the approach used to induce activity in particles can influence large-scale collective behaviour [4–12]. Such a practice of simulating the behaviour of a complex system with

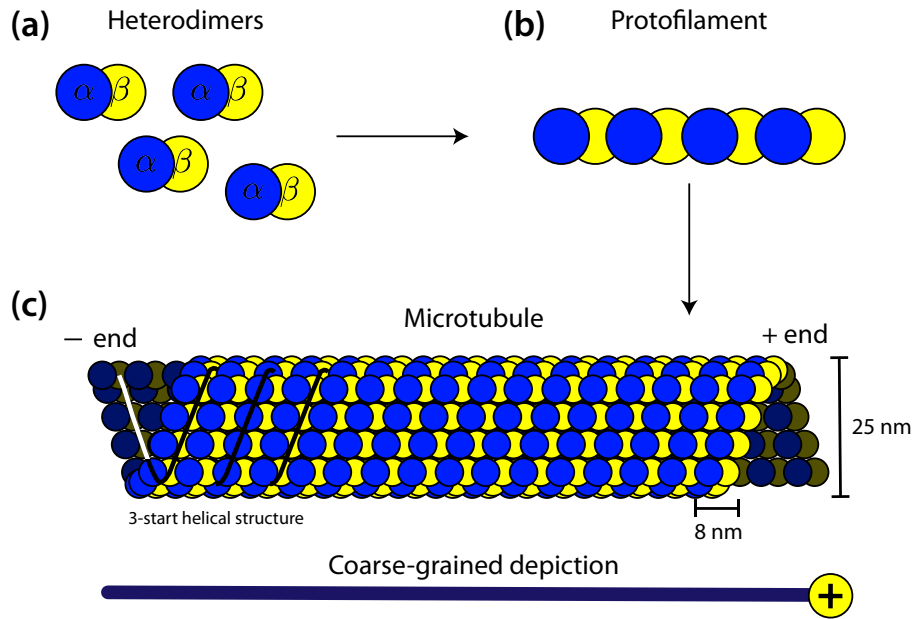


Figure 1.1: Schematic of hierarchical organization in MTs. (a) Tubulin heterodimers made up of  $\alpha$  and  $\beta$  subunits. (b) Regulated assembly of the stable  $\alpha\beta$  heterodimer gives the protofilament. (c) 13 Protofilaments assemble to give the MT. The lattice structure of a 3-start (composed of three helices of monomers), 13-protofilament MT is illustrated. The axial periodicity of an MT is 8 nm (the height of the heterodimer) [13]. The dimer polarity can be identified by the orientation of the heterodimers that make up an MT. They are oriented in such a way that the  $\beta$ -tubulin is at the plus end and the  $\alpha$ -tubulin is at the minus end.

multiple components over various length and time scales, using a simplified representation is known as coarse-graining.

Although the overall dynamics of the cytoskeleton is an interplay of active motion, stochastic fluctuations, and steric interactions, activity and global structure of systems can be qualitatively and quantitatively different between two coarse-graining choices. In order to model active biological phenomena, a careful consideration of the length and time scale of interest, and a deeper understanding of the microscopic origins of activity are important. Also, a close look at the biomolecules being modelled is crucial before comparing biophysical computer models to experiments.

## 1.1 Microtubules

### 1.1.1 Structure

MTs are polar, hollow, cylindrical polymers made up of  $\alpha\beta$  tubulin heterodimers, as shown in Fig. 1.1(a) [2]. The heterodimers are arranged in a head-to-tail fashion forming a protofilament, as shown in Fig. 1.1(b). Such protofilaments associate laterally to form a sheet which closes to form a hollow cylindrical tube, making up the MT, with the + and - end structure shown in Fig. 1.1(C). Most MTs found in cells have 13 protofilaments and

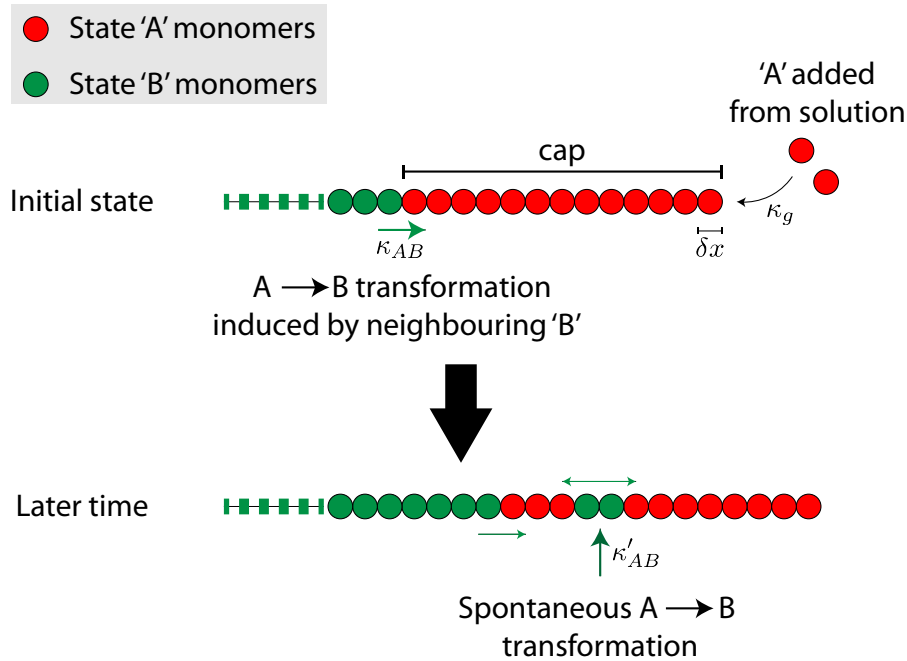


Figure 1.2: Sketch showing cap assembly on a MT made up of GTP tubulin (state  $A$ ) and GDP tubulin (state  $B$ ) monomers.  $A$  monomers are added at the cap, and they can either be transformed to  $B$ , spontaneously or due to its  $B$  neighbour [15].

can be thought of as being composed of three helices of monomers.<sup>1</sup> The outer diameter of this structure is 25 nm [13].

MTs are also the thickest and most rigid of the three cytoskeletal components [2]. The rigidity of a polymer can be measured using its persistence length. This is defined to be the length over which correlations along its contour vanishes, or the length required for thermal fluctuations at 300K to bend it. For polymers with short persistence lengths, such as intermediate filaments ( $1\mu\text{m}$ ) and actin ( $15\mu\text{m}$ ), the polymers behave as semi-flexible chains. The Young's modulus on the other hand, is the polymer's resistance to being deformed elastically, or the energy cost associated with stretching the polymer, see Table 1.1. It thus suffices to model MTs as rigid rods. Although it is difficult to elastically deform MTs, MT lengths are not necessarily constant.

### 1.1.2 Polymerisation dynamics

MT lengths vary because they can oscillate between assembly and disassembly phases, depending on tubulin concentration, temperature and microtubule-associated protein (MAPs) [2, 14]. MTs are assembled by the addition of GTP tubulin, which forms a stable cap. When the hydrolysis of GTP tubulin to GDP tubulin overtakes the assembly, the cap is eroded and the MT undergoes rapid disassembly known as a catastrophe.

This abrupt transition from assembly to disassembly has been modelled using a simple

<sup>1</sup>There is an offset of 0.92nm between dimers of adjacent protofilaments. This offset accumulates for 13 protofilaments to 12nm, which is exactly the length of three monomers. This gives the 3-start helical structure, and ensures that the protofilaments run parallel to the axis of the MT.

Material	Young's Modulus (GPa)	Polymer Diameter (nm)	Persistence Length
<b>Proteins</b>			
Actin	2	6	15 $\mu\text{m}$
Microtubule	2	25	6 mm
IF protein	2	10	1 $\mu\text{m}$
<b>Others</b>			
DNA	1	2	50 nm
fd virus	-	7	2.2 $\mu\text{m}$

Table 1.1: Comparison of elasticity, thickness and flexibility of biological materials. IF protein refers to Intermediate Filament proteins, namely hydrated keratins and filaments. Values are obtained from Ref. [3, 13, 14, 16–19]

1-D stochastic model [15], sketched in Fig. 1.2. GTP tubulin (state A) monomers are added to the MT at rate  $\kappa_g$ . These monomers can be converted to GDP tubulin (state B), at a rate  $\kappa_{AB}$ , if this is induced by neighbouring state B monomers. Or, state A monomers can be spontaneously converted at rate  $\kappa'_{AB}$  when they are not neighbored by state B monomers.

Given that A and B monomers are of length  $\delta x$ , the MT grows at  $v_g = \kappa_g \delta x$ , and the interface between A and B recedes at  $v_{AB} = \kappa_{AB} \delta x$ . Thus the cap length increases at an average velocity,  $v = v_g - v_{AB}$ . New interfaces are created within the cap at a rate  $r = \kappa'_{AB} / \delta x$ .

The master equation for the cap length distribution,  $p(x, t)$ , is given by,

$$\partial_t p = -v \partial_x p + D \partial_x^2 p - r x p + r \int_x^\infty dy p(y, t). \quad (1.1)$$

The first two terms on the right describe the rate of cap length growth, and the noise associated with this average growth rate, respectively. The third term is the rate at which caps of length  $x$  are abruptly shortened, and the last term is the rate at which caps longer than  $x$  are shorted to length  $x$ . The boundary condition is given by  $p(x = 0, t) = 0$ , and the initial condition is obtained from experiments.

Such simple models are remarkably successful in modelling the rate of MT catastrophes under different GTP tubulin concentrations in solution [15].

### 1.1.3 Filament polarity

The polarity of MTs comes from the asymmetry of the heterodimers: (1) Protofilaments are made up of dimers associated head-to-tail, and (2) protofilaments are parallel. The heterodimers orient such that the  $\beta$ -tubulin is at the plus end and the  $\alpha$ -tubulin is at the minus end. The rates of growth of MTs at either of these ends are not equal. The plus end grows more rapidly, and the minus end, which can be anchored to structures called microtubule organising centers (MTOCs), grow slowly [14].

Active MT motion can occur due to the polymerisation/depolymerisation events occurring at both ends of the filament, or due to the work done by molecular motors. Namely, motors are able to detect MT polarity, carry cargo and “walk” along the filaments in a given direction over relatively long distances. This makes MT polarity an important parameter, which must be carefully controlled by the cell, for the effective redistribution of molecules and organelles.

Apart from the redistribution of material, the polarity of MTs is important for their own dynamics. The polar nature of MTs determines the unidirectional motion of associated molecular motors, such as kinesin and dynein [20]. Experiments have shown that motors can cross-link adjacent MTs and cause active sliding between them, disrupting traditional ideas of MTs as stationary tracks along which motor proteins only move cargo [21]. It has been shown, both *in vitro* and *in vivo*, that the motor-arm motion causes the motors to stretch and imparts active stresses resulting in MT sliding [21–23].

In fact, kinesin-mediated MT sliding plays an ubiquitous role in transporting MTs against one another, important during cell division [24]. The mechanism is powerful enough to form parallel microtubule bundles which can deform membranes, and drive shape changes in cells [25].

## 1.2 Molecular motors

The conventional kinesin-1 molecular motor is a mechanochemical enzyme [26]. These molecules hydrolyse approximately 125 molecules of ATP for the motor to take 125, unidirectional steps of length 8 nm, before dissociating [27]. This continuous motion, called processivity, requires a highly-coordinated mechanism to prevent premature MT dissociation and wasteful ATP cycling [28, 29]. Understanding the structure and mechanism of kinesin motion will greatly help computational modelling of the transportation of attached cargo, or the sliding of MTs along other MTs.<sup>2</sup>

### 1.2.1 Kinesins

The kinesin motors are composed of two heads, called the kinesin heavy chain (KHC), and a coiled stalk which connects the heads to cargo via the kinesin light chain (KLC). The kinesin-1 motor, in particular, can perform two tasks:

1. Transport cargo along MTs,
2. transport other MTs, called MT-MT sliding.

Kinesin walking is crucial for both processes.

Kinesin motor heads walk towards the + end of MTs using a hand-over-hand mechanism. This highly-coordinated mechanism, where the release of the trailing head is contingent on the binding of the leading head, allows for kinesin to continuously walk on MTs an average distance of  $1\mu\text{m}$  without falling off, making them highly processive [3, 27]. The mechanism by which kinesin hydrolyses ATP to walk on MTs is sketched in Fig. 1.3.

---

<sup>2</sup>Although we focus on the more processive kinesin motors in this thesis, non-processive motors at higher motor concentrations can also bring about coherent sliding of filament pairs due to cooperative motor action.

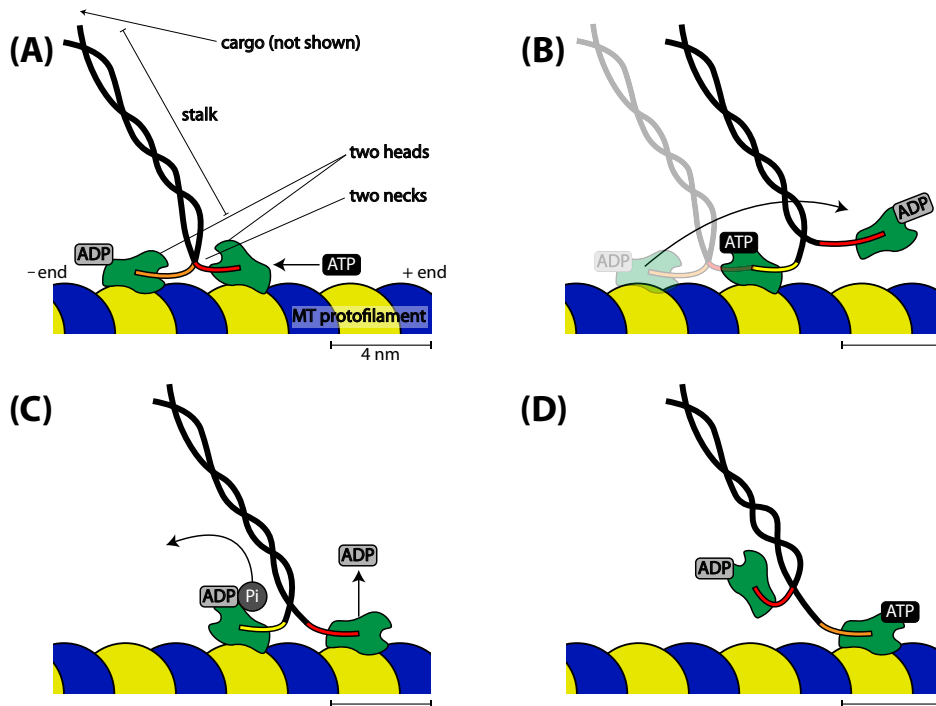


Figure 1.3: Schematic of kinesin motor heads “walking” towards the + end of the MT. The tubulin heterodimers are coloured blue and yellow for the  $\alpha$  and  $\beta$  subunits respectively. The colours of the neck linker indicates if it is released, partially or fully docked. (A) ATP binds to the leading head, initiating the docking of the neck linker. (B) This initiates the “zippering” of the neck linker, detaching the trailing head from its binding site, and thrusts it forward, in what is known as the “power stroke”. (C) Docking of the new leading head releases its Adenosine diphosphate (ADP), and the new trailing head hydrolyses ATP to ADP and inorganic phosphate ( $P_i$ ). (D) ATP binds to the trailing head, and the neck linker “zippering” begins once again [20].

### 1.2.2 Molecular motors obey equilibrium laws

The motor action sketched in Fig. 1.3 is conducted in an environment which is far from chemical equilibrium. Biologically, this is because ADP is converted back to replenish ATP through the oxidative phosphorylation cycle in the mitochondria of cells, and ATP in the bulk is not in chemical equilibrium with ADP and  $P_i$ . Nevertheless, it is important to make the distinction that the molecular motors themselves obey equilibrium laws, *i.e.*, all the constituent reactions that lead to the ultimate catalysed reaction ( $ATP \rightleftharpoons ADP + P_i$ ) follow Michaelis-Menten kinetics and every forward motion is exactly cancelled by its microscopic reverse [30].

The schematic in Fig. 1.4 reduces the mechanical narrative of the kinesin walk to a chemical one. Firstly, from the two descriptions of the motor walk, we see that there is no mechanism by which motors sense bulk concentrations of ATP, ADP and  $P_i$ . Secondly, the seemingly non-equilibrium “power stroke” (Fig 1.3B) can in fact be an equilibrium process [30].

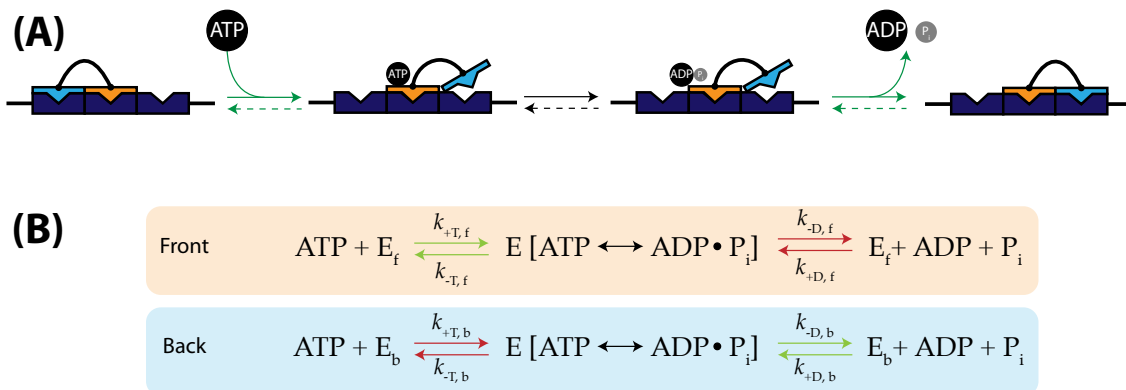


Figure 1.4: Chemical perspective of the ATP hydrolysis-powered molecular walk of kinesin. (A) We indicate that the motor heads, orange and blue, when bound to the MT, are chemically distinct from each other. The walking of the kinesin is described here from left to right: ATP binds to the front head (orange) and causes “zippering” of the neck-linker, throwing the back head (blue) forward. The orange head now becomes the back head and hydrolyses ATP. The products of the reaction dissociate, and the blue head is ready for ATP binding, and the cycle can continue forward. (B) The constituent enzymatic reaction mechanism for both the front ( $E_f$ ) and back ( $E_b$ ) heads are shown. Directional motion is possible because of a difference in specificity between the head bound in the front and back position. The green arrows indicate fast reaction rates, and the red arrows indicate slow reaction rates.

The overall equilibrium constant for the motor walk, according to the schematic in Fig. 1.4, is

$$K_{\text{eq}} = \frac{k_{+T,i}k_{-D,i}}{k_{-T,i}k_{+D,i}}, \quad (1.2)$$

where  $k_{T,i}$  and  $k_{D,i}$  are the rates of binding and dissociation of ATP and ADP from enzyme  $E_i$ .  $E_i$  refers to the front and back catalytic cores, or motor heads,  $E_f$  and  $E_b$ . Since the enzymes  $E_f$  and  $E_b$  are identical, the equilibrium constant is the same at the front and the back. Also, since the reaction intermediate is common for both reactions involving the front and back cores, the ratios of the on and off rates for ATP and ADP is the same at the front and the back,

$$\frac{k_{+T,f}}{k_{-T,f}} = \frac{k_{+T,b}}{k_{-T,b}}, \quad \frac{k_{-D,f}}{k_{+D,f}} = \frac{k_{-D,b}}{k_{+D,b}}. \quad (1.3)$$

This relationship is sufficient to satisfy the principle of microscopic reversibility for the motor walking mechanism. However, we saw that kinesins move unidirectionally on MTs. How can a molecular motor walk in only one direction when for both motor heads there is no special direction in which the reaction proceeds? Namely, how do we establish direction when the forward reaction  $\text{ATP} \longrightarrow \text{ADP} + \text{P}_i$  is not favoured?

This is resolved by the fact that the relative specificities of the front and back catalytic cores need not be the same. The specificity of the enzyme is the ratio of the “off” rates for ATP and ADP,  $s_i = k_{-T,i}/k_{-D,i}$ . For instance, if  $s_f/s_b \gg 1$ , the binding/release of ATP will be much faster than the binding/release of ADP at the front head. This allows

for the “zippering” mechanism; and the binding/release of ADP will be much faster than the binding/release of ATP at the back head.

For the enzymatic reaction mechanism shown in Fig 1.3B, the differences in specificity indicate a mechanism for allosteric feedback from the connecting neck linkers, *i.e.*, the front head of the walker preferentially binds/releases ATP relative to the back head, even though they are capable of identical roles when they swap positions on the MT track. This allosteric bias towards the forward reaction, effectively implements a Maxwell’s demon, which accepts motor steps predominantly towards the + end of the MT, and inhibits backward steps via a higher energy barrier [30].

Effectively, when we follow the green arrows of Fig 1.4B, we get the following mechanism of the catalysis for ATP hydrolysis,



Within a cell, we say that the system is far from equilibrium because the chemical potential due to ATP being in excess of its equilibrium concentration. This shifts the direction of Eq. 1.4 in favour of ATP hydrolysis and the stepping of the motor towards the + end of the MT.

Nevertheless, motors can move towards the – end and the relative specificity of the motor is such that  $s_f/s_b < 1$ . Such an approach to kinesin activity, highlights the notion that the asymmetric direction of motor motion depends only on the position of the motor heads, and their relative enzymatic specificities. Particularly, it does not arise from the mechanistic structure of the power stroke.

### 1.2.3 Two-state motor model

According to Fig. 1.3 and Fig.1.4B, modelling the kinesin walk requires a complex model with eight states.<sup>3</sup> However, we can simplify this to a two-state model. We can construct,  $W_1(x)$  (periodic, saw-tooth potential) and  $W_2(x)$  (flat potential), such that ATP hydrolysis triggers the change of the motor from state  $W_1(x)$  to  $W_2(x)$  [10]. The potential is dependent on  $x$ , which is the position of the motor head on a MT (Fig. 1.5).

Consider a single motor head that starts at the energy minimum in potential  $W_1$ , and via ATP hydrolysis, gets excited to  $W_2$ , as shown in Fig. 1.5. In this state, since  $W_2$  is flat, the motor head is free to diffuse. After a time  $t$ , the probability of the motor arm position can be described by  $P_2(x, t)$ . Due to diffusion, the probability distribution of the motor arm will be a Gaussian that has a halfwidth  $(2k_B T \mu_2 t)^{1/2}$ , where  $\mu_2$  is the mobility of the motor head at  $W_2$ .

After a typical lifetime in this state,  $\tau_2 = \omega_2^{-1}$ , the particle returns to  $W_1$ . Depending on where this transition takes place to the right or left of the maximum of  $W_1$ , the motor head will move to the right or left. Since  $W_1$  is periodic in  $x$ , this process continues. If the motor head position is also affected by an external force,  $f_{\text{ext}}$ , this system can be described using the following Fokker-Planck equations [10, 31],

---

<sup>3</sup>Four states for each of the two heads: (1) E, (2) E-ATP, (3) E-ADP- $P_i$ , (4) E-ADP.

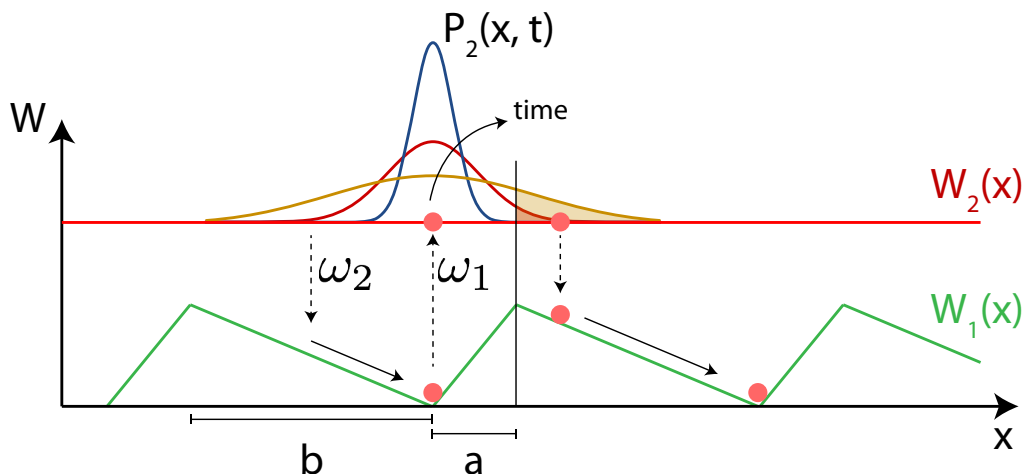


Figure 1.5: Two-state motor model that gives directed motor head motion. The two states correspond to the two potentials  $W_1$  (saw-tooth) and  $W_2 = \text{const}$ . A motor head that remains in the minimum of  $W_1$  for a typical time  $\tau_1 = \omega_1^{-1}$ , can be excited to  $W_2$  after ATP hydrolysis. It returns to  $W_1$  after a typical lifetime  $\tau_2 = \omega_2^{-1}$ , as indicated by the red marker. The Gaussian probability distributions of the motor head at state 2,  $P_2(x, t)$ , are shown evolving as a function of time.

$$\partial_t P_1 + \partial_x J_1 = -\omega_1(x)P_1 + \omega_2(x)P_2, \text{ and} \quad (1.5)$$

$$\partial_t P_2 + \partial_x J_2 = \omega_1(x)P_1 - \omega_2(x)P_2, \quad (1.6)$$

where the probability current  $J_i$ , is given by,

$$J_i = \mu_i^{-1} (-k_B T \partial_x P_i - P_i \partial_x W_i + P_i f_{\text{ext}}). \quad (1.7)$$

The average velocity of the motor head at steady state over one period,  $l = a + b$ , is given by,

$$v = \frac{\int_0^l dx (J_1 + J_2)}{\int_0^l dx (P_1 + P_2)}, \quad (1.8)$$

where distances  $a$  and  $b$  are given in Fig. 1.5.

The velocity of the motor head will depend on the typical residence time on each state  $\tau_1$ , and  $\tau_2$ . For instance, a short lifetime  $\tau_2$  could lead to a smaller probability of moving to the right. However, a very long  $\tau_2$  could mean that the motor head could also move to the left. The optimal residence time for the fastest velocity is  $\tau_2 \simeq a^2 / (\mu_2 k_B T)$ . In order to give sufficient time for the motor head to drift down the potential slope of  $W_1$  and reach the minimum, we can similarly write  $\tau_1 \simeq b^2 / (\mu_1 k_B T)$ , [10].

The hand over hand motion of two kinesin heads will require two such two-state potentials. The energy landscapes of each head will be shifted with respect to each other by  $l$  [31].

### 1.2.4 Dimeric vs. tetrameric motors

Although experimentally prepared motor clusters can crosslink multiple MTs [32, 33], in our simulations we only consider kinesin motors that crosslink MT pairs. Namely, in experiments, two different classes of kinesin motors have been shown to crosslink and cause sliding between MTs.

1. Dimeric motors (*e.g.* kinesin-1 and kinesin-14 [22, 25, 34, 35]) are composed of a motor domain, motile on one MT and a secondary, non-motor MT-binding site which is anchored and not motile on the other MT as shown in Fig. 1.3A.
2. Tetrameric motors (*e.g.* kinesin-5 [36–38]) have two motile motor domains at opposite ends, on both crosslinked MTs. Polymeric motors can also be artificially conjugated by assembling kinesin-1 into multi-motor clusters by tetrameric streptavidin [32, 33]. This allows the motor cluster to simultaneously bind and walk along multiple MT.

When multiple dimeric motors crosslink a MT pair, tangential forces on the MTs arise based on whether the bound motor orientations are correlated (with all anchored arms on one MT and all motile arms on the other MT) or uncorrelated (with anchored arms and motile arms bound on different MTs). Although many simulations have studied the role of tetrameric/polymeric motors on MTs [4–6, 8], important aspects in MT-motor protein mixtures, such as different motor-arm speeds [40], and dimeric motors [41, 42], have rarely been considered so far. In Fig. 1.6, we explicitly consider all the possible orientations that two dimeric and tetrameric motors can adopt when crosslinking two neighbouring MTs.

Since tetrameric motors are symmetric upon motor-arm exchange, only the relative alignment of the crosslinked MTs determines the dynamics (Fig. 1.6A and B). When polar-aligned MTs are crosslinked by tetrameric motors (Fig. 1.6A), the relative velocities of the MTs are small and the force generated by the molecular motors vanishes. Antialigned MTs crosslinked by tetrameric motors (Fig. 1.6B), on the other hand, generate the largest tangential velocity between crosslinked MTs because both arms move at the same time.

Dimeric motors are not symmetric with respect to motor-arm exchange. Thus, for two dimeric motors crosslinking two MTs, four states corresponding to two relative combinations of motors, and two combinations of MT polarity (Fig. 1.6C–F) can be constructed. One possibility is that motors bind to MTs in a spatially correlated manner, such that all motors have their motile arms on one MT and the anchored arms on the other MT (Fig. 1.6C, D). In this case, both polar-aligned and antialigned MT orientations cause relative sliding between them. The other possibility is that motors bind in an uncorrelated manner, such that the motile and anchored arms are bound randomly on either MT. Uncorrelated motors crosslinking a polar-aligned MT pair will act antagonistically because the force imparted by a dimeric motor is counteracted by the force imparted by a motor that binds in the conjugate orientation (Fig. 1.6E). This leads to relatively small forces between MT pairs. Uncorrelated motors between antialigned MTs, however, act cooperatively, and cause relative sliding between MTs (Fig. 1.6F).

In most cases, MT pairs remain in the polar-aligned (or antialigned) orientation for the duration that the motor is bound. This allows us to study the properties of tetrameric

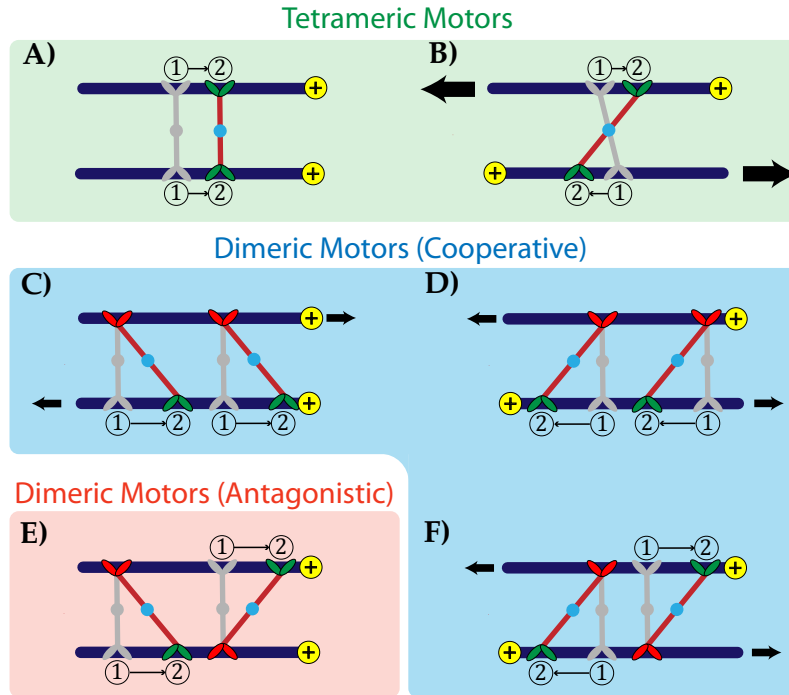


Figure 1.6: Schematic showing the effects of tetrameric and dimeric motors on polar-aligned and antialigned MTs. motor-arms are shown to move from position (1) to position (2), in the direction of MT polarisation, represented by the yellow marking at the MT tip. The grey representations show the initial attachment positions of motors. Active motor-arms that move on the MT direction of polarisation are coloured green, and immobile, anchored motor-arms are coloured red. Tetrameric motors have two motile arms on either crosslinking MT. Dimeric motors have an anchored arm and a motile arm. (A) Tetrameric motors crosslinking aligned MTs induce small velocities. (B) Tetrameric motors crosslinking antialigned MTs induce larger velocities. (C) Correlated dimeric motors crosslinking aligned MTs have the same effect as (D) dimeric motors crosslinking antialigned MTs. (E) Uncorrelated dimeric motors crosslinking aligned MTs act antagonistically, (F) whereas uncorrelated dimeric motors crosslinking antialigned MTs act cooperatively [39].

and dimeric motors crosslinking polar-aligned and antialigned MTs separately, giving four motor categories: dimeric/polar-aligned, dimeric/antialigned, tetrameric/polar-aligned and tetrameric/antialigned.

### 1.3 Cytoplasmic streaming

Diffusion can be ineffective in distributing organelles and molecules homogeneously throughout the cell, or to specific locations. Studies have shown that cells use a combination of specific anchoring mechanisms and cytoplasmic streaming to actively transport molecules throughout the cell, *i.e.*, molecules travel due to the advection of MTs, and localise in certain locations due to the anchoring and adhesion specific to those regions [43]. The mechanism of streaming, in particular, circulates the fluid contents by bulk motion of cytoskeletal components.

This mechanism is ubiquitous across eukaryotic cells, namely during reproduction, growth and development of cells in plants [44–46] and animals [34, 43, 47–50]. Although there is still only a poor quantitative understanding of cytoplasmic streaming and its mechanism, its importance in the distribution of chloroplasts in plants [51], and the asymmetric position of the meiotic spindle in mammalian embryos [52], is clear. Mechanisms for cytoplasmic streaming have been described using either the hydrodynamic effect of motors on cytoskeletal filaments, or the sliding of neighbouring cytoskeletal filaments on each other facilitated by motors.

### 1.3.1 Flows due to microtubule sliding

Although molecular motors are small, vesicles and organelles carried by the motors are large compared to the motors [53]. Considerable fluid can be entrained by the motion of this cargo along the cytoskeletal filaments giving large-scale flows. According to some theories, these flows are enough to generate fast + end directed fluid flows to facilitate mixing at low Reynolds numbers [46, 54]. Other theories have suggested that the hydrodynamic drag on motor-driven cargoes can mediate equal and opposite forces, between the cytoplasmic fluid and filaments tethered to cell membranes, causing them to align and buckle [55]. These theories are particularly attractive to explain unidirectional MT streaming. However, they are inadequate to reconcile a bidirectional MT sliding mechanism.

This question was partially addressed by the discovery of two distinct populations of MTs: immotile MTs anchored to the actin cortex near the cell membrane, and free cytoplasmic microtubules that move in the ooplasm. Lu *et al.* posit that the directed streaming process is carried out by the motors which use the anchored MTs that serve as tracks to propel cytoplasmic MTs against, as shown in Fig. 1.7. In fact, MTs anchored to the cortex do not have to be aligned in any coordinated fashion. As long as cytoplasmic MTs encounter an antialigned anchored counterpart, the system will be mixed by active flows from the cortex.

It is well established that MT-MT sliding is a crucial process that drives anaphase during mitosis,<sup>4</sup> and flagellar movement. However, recent experiments *in vivo* have shown that MT-MT sliding is ubiquitous, and widely used for biological processes across organisms that require bulk MT motion within a cell [25]. In particular, these experiments challenge theories that suggest MT buckling and streaming is due to motion of cargo.

It was shown that the two roles of kinesin-1: transporting cargo and MT-MT sliding, are distinct and are carried out by two different mechanisms within the motor complex. Namely, knocking down the cargo-binding light chain did not affect MT-MT sliding, but knocking down the kinesin heavy chain affected it. This was further substantiated by MT transport being 10-fold slower than cargo transport, which was due to a decrease in motor velocity due to higher load [25].

---

<sup>4</sup>Anaphase is the third stage of cell division, where chromosomes separate from one another to apposite poles of the mitotic spindle. This is a well-studied phenomena which is known to be driven by MT mediated motion.

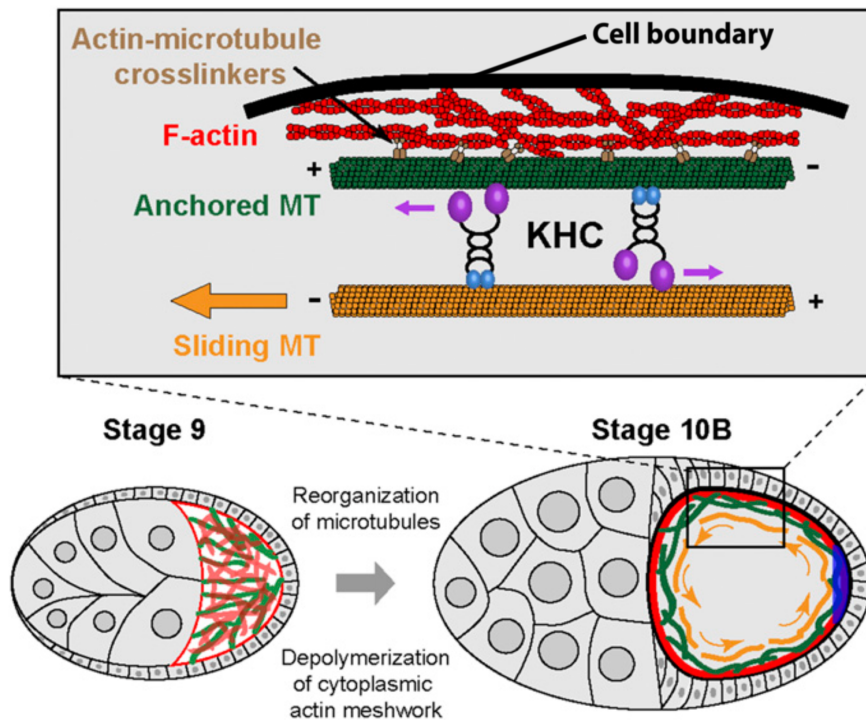


Figure 1.7: Illustration of a dimeric kinesin-based MT sliding mechanism in *Drosophila* ooplasm. Stage 9 and stage 10B, refer to the stages of the cell cycle of the oocyte. Between the two stages, MTs are actively organised. At stage 10B, the F-actin cortex at the cell boundary stabilises a layer of anchored MTs via actin-microtubule crosslinkers. This allows for the sliding and circulation of MTs throughout the cell. KHC refers to the kinesin heavy chain. Image is adapted from Ref. [50].

### 1.3.2 Streaming in cells

To realistically capture aspects of streaming in a cell, cytoskeletal activity must occur within a confined and crowded environment [56]. For instance, it has been shown that confinement can decrease the critical filament density for the isotropic-nematic phase transition [57] and induce formation of clustering and bundle-like structures [58]. Also, it is known that confining the cytoskeleton within cells influences mitotic organization and spindle positioning [59,60], the deformation and orientation of the nucleus [61] and cellular protrusions produced by actively treadmilling actin filaments called the lamellipodium<sup>5</sup> [62] (see Sec. 1.1.2 for a physical model for MT polymerisation).

In the *Drosophila* oocyte at mid-oogenesis, this leads to the striking phenomena, where cytosolic molecules such as the body plan determinant *oskar* mRNA are localized inhomogeneously within the cell, as shown in Fig. 1.8(c) and (d) [43]. Inhomogeneities in MT distribution, like the anchored MTs at the oocyte cortex, upon which cytoplasmic MTs push against with the aid of kinesins have been reported to be key for bulk motion within the cytoplasm [50].

<sup>5</sup>Lamellipodia are cytoskeletal projections that develop at the leading edge of the cell assisting cell motion.

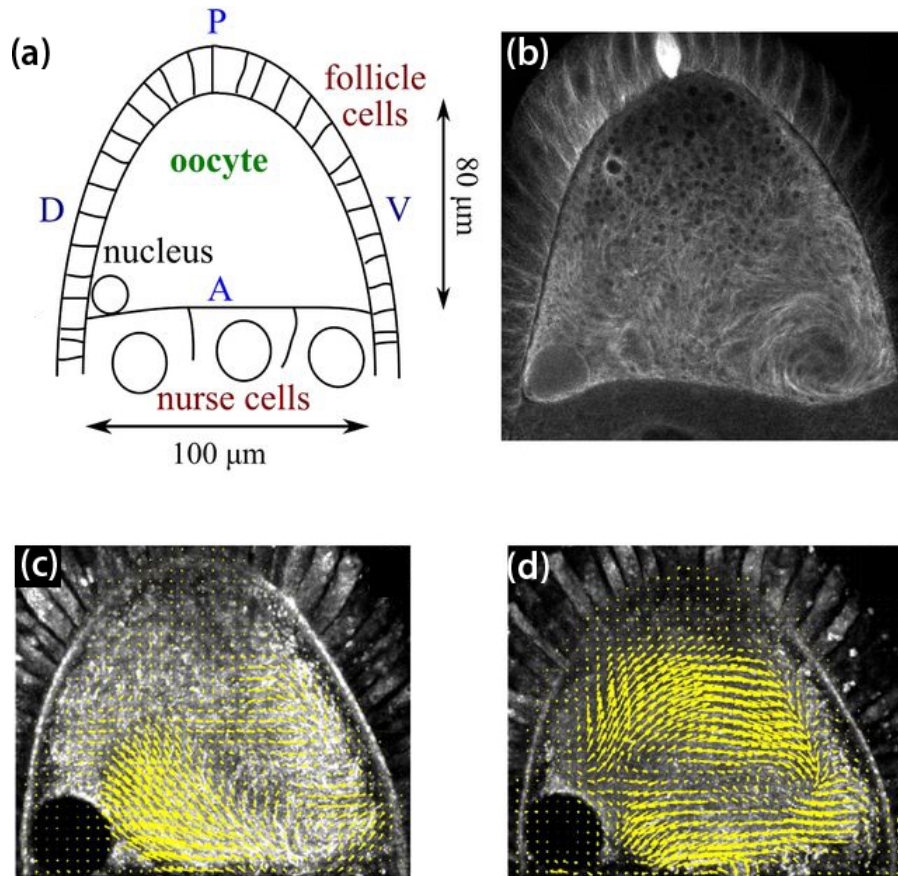


Figure 1.8: **(a)** Illustration of *Drosophila* oocyte indicating the positions of the anterior *A*, posterior *P*, dorsal *D*, and ventral *V* regions. **(b)** Photograph of a dense network of fluorescently labelled microtubule within the oocyte. **(c)** and **(d)** Dynamic flow field of swirls and streams, indicated by the yellow arrows at different times. The flow field is generated using particle image velocimetry, where passive tracers are used to track microtubule advection, and the trajectories of 10 frames are visualised. The nucleus (circular black region) in each image is approximately  $15 \mu\text{m}$ . Image is adapted from Ref. [43].

In coarse-graining the molecular details of the cytoskeleton, most simulation studies have largely ignored depletion interactions between MTs, which can occur from the cytoplasm being a crowded environment [46], where macromolecules occupy 20–30% of the total volume [56]. MT bundling frees up additional volume for smaller particles, increasing the overall system entropy resulting in an effective attraction [32,63].<sup>6</sup> On top of having an effect on the overall structure of a passive MT system without motors, depletion interactions bring MTs together making them amenable to the crosslinking of molecular motors.

<sup>6</sup>see Fig. 1.11(a), Figs. 2.2(c) and (d)

## 1.4 Theoretical Descriptions

Remarkable examples of these microscopic engines have also been observed in cases of reconstituted systems of MTs and kinesin motors *in vitro*, *e.g.*, the self-organization of MT-motor mixtures into dynamic asters and vortices [64], and the spontaneous motion in an active gel of stabilised MT bundles under the activity of multi-motor clusters of kinesins [32, 33]. When MTs and motors were topologically constrained within a deformable, giant, lipid vesicle, spatiotemporal patterns that gave interacting defect configurations and filopodia-like protrusions were observed [65].

Although active biological molecules move because of microscopic driving mechanisms, the collective motion and structures in active gels have been attributed to a combination of hydrodynamics (wet) or steric and stochastic effects (dry). Active systems with hydrodynamic interactions have an energy input which is dissipated by the damping from the viscosity of the bulk medium. Orientable active objects in such a solution, exhibit large-scale, long-time correlations due to their interactions through the solute medium between them.

However, many active materials can dissipate energy in other ways, such as friction between particle and substrate, or steric effects due to high density. In this limit, there is no momentum conservation *i.e.*, all of the momentum is damped by friction with the substrate. The Toner-Tu model [66] gives a phenomenological continuum model, of a self-propelled active system, by coarse graining the microscopic Vicsek model [9, 67].

### 1.4.1 Phase transitions in confinement

Before studying the structure and dynamics of rigid rods in an active system, it is instructive to understand the density-dependent phase transition for a passive system of rods. For a dilute mixture of rods, the orientation of rods are isotropic, maximising rotational entropy. When density is increased, steric interactions between rods dominate and drive up the free energy, and the rods pack parallel to each other. The isotropic-nematic phase transition, as described by Onsager, occurs due to the competition of entropic and steric effects. Structures formed by nematic rods in two dimensions have a two fold-rotational symmetry in embedding plane.

Confining the rods causes geometric frustration, which leads to topological defects. A system of  $N$  passive rods of length  $L$  in a circular confinement of diameter  $a$  was recently studied [68]. At low densities, the rods are disordered and isotropic giving the  $D_\infty$  state. Increasing the density above a critical reduced rod density  $\tilde{\rho}_c = L^2 N/A$  gives either an ordered  $O_2$  state or a metastable  $O_\infty$  state, as shown in Fig. 1.9. The  $O_2$  state gives two  $+1/2$  defects at the boundary. We can define an order parameter,  $S$ , based on the angle of the rods with respect to an arbitrary horizontal line,

$$S(r, \phi) \equiv \int_0^{2\pi} d\theta \cos(2\theta + 2\phi) f(r, \phi, \theta), \quad (1.9)$$

where  $f(r, \phi, \theta)$  is a mean segmental distribution. The symbols  $r$ ,  $\theta$  and  $\phi$  are according to Fig. 1.9(a). Thus, the overall orientational order parameter can be written as,

$$\bar{S} = \frac{4}{\pi a^2} \int_0^{a/2} dr \int_0^{2\pi} d\phi r S(r, \phi). \quad (1.10)$$

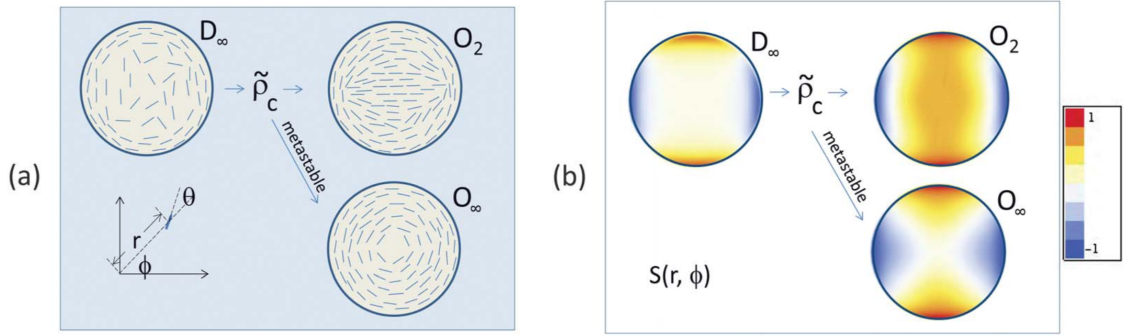


Figure 1.9: **(a)** Schematic for the structures formed by rods confined within a circular line boundary. The system transitions from a disordered/isotropic state,  $D_\infty$ , to a stable  $O_2$  state or a metastable  $O_\infty$  state, after reaching a critical reduced rod density  $\tilde{\rho}_c$ . **(b)** Resulting orientational order parameter for the structures described in **(a)**. Image is reproduced in part from [68] with permission of The Royal Society of Chemistry.

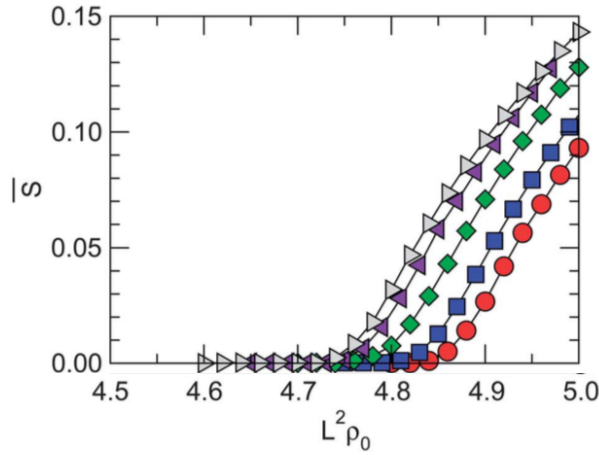


Figure 1.10: **(a)** Schematic for the structures formed by rods confined within a circular line boundary. The system transitions from a disordered/isotropic state,  $D_\infty$ , to a stable  $O_2$  state or a metastable  $O_\infty$  state, after reaching a critical reduced rod density  $\tilde{\rho}_c$ . **(b)** Orientational order parameters for the structures described in **(a)**. Image is reproduced in part from [68] with permission of The Royal Society of Chemistry.

As shown in Fig. 1.10, below  $\tilde{\rho}_c$ , when the rods are disordered,  $S = 0$ . When the density is above  $\tilde{\rho}_c$ ,  $S(r, \phi)$  increases significantly in the  $O_2$  state. The local orientational order near the boundary for low rod densities does not contribute to  $S(r, \phi)$  because the contributions along the entire boundary cancel each other. This is schematically illustrated in Fig. 1.9(b).

#### 1.4.2 Continuum theories of active nematics

Various works have used Brownian dynamics simulations without hydrodynamics to understand the underlying mechanisms of filament-motor systems [6, 7]. Works that treat MTs as rigid rods, using what is known as the Mikado model, and perform simulations

at the isotropic-nematic phase transition density, report propulsion-like forces arising due to the effect of motors crosslinking antialigned MTs [4, 5]. However, they resort to a continuum hydrodynamic theory, driven by polarity-dependent active stresses, to obtain large-scale flows and defect structures [5]. Although these theories that use a continuum model for an active nematic [5, 69, 70] are useful in giving good agreement to experiments discussed in the next section, they fail to explain the onset of large-scale phenomena (hydrodynamic or otherwise) from the level of molecular motors.

### 1.4.3 Large-scale motion in active nematics

In the case of structures formed by rigid filaments interacting only via steric interactions, entropy favours states with higher degrees of randomness. Hence, at low densities, we expect an isotropic distribution of rods, maximising rotational entropy. As the density increases, the excluded volume of the rods become significant, and drives the free energy up. Onsager showed that, for thin rods, above a critical packing density purely determined by the rods' aspect ratio, a nematic phase where rods spontaneously align arises. At high densities, this liquid crystalline state minimises the energy due to excluded volume [71]. Both length polydispersity and filament flexibility increase the critical density [72].

Apart from biological applications, the MT-MT sliding mechanism, shown in Fig. 1.11(a) and (b), have generated complex streaming flows, and a continuous creation and annihilation of topological defects in reconstituted liquid crystals out of equilibrium [33]. Multiple kinesin motors were conjugated using streptavidin clusters and applied to a mixture of MTs which are depleted onto a surfactant-stabilised oil/water interface [32]. This internally generates activity causing the MT pairs to extend, driving chaotic flows, shown in Fig. 1.11(c). Moreover, by using topological constraints, and confining the active nematics to the surface of a vesicle, it is possible to control the non-equilibrium dynamical modes [65]. Remarkable examples of collective motion have also been observed in a dense motility assay of actin filaments driven by immobilized molecular motors in a planar geometry. The filaments form structures that move together forming clusters, swirls and bands [74, 75]. To turn such interesting phenomena into biomimetic active materials, it is important to understand the mechanisms involved that give rise to such large-scale phenomena.

Namely, in such works it is difficult to disentangle to what extent these features, observed at high density, arise due to hydrodynamic flows generated in the smaller length scale by molecular motors. Long-range order, and the bending and buckling, and persistent flows, can also result due to steric forces at high density, and “dry” active motion due to the handing off of MT-MT sliding from one antiparallel MT pair to another.

## 1.5 Outline

In this thesis, with the use of computational tools and phenomenology-based physical models, we will focus on one of the most intriguing questions of cell biology: How do kinesin motors mediate motion in MTs inside cells?

In Chapter 2, we define the model used to study two systems: two different types of explicit motors mediating MT activity in confinement, and an effective motor potential

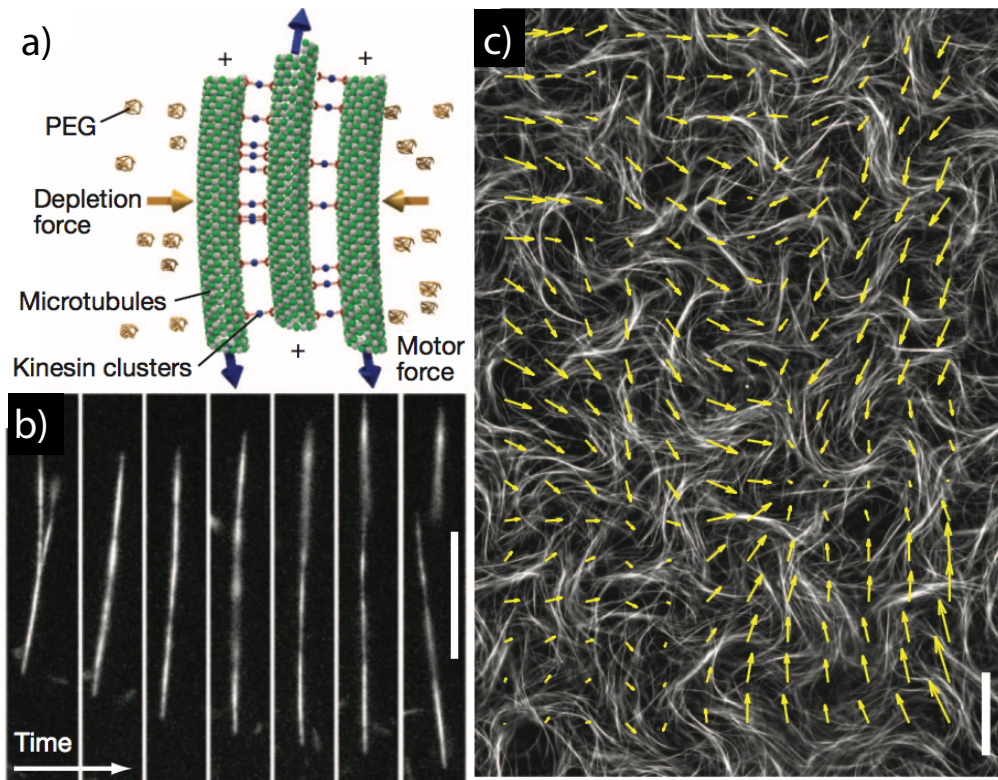


Figure 1.11: (a) Illustration of MT bundles brought together by depletion forces due to PEG polymers, and extensile forces generated by kinesin motor clusters between them. (b) Merging and extension of antialigned MTs in the reconstituted *in vitro* experiment. The time interval between each of the seven images is 5 seconds. Scale bar represents 15  $\mu\text{m}$ . (c) Microtubule network with arrows indicating the velocity field of bundles. Scale bar represents 80  $\mu\text{m}$ . Image adapted from Ref. [73].

that drives MT activity under periodic boundary conditions. On top of studying a phenomenological 1-D model, which inspired the effective motor potential, we also define the theory behind the dynamics of passive and active filaments. In Chapter 3, we qualitatively describe confined MT structures that arise due to explicitly modelled tetrameric and dimeric motors. We present these results as a function of all system parameters. We also introduce the local polar order parameter, which describes the local orientation of MTs surrounding the MT in question. In Chapter 4, we explain the dynamical properties of MTs under various motor concentrations and MT-MT depletion interaction strengths, for both classes of motors. We highlight that the attractive confinement is important for higher MT dynamics near the confining wall. In Chapter 5, instead of using explicitly defined motors, we use an effective motor potential to give the effect of motors on MT. We quantify the occurrence of coherent MT streams under periodic boundary conditions, for various activities and surface fractions. In this chapter, we also systematically study the time scale of diffusion, motor propulsion, and coherent streaming. In Chapter 6, we summarise the findings in this thesis, explain the limitations of the models, and give an outlook for future studies.

## Chapter 2

# Multiscale model of microtubules and motors

Many cellular-level processes, such as cytoplasmic streaming, require molecular level characterisation and the unification of complex biomolecular systems across length and time scales. Motile systems can be studied either by ignoring microscopic mechanisms and focussing on macroscopic properties, or by just measuring the microscopic properties of individual components. In order to capture cellular-scale phenomena, we begin by describing the marriage between three distinct length scales:

1. molecular motors; the smallest elements,
2. MTs; the major components whose activity is of main interest, and
3. the confining wall; the largest length scale.

We describe how these components are numerically modelled to obtain a variety of large-scale structures in 2-D. Although real cells are intrinsically 3-D, this model is relevant to experiments that study cytoplasmic streaming within a plane for cells that are attached to a substrate. Moreover, our simulations directly apply to experimental 2-D model systems of cytoskeletal filaments [32, 33, 65], and extends previous studies of MT-motor systems [4–6].

In Sec. 2.1, we describe the theoretical framework for the introduction of stochasticity through the Langevin equation. In this section, we also provide a description for the anisotropic friction of rigid rods, and the translational and rotational diffusion of their centers of masses due to their interaction with a solvent. In Sec. 2.2 we detail the simulation schematic by describing the penetrable MT-MT interaction potential, the forces mediated by tetrameric and dimeric motors, and the Lennard-Jones force between MTs and the confinement. We also explain the set up of the initial condition for MTs and provide the dynamical equations integrated to obtain Brownian Dynamics. In Sec. 2.3, we explain the model used for the effective motor system. We explain a phenomenological model of an equivalent 1-D system, and describe the MT-MT interactions and the effective motor interaction used to propel neighbouring antialigned MTs. In Sec. 2.4, we provide a tabulated list of differences between the two models.

## 2.1 Langevin dynamics for active rods

Active filament motion can be understood from the mean-squared displacement (MSD) of either its composing beads, or the filament center of mass. In most cases, it is useful to compare the active MSD with passive diffusion.

One possible description of Brownian motion is given in the Langevin equation. Assuming we have a Brownian particle of mass  $m$ , whose velocity is denoted by  $v$ , experiencing a stochastic force  $\delta F(t)$ , we can write

$$m \frac{dv}{dt} = -\zeta v + \delta F(t), \quad (2.1)$$

where  $\zeta = 6\pi\eta a$  is the friction experienced by the particle from Stokes' law. Both friction,  $\zeta v$ , and noise,  $\delta F(t)$ , are forces which arise from the interaction of the particle with the environment. The fundamental relationship between these two forces is known as the fluctuation-dissipation theorem [76].

### 2.1.1 Fluctuation-dissipation theorem

We assume that the random force,  $\delta F(t)$ , varies rapidly over the time of any observation. This fluctuating force is Gaussian distributed, with moments,

$$\langle \delta F(t) \rangle = 0, \quad \langle \delta F(t) \delta F(t') \rangle = 2B\delta(t - t'), \quad (2.2)$$

where  $B$  in the standard deviation of the stochastic force denotes its strength. The delta function,  $\delta(t - t')$ , is used such that there is no correlation in  $\delta F$  between  $t$  and  $t'$ .

Equation 2.1 is a linear, first-order, inhomogeneous differential equation, for which the solution is

$$v(t) = e^{-\zeta t/m} v(0) + \int_0^t dt' e^{-\zeta(t-t')/m} \frac{\delta F(t')}{m}. \quad (2.3)$$

The first term gives the exponential decay of any initial velocity, and the second term provides the thermal kicks from the stochastic force. From the equipartition theorem, we expect that  $\langle v^2 \rangle_{eq} = k_B T/m$ . Eq. 2.3 provides three contributions to  $v^2$ . The first of which,

$$e^{-2\zeta t/m} v(0) \quad (2.4)$$

decays to zero at long times. The cross terms, each first order in noise,

$$2v(0)e^{-\zeta t/m} \int_0^t dt' e^{-\zeta(t-t')/m} \frac{\delta F(t')}{m}, \quad (2.5)$$

vanish when averaged over noise. The third term is second order in noise,

$$\int_0^t dt' e^{-\zeta(t-t')/m} \frac{\delta F(t')}{m} \int_0^t dt'' e^{-\zeta(t-t'')/m} \frac{\delta F(t'')}{m}. \quad (2.6)$$

We can average the two noise factors using Eq. 2.2,

$$\int_0^t dt' e^{-\zeta(t-t')/m} \int_0^t dt'' e^{-\zeta(t-t'')/m} \frac{2B\delta(t' - t'')}{m^2}. \quad (2.7)$$

This gives,

$$\langle v(t)^2 \rangle = e^{-2\zeta t/m} v(0)^2 + \frac{B}{\zeta m} (1 - e^{-2\zeta t/m}). \quad (2.8)$$

For  $t \rightarrow \infty$ , we find,

$$\langle v(t)^2 \rangle = \frac{B}{\zeta m}. \quad (2.9)$$

Since we know that in the long-time limit,  $\langle v(t)^2 \rangle = k_B T/m$ , we get,

$$B = \zeta k_B T. \quad (2.10)$$

Brownian motion in stiff filaments manifests as translational and rotational motion. Translational diffusion is the stochastic motion of the filament's center of mass denoted by position vector  $\mathbf{r}$ . Rotational diffusion is the stochastic motion of the filament's orientation vector denoted by unit vector  $\mathbf{p}$ .

### 2.1.2 Rotational diffusion

In order to calculate the torque due to hydrodynamic friction, let us consider a rod, made up of  $N = L/b$  beads in a viscous fluid [77]. The rod is subject to a torque  $\mathbf{T}$ , which causes it to rotate with angular velocity  $\boldsymbol{\omega}$ . For the following calculations we assume that the rod is thin, neglect rotation along the axis  $\mathbf{p}$ , and that both  $\mathbf{T}$  and  $\boldsymbol{\omega}$  are perpendicular to  $\mathbf{p}$ .

The rotational diffusion constant,  $D_R$  of such a rod in 2-D, can be calculated using,

$$\langle \mathbf{p}(t) \cdot \mathbf{p}(0) \rangle = e^{-D_R t}. \quad (2.11)$$

Note that the dimension of  $D_R$  is  $[\text{time}]^{-1}$ . The characteristic rotation time is  $\tau_R = D_R^{-1}$ .

Assuming  $\mathbf{T}$  is small, and  $\boldsymbol{\omega}$  is linear in  $\mathbf{T}$ , we can write,

$$\boldsymbol{\omega} = \frac{1}{\gamma_r} \mathbf{T}, \quad (2.12)$$

where  $\gamma_r$  is the rotational friction constant. We can estimate  $\gamma_r$ , by considering the frictional forces acting on each segment of the rod. The bead  $n$ , numbered from  $-N/2$  to  $N/2$ , is a distance  $nb$  away from the centre of mass of the rod and moves with velocity  $\mathbf{V}_n = \mathbf{T} \times nb\mathbf{p}$ . The frictional force acting on segment  $n$  is  $-\zeta_0 \mathbf{V}_n$ , where  $\zeta_0$  is again obtained from Stoke's law. Since  $b$  is the diameter of the bead,  $\zeta_0 = 3\pi\eta b$ , where  $\eta$  is the viscosity of the solution. The total torque due to the hydrodynamic friction,  $\mathbf{T}_f$  can thus be calculated using,

$$\mathbf{T}_f = - \sum_{n=-N/2}^{N/2} nb\mathbf{p} \times \zeta_0 \mathbf{V}_n \quad (2.13)$$

$$= -\eta \frac{\pi L^3}{4} \boldsymbol{\omega}. \quad (2.14)$$

Since, there is no net torque on the rod,  $\mathbf{T}_f$  must balance the external torque  $\mathbf{T}$  (due to an external field, or active forces). Using  $\mathbf{T} = -\mathbf{T}_f$ , we can compare Eq. 2.14 with Eq. 2.12 and get,

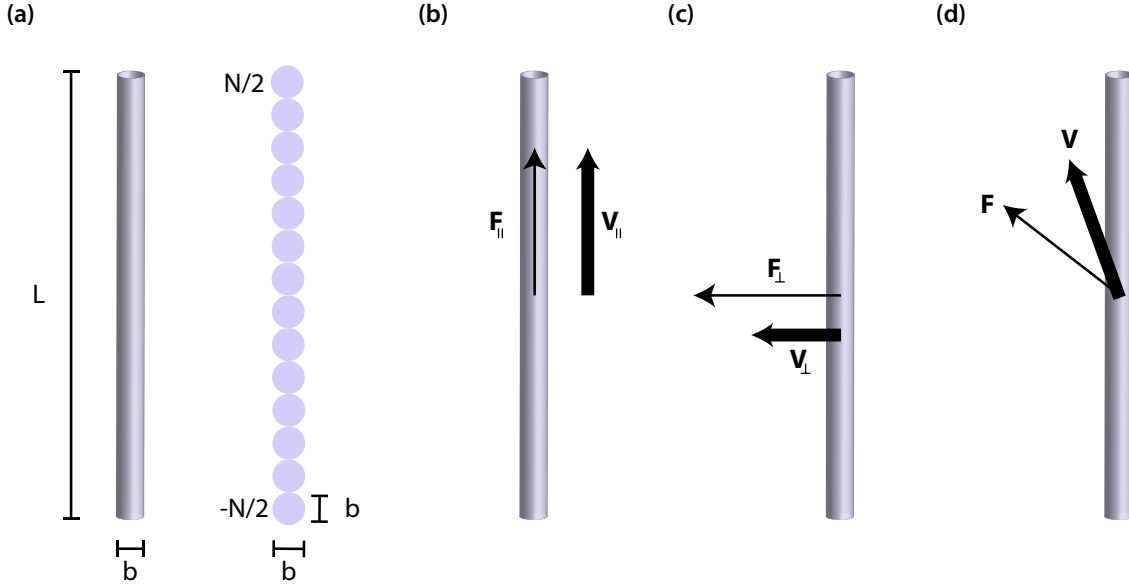


Figure 2.1: (a) Bead based model for a rigid rod used for rotational friction calculation. Velocity,  $\mathbf{V}$ , decomposed into parallel (b) and perpendicular (c) components. (d) The overall anisotropic translational velocity in response to force,  $\mathbf{F}$ .

$$\gamma_r = \frac{\pi\eta L^3}{4}. \quad (2.15)$$

A more precise hydrodynamic calculation of  $\gamma_r$  with a correction  $\alpha$  is found to be [77],

$$\gamma_r = \frac{\pi\eta L^3}{3\ln(L/b) - \alpha}. \quad (2.16)$$

Following a similar treatment as in Sec. 2.1.1, we obtain [77],

$$D_r = \frac{k_B T}{\gamma_r} = \frac{3\ln(L/b) - \alpha}{\pi\eta L^3}. \quad (2.17)$$

### 2.1.3 Translational diffusion

Consider the rod moving with velocity  $\mathbf{V}$  in the same fluid, along its orientation vector  $\mathbf{p}$ . The rod will feel a hydrodynamic drag,  $\mathbf{F}_{\parallel}$ , parallel to its axis, proportional to its velocity, and can be written as  $\mathbf{F}_{\parallel} = \gamma_{\parallel} \mathbf{V}$ , as shown in Fig. 2.1(b). If  $\mathbf{V}$  is perpendicular to  $\mathbf{p}$ , the drag is still parallel to  $\mathbf{V}$ , and is written as  $\mathbf{F}_{\perp} = \gamma_{\perp} \mathbf{V}$ , as shown in Fig. 2.1(c).

In general, the parallel and perpendicular components of the translational friction constant are not equal,  $\gamma_{\parallel} \neq \gamma_{\perp}$  [77]. Hence, the response of the rod to force,  $\mathbf{F}$ , is anisotropic with respect to  $\mathbf{p}$ , as shown in Fig. 2.1(d). We can write this using,

$$\mathbf{F} = \gamma_{\parallel} \mathbf{V}_{\parallel} + \gamma_{\perp} \mathbf{V}_{\perp}. \quad (2.18)$$

The parallel and perpendicular component of velocity can be written as,

$$\mathbf{V}_{\parallel} = (\mathbf{V} \cdot \mathbf{p}) \mathbf{p}, \quad (2.19)$$

and,

$$\mathbf{V}_\perp = (\mathbf{V} - \mathbf{V}_\parallel), \quad (2.20)$$

respectively. We now have,

$$\mathbf{F} = \gamma_\parallel \mathbf{pp} \cdot \mathbf{V} + \gamma_\perp (\mathbf{I} - \mathbf{pp}) \cdot \mathbf{V}, \quad (2.21)$$

where,

$$\gamma_\parallel = \frac{2\pi\eta L}{\ln(L/b)}, \quad (2.22)$$

and,

$$\gamma_\perp = 2\gamma_\parallel, \quad (2.23)$$

from Kirkwood theory [77,78]. Finally, solving for  $\mathbf{V}$  from Eq. 2.21 gives,

$$\mathbf{V} = \left( \frac{1}{\gamma_\parallel} \mathbf{pp} + \frac{1}{\gamma_\perp} (\mathbf{I} - \mathbf{pp}) \right) \cdot \mathbf{F}. \quad (2.24)$$

From the Smoluchowski equation, we can also derive the parallel and perpendicular diffusion constants [77],

$$D_\parallel = \frac{k_B T}{\gamma_\parallel} = \frac{k_B T \ln(L/b)}{2\pi\eta L}, \quad (2.25)$$

and,

$$D_\perp = \frac{k_B T}{\gamma_\perp} = \frac{k_B T \ln(L/b)}{4\pi\eta L}. \quad (2.26)$$

For a passive rod, we can write the purely parallel or perpendicular displacement of its center of mass,  $\mathbf{r}$ , in a small time interval  $\delta t$  as,

$$\langle (\mathbf{r}(\delta t) - \mathbf{r}(0))^2 \rangle = 2D_p \delta t, \quad (2.27)$$

where  $D_p$  can either be  $D_\parallel$  or  $D_\perp$  diffusion depending on the direction in which the rod is translating. We use  $D$  to describe the translational diffusion coefficient.

#### 2.1.4 Active fluctuations

Thermal and active fluctuations are the two main contributions to stochasticity in active systems. Thermal fluctuations are present in both active and passive systems, since particles are linked inextricably to their surrounding, and thus a temperature bath. Active fluctuations, on the other hand, can arise due to various other seemingly stochastic, often biological, events. Activity in MT-motor systems is sensitive to the number of kinesins that connect two MTs, or the quantity of ATP available in the environment where the motors are walking. The importance of such active fluctuations increases with decreasing system size.

The Péclet number is commonly used as a measure of activity. It is defined to be the ratio of advection and diffusion time scales. Self-advection time-scale gives the typical time which an active filament takes to cross its own contour length. It is given by  $L/v_0$ ,

where  $L$  is the contour length of the filament, and  $v_0$  is typical filament velocity. The diffusion time scale is given by  $L^2/D$ . The Péclet number is thus,

$$Pe = \frac{v_0 L}{D}. \quad (2.28)$$

The MSD for active particles (*e.g.* point particles, spheres, or stiff rods) in 2-D is given by [79, 80],

$$\langle |\mathbf{r}(t) - \mathbf{r}(0)|^2 \rangle = 4Dt + \frac{2v_0^2}{D_r^2} (D_r t + e^{-D_r t} - 1). \quad (2.29)$$

At short times,  $t \ll \tau_R$ ,

$$\langle |\mathbf{r}(t) - \mathbf{r}(0)|^2 \rangle = 4Dt + v_0^2 t^2, \quad (2.30)$$

which can be thought of superposing the active piece,  $v_0^2 t^2$ , to passive diffusion,  $4Dt$ . At long times,  $t \gg \tau_R$ ,

$$\langle |\mathbf{r}(t) - \mathbf{r}(0)|^2 \rangle = 4Dt + \frac{2v_0^2}{D_r} t. \quad (2.31)$$

We use Eq. 2.31 to define the active translational diffusion coefficient,

$$D_{\text{active}} = D + \frac{v_0^2}{2D_r}. \quad (2.32)$$

## 2.2 Explicit motor system

### 2.2.1 Volume exclusion and depletion interactions

When we ignore hydrodynamic interactions, we rely on steric, depletion and active forces to induce large scale structures. In order to study the effects of depletion interactions, and MT overlap penalties on large scale structures, we need to be able to tune them carefully. To this end, we reduce the MTs' molecular details explained in Sec.1.1.1 to a 2-D coarse-grained model.

Because MTs are rigid objects, see Table 1.1, for analytical tractability and for quantifying observables, it suffices to describe them using only their center-of-mass,  $\mathbf{r}_i$ , and their orientation,  $\mathbf{p}_i$  (Fig. 2.2). In order to numerically model them, we describe MTs as semi-penetrable, rigid rods of length,  $L$ , discretised into linearly arranged  $n_b$  beads of diameter  $r_{\min}$  as described previously in Sec. 2.1.2. We define the bead diameter to be the position of the minimum of the MT-MT interaction potential. In order for MTs to “feel” each other as contiguous entities, and not a collection of discrete beads, the beads overlap. We place a bead every  $0.5r_{\min}$ , such that  $L = 0.5r_{\min} (N_B - 1)$ .

Such a description of a filament entity is known as a linear site-site potential, and it makes calculation of interactions between beads of neighbouring filaments easy.<sup>1</sup> Each bead, which makes up a MT, interacts with beads from neighbouring MTs with a capped

---

<sup>1</sup>Note that single-site potentials, used extensively in liquid crystalline simulations, such as the Gay-Berne potential, are available to model interactions between rods and ellipsoids. They use the distance between two filament's center of masses, and their relative orientations to give the interaction force between them. Such potentials are well capable of capturing the behaviour of linear site-site potentials [81]. Despite the 10 – 20% improvement in computational speed and accuracy [82], we have avoided using such a potential, because it is difficult to implement, and attractive Gay-Berne potentials are not well studied

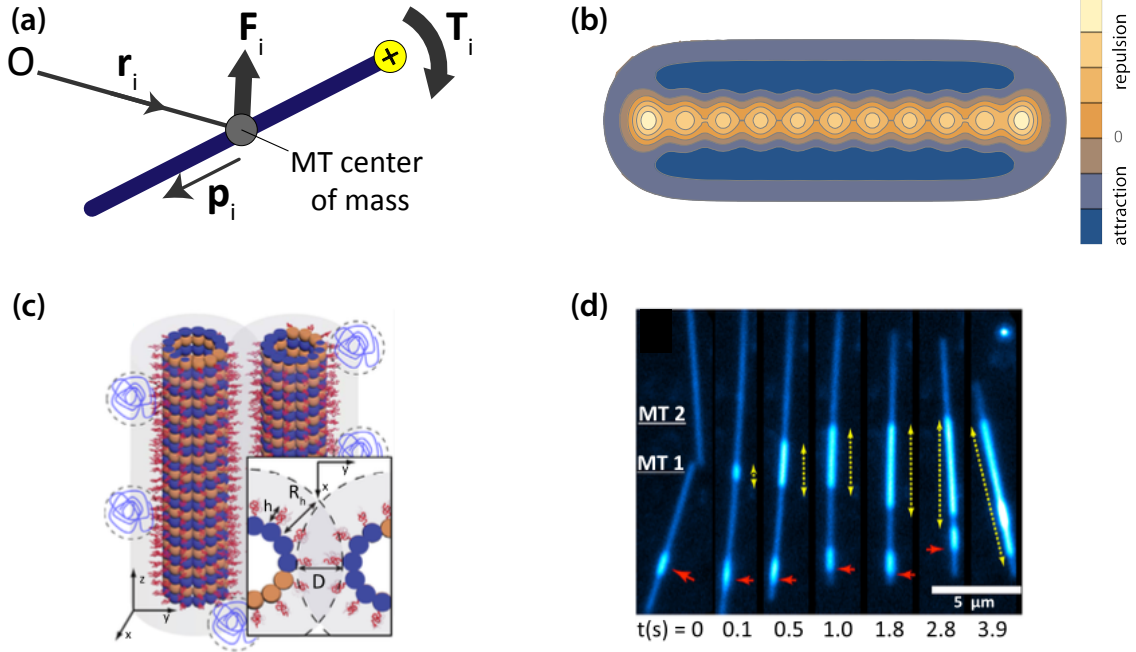


Figure 2.2: (a) Force,  $F_i$ , and torque,  $T_i$ , acting on MT  $i$ , with center-of-mass,  $r_i$ , with respect to an origin,  $O$ , and orientation,  $p_i$ , which is in the opposite direction of motor-arm motion. (b) Schematic showing a MT composite of 11 beads, with a repulsive core and an attractive halo. Colours represent the potential as realised by a probe bead from a neighbouring MT. (c) Illustration of PEG-induced depletion interactions between MT bundles, showing the PEG molecules. The overlapping area between the two MTs are inaccessible to the PEG polymers. Inset shows relevant length scales of bristle-stabilised MTs:  $R_h$  is the effective radius of polymer coils of PEG;  $h$  is the bristle height.  $D$  is the surface-to-surface MT separation. (d) Time lapse images of two MTs coming overlapping due to depletion interactions. (c) and (d) are adapted from Ref [63].

interaction potential that has an attractive component. The capped interaction potential simulates a penalty for MT-MT overlap [83]. We include the attractive component in order to simulate the cohesive forces from depletion interactions which can be caused by macroscopic crowding under physiological conditions, and polymers like polyethylene glycol (PEG) in reconstituted *in vitro* experiments, as shown in Fig. 2.2(c) and (d) [63].

In our simulations MTs interact via a generalised separation-shifted Lennard-Jones-like potential [84],

$$U(r) = A_R \left( \frac{s^m}{r^m + \alpha^m} \right)^n - A_A \left( \frac{s^m}{r^m + \alpha^m} \right)^{n/2}, \quad (2.33)$$

where  $r$  is the distance between two beads belonging to two neighbouring MTs;  $A_R$ ,  $A_A$  and  $\alpha$  determine the energy of the repulsive peak ( $E_R$ ), the attractive well ( $E_A$ ), and the position of the energy minimum ( $r_{\min}$ ). In units of thermal energy ( $k_B T$ ),  $E_R = 20$ , and  $E_A$  is varied between 0.2 and 1.0. The aspect ratio of MTs is  $L/r_{\min} = 5$ .  $\alpha$ ,  $A_A$  and  $A_R$  are dependent on overlap penalty,  $E_R$ , attraction energy,  $E_A$ , and the position of the attractive well,  $r_{\min}$ ,

$$\alpha = r_{\min} \left( \left( 1 + \sqrt{E_{\text{R}}/E_{\text{A}}} \right)^{2/n} - 1 \right)^{-1/m}, \quad (2.34)$$

$$A_{\text{A}} = 2\alpha^{mn/2} s^{-mn/2} E_{\text{A}} \left( 1 + \sqrt{E_{\text{R}}/E_{\text{A}}} \right), \quad (2.35)$$

and

$$A_{\text{R}} = \frac{A_{\text{A}}^2}{4E_{\text{A}}}. \quad (2.36)$$

The variable  $s$  depends on the length of MTs,  $L$ , and the number of particles that makes up this MT,  $N_{\text{B}}$ :

$$s = \frac{L}{(N_{\text{B}} - 1)}. \quad (2.37)$$

For all of our simulations,  $m = 2$ ,  $n = 8$  and  $r_{\min} = 1$ . The exponents of the potential are chosen such that the superposition of multiple, overlapping beads gives a smooth, attractive MT-MT interaction, with a repulsive core shown in Fig. 2.2(B). At the same time, when the MT encounters large forces and torques, the capped potential will allow for MTs to slide over each other, resembling a crossing in the third dimension [83,85]. The advantage of using the interaction potential is that on top of allowing MT-MT overlaps, we are able to control the position and depth of the repulsive peaks and attractive wells independently.

To characterise the MT-MT interaction, instead of looking at interaction energies between particles, we look at interaction energies between MTs in different orientations. In the following examples, one of the MTs (dark blue MT in Figs. 2.3, 2.4, 2.5) is fixed in position, and the position of the other MT is varied. We plot the energy that arises as a result of the superposition of the potentials between beads from the neighbouring MT.

Figure 2.3 shows the energy of the two MTs as function of the separation distance,  $\Delta x$  for  $E_{\text{R}} = 6k_{\text{B}}T$  and  $E_{\text{R}} = 20k_{\text{B}}T$ . We notice that the position of the minimum attraction energy shifts closer to the core of the MT than  $r_{\min}$ , because of the superposition of the energy wells of multiple beads. We will call this distance  $x_{\min}$  and use it only for the MT sliding example discussed below. Compared to  $E_{\text{R}} = 6k_{\text{B}}T$ ,  $E_{\text{R}} = 20k_{\text{B}}T$  gives repulsive peaks which are about five fold higher, although the depth of the attractive wells are conserved. We use  $E_{\text{R}} = 20k_{\text{B}}T$  for all calculations in Chapters 3 and 4. At this level of repulsion, the overlap penalty is six fold higher than the energy of attraction.

In order to ensure that  $A_{\text{R}}$  does not diverge for vanishing attraction, we take the limit  $E_{\text{A}} \rightarrow 0$  for curves marked  $E_{\text{A}} = 0.0$ . Because of the manner in which our potential is constructed, the shape of the potential for  $E_{\text{A}} = 0$  differs substantially from larger values of  $E_{\text{A}}$ , see Fig. 2.3. We, thus, do not use this potential to simulate systems which are not attractive.

Figure 2.4 shows the energy of the MTs as functions of their parallel displacement,  $\Delta y$ . In this instance, we slide two aligned MTs apart, along their longitudinal axis. We keep the orthogonal displacement to be the position where the inter-MT energy is the smallest,  $x_{\min} = 0.8r_{\min}$ . The energy increases monotonically as the filaments slide away from each other, since the attractive interactions decrease, as the number of interacting

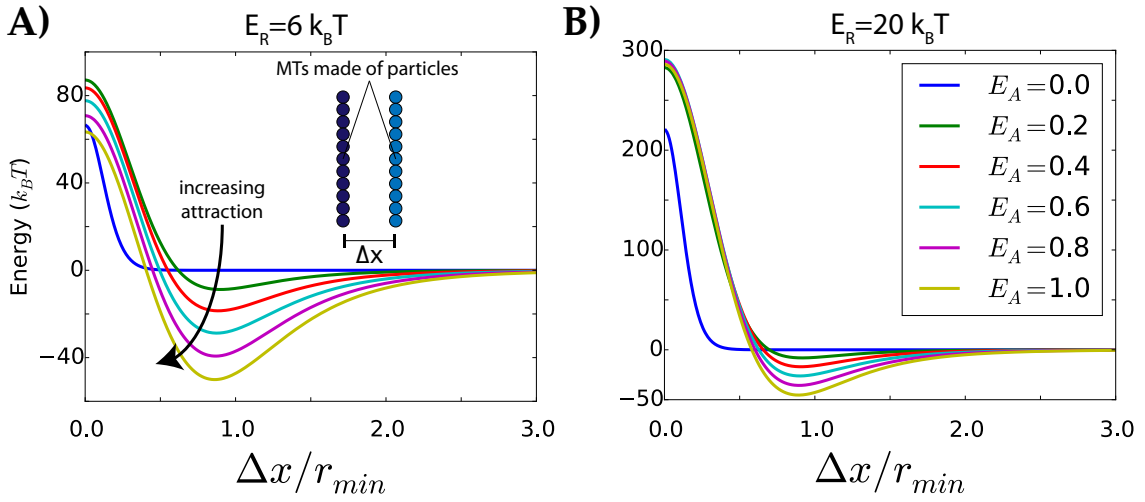


Figure 2.3: Inter-MT energy as a function of separation distance,  $\Delta x$ , between an aligned MT pair, for different  $E_A$  values. Two regimes of repulsion are illustrated: **(A)**  $E_R = 6k_B T$  and **(B)**  $E_R = 20k_B T$ . Negative energies indicate attraction, and positive energies indicate repulsion. Inset in **(A)** shows the orientation with which the calculation is conducted.

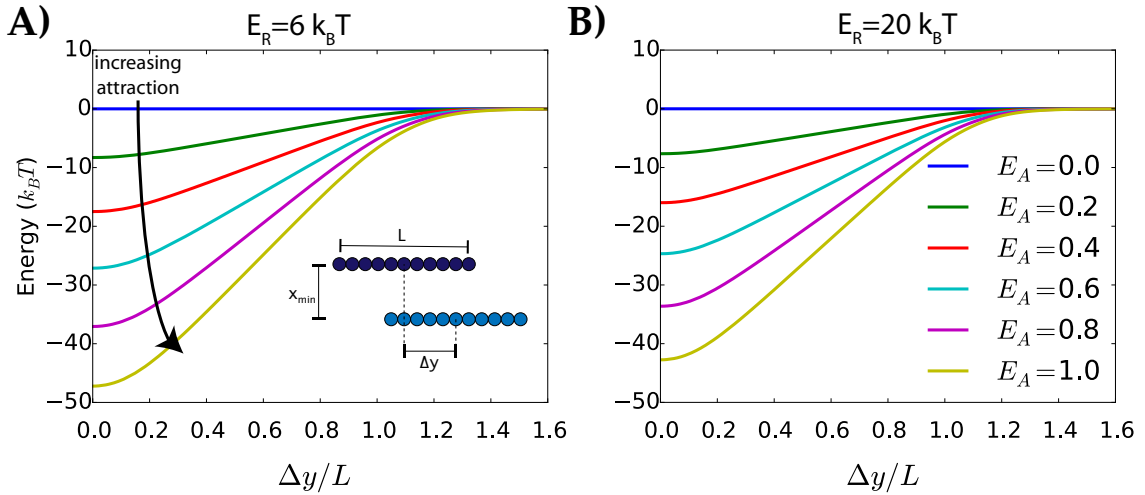


Figure 2.4: Inter-MT energy as a function of parallel displacement between MTs' centers of masses,  $\Delta y$ , for different  $E_A$  values. The orthogonal displacement is set to be  $x_{\min}$ , the position of the energy well, seen in Figure 2.3. We illustrate two regimes of repulsion: **(A)**  $E_R = 6k_B T$  and **(B)**  $E_R = 20k_B T$ . In both cases  $x_{\min} = 0.8r_{\min}$ . Inset in **(A)** shows the orientation with which the calculation is conducted.

beads decreases. When the centers of masses are separated further than the MT length, the number of interacting beads decreases to 1, and then the energy vanishes as the MTs are moved further away. The values chosen for the attraction energies correspond with the range of cohesion energies for the *in vitro* MT sliding experiment calculated for different PEG concentration [63].

In Fig. 2.5, two MTs are rotated with respect to each other, with the center beads of

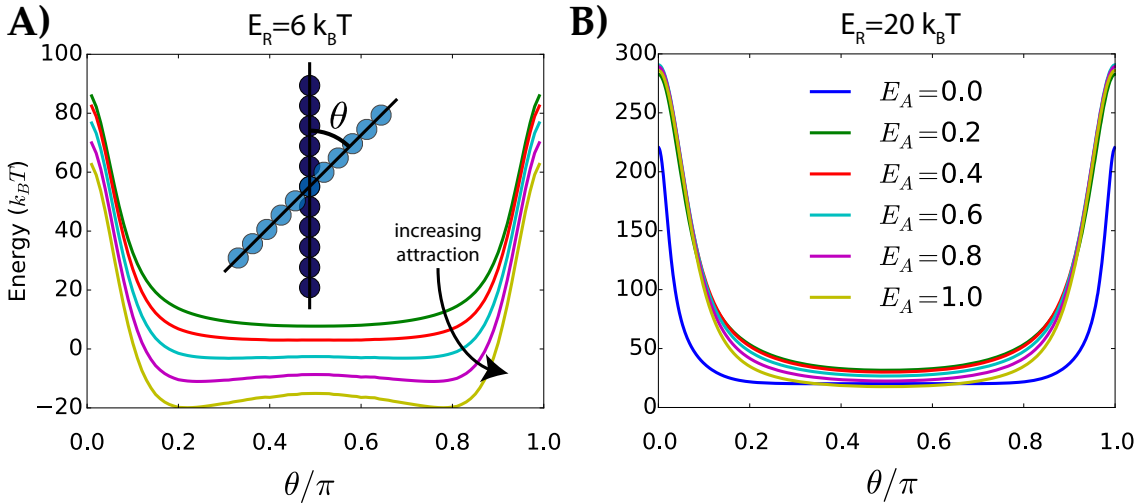


Figure 2.5: Inter-filament energy as a function of increasing the angle of crossing between two overlapping filaments,  $\theta$ , for different  $E_A$  values. We illustrate two regimes of repulsion: (A)  $E_R = 6k_B T$  and (B)  $E_R = 20k_B T$ . Inset in (A) shows the orientation with which the calculation is conducted.

both MTs overlapping. For  $E_R = 6k_B T$ , and for  $E_A < 0.6k_B T$  the potential is repulsive for all angles. For  $E_R = 6k_B T$ ,  $E_A > 0.6k_B T$ , the potential has minima in two orientations. One must keep this in mind before using this potential for smaller overlap penalties, which can lead to clustering of filaments due to such stable orientations. We avoid this issue here by using  $E_R = 20k_B T$ . This makes the potential repulsive for all values of  $E_A$ .

In a 2-D system, a filament potential which is soft and tolerates overlaps makes the definition of surface fractions difficult. We overcome this by calculating the resulting radial distribution of MTs to different levels of attractions and motors, Fig. 2.6. We can approximate the first peak of radial distribution function to be the MT diameter, which we can then use to compute an estimation of the surface fraction ( $\phi = N_f r_{\text{eff}} L / \pi R_W^2$ ).

## 2.2.2 Wall interactions

Beads which make up the MTs interact with the wall with a 6-12 Lennard Jones potential,

$$U_w(r) = \begin{cases} 4\epsilon \left[ \left( \frac{r_{\min}}{r_w} \right)^{12} - \left( \frac{r_{\min}}{r_w} \right)^6 \right] & r \leq 3r_{\min} \\ 0 & r > 3r_{\min} \end{cases}, \quad (2.38)$$

where  $r_w$  is the distance between a bead and the wall, and  $r_{\min}$  is the position of the attractive energy well and  $\epsilon$  describes the attraction well depth of the wall in units of  $k_B T$ . We choose the same range,  $3r_{\min}$ , for MT-MT interactions and MT-wall interactions. Superposition of these potentials between all the beads that make up a MT and the wall gives the curve shown in Fig. 2.7.

Comparing the energies in Fig. 2.7, with those of Fig. 2.3, Fig. 2.4 and Fig. 2.5, shows that the attractive MT-wall interaction energy is sufficient to stabilise a layer of partially overlapping MTs close to the wall [50], because the level of attraction is relatively larger ( $-90 k_B T$ ) than the other energies (attractive or repulsive) involved in the system.

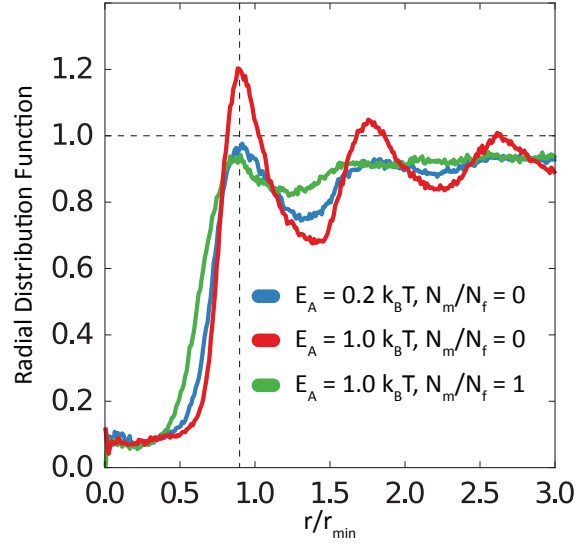


Figure 2.6: Time-averaged radial distribution function of beads that make up MTs. We used dimeric motors for the curve which has  $N_m/N_f = 1$ . The beads belonging to the same MT as the bead in question were omitted for this calculation. The first peak occurs in the same point as the energy well indicated in Fig. 2.3. The beads which are at overlapping distances ( $0.0 < r/r_{\min} < 0.5$ ) occur near the confining wall due to the high attraction potential. The plot is normalised with the packing fraction of beads within the confinement.

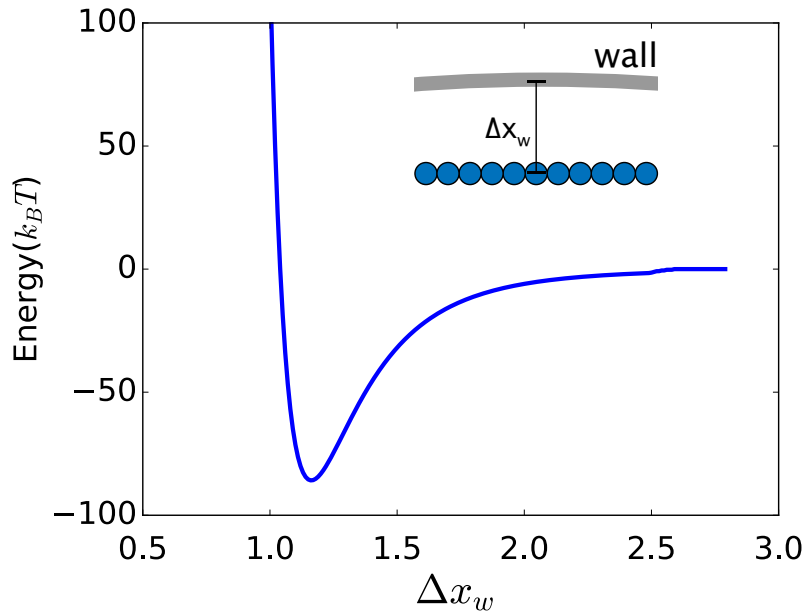


Figure 2.7: Interaction energy of MT with the wall with a 6-12 Lennard Jones potential.  $\epsilon_w = 8k_B T$ ,  $\sigma_w = r_{\min}$ .  $\Delta x_w$  are given in units of  $r_{\min}$ .

### 2.2.3 Simplified motor walking

There are two stochastic processes in our simulations. The first is the Gaussian distributed random displacements,  $\delta \mathbf{r}_i(t)$ , and rotations,  $\delta \mathbf{p}_i(t)$  of MTs. The second is the selection

of the attachment position of the motor arms.

At each time step, the distances between beads on neighbouring MTs are checked. If the number of motors attached in the system is less than the predefined number of motors in the entire system,  $N_m$ , bead pairs that have inter-particle distance smaller than the threshold distance,  $d_t$ , are picked randomly, and motors are attached between them.

Consider two MTs,  $i$  and  $j$ , each of length  $L$ , with orientations  $\mathbf{p}_i$  and  $\mathbf{p}_j$ , which correspond with the directions of motor arm motion, and center-of-masses  $\mathbf{r}_i$  and  $\mathbf{r}_j$ . Note that orientation vectors  $\mathbf{p}_i$  and  $\mathbf{p}_j$  are necessarily unit vectors. They are parametrised by contour variables  $s_i$  and  $s_j$  that equal 0 and 1 at the negative and positive ends of the MTs respectively. A motor that crosslinks these MTs will have arms at positions  $\mathbf{m}_i$  and  $\mathbf{m}_j$  on MTs  $i$  and  $j$  respectively, with motor lengths  $|\mathbf{m}_{ij}| = |\mathbf{m}_j - \mathbf{m}_i|$ . We can write a motor arm position,  $\mathbf{m}_i$  using,

$$\mathbf{m}_i = \mathbf{r}_i + Ls_i\mathbf{p}_i. \quad (2.39)$$

This description of motor arm position is similar to the description of bead position described in Sec. 2.1.2. The motors act as harmonic bonds with stiffness  $k_m$ , and energy,

$$U_m = \begin{cases} \frac{1}{2}k_m|\mathbf{m}_{ij}|^2, & |\mathbf{m}_{ij}| \leq d_t \\ 0, & |\mathbf{m}_{ij}| > d_t \end{cases}, \quad (2.40)$$

A motor arm that is attached to a MT walks with velocity  $v_m$  until the distance between the two motor arms reaches the stall length,  $d_s$ . For extensions beyond  $d_s$ , the motor arms stop walking. If the motor extension is greater than  $d_t$ , both arms of the motor detach simultaneously, see Fig. 2.8.

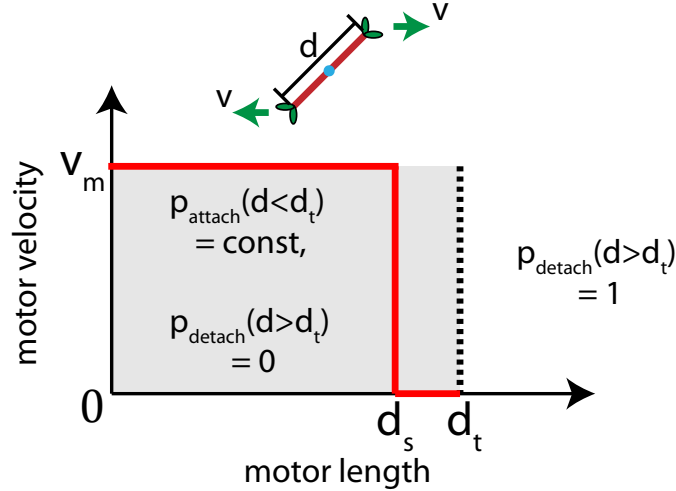


Figure 2.8: Motors bind to neighbouring MTs with a constant probability if their length,  $d$ , is less than threshold distance,  $d_t$ , until the predefined number of attached motors in the system,  $N_m$  is reached. Motors that are longer than  $d_t$  detach. If the motor length is less than the stall length, *i.e.* for  $d < d_s$ , active motor arms move with constant velocity,  $v_m$ .

Motion of the motor arms also depends on whether the motors are dimeric or tetrameric.

Dimeric motors have one randomly-picked anchored motor arm, which remains anchored to one MT until the motor extension is greater than  $d_t$ . The other motor arm walks on the MT with the velocity shown in Fig. 2.8, as do both arms of a tetrameric motor. We have no stochastic motor detachment rate, since kinesin molecules are known to be very processive [3].

We choose the motor model described in Fig. 2.8, instead of a conventional linear force velocity relationship, to emphasise the difference between dimeric and tetrameric motors. For instance, a tetrameric motor arm can behave like a dimeric motor if one of the two arms is given a walking probability and is chosen to move during the simulation step, and the other arm is chosen to remain anchored. Coupling the walking probabilities between both the arms will alleviate the problem, but can lead to both dimeric and tetrameric motors behaving in a similar manner if the motor is stretched and both motor arms are not walking.

### 2.2.4 Simulation schematic

The initial distribution of MTs is straightforward, because the inter-MT potential allows for overlap. First, we pick a random point within the circle defined by the confinement wall, which will potentially be the center of mass of a new MT. Next, we pick a random orientation, and check if the MT intersects with the confining wall. If it does not, we place the MT and proceed to placing the next MT until the necessary number of MTs are placed within the confinement. High overlap penalties tend to remove overlaps within a few thousand molecular dynamics steps, even at high densities.

In each simulation, the number of MTs,  $N_f$ , and attached motors,  $N_m$  are independently held constant. Motors are modelled as harmonic springs with equilibrium length zero, with two arms, each attached to a point on a MT. Following the initial set up, and an equilibration period, the motors driven MT dynamics is conducted.

MTs are subject to force,  $\mathbf{F}_i$ , torque,  $\mathbf{T}_i$ , (Fig. 2.2) and anisotropic friction,  $\mathbf{\Gamma}_i$ . Hydrodynamic interaction of each MT with the background fluid is modelled using resistive-force theory; long-range hydrodynamic interactions between MTs are ignored [86]. We use overdamped Brownian dynamics, *i.e.*, the momenta of the MTs lose their memory and relax to thermal equilibrium between consecutive time intervals,  $\delta t$ . The

MTs obey the dynamical equations for translation and rotation,

$$\mathbf{r}_i(t + \delta t) = \mathbf{r}_i(t) + \mathbf{\Xi}_i^{-1}(t) \cdot \mathbf{F}_i(t) \delta t + \delta \mathbf{r}_i(t) \quad (2.41)$$

and

$$\mathbf{p}_i(t + \delta t) = \mathbf{p}_i(t) + \gamma_r^{-1} (\mathbf{T}_i(t) \times \mathbf{p}_i) \delta t + \delta \mathbf{p}_i(t), \quad (2.42)$$

respectively. The inverse friction tensor,  $\mathbf{\Xi}_i^{-1}(t)$ , is orientation dependent and is given by

$$\mathbf{\Xi}_i^{-1}(t) = \gamma_{\parallel}^{-1} \mathbf{p}_i(t) \mathbf{p}_i(t) + \gamma_{\perp}^{-1} (\mathbf{I} - \mathbf{p}_i(t) \mathbf{p}_i(t)), \quad (2.43)$$

where  $\gamma_{\parallel}$ ,  $\gamma_{\perp}$  and  $\gamma_r$  are the parallel, perpendicular and rotational friction coefficients of the MT, respectively.  $\mathbf{F}_i$  and  $\mathbf{T}_i$ , are sums of deterministic forces and torques on MT  $i$ , respectively, *i.e.*, the forces and torques due to motors, steric forces from neighboring

MTs, and steric repulsion from the confining wall. From hydrodynamics, the following expressions for hard spherocylinders can be derived:  $\gamma_{\parallel} = \gamma_0 L$ ,  $\gamma_{\perp} = 2\gamma_0 L$ , and  $\gamma_r = \gamma_0 L^3/6$  [87, 88]. The friction coefficients are a function of the solution viscosity and the MT's aspect ratio. For the purpose of this simulation,  $\gamma_0$  is constant for all three friction coefficients, because for the chosen aspect ratios, the correction term for  $\gamma_0$  is approximately equal for all three cases.

The Gaussian-distributed random displacements,  $\delta\mathbf{r}_i(t)$ , and rotations,  $\delta\mathbf{p}_i(t)$ , are related to the friction tensors by the fluctuation-dissipation theorem. The anisotropic random displacement and random reorientation vector have the variances

$$\langle \delta\mathbf{r}_i(t)\delta\mathbf{r}_i(t) \rangle = 2k_B T \boldsymbol{\Xi}_i^{-1} \delta t \quad (2.44)$$

and

$$\langle \delta\mathbf{p}_i(t)\delta\mathbf{p}_i(t) \rangle = 2k_B T \gamma_r^{-1} (\mathbf{I} - \mathbf{p}_i(t)\mathbf{p}_i(t)) \delta t. \quad (2.45)$$

The overall Brownian dynamics scheme is:

1. Compute forces and torques due to MT attraction and repulsion.
2. If the number of attached motors is less than  $N_m$ , look for beads on two different MTs which are closer than  $d_t$ , and attach motor arms to these MT pairs. If motors are active, i.e.  $d < d_s$ , displace each arm by  $v_m \delta t$  along the polar direction of the MT to which it is attached.
3. Calculate forces and torques on the MTs due to motors and confinement. Add these values to those obtained from 1.
4. Move MTs based on their respective forces and torques.
5. Update motor arm positions, such that the positions of the arms are conserved after step 4 on the MTs from before step 4. Remove the motors that are stretched beyond the motor threshold, i.e.  $d > d_t$ , and those motors that contain arms that have walked off the MT.

All the data collected from systems has been measured after the simulations have run for at least  $1.5 \times 10^3 \tau$ , where  $\tau$  is the onset of the activity time scale.

### 2.2.5 System parameters

Despite having taken a step toward capturing cellular scale phenomena by marrying three distinct components of very different length scales, we have tried to capture biologically accurate lengths in the simulation (Table 2.1). However, in our coarse-grained model we chose constant motor speeds which are faster than motor speeds from single molecule experiments. In so doing we remove the force dependency on motor speed and shift the focus from the loads on individual motors to conduct MT sliding. Instead, we use motors as coarse-grained entities that propel MTs based on the MT pair's orientation. In order to traverse another order of magnitude in length scale and simulate MTs in cell-sized confinements, such coarse-graining choices need to be explored.

## 2.2 Explicit motor system

Parameter	Symbol	Value	Notes/Biological Values
Thermal energy	$k_B T$	4.11 pN nm	Room Temperature
MT length	$L$	0.125 $\mu\text{m}$	$2.5 \pm 1.4 \mu\text{m}$ [28]
MT diameter	$r_{\min}$	25 nm	25 nm [16]
Confinement radius	$R_W$	1 $\mu\text{m}$	Oocyte $\sim 200\mu\text{m}$ [50]
Repulsive peak	$E_R$	$20k_B T$	Chosen
MT Attractive well	$E_A$	$0.2 - 1.0k_B T$	<i>in vitro</i> experiments [63]
Confining wall attraction	$\epsilon_w$	$8.0k_B T$	Chosen
Confining wall sigma	$\sigma_w$	25 nm	Chosen
Fluid viscosity	$\eta$	1 Pa s	Cytoplasmic viscosity [89]
Maximum motor speed	$v_m$	6.5 $\mu\text{m/s}$	$\sim 1.8 \mu\text{m/s}$ [90]
Maximum motor extension	$d_t$	25 nm	80 nm [36]
Motor stall force	$f_s$	7.83 pN	5 pN [91]
Motor spring constant	$k_m$	0.33 pN/nm	Single kinesin molecule [92]

Table 2.1: Simulation parameters for explicit motor system

The viscosity of the cytosol is dependent on the length scale in question. At small length scales, the viscosity of the cytoplasm, obtained by calculating the diffusion constant of fluorescently labelled DNA, is close to that of water, *i.e.*, 1.2 – 1.4 times the viscosity of water: approximately 0.01 Pa s [93]. However, at cellular length scales which is larger than the effective mesh size of the cytoskeleton, the viscosity is 1 Pa s [89]. Since we are interested in modelling cellular-scale phenomena, in our simulations we use the latter value.

The dynamic viscosity can be written using,  $\eta = k_B T / D_0 L$ , where  $D_0$  is linearly related to the translational and rotational diffusion coefficients of a filament of fixed aspect ratio [87]. The dynamic viscosity is related to the friction coefficient used in the dynamical equations using  $\gamma_0 = 2\pi\eta$  [5, 87, 88]. We can obtain the time scaling used in the simulation by equating,  $\eta = 1 \text{ Pa s}$ .

For this system, we can nondimensionalise the key parameters using the MT diameter,  $r_{\min}$ , thermal energy  $k_B T$ , and typical activity time scale,  $\tau$ , which indicates the onset

Parameter	Symbol	Value
Area fraction	$N_f r_{\text{eff}} L / \pi R_W^2$	0.74
MT aspect ratio	$L / r_{\text{min}}$	5
Confinement diameter	$R_W / r_{\text{min}}$	80
Motor to MT ratio	$N_m / N_f$	1
Maximum motor speed	$v_m \tau / r_{\text{min}}$	50
Maximum motor extension	$d_t r_{\text{min}}$	1
Motor stall force	$f_s r_{\text{min}} / k_B T$	47.7
Motor spring constant	$k_m d_t / f_s$	1

Table 2.2: Dimensionless groups for explicit motor system

of MT dynamics because of motors. Our simulations depend on eight dimensionless parameters: MT surface fraction  $\phi = N_f r_{\text{eff}} L / \pi R_W^2$ , MT aspect ratio  $L / r_{\text{min}}$ , confinement diameter  $R_W / r_{\text{min}}$ , motor concentration  $N_m / N_f$ , maximum motor speed  $v_m \tau / r_{\text{min}}$ , motor stall force  $f_s r_{\text{min}} / k_B T$ , motor spring constant  $k_m d_t / f_s$ .

In chapters 3 and 4 we systematically study the effect of MT attraction,  $E_A$ , and motor concentration,  $N_m / N_f$ , on parallel MT velocity, global MT structure, MT velocity at the confinement edge, and local polar order. For these key results we use  $\phi = 0.74$  and  $R_W / r_{\text{min}} = 80$  to demonstrate typical structures observed in our system.

However, we have also studied the structure and dynamics of MTs as a function of different surface fractions, confinement diameter, motor spring constants and motor velocity. In all cases, we keep MT aspect ratio, maximum motor extension and motor stall force constant. A list of the eight dimensionless parameters that determine structure and dynamics in our simulation are given in Table 2.2.

### 2.3 Effective motor system

As described in Fig. 1.3, molecular motors induce activity in the cytoskeleton because microtubules are polar. Motors sense this polarity and in the presence of ATP “walk” on the filament primarily along one direction. This induces force-dipoles that break nematic symmetry, and leads to very different dynamics between filament pairs that are aligned and antialigned. Despite the active “walking”, motors that connect aligned filaments induce less sliding between them, and hold them together, as shown in Fig. 1.6, and in other works [4, 5].

Motors that connect antialigned filaments have arms on either filament “walking” in opposite directions. Accommodating the stress from the motor, causes filaments to slide over each other, which causes large-scale flows in the cytoskeleton. In order to capture and explain cellular-scale dynamics induced by cytoskeletal motion, modelling thousands of individual motors, although done before in some studies, can prove unwieldy. Although

a network of microtubules can be kept track of, book-keeping a bath of attached and unattached motors in the context of simulations is challenging. Moreover, accurately depicting *both* motors and filaments at cellular scale geometries, although have been attempted before, proves to be difficult. In order to capture cellular level phenomena, such as organelle distribution, cytoplasmic streaming, and active cytoskeleton induced lipid bilayer fluctuations, a coarse-grained description of activity in networks is required.

For the second set of simulations, we use the simulation methodology described in this section. The findings from these simulations, performed using the open source massively parallel simulator (LAMMPS) [94], are presented in Chapter 5. The coarse-graining of explicit motors to the effective motor potential removes the emphasis on individual motors. The focus is now on the relative orientation of MTs, *i.e.*, antialigned MTs propel each other, and polar-aligned MTs do not propel each other. Also, in this method motor forces are instantaneous, *i.e.*, there is no memory of where motors were in previous steps, as in the case of explicit motors. Since, the time-span of the processivity of each motor is now effectively reduced to a single simulation step, this means that we are also coarse-graining in time. Using this method, we can capture longer length and time-scale phenomena.

Effectively, instead of resorting to the details of the dynamics of individual motors, in this model, we use symmetry arguments to express active currents. Similar coarse-graining approaches have been taken by a number of analytic and simulation works to explain various physiological phenomena in active networks [95–97].

### 2.3.1 Phenomenological model

For simplicity, we motivate a simple, phenomenological, one dimensional model describing the dynamics of a linear bundle of polar filaments of length  $L$  [96]. The concentration of filaments pointing at either direction, with center of masses located at  $x$ , in a one dimensional track is given by  $c^+(x)$  and  $c^-(x)$ , respectively. These quantities must satisfy the conservation laws,

$$\begin{aligned}\frac{d}{dt}c^+ &= D\frac{d^2}{dx^2}c^+ - \frac{d}{dx}J^{++} - \frac{d}{dx}J^{+-}, \\ \frac{d}{dt}c^- &= D\frac{d^2}{dx^2}c^- - \frac{d}{dx}J^{-+} - \frac{d}{dx}J^{--},\end{aligned}\tag{2.46}$$

where,  $D$  is the filament diffusion coefficient. Motor-mediated interactions between antialigned filament pairs give filament currents,  $J^{+-}$  and  $J^{-+}$ . Similarly, motor-mediated interactions between parallel filament pairs give filament currents,  $J^{++}$  and  $J^{--}$ . These currents are a function of filament overlap. In other words, a filament located at  $x$  moves due to the interactions induced by the interaction with filaments located at  $x + \xi$ , where  $\xi < L$ . Using this approach, we can write the filament current for antialigned filaments (current of + oriented filament located at  $x$  due to - oriented filament located at  $x + \xi$ ),

$$J^{+-}(x) = \int_{-L}^L d\xi v^{+-}(\xi)c^+(x)c^-(x + \xi),\tag{2.47}$$

where  $v^{+-}(\xi)$  is the effective relative velocity between two antialigned filaments which are separated by a distance  $\xi$ . Similarly, for parallel filaments, (current of + oriented filament

located at  $x$  due to + oriented filament located at  $x + \xi$ ), we can write,

$$J^{++}(x) = \int_{-L}^L d\xi v^{++}(\xi) c^+(x) c^+(x + \xi). \quad (2.48)$$

In a homogenous state (or when filaments are homogeneously distributed),  $J = J^{++} + J^{--} + J^{+-} + J^{-+}$  vanishes.

Assuming that independent motor forces act in equally in opposite directions, on either filament, the center of gravity of interacting filament pairs must remain fixed. This gives:  $v^{\pm\pm}(\xi) = -v^{\pm\pm}(-\xi)$  and  $v^{+-}(\xi) = -v^{+-}(-\xi)$ . System invariance with respect to space inversions additionally gives,  $v^{++}(\xi) = -v^{--}(-\xi)$ . We can simplify these relative velocities by writing,

$$\begin{aligned} -v^{+-}(\xi) &= v^{+-}(-\xi) = \beta, \\ v^{++}(\xi) &= v^{--}(\xi) = \alpha \text{sign}(\xi), \end{aligned} \quad (2.49)$$

where  $\alpha$  and  $\beta$  are constants that are independent of  $\xi$  and  $\text{sign}(\xi) = \pm 1$ , depending on the sign of  $\xi$ . The quantify velocities of filaments due to antialigned and aligned interactions respectively.

The filament currents due to parallel and antialigned filament interactions can now be written using,

$$\begin{aligned} J^{\pm\pm}(x) &= \alpha \int_{-l}^l d\xi (c^\pm(x + \xi) - c^\pm(x - \xi)) c^\pm, \text{ and} \\ J^{\pm\mp}(x) &= \mp\beta \int_{-l}^l d\xi c^\mp(x + \xi) c^\pm, \end{aligned} \quad (2.50)$$

respectively. Equations 2.46 and 2.50 describe all the dynamics within the system.

A linear stability analysis under periodic boundary conditions was performed using  $c^\pm(x) = c_0^\pm$ , for a 1-D system of length  $L_A$  [96]. It was shown that the homogenous state of the system becomes linearly unstable when  $\alpha > \alpha_c$ . The critical value of parallel velocity is given by,

$$\alpha_c = \frac{D}{L^2 c} f\left(\frac{\beta L c L_A}{D}, \frac{\delta c}{c}, \frac{L_A}{L}\right), \quad (2.51)$$

where  $c \equiv c_0^+ + c_0^-$ ,  $\delta c \equiv c_0^+ - c_0^-$ , and  $f(u, v, w)$  is a dimensionless scaling function. For all parameters it was noted that  $\alpha_c \geq 0$ , and that the system became unstable necessarily when  $\alpha > 0$ , due to the velocity induced by parallel filament interactions.

Also, it was found in Ref. [96] that  $\alpha_c$  decreased with increasing  $\delta c$  (as filaments point in the same direction).  $\alpha_c$  also increases with increasing  $D$ . The relationship between  $\alpha_c$  and  $\beta$  is shown in Fig. 2.9. It shows that the homogenous system is stable at larger  $\alpha$  values only for small  $\beta$ . The final inhomogeneous stationary state is made up of filament bundles that are shortened due to the forces induced by motors crosslinking parallel filaments. These bundles are separated by empty regions.

### 2.3.2 Volume exclusion and internal forces

We extend the one-dimensional analytic model in Sec. 2.3.1, and analyse its effects in 2-D using computer simulations. Here, we simulate MTs as semi-flexible filaments of length  $L$ ,

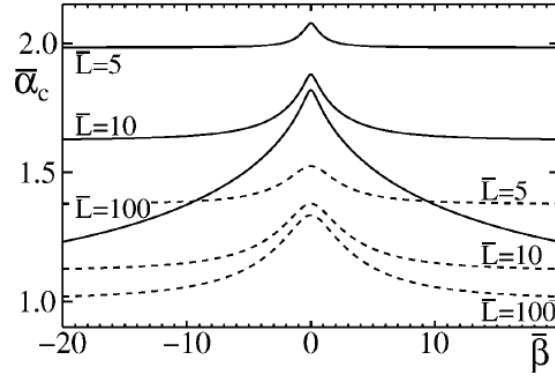


Figure 2.9: The critical value of parallel filament interaction strength,  $\bar{\alpha}_c = \alpha_c L^2 c / D$  is plotted as a function of antialigned filament interaction strength,  $\bar{\beta} = \beta L c L_A / D$ , for different values of system size  $\bar{L} = L_A / L$ . Solid lines and dashed lines correspond to  $\delta c = c/10$  and  $\delta c = c/2$ . When  $\alpha > \alpha_c$ , the homogeneous state is found to become linearly unstable. Reprinted with permission from Ref. [96] Copyright (2000) by the American Physical Society.

diameter  $\sigma$  and aspect ratio  $L/\sigma = 10$ , under periodic boundary conditions. The filament is discretised into a chain of  $N_F$  beads connected by harmonic bonds. The motion of the beads is described by the Langevin equation,

$$m \frac{d^2 \mathbf{r}_i}{dt^2} = -\gamma \frac{d\mathbf{r}_i}{dt} - \nabla U_i + \boldsymbol{\eta}_i(t) \quad (2.52)$$

where  $\mathbf{r}_i$  is the position of bead  $i$ ,  $m$  is the mass of a bead,  $\gamma$  is the friction coefficient of the solvent on the bead, and  $\boldsymbol{\eta}_i$  is the Gaussian distributed thermal force. We operate at the Brownian dynamics regime by setting a high viscous to inertia ratio, *i.e.*,  $m = 1$  and  $\gamma = 1$ .

The thermal force,  $\boldsymbol{\eta}_i$  has the correlation function, from the fluctuation-dissipation theorem,

$$\langle \eta_\alpha(t) \eta_\beta(t') \rangle = 2\gamma k_B T \delta_{\alpha\beta} \delta(t - t'), \quad (2.53)$$

where  $k_B$  is the Boltzmann constant,  $T$  is the temperature and  $\eta_\alpha(t)$  is the  $\alpha$ -th component of the vector  $\boldsymbol{\eta}_i(t)$ .

Unlike the filaments described in Sec. 2.2, in this model, filaments are flexible. This gives the configurational potential,  $U_i$ ,

$$U_i = U_{\text{bond}} + U_{\text{angle}} + U_{\text{wca}} + U_{\text{motor}}. \quad (2.54)$$

where,  $U_{\text{bond}}$  is the spring contribution

$$U_{\text{bond}} = \frac{k_s}{2} \sum_{\text{bonds}} (|\mathbf{r}_{i,i+1}| - r_0)^2, \quad (2.55)$$

that acts between adjacent beads of the same filament.  $k_s$  is the bond stiffness,  $r_0 = \sigma/2$  is the equilibrium bond length, and  $r_{i,i+1}$  is the distance between adjacent beads  $i$  and

$i + 1$  which make up the filament.  $U_{\text{angle}}$  is the bending energy, which is calculated using the position of three adjacent beads,

$$U_{\text{angle}} = \kappa/r_0 \sum_{\text{angles}} (1 - \cos \theta_i), \quad (2.56)$$

that make up the angle  $\theta_i$  [98]. It acts between all groups of three adjacent beads that make up the same filament.  $\kappa$  is the bending modulus of the filament and it determines the persistence length,  $\xi_p = \kappa/k_B T$ .

Adjacent beads from the same filament are impervious to each other, but they interact with other beads with the Weeks-Chandler-Andersen (WCA) potential [99],

$$U_{\text{wca}} = 4\epsilon \left[ \left( \frac{r_{i,j}}{\sigma} \right)^{12} - \left( \frac{r_{i,j}}{\sigma} \right)^6 \right] + \epsilon \quad (2.57)$$

with interaction cutoff  $r_{\text{cut}} = 2^{1/6}\sigma$ .

### 2.3.3 Effective motor potential

We coarse-grain MT-motor interactions using an effective motor potential, which gives the motor potential  $U_{\text{motor}}$  to each bead. Instead of modelling individual motors, MT dynamics manifests as a result of a distribution of motors in an ensemble of orientations between neighbouring MT pairs.

A local orientation vector is computed for each bead that makes up a MT. This vector is assigned to each bead as,

$$\mathbf{p}_i = \frac{\mathbf{r}_{i+1} - \mathbf{r}_i}{|\mathbf{r}_{i+1} - \mathbf{r}_i|}. \quad (2.58)$$

Note that if the persistence length is greater than the length of the filament,  $\xi_p > L$ , the bond between any two beads is approximately the orientation vector of the MT itself. Since each MT is composed of many beads the issue of the last local orientation vector,  $\mathbf{p}_{i+n-1}$ , being undefined does not affect the results appreciably.

The implicit motor interaction between beads of neighbouring MT pairs, within motor cutoff range,  $d_t = 2\sigma$ , is modelled as a harmonic bond that lasts for only one simulation time step. The motor potential has an equilibrium bond length  $d_{\text{eq}} = \sigma$ , and can be written as,

$$U_{\text{m}} = \begin{cases} \frac{1}{2}k_{\text{m}}(d - d_{\text{eq}})^2, & d \leq d_t \\ 0, & d > d_t \end{cases}, \quad (2.59)$$

where  $d = |\mathbf{m}_{ij}|$ . This allows us to calculate a motor binding rate,

$$k_{\text{on}}(d) = k_0 \exp\left(-\frac{U_{\text{m}}(d)}{k_B T}\right), \quad (2.60)$$

where  $k_0$  is either antialigned or polar aligned motor probability,  $p_a$  or  $p_p$ , depending on motor binding rules.

Motor bond forms when the MTs are antialigned and the angle that the motor makes with the orientation vector is acute on both MTs simultaneously. This is similar to the activity-inducing scenario a dimeric/tetrameric motor encounters when it crosslinks a pair of antialigned MTs, *i.e.*, the motor arms are oriented towards the + direction of either

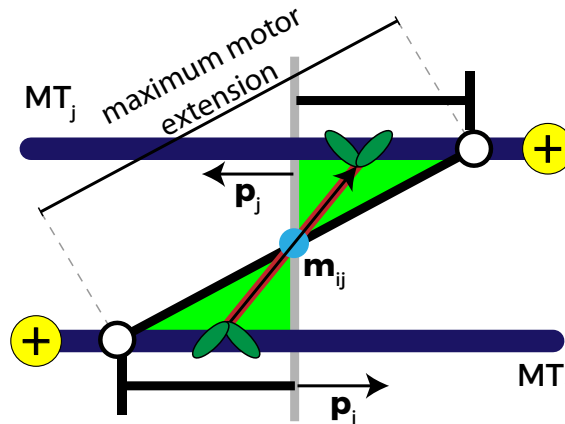


Figure 2.10: Schematic explaining the conditions which satisfy antialigned motor potential. Vectors,  $\mathbf{p}_i$ ,  $\mathbf{p}_j$ , and  $\mathbf{m}_{ij}$ , represent the orientation vectors of a stiff MT  $i$ , MT  $j$ , and the motor vector that crosslinks the beads of adjacent MTs, respectively. The white circles represent the maximum extension of motors between two MTs.

crosslinked MT. The effective motor potential is cutoff analogously where the explicit motor would have its motor threshold, and has reached its maximum extension. Fig. 2.10 provides a comparison between the effective motor potential and the similar explicit motor scenario.<sup>2</sup>

The motor bond formation between neighbouring MT beads are:

1. ( $|\mathbf{m}_{ij}| < d_t$ ) Beads of neighbouring MTs are within cutoff range.
2. ( $\mathbf{p}_i \cdot \mathbf{p}_j < 0$ ) MTs must be anti-aligned.
3. ( $\mathbf{p}_i \cdot \mathbf{m}_{ij} > 0$ ) Orientation of motor arm is towards the polarity of MT  $i$
4. ( $\mathbf{p}_j \cdot \mathbf{m}_{ij} < 0$ ) Orientation of motor arm is towards the polarity of MT  $j$
5. Random number picked from a uniform distribution is smaller than  $p_a e^{-U_m(d)/k_B T}$ , for each bead pair, at each time step.

Similarly, we can also implement motors between aligned MTs, which will appear with a motor probability,  $p_p$ . These will appear indiscriminate of the MT pair orientation as long as the beads that compose the MTs are within motor cutoff,  $d_t$ . Since the orientation of motors that bind the aligned MTs is symmetric with respect to the MT orientations, the bonds only serve to bundle aligned MT pairs, and there is no propulsion mechanism, like the antialigned implicit motor.

This motor model described here for two dimensions is analogous to phenomenological model described in Sec. 2.3.1. Namely,  $\beta$  is a linear function of  $p_a$  and  $k_m$ , and  $\alpha$  is a linear function of  $p_p$  and  $k_m$ .

<sup>2</sup>Although, MTs in Fig. 2.10 are represented simplistically as stiff rods (with large persistence lengths), the following rules are also valid for flexible MTs, because  $\mathbf{p}_i$  and  $\mathbf{p}_j$  can be calculated between any two connected beads that make up the same MT.

Parameter	Symbol	Value	Notes/Biological Values
Thermal energy	$k_B T$	4.11 pN nm	Room Temperature
MT length	$L$	0.625 $\mu\text{m}$	$2.5 \pm 1.4 \mu\text{m}$ [28]
MT diameter	$\sigma$	25 nm	[16]
MT bond angle constant	$\kappa$	$200k_B T$	Rigid MTs
MT bond spring constant	$k_s$	$2000k_B T/\sigma^2$	MTs cannot stretch [80]
Dynamic viscosity	$\eta$	1 Pa s	Cytoplasmic viscosity [89]
Energy scale of the WCA potential	$\epsilon$	$k_B T$	[100–102]
Motor spring constant	$k_m$	$6.6 \times 10^{-3}$ pN/nm	Single kinesin molecule, 0.33 pN/nm [92]
Motor threshold	$d_t$	$2\sigma$	Chosen
Equilibrium motor length	$d_{\text{eq}}$	$\sigma$	Chosen

Table 2.3: Simulation Parameters for effective motor system

### 2.3.4 System parameters

Even though the effective motor model does not model real motors, the motor parameters were picked such that the overall dynamics mimicked that of biological systems. The MT parameters were chosen such that the filaments were rigid and has an approximately constant length. The dynamic viscosity is 1Pa s. This sets the viscous time scale  $t^* = \eta\sigma^3/k_B T = 3.8 \times 10^{-3} s$ . The WCA potential is used with the interaction cutoff at  $2^{1/6}\sigma$ , such that we do not simulate the attractive effect of the Lennard Jones potential.

For this system, we can nondimensionalise the key parameters using the MT diameter,  $\sigma$ , or length,  $L$ , thermal energy  $k_B T$ , and the viscous time scale,  $t^*$ . Our simulations depend on eight dimensionless parameters, given in Table 2.4. We have studied the structure and dynamics of MTs as a function of  $\phi$ ,  $p_a$  and  $p_p$ .

## 2.4 Explicit vs. effective motor system

In this chapter we provide the theoretical framework for modelling rigid and semi-flexible filaments using both Brownian and Langevin dynamics. We have used two methods that model motor interactions to capture cytoskeletal phenomena at two different length and time scales. The first method uses explicit motors to crosslink neighbouring MT pairs,

## 2.4 Explicit vs. effective motor system

Parameter	Symbol	Value
Surface fraction	$\phi$	0.2 – 0.5
MT aspect ratio	$L/\sigma$	10
MT persistence length	$\xi/L$	200
Motor spring constant	$k_m d_{eq}^2/k_B T$	1
Motor threshold	$d_t/\sigma$	2
Motor equilibrium length	$d_{eq}/\sigma$	1
Polar-aligned motor probability	$p_p$	0 – 1.0
Antialigned motor probability	$p_a$	0 – 1.0

Table 2.4: Dimensionless groups for effective motor system

	Explicit motor model	Effective motor model
Motor-MT interaction	Explicit tetrameric and dimeric motors	Implicit motor potential between antialigned MTs
MT-MT interaction	Penetrable MTs in the impenetrable regime	Impenetrable WCA potential
Boundary conditions	Confined system	Periodic boundary conditions
MT aspect ratio	5	10
Dynamics	Brownian Dynamics	Langevin dynamics at overdamped regime
Persistence length	Rigid MTs	Flexible MTs in the rigid regime

Table 2.5: Difference between methods for results presented in chapters 3 and 4 (explicit motor model), and chapter 5 (effective motor model).

and the second method uses an effective motor potential to propel antialigned MTs.

The results from the first model are described in Chapters 3, 4 and the results from the second model are described in Chapter 5. A detailed list of differences between the two methods are given in Table 2.5.

## Chapter 3

# Motor-induced microtubule structures within confinement

Cytoskeletal structure and dynamics, important for vital biological processes, are dependent on numerous variables such as MT surface fraction, motor and specific enzyme concentrations. Understanding these non-equilibrium phenomena as a function of physiological variables is valuable in both reconstituted *in vitro* systems and coarse-grained computer simulations. In our system, we generate a coarse-grained model of MT-motor mixtures to capture key features of MT advection within a confinement. To account for depletion interactions arising from the crowded environment in the cytoplasm, we apply an attractive interaction between MTs, assisting MT bundling [63], which has been largely ignored in similar studies. Also, we use an attractive wall, according to the findings from *in vivo* experiments, which observed an anchored layer of stabilised MTs at the confinement boundary [50].

In this chapter, we qualitatively analyse the structural differences due to relevant system parameters. In particular, we compare the differences due to tetrameric and dimeric motors. Furthermore, we study the effect of MT attraction (Sec. 3.1), MT packing fraction (Sec. 3.2), confinement curvature (Sec. 3.3), motor concentration (Sec. 3.4), motor spring constant and motor velocity (Sec. 3.5), in order to study their effect on overall collective MT structure within the circular confinement. In Sec. 3.6 we describe the definition of the local polar order parameter used to capture the polarity of an individual MT's environment. In Sec. 3.7, we discuss the time-scale during which MTs order and form these structures. In Sec. 3.8, we discuss the findings from this chapter in the context of existing literature.

We use the model described in Sec. 2.2 to obtain the findings in the following sections. For all figures in Secs. 3.1 - 3.5, we have taken snapshots of the systems once the MT-motor systems are well-equilibrated and the structures have reached a steady-state, *i.e.*, a condition where motor energies, MT-MT and MT-wall interaction energies are fluctuating about a constant value, and is on average, unvarying in time.

In the following figures, MTs are coloured based on the colour legend given in Fig. 3.1. This helps us identify differences in structures and the relative alignment of clusters within the confinement.

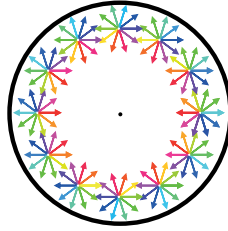


Figure 3.1: Colour legend. Colours of MTs depend on their orientation with respect to the confinement and their position within the confinement. The colour scheme helps distinguish clockwise from counterclockwise, and radially inwards from radially outward orientations. For instance, because MTs are polar, MTs that are tangentially aligned to the confinement radius can either be aligned in a clockwise (yellow) or counterclockwise (dark blue) manner. Similarly, radially-aligned MTs can be pointing towards the center of the confinement (red) or towards the wall (light blue).

### 3.1 Depletion forces and tetrameric motors give microtubule bundles

Figure 3.2 shows MTs in circular confinements with dimeric and tetrameric motors and without motors for weak ( $E_A = 0.2k_B T$ ) and strong ( $E_A = 1.0k_B T$ ) attractions. In the case without motors, Fig. 3.2A, structures form because of steric interaction between MTs and geometric frustration from the boundary. For weak attraction, we observe nematic ordering of MTs at the center of the confinement giving rise to defects at the edge of the confinement. Stronger attraction induces the formation of strong local alignment that forms a tiling pattern of MT stacks. We call these structures bundles.

Dimeric motors (Fig. 3.2B) lead to the formation of large polarity-sorted clusters. For weak attraction, we see MTs filling the entire confinement area, and multiple  $+1/2$  defects appear close to the confinement boundary. These defects are clearly visible for higher packing fractions shown in the following section. For the higher attraction energy, just like in the lower attraction case, we observe relative sliding between both polar-aligned and antialigned MTs. The motor forces are stronger than attraction forces and bundles of MTs are broken up. However, due to the higher attraction between MTs, empty spaces appear between the MT bundles. Apart from the density inhomogeneity within the confinement, for dimeric motors, the structural differences between the two attraction regimes is small.

Tetrameric motors (Fig. 3.2C) bring about a motor-induced polarity-sorting mechanism as well. Tetrameric motors induce the formation of polar-aligned MT bundles. These bundles are stabilised because motor arms walk at equal rates, towards the same cardinal direction on MT pairs. The lack of motor stresses on polar-aligned bundles means that polar-aligned orientations are preferred in tetrameric motor systems, which is not the case in the dimeric motor system.

However, as explained in Fig. 1.6, only motors that crosslink antialigned MT pairs induce large forces that slide MT pairs relative to each other. As a result, antialigned MTs are kinetically disadvantaged and are quickly removed from the system. In contrast to the case of dimeric motors, polar-aligned bundles are formed because motors do not

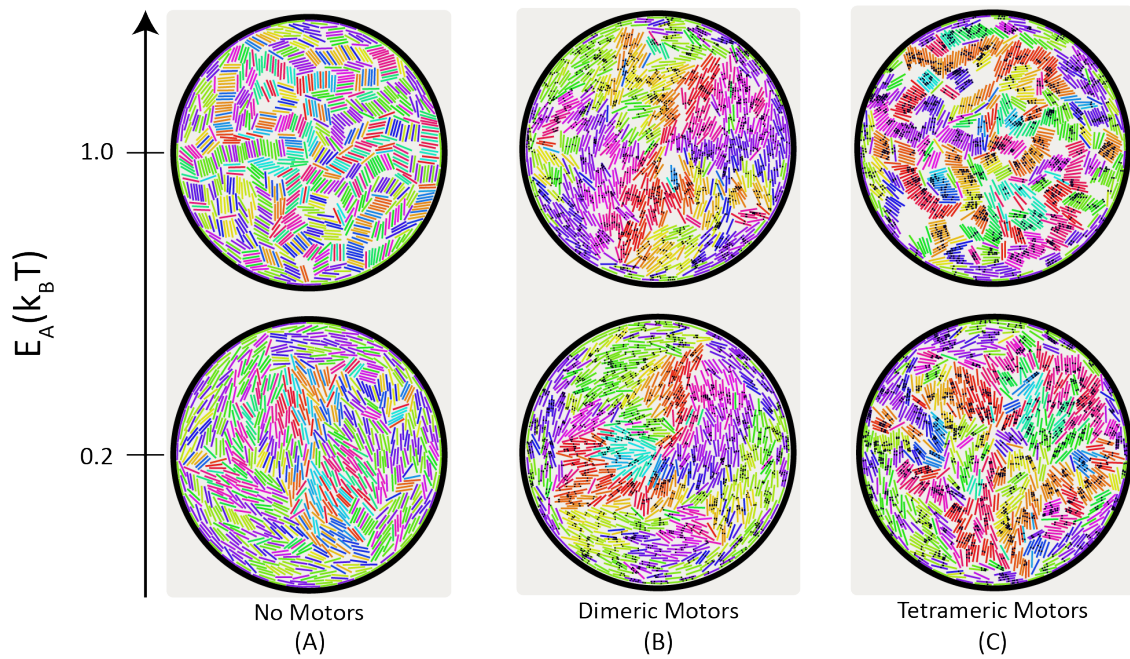


Figure 3.2: Stationary configuration of MTs with (A) no motors, (B) dimeric motors and (C) tetrameric motors within circular confinement for two attraction energies,  $E_A = 0.2 k_B T$  and  $1.0 k_B T$ . Number of motors is equal to the number of MTs for the four cases with motors *i.e.*  $N_m/N_f = 1$ . Colours of MT represent their orientation with respect to the radial direction from the center. Small black dots represent the position of each motor-arm on MTs.

develop large sliding forces between polar-aligned MTs. For low MT-MT attraction, we observe that bundles are not as prevalent as in the case of higher attraction. Under high MT-MT attraction, bundling is enhanced by the attractive interaction and multiple large bundles make up the entire system. Besides that, larger-scale polar order is absent. There are larger empty spaces between the MT bundles for the case of tetrameric motors than for dimeric motors at the higher attraction regime.

### 3.2 Effect of microtubule packing fraction

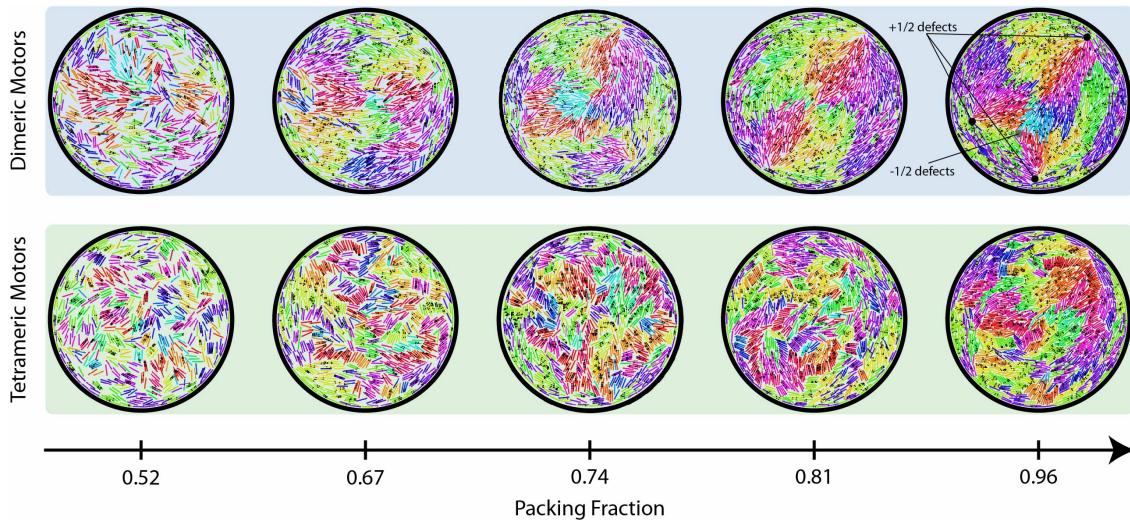


Figure 3.3: Snapshots of steady-state structures for different area fractions for dimeric and tetrameric motors. The area fractions correspond to 649, 834, 927, 1020, and 1205 MTs within the confinement. All packing fraction are computed using  $r_{\text{eff}} = 0.8r_{\text{min}}$ . 927 MTs are used for all the simulations in this chapter. For these simulations,  $R_W/r_{\text{min}} = 80$ ,  $\epsilon_w = 8k_B T$ ,  $E_A = 0.2$ ,  $v_m \tau / r_{\text{min}} = 50$ ,  $k_m d_t / f_s = 1$  and  $N_m / N_f = 1$ .

To understand the effect of MT packing fraction on large-scale structure formation we performed simulations for 649, 834, 927, 1020, and 1205 MTs.<sup>1</sup> At low densities, the structures away from the confining wall are isotropic, and there are no clear differences between the structures observed in tetrameric and dimeric motor systems. However, MTs away from the center are aligned tangentially to the confining wall due to the attraction with the wall. With increasing density, for  $\phi = 0.74$  and  $E_A = 0.2k_B T$ , large polar-aligned MT clusters start to form for the dimeric motor systems.

At the highest packing fractions,  $\phi = 0.96$ , we observe that large polar clusters also form for the tetrameric motor systems that accommodates the curvature of the confining wall and there are fewer MT bundles. This is because the steric effects dominate at this density and bundles are unfavourable. Polar alignment of MTs is maintained in this clustered arrangement. Additionally, in the dimeric motor system, there is a clear emergence of multiple  $+1/2$  topological defects indicated for  $\phi = 0.96$ . These defects mark the boundary between clockwise-oriented and counterclockwise-oriented MTs.

<sup>1</sup>This corresponds with packing fractions of 0.52, 0.67, 0.74, 0.81 and 0.96. These densities are calculated using  $r_{\text{eff}}$  obtained from the radial distribution function for the  $\phi = 0.74$  density, Fig. 2.6.

### 3.3 Domain sizes are conserved with confinement size

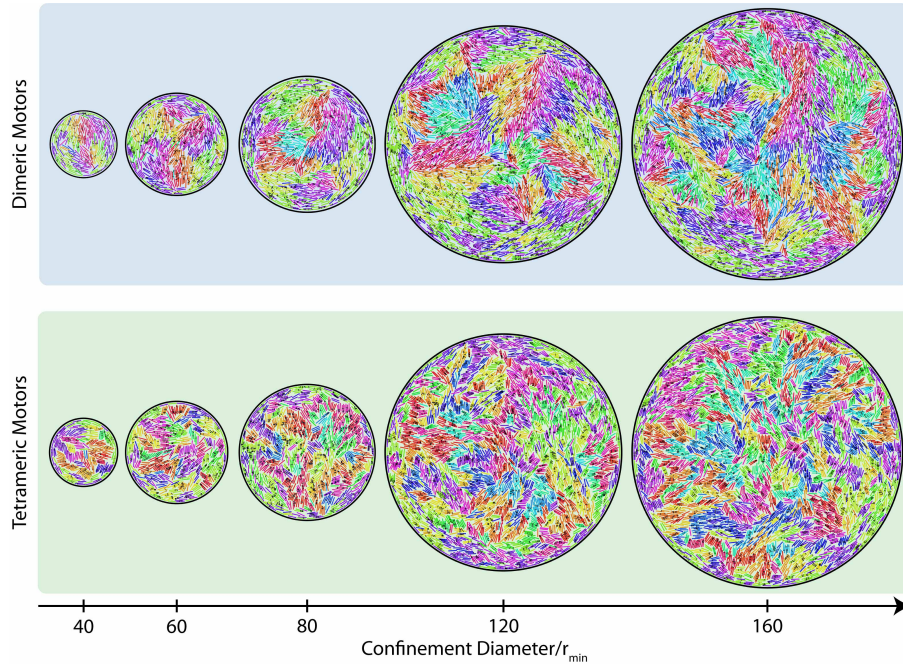


Figure 3.4: Snapshots of steady-state structures for different diameters of confinement relative to  $r_{\min}$ . We use  $R_W/r_{\min} = 80$  for all findings. The area fraction is kept constant at 0.74,  $\epsilon_w = 8k_B T$ ,  $E_A = 0.2k_B T$ ,  $k_m d_t/f_s = 1$ ,  $v_m \tau/r_{\min} = 50$  and  $N_m/N_f = 1$ .

To understand the effect of the confinement radius on the overall MT structure, we simulated systems with five different confinement radii, Fig. 3.4. The differences between dimeric and tetrameric motors are clearly visible even for the smallest confinement radius. Stable polar-aligned bundles form in the tetrameric motor system, and structures with multiple  $+1/2$  topological defects at the boundary form in the dimeric motor system.

For dimeric motors, polar-aligned domains span half of the confinement for  $R_W/r_{\min} = 60$ , as indicated by the similarly coloured filaments. The domain size is independent of the confinement radius, suggesting that the sizes of domains away from the confining wall are not affected by the confinement.

MT structures induced by tetrameric motors, on the other hand, are less ordered than structures induced by dimeric motors. At this level of attraction bundles of MTs make up the overall structure of the system. Note that the number of motors increases with increasing system size, since we keep the motor to MT ratio constant.

### 3.4 Polarity sorting can occur at low motor concentrations

In order to study the effect of motor concentrations on global MT structure, we studied five motor concentrations. Without motors, there was no polarity-sorting, and MTs appear with equal probability in clockwise/counterclockwise, and inward/outward orientations, Fig. 4.1. However, even at the lowest motor concentration,  $N_m/N_f = 0.5$ , the polarity-sorting mechanism leads to the formation of large polar-aligned clusters for both

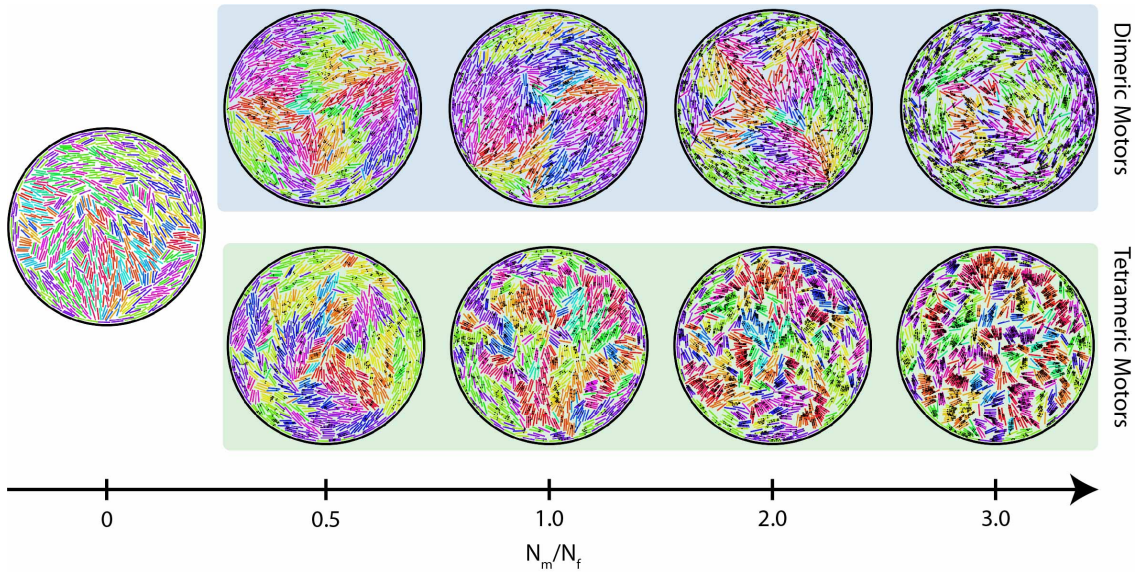


Figure 3.5: Snapshots of steady-state structures for different  $N_m/N_f$  for dimeric and tetrameric motors. We use  $N_m/N_f = 1$  for all findings. The area fraction is 0.74,  $R_W/r_{\min} = 80$ ,  $\epsilon_w = 8k_B T$ ,  $E_A = 0.2k_B T$ ,  $k_m d_t/f_s = 1$  and  $v_m \tau/r_{\min} = 50$ .

tetrameric and dimeric motors. Due to the lack of motors to form pronounced bundles, there is a remarkable similarity in the structures formed between the two motor systems at this concentration regime.

For higher motor concentrations significant differences in MT structures are observed. For  $N_m/N_f = 3$  a large fraction of MTs are aligned with the confining wall in the dimeric motor system. This disrupts the large polar-aligned clusters that are observed for lower motor concentration. Furthermore, higher motor concentrations, induce bundling of MTs in the tetrameric motor system.

## 3.5 Effects of other parameters on structure

### 3.5.1 Motor spring constant

At small motor spring constants,  $k_m d_t/f_s = 0.1$ , the motors are weak and the structures observed are similar to those without motors (Fig. 3.6). At higher motor spring constants, polarity-sorting induces structures similar to those described in the previous figures.

### 3.5.2 Motor velocity

Increasing motor velocity in the range  $5 \leq v_m \tau/r_{\min} \leq 500$  does not change the overall structure of the system for both motor systems (Fig. 3.7).

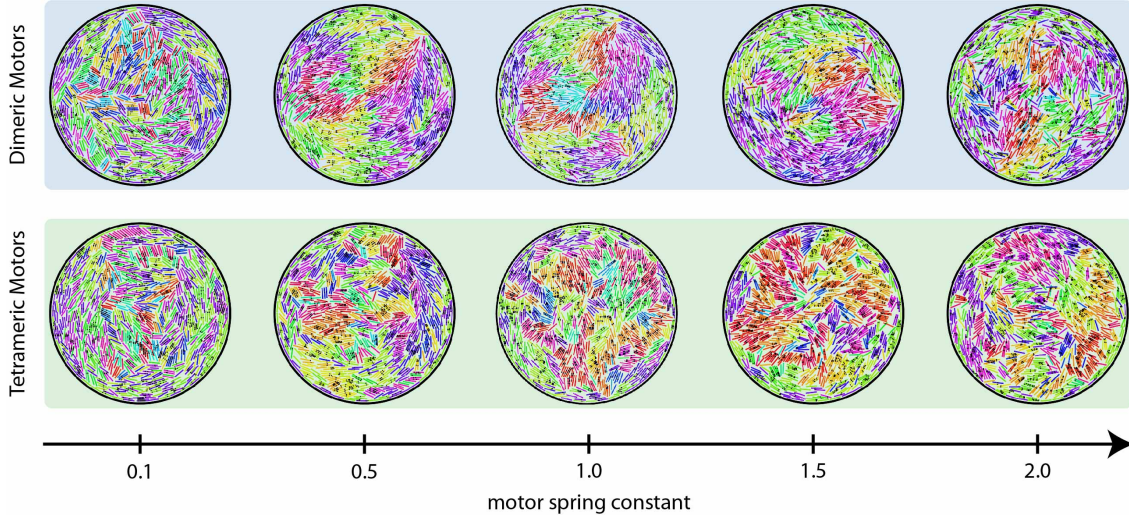


Figure 3.6: Snapshots of steady-state structures for different  $k_m d_t / f_s$ . A motor spring constant of  $k_m d_t / f_s = 1$  was used for all findings. The area fraction is 0.74,  $R_W / r_{\min} = 80$ ,  $\epsilon_w = 8k_B T$ ,  $E_A = 0.2k_B T$ ,  $k_m d_t / f_s = 1$ ,  $v_m \tau / r_{\min} = 50$  and  $N_m / N_f = 1$ .

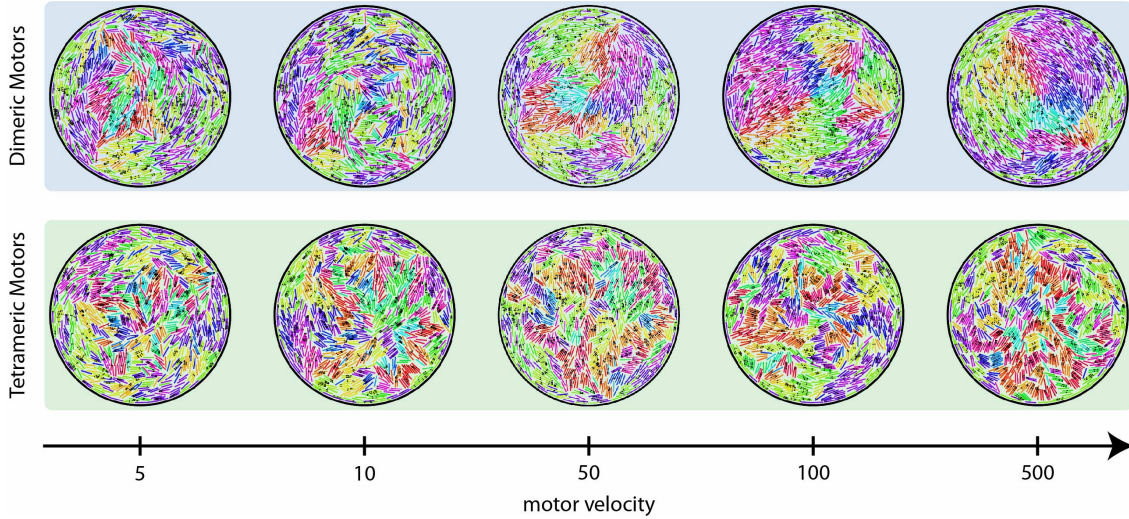


Figure 3.7: Snapshots of steady-state structures for different  $v_m \tau / r_{\min}$ . A motor velocity of  $v_m \tau / r_{\min} = 50$  was used for all findings. The area fraction is 0.74,  $R_W / r_{\min} = 80$ ,  $\epsilon_w = 8k_B T$ ,  $E_A = 0.2k_B T$ ,  $k_m d_t / f_s = 1$  and  $N_m / N_f = 1$ .

### 3.6 Local polar order parameter

In order to characterise a MT's neighbourhood, we define a pairwise motor partition function [5],  $q_{ij}(\mathbf{r}_i, \hat{\mathbf{p}}_i, \mathbf{r}_j, \hat{\mathbf{p}}_j)$ ,

$$q_{ij} = \rho^2 \int_{-1/2}^{1/2} ds_i \int_{-1/2}^{1/2} ds_j e^{-\beta U_m(|\mathbf{m}_{ij}|)}, \quad (3.1)$$

where  $\rho$  is the linear density of binding sites on a single MT, and  $s_i$  and  $s_j$  parametrise the positions of motor arms on MTs  $i$  and  $j$ , respectively (Eq. 2.39).

The center of mass distance between MT pairs,  $|\mathbf{r}_i - \mathbf{r}_j|$ , is a poor metric to quantify

whether the pair is amenable to motor binding. For instance, two different orientations of MT pairs can have the same  $|\mathbf{r}_i - \mathbf{r}_j|$ , but depending on their relative orientations, one might be available for motor binding, while the other may not.

Local polar order, on the other hand, weights pairwise interactions of MTs on the basis of motor binding site availability. It is a function of MT pair's relative orientation and distance. Because of the Boltzmann weight,  $q_{ij}$  is significant only for pairs of MTs in close proximity. When they are perfectly overlapping each other,  $q_{ij} = 1$ . When two MTs are sufficiently far away, such that no motors can crosslink them,  $q_{ij} = 0$ ; the MTs are outside motor range (Fig. 3.8(A and E)). Since the motor energy  $U_m(|\mathbf{m}_{ij}|)$  increases quadratically with increasing motor extension (Eq. 2.40), the partition function,  $q_{ij}$ , decays rapidly as binding sites for motors on the MTs become farther and less (Figure 3.8).

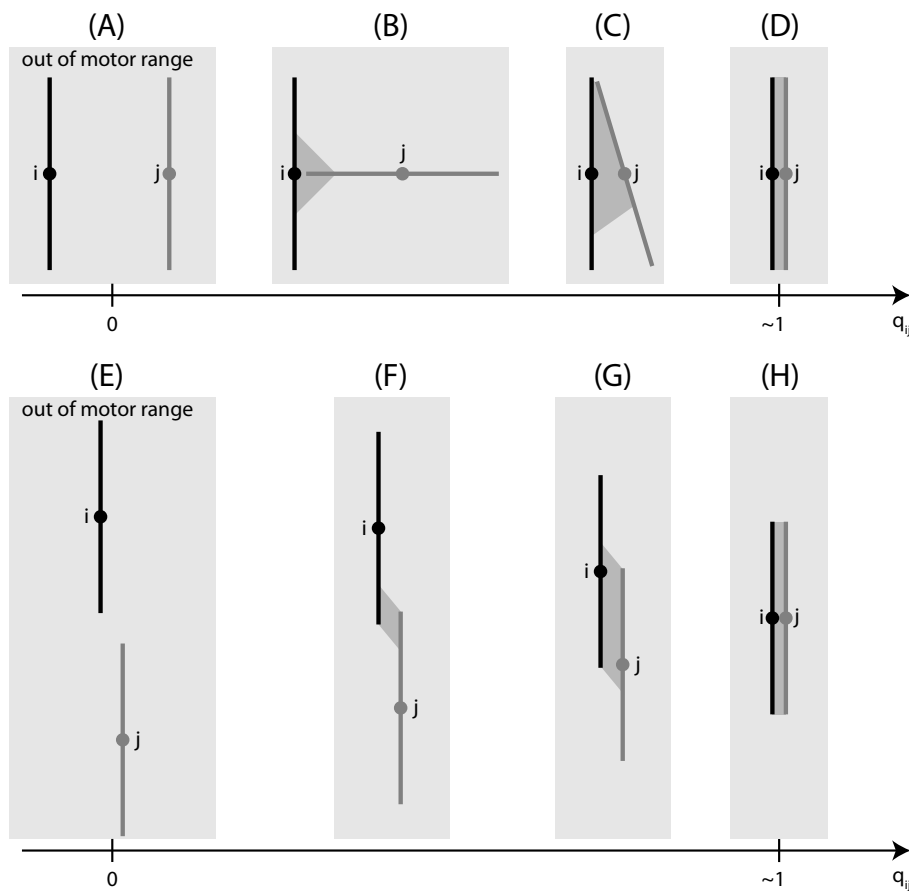


Figure 3.8: Pairwise motor partition function,  $q_{ij}$ , quantifies the availability of motor binding between MT pairs. (A, B, C, D) shows the effect of rotational degrees of freedom on MT pairs. (E, F, G, H) shows the effect of translational degrees of freedom on MT pairs. The shaded region indicates the region available for motor binding. (D) and (H) are identical and show an instance of near perfect overlap, and availability of motor binding between MT pairs.

For MTs within motor range, we define them to be antialigned if  $(\mathbf{p}_i \cdot \mathbf{p}_j) < 0$  and polar-aligned if  $(\mathbf{p}_i \cdot \mathbf{p}_j) \geq 0$ . Weighing  $(\mathbf{p}_i \cdot \mathbf{p}_j)$  by  $q_{ij}$  gives a good representation of local polar order, because it invokes the polarity of just the neighbourhood of the MT in

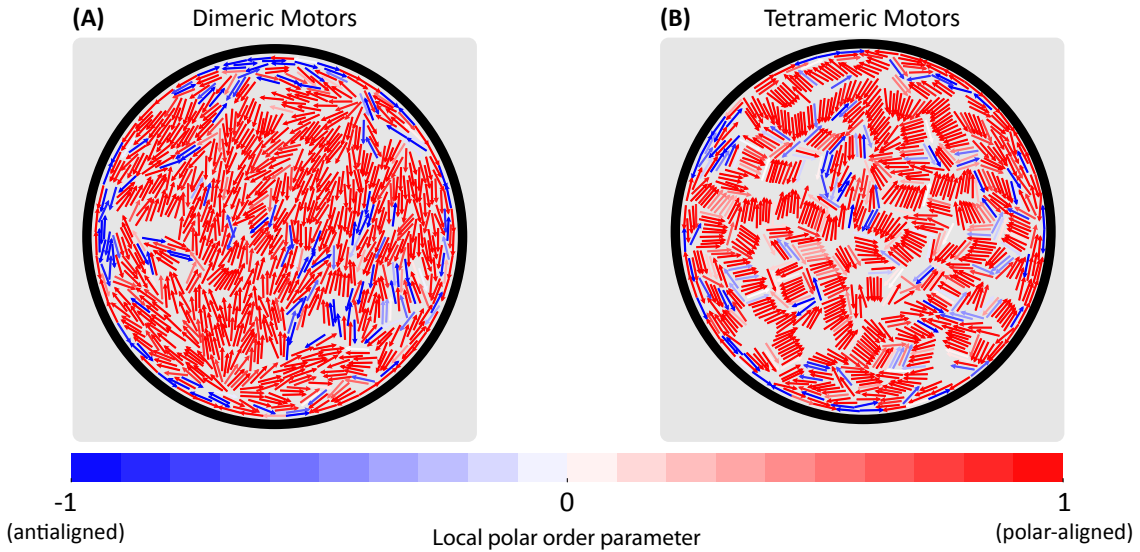


Figure 3.9: Stationary configuration of MTs in systems with (A) dimeric and (B) tetrameric motors for  $E_A = 1.0k_B T$  and  $N_m/N_f = 1$ . Arrow heads represent the direction of motor-arm motion on MT. The colour of each arrow represents the local polar orientational order parameter.

question. And the notion of neighbourhood is clearly defined by the motor range around the MT in question. By taking the sum of all interacting MTs with MT  $i$ ,

$$\psi(i) = \frac{\sum_{j \neq i} (\mathbf{p}_i \cdot \mathbf{p}_j) q_{ij}}{\sum_{j \neq i} q_{ij}}, \quad (3.2)$$

we ensure that the local polar order parameter depends on the polarity of the neighbourhood of MT  $i$ . In the following, we employ  $\psi(i)$  to find correlations in velocities with the polarity of MT neighbourhood.

Active stresses due to tetrameric and dimeric motors are dependent on the orientation of MT pairs. Both types of molecular motors induce an effective polarity-sorting, breaking the symmetry between these two orientations. For antialigned MTs, motor arms walk in opposite directions, imposing stress, inducing MT propulsion, thus making such orientations kinetically unfavourable. As a consequence, most MTs are in the polar-aligned orientation, and not the antialigned orientation.

For instance, an antialigned MT system ( $\langle \psi_i \rangle < 0$ ), under motor activity, will undergo higher active stresses than a system which starts from being polar-aligned ( $\langle \psi_i \rangle > 0$ ). The rate at which MTs become polar-aligned (or reach their steady-state structures), and the level of polar alignment that the system reaches at steady-state, depends on the type of motor MTs are exposed to and the motor concentration,  $N_m/N_f$ .

Figure 3.9 shows antiparallel and parallel orientations of MTs in the stationary state for systems with dimeric and tetrameric motors at the highest level of attraction, where MTs are coloured based on their local polar order parameter. In the dimeric motor system (Fig. 3.9A), large polar-aligned MT clusters compose the entire system. Geometric frustration due to the confinement, and the motion of MTs within polar-aligned clusters give rise to an interface of antialigned MTs that is perpetually created and destroyed

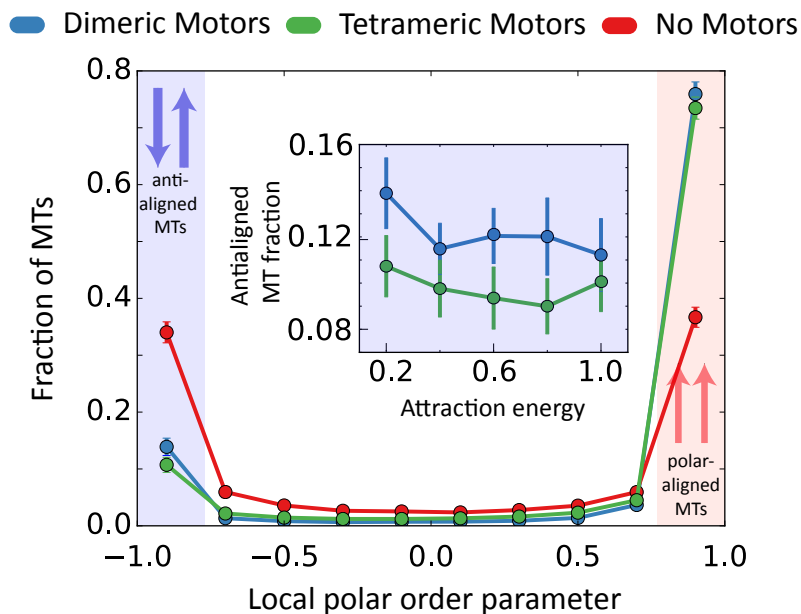


Figure 3.10: Fraction of MTs in the system as a function of their local polar order parameter for the  $E_A = 0.2k_B T$ ,  $N_m/N_f = 1$  systems. Inset shows the fraction of antialigned MTs in systems as a function of different  $E_A$  values for  $N_m/N_f = 1$ . Attraction energy is normalised by  $k_B T$ .

throughout the simulation. In particular, a significant population of motile, antialigned MTs are observed close to the confining wall. For the system with tetrameric motors (Fig. 3.9B), static, polar-aligned bundles of strongly attracting MTs make up the system. The strong attraction within aligned bundles hinders the formation of interfaces of antialigned MTs. Nevertheless, the confinement and the attractive wall hinder the sorting mechanism, such that a considerable population of antialigned MTs is observed. They appear intermittently, and quickly become members of polar-aligned bundles.

We have quantified the difference in the number of antialigned and polar-aligned MTs in Fig. 3.10. It shows the probability of finding a MT with the local order parameter,  $\psi$ . We find that due to steric interactions, MTs orient parallel to each other, such that most MTs have  $\psi_i$  values of either  $-1$  or  $1$ . This is apparent from the system without motors, where there is a higher, yet equal MT fraction in the polar-aligned and antialigned orientation ( $-1$  and  $+1$  respectively). For passive systems without motors, we cannot distinguish between polar-aligned and antialigned orientations, and either orientations are equally probable.

Remarkably, we observe that there is a slightly larger number of antialigned MTs in dimeric motor systems relative to tetrameric motor systems, and this is the case for all values of attraction energy  $E_A$  (Fig. 3.10 inset). This is because polar-aligned MTs crosslinked by tetrameric motors are more stable relative to the polar-aligned MTs crosslinked by dimeric motors, because the dimeric motors induce relative sliding between these MTs too. In chapter 4, we will see the implication of this higher population of antialigned MTs on overall dynamics.

### 3.7 Reaching steady-state structure

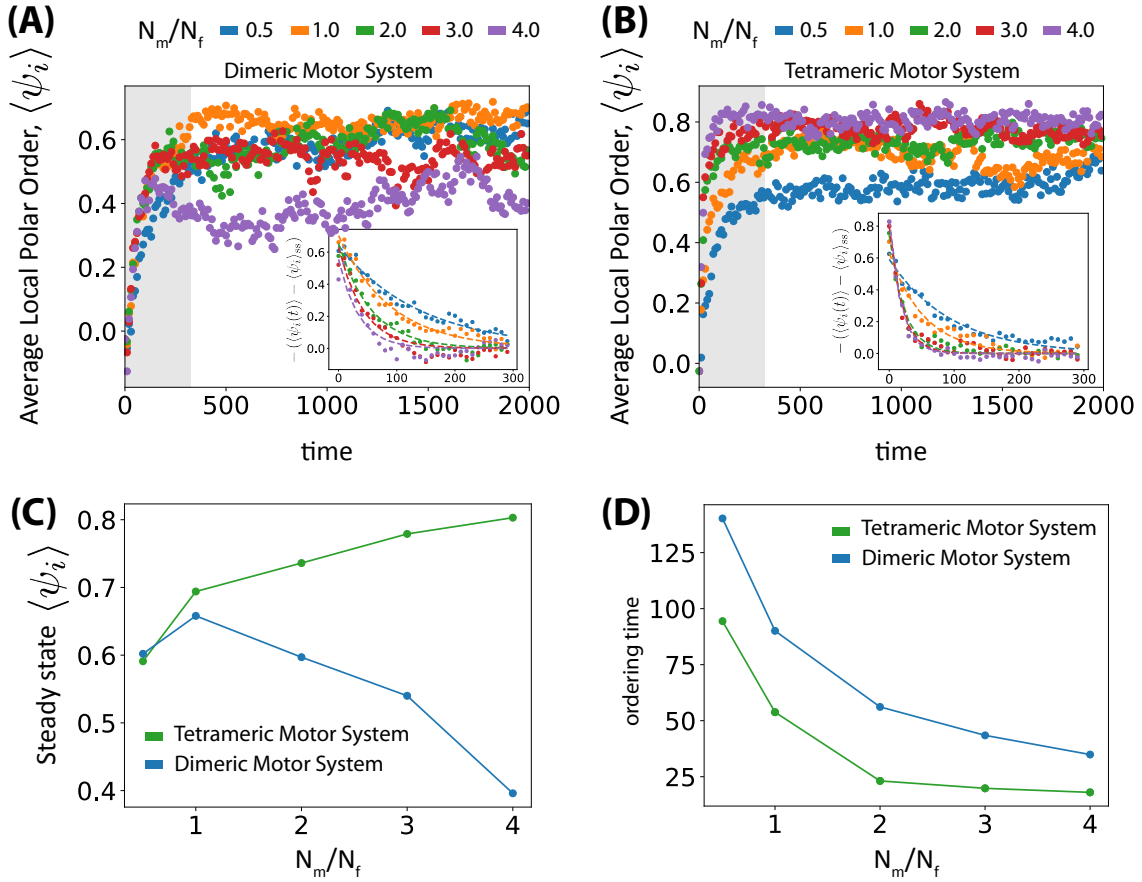


Figure 3.11: Estimation of time taken to form structures for dimeric and tetrameric motor systems for different motor concentrations. The system evolves from the initial state of an equilibrated passive system. The average local polar order  $\langle \psi_i \rangle$  is the mean  $\psi_i$  of all MTs in the system at a given time. This is seen to fluctuate about a fixed value for both dimeric (A) and tetrameric (B) motor systems. Assuming that the ordering only happens initially, we fit a decaying exponential,  $A \exp(-t/\lambda)$  to this data,  $-\langle \psi_i(t) \rangle - \langle \psi_i \rangle_{ss}$  (insets).  $\langle \psi_i \rangle_{ss}$  is the steady-state, average local polar order obtained from the last 1000 steps. (C)  $\lambda$  is reported as the ordering time as a function of different motor concentrations. Ordering time is normalised by,  $\tau$ , the timescale for the onset of activity. Area fraction is 0.74,  $R_W/r_{\min} = 80$ ,  $\epsilon_w = 8k_B T$ ,  $E_A = 0.2k_B T$ ,  $v_m \tau / r_{\min} = 50$  and  $k_m d_t / f_s = 1$

We take an equilibrated passive configuration, such as that shown in Fig. 3.9A. We then introduce dimeric and tetrameric motors at different concentrations to study the onset of global order (Figs. 3.11A and B). Since there is no polarity-sorting initially, and the occurrence of either polar-aligned or antialigned MT pair configurations are equally likely,  $\langle \psi_i \rangle(t = 0)$  is approximately 0. Upon introduction of motors, in all cases the polarity-sorting mechanisms of both dimeric and tetrameric motors necessarily leads to greater polar order, and an increase in polar order. The polar order parameter at steady-state fluctuates around  $\langle \psi_i \rangle_{ss}$ .

For the dimeric motor system, Fig. 3.11C shows that increasing motor density leads to a general decrease in steady-state polar order. At low motor concentrations,  $N_m/N_f = 0.5$ ,  $\langle\psi_i\rangle_{ss}$  is similar to that of the tetrameric motor system. However, at higher motor concentrations,  $\langle\psi_i\rangle_{ss}$  decreases due to the formation of antialigned MT interfaces, which drives activity. This is further observed in the higher fluctuations in  $\langle\psi_i\rangle$  compared to the tetrameric motor system shown in Fig. 3.11B. This is particularly the case for the largest motor concentration,  $N_m/N_f = 4$ .

For the tetrameric motor systems, when there are too few motors to crosslink MTs, like when  $N_m/N_f = 0.5$ , there are not enough motors to form bundles as much as what is observed for higher  $N_m/N_f$ . As a result, we find a generally lower level of global order. Beyond when  $N_m/N_f > 0.5$ , we find a linear increase in  $\langle\psi_i\rangle$  with increasing  $N_m/N_f$ . This is due to the polar-aligned bundling of MTs seen in Fig. 3.5. Due to the lack of perpetual generation of antialigned MT interfaces, we notice that  $\langle\psi_i\rangle$  fluctuations are smaller across all motor concentrations for tetrameric motor systems compared to dimeric motor systems. These findings further confirm that MTs in polar bundles are less stable in dimeric than in tetrameric motor systems. As posited in Fig. 1.6, this is because of the relative sliding that dimeric motors can induce even for polar-aligned bundles, which tetrameric motors are not capable of.

From Fig. 3.11D, due to an increase in active stress with increasing motor concentration, we find that the time taken for polarity-sorting shortens with increasing motor concentration for both motor types. Sorting occurs faster in the tetrameric motor systems than the dimeric motor systems for all motor concentrations, due to higher motor stresses generated by tetrameric motors for antialigned MT pair configurations. However, we find that, for tetrameric motors, there are only small differences in ordering times for higher motor concentrations,  $N_m/N_f > 1$ . This indicates that the formation of larger bundles can happen as quickly as smaller bundles if there are enough motors to facilitate the process. For dimeric motors, in the motor concentrations that we simulated, however, we observe a monotonous decrease in ordering times.

## 3.8 Conclusions

Although the cytoskeleton is a dynamic scaffold, the steady-state structure of the filaments inside cells is of particular importance to intracellular processes. In this chapter, we studied the differences in structures brought about by dimeric and tetrameric motors under different parameter regimes.

### 3.8.1 Steric effect and depletion forces

We show that the geometric frustration induced by confining a dense mixture of MTs within a circular confinement leads to topological defects at the boundary, in the case without motors. The structure observed for passive MTs, under low attraction, is consistent with calculations based on the generalised Onsager model, where ordered two-fold symmetric defect structures are observed between non-attractive filaments within a line boundary at high densities [68].

In our model, activity mediated by dimeric motors leads to large polar-aligned MT

clusters, which are non-motile at short timescales. Tuning MT-MT attraction levels to those found in experiments does not have a significant effect on the structure of this system [63]. MTs subject to tetrameric motors formed small polar-aligned bundles, and increasing MT-MT attraction enhances MT bundling in these systems. Bundling of MTs subject to tetrameric motors were similarly observed in the literature in cases of high motor concentrations, and small motor run lengths in two-dimensional simulations of a minimal physical model of MTs, motors, and static crosslinkers [4]. Similar bundles were also reported in simulations of active gels of filaments and motors between two infinite parallel walls, at high motor attachment rates [6].

### 3.8.2 Filament-motor mixtures

In computer simulations of filament-motor system confined to a pressurised cylindrical box, where the confinement radius was slightly larger than the length of a semiflexible filament, rotational motion of filaments and motors during a transient vortex phase was observed [7]. This system ultimately collapsed into a semi-aster. In contrast, for our circular confinement with a radius eight times the MT length, we find persistent flows close to the confinement wall. Although the large polar-aligned clusters in the case of the dimeric motors does not exhibit significant short-time dynamics (Fig. 4.10), fluctuations in MT orientations within these clusters close to the confining wall gives antialigned MTs which result in persistent flows and redistribution of MTs throughout the confinement. This activity can be seen in the velocities of MTs in antialigned environments and their trajectories.

Moreover, with filament lengths comparable to the radius of the confinement, two  $+1/2$  defects were observed at the confinement edge in both active [7] and passive [68] cases. We recovered such defects in passive cases. However, with shorter filaments relative to confinement radius, defects were not distinguishable in the tetrameric motor systems, and multiple  $+1/2$  defects were observed in the dimeric motor system, close to the confinement, and conjugate  $-1/2$  defects in the bulk. We posit that a sufficiently flexible boundary can lead to filopodia-like protrusion, which will be actively extended by the  $+1/2$  defect tip, as observed in experiments where MTs are confined to the surface of a spherical vesicle [65].

## Chapter 4

# Motor-induced microtubule dynamics within confinement

By far, we have understood the onset of large-scale confined structures induced by dimeric and tetrameric motors. However, a description of the structure only gives a portion of the insight that makes the cytoskeleton biologically functional. Most physiological processes are reliant on dynamical properties of the MT network, and the dynamics, similar to the network structure, is dependent on the parameters that were explored in the previous chapter. Although these networks are at steady-state, due to the work of crosslinking kinesin motors on neighbouring MTs, we expect them to be perpetually dynamic, and always changing in structure.

In this chapter, using the methods described in Sec. 2.2, we will primarily study the effect of motor concentration and MT attraction on MT dynamics mediated by tetrameric and dimeric motors within a circular confinement. In Sec. 4.1, we use the MSD to categorise the different regimes of length and time scales involved in the system. We study how these scales change as a result of changing the variables studied in Chapter 3. In Sec. 4.2, a MT's local polar order is linked to its velocity, and the difference between cooperative and antagonistic effects of dimeric motors is distinguished. In Sec. 4.3, the large-scale dynamics of MTs and how they move within the confinement is detailed. In Sec. 4.4, life cycles of the different types of motors, and the evolution of their lengths after crosslinking are shown. In Sec. 4.5, the connection between our work to existing experimental and theoretical studies is discussed.

## 4.1 Motor-mediated microtubule motion

### 4.1.1 Time scales for diffusion and activity

To quantify the influence of local polar order on MT dynamics, we investigate it in two regimes separated by a crossover time  $\tau$ . At short time scales, MT motion is driven by the thermal bath. At large time scales, collective interaction between multiple MTs takes place. At time scales comparable to  $\tau$ , stresses generated by the motors are dissipated in the thermal bath. To quantify the displacement of MTs due to motor stresses, we need to estimate  $\tau$ . To do so, we define the MSD of the MTs' centers of masses using,

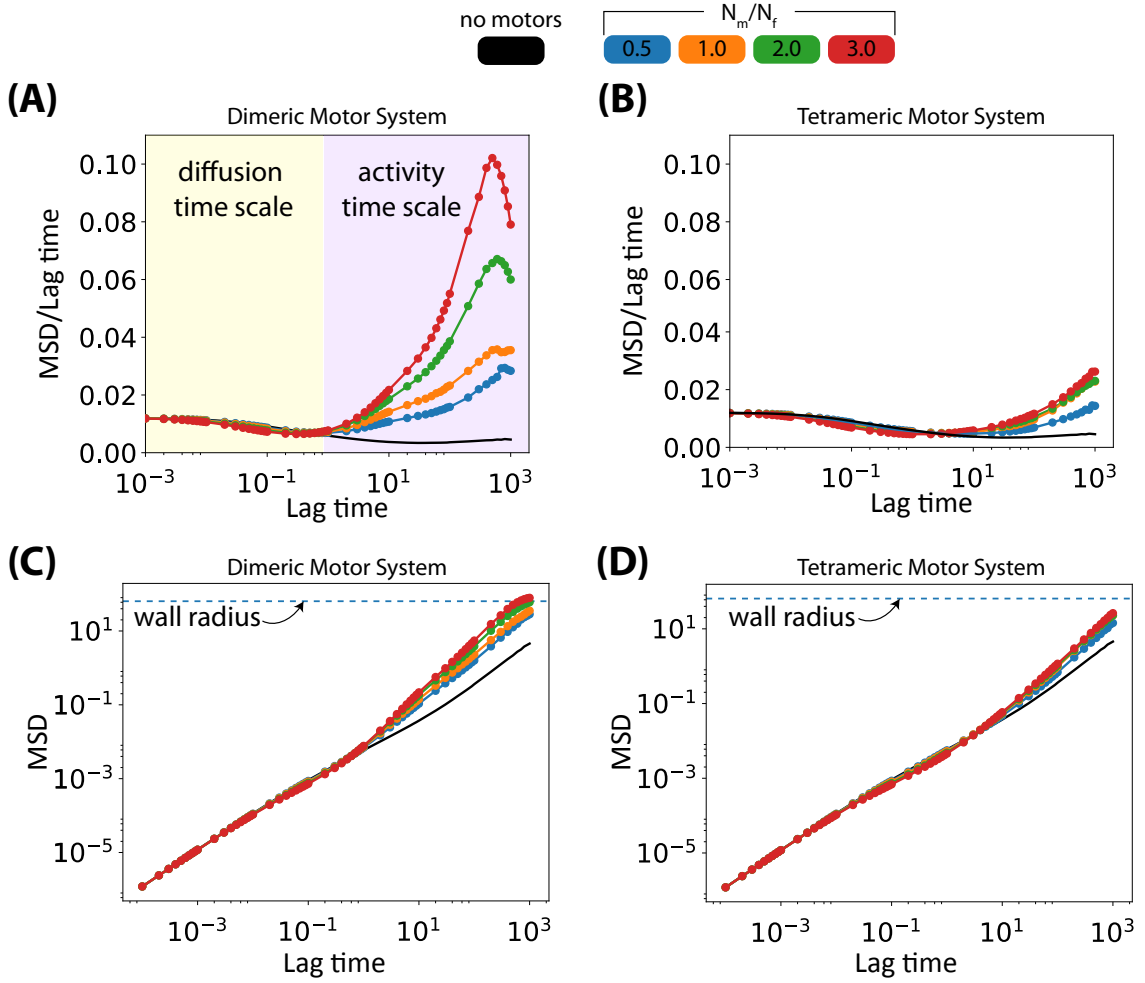


Figure 4.1: MSD/Lag time for different  $N_m/N_f$  for dimeric (A) and tetrameric (B) motors. MSD vs. lag times for dimeric (C) and tetrameric (D) motors. MSD is normalised using  $L^2$  and lag time is normalised using the onset of the activity time scale,  $\tau$ , *i.e.*, the lag time where motor stresses are manifested in the MT dynamics. The squared confinement radius is represented by the dotted blue line in (C) and (D). The area fraction is 0.74,  $R_W/r_{\min} = 80$ ,  $\epsilon_w = 8k_B T$ ,  $E_A = 0.2k_B T$ ,  $k_m d_t/f_s = 1$  and  $v_m \tau/r_{\min} = 50$ .

$$\text{MSD}(t') \equiv \langle |\mathbf{r}_i(t) - \mathbf{r}_i(t+t')|^2 \rangle_{t,i}, \quad (4.1)$$

where  $t'$  is the lag time.<sup>1</sup> The characteristic lag time,  $t' = \tau$ , is chosen such that the MTs' MSD is just out of the diffusive regime for the dimeric motor system with  $N_m/N_f = 2.0$  and  $E_A = 0.2k_B T$ . At lag times smaller than  $\tau$ , Fig. 4.1 shows that MTs are diffusing, because  $\text{MSD}/t'$  is constant. At lag times larger than  $\tau$ , systems with motors cause MTs to displace actively, and activity increases with the concentration of motors. In this time regime, for passive systems, steric interactions with neighbouring MTs become dominant, since MSDs of MTs without motors show a decrease in diffusion.

Figure 4.1(A) shows that at lag times smaller than  $\tau$ , the constant  $\text{MSD}/t'$  indicates

<sup>1</sup>See Appendix B for algorithms for computing time correlations.

that MTs diffuse at this time scale. This is also represented by the similar behaviour of systems with motors with systems without motors at these shorter time scales. At lag times greater than  $\tau$ , MTs in systems with motors displace actively, and the activity increases with the concentration of motors. In this time scale, we observe a decrease in diffusion in the MSD of MTs without motors due to steric interactions.

On average, we find that dimeric motors induce significantly larger displacements than tetrameric motors, despite having only half of the mobility of the tetrameric motors. This is contrary to the case of a single pair of MTs that was posited in Fig. 1.6. Activity increases with increasing motor concentration, because there are more active elements to slide MTs. This is especially prominent for dimeric motors compared with tetrameric motors. In Fig. 4.1C we show the onset of the plateau in the MSD upon reaching  $R_W^2$ , where a significant proportion of MTs' displacements are limited by the confining wall. In this time scale, we do not observe this for the tetrameric motors, because they are yet to reach this limit (Fig. 4.1D).

#### 4.1.2 Effect of confinement diameter

The peaks in Fig. 4.1 A and the plateau at  $10^3\tau$  in Fig. 4.1 C indicate that at large time scales MTs are hindered by the confinement and the squared displacements are limited by confinement size. These trends would be clearer in these plots if we had accessed longer time scales in our simulations.

The MSD plateaus approximately at  $R_W^2$  for lag times greater than  $10^3\tau$ , indicated by “wall radius” and the dotted line on Fig. 4.1 C and D. When the curves reach this length scale, it indicates that a significant proportion of MTs have displaced a distance  $R_W$ , and that they are obstructed by the confinement. This effect results in the curves in Fig. 4.1 falling to 0 despite the motor-induced activity. Comparing Fig. 4.1 A to B, which are both plotted in the same scale, shows that in these time scales MTs driven by dimeric motors are significantly more dynamic than MTs driven by tetrameric motors for all motor concentrations.

Each data point in Fig. 4.1 represents the mean of a distribution of squared displacements between 0 and  $R_W^2$ . We found that, for a given lag time, these squared displacement distributions are largest at 0, and decay with increasing displacements. For longer lag times,  $t' \sim 10^3\tau$ , when the curves in Fig. 4.1 are nearing their peaks, the squared displacement distribution falls abruptly at  $2R_W$ , because the MSD is strictly bound by the confinement diameter.

MT dynamics in the bulk, especially for the dimeric motor system, is unaffected by the confinement diameter in the range  $40 < R_W/r_{\min} < 160$ , as the MSDs in the time regime  $10^{-3} < \tau < 10$  are identical, Fig. 4.2. At larger lag times,  $\tau > 10$ , the slope of the MSD begins to decrease and reaches the peaks shown in Fig. 4.1A. The onset of this decrease in lag time, and in space, depends on the size of the confinement. In larger confinements, we do not see the effect of the confinement until we access much larger lag times than for the smaller confinements.

For the tetrameric motor system, dynamics is substantially affected by confinement size, even for lag times smaller than  $\tau < 10$ . In general, dynamics becomes faster with increasing confinement size. This is because smaller confinements cause large MT bundles

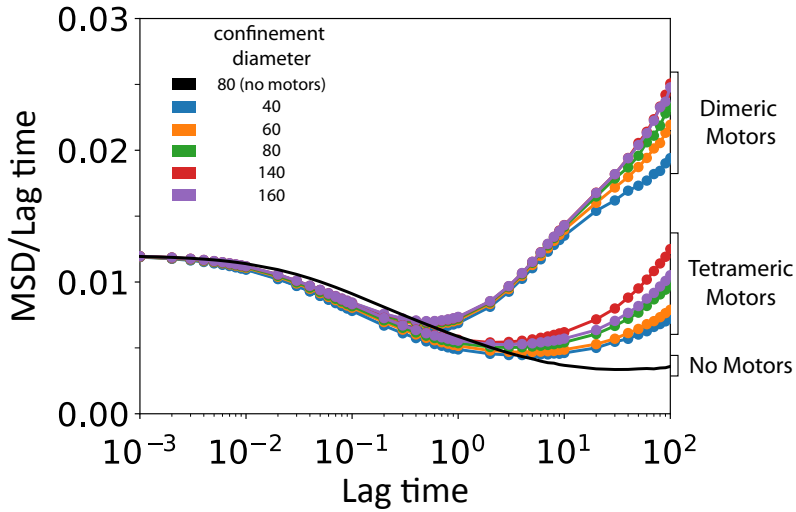


Figure 4.2: MSD/Lag time for different confinement diameters with  $\phi = 0.74$ ,  $\epsilon_w = 8k_B T$ ,  $E_A = 0.2k_B T$ ,  $k_m d_t / f_s = 1$ ,  $v_m \tau / r_{\min} = 50$  and  $N_m / N_f = 1$ . Note that we use more MTs and more motors in systems with larger confinements. Lag time is given in units of  $\tau$ .

to form that span the entire confinement, Fig. 3.4. The polar-aligned bundles do not allow for large motor stresses, and lead to slower dynamics. With larger confinements, the bundles make up a smaller fraction of MTs in the system, and there are more antialigned MT interfaces which drive dynamics.

#### 4.1.3 Effect of motor stiffness

In all our results, we have used a motor stiffness that corresponds to the stiffness measured from single kinesin molecule experiments [92]. However, in experiments similar to our simulations, multi-motor clusters formed using tetrameric streptavidin, crosslink MTs [32, 33]. The spring constant of such motor clusters is difficult to estimate. It is, thus, instructive to understand the effect of various motor stiffnesses on the collective dynamics of MTs.

Figure 4.3 shows that at a low motor stiffness dynamics slows down, because motor stresses are not large enough to overcome the friction of MTs' surrounding, and the MSD is similar to that for the system without motors. MTs are more dynamic at higher motor stiffness but for dimeric motors, the effect of MT stiffness does not result in higher MT dynamics after a certain point. For the stiffnesses in our simulations, we do not reach this regime in the tetrameric motor system, even with  $k_m d_t / f_s = 2$ . In fact, at this motor stiffness, the MSDs between the two motor types are similar at long lag times,  $t' / \tau > 10^2$ . We also observe general structural similarities between the two systems in this regime. This is because global ordering of MTs observed at lower motor stiffness is absent, as the motor stresses become comparable to the steric forces.

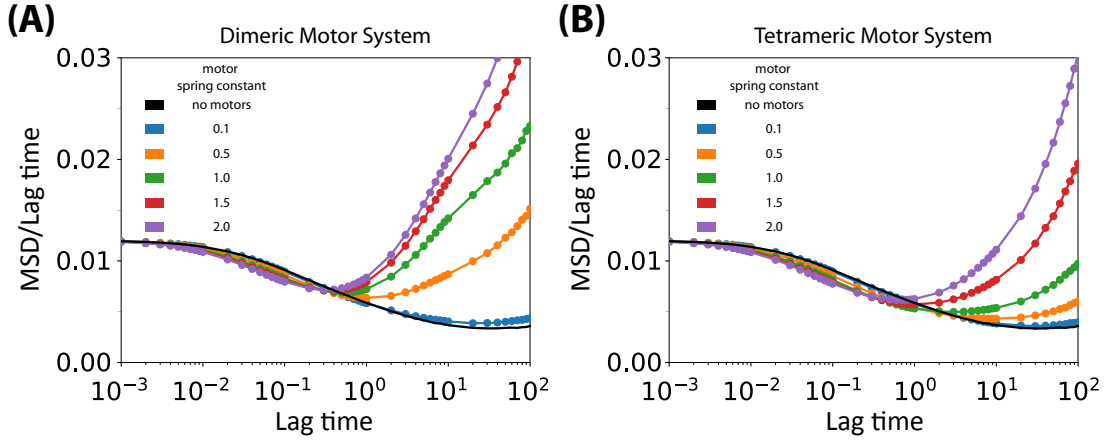


Figure 4.3: MSD/Lag time for various values of  $k_m d_t / f_s$  with  $\phi = 0.74$ ,  $\epsilon_w = 8k_B T$ ,  $E_A = 0.2k_B T$ ,  $v_m \tau / r_{\min} = 50$ ,  $R_W / r_{\min} = 80$  and  $N_m / N_f = 1$ . Lag time is given in units of  $\tau$ .

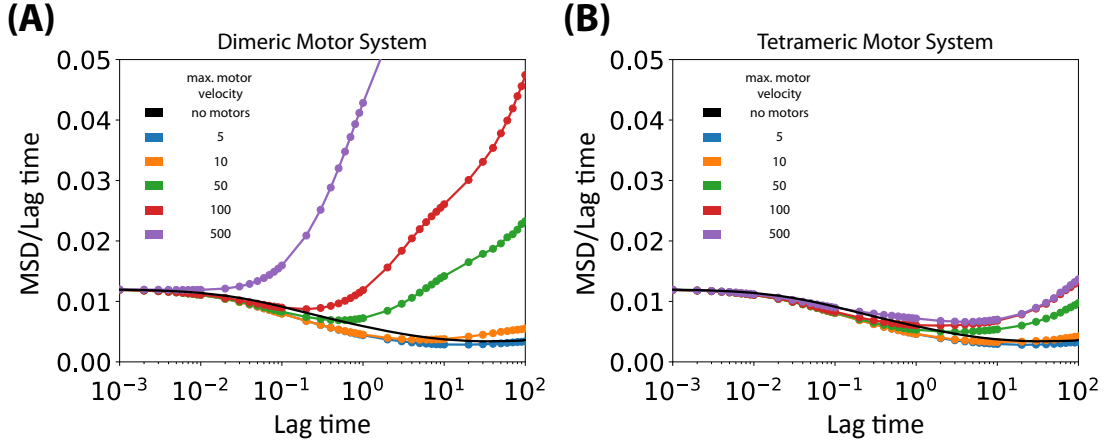


Figure 4.4: MSD/Lag time for different  $v_m \tau / r_{\min}$ . The area fraction is 0.74,  $R_W / r_{\min} = 80$ ,  $\epsilon_w = 8k_B T$ ,  $E_A = 0.2k_B T$ ,  $k_m d_t / f_s = 1$  and  $N_m / N_f = 1$ . Lag time is given in units of  $\tau$ .

#### 4.1.4 Effect of motor velocity

Figure 4.4 shows that higher motor velocities increase MT dynamics for both motors, and is particularly prominent for dimeric motors. This is because there are more antialigned interfaces, which can lead to higher motor stresses in the dimeric motor system than the tetrameric motor system. With higher motor velocities, in the tetrameric motor system, we observe a higher level of MT bundling, which causes motor arms to walk equally fast on either polar aligned cross-linked MT. This does not lead to large motor stresses, and MT dynamics is not dramatically different. Larger motor velocities lead to greater global structural order for both motor systems shown in Fig. 3.7.

Note that we use the time scale,  $\tau$ , to nondimensionalise motor velocity, which was obtained for the system with  $v_m \tau / r_{\min} = 50$ . For higher motor velocities, the onset of activity occurs at smaller lag times for the dimeric motor system. Given that the value of

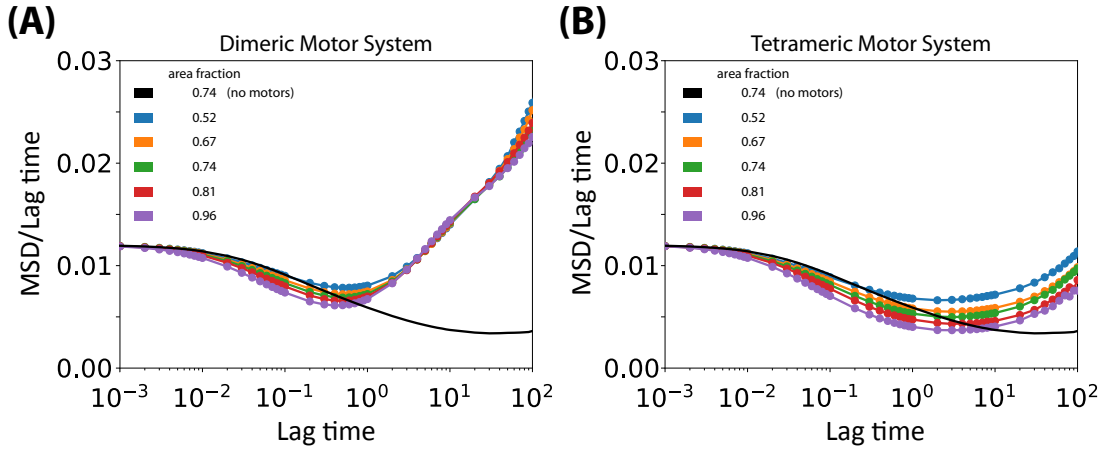


Figure 4.5: MSD/Lag time for different area fractions for dimeric and tetrameric motors. The area fractions correspond to 649, 834, 927, 1020, and 1205 MTs within the confinement.  $R_W/r_{\min} = 80$ ,  $\epsilon_w = 8k_B T$ ,  $E_A = 0.2k_B T$ ,  $v_m \tau / r_{\min} = 50$ ,  $k_m d_t / f_s = 1$  and  $N_m / N_f = 1$ . Lag time is given in units of  $\tau$ .

$\tau$  is conserved when other parameters are changed, we can conclude that motor velocity determines the activity time scale in the system. For  $v_m \tau / r_{\min} = 500$ , MTs go from the diffusive regime,  $t'/\tau < 10^{-2}$ , to the active regime,  $t'/\tau > 10^{-2}$ , without a decrease in MSD slope, which indicates the onset of steric forces.

Increasing the motor velocity leads to motors taking larger steps in a given simulation step. Crosslinked MTs would have less time to relax to accommodate the motor stresses. In other sections we used the maximum motor speed to be close to values observed in experiments for single motors [90]. Here, we study the effect of motor speed on the MSD of MTs.

#### 4.1.5 Effect of microtubule area fraction

In Sec. 4.1 we explained how MT dynamics can be divided into diffusive, steric and active regimes. We can see in Fig. 4.5 that the slope of the MSD decreases with increasing area fraction in the steric regime, at lag times  $10^{-2} < t'/\tau < 1$ . This is because steric forces hinder diffusive motion at this time scale.

For the dimeric motor system, Fig. 4.5A shows that at lag times  $t'/\tau > 1$ , in the active regime, the MSDs are similar regardless of the area fraction. Fig. 3.3 does not show any large-scale structural changes with increasing area fraction. Area fraction does not affect MT dynamics at this time scale for dimeric motor systems. In the tetrameric motor system, Fig. 4.5B, we see that dynamics is faster at lower area fractions at lag times  $t'/\tau > 1$ . Fig. 3.3 shows that with increasing area fraction, the tetrameric motor system becomes more ordered, and the number of antialigned interfaces decreases, leading to slower dynamics.

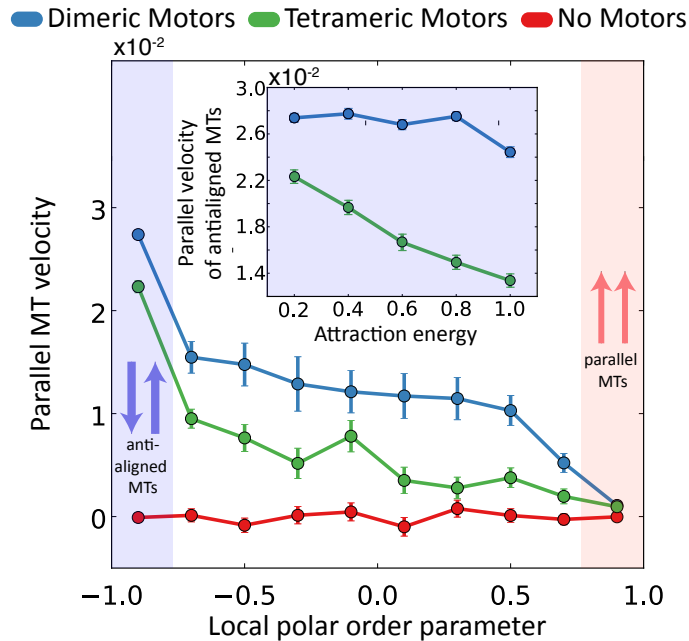


Figure 4.6: Parallel velocities as a function of local polar order parameter for  $E_A = 0.2k_B T$  systems and  $N_m/N_f = 1$ . The inset shows the velocity of antialigned MTs in systems with different  $E_A$  values for  $N_m/N_f = 1$ . Since motor-arms move in the opposite direction of  $\mathbf{p}$ , by this convention, a propelled MT moves in the opposite direction, giving positive values for  $v_{\parallel}$ . Velocities are normalised by  $L/\tau$ . Attraction energy is normalised by  $k_B T$ .

## 4.2 Motor propulsion and local order

### 4.2.1 Antiparallel microtubules induce maximum motor propulsion

To estimate the propulsion of MTs, we use the displacement of the MTs center of mass in the characteristic lag time,  $\tau$ . This defines a MT velocity,

$$\mathbf{v}(t) = \frac{\mathbf{r}(t + \tau/2) - \mathbf{r}(t - \tau/2)}{\tau}. \quad (4.2)$$

We compute an effective, average MT propulsion velocity due to motor stresses,  $v_{\parallel}$ , by projecting  $\mathbf{v}(t)$  on  $\mathbf{p}(t)$ .

For both dimeric and tetrameric motors, Fig. 4.6 shows that the MT velocity is strongly correlated to the polarity of its environment; with highest propulsion velocities measured for MTs antialigned with respect to their environments, and smallest velocities measured for MTs polar aligned with respect to their environments. There are significantly fewer MTs where their local polar order is  $-0.8 < \psi_i < 0.8$  (Fig. 3.10), which leads to larger error bars. These findings also establish that antialigned MT configurations are, on average, kinetically unstable and short lived, compared to polar aligned bundles.

Velocities generated by the two types of motors depend also on the MTs attraction energy  $E_A$  (Fig. 4.6 inset). Namely, tetrameric motors are less able to overcome opposing attractive forces that favour bundle formation (Fig. 2.4B), compared with dimeric motors. At  $E_A = 0.2k_B T$ , dimeric motors induce an antialigned parallel MT velocity only 1.2 times higher than that induced by tetrameric motors. At  $E_A = 1.0k_B T$ , however, we notice a

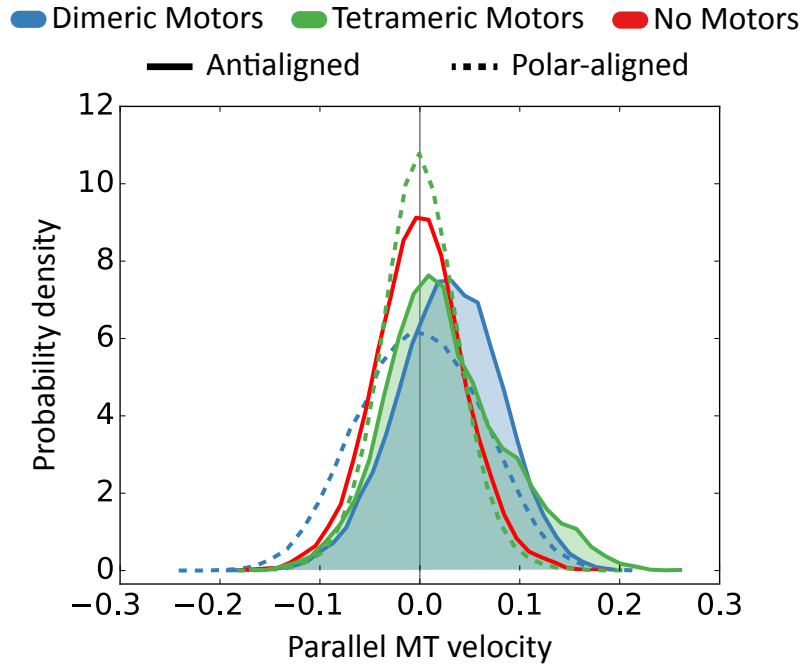


Figure 4.7: Histogram of parallel velocities for antialigned and polar-aligned MTs from the antialigned bins (blue) and the polar-aligned bins (red) from Fig. 4.6 ( $E_A = 0.2k_B T$  and  $N_m/N_f = 1$ ). Table 4.1 shows the first three moments of the distribution. The area under the curve from antialigned MTs in dimeric and tetrameric motor systems are coloured blue and green respectively. The black vertical line represents a parallel MT velocity of zero. Velocities are normalised by  $L/\tau$ .

Motor Type	MT orientation	Mean	Standard Deviation	Skew
Dimeric	Antialigned	0.029	0.052	-0.154
	Polar-aligned	-0.001	0.061	-0.003
Tetrameric	Antialigned	0.025	0.060	0.405
	Polar-aligned	-0.001	0.040	0.092
No Motors	-	0.000	0.045	0.012

Table 4.1: First three moments for the parallel MT velocity distribution from Fig. 4.7.

relative decrease in MT velocities in the tetrameric motor system, making it 1.9 times smaller than velocities in the dimeric motor system.

### 4.2.2 Decomposed histogram of microtubule propulsion

Figure 4.7 shows histograms of parallel velocities of MTs for polar-aligned and antialigned MTs (left-most and right-most bins in Fig. 4.6). The histogram without motors shows the effect of thermal forces at this time scale. Dimeric motors that crosslink polar-aligned MT pairs also cause a parallel MT velocity distribution that is centred around zero, but has a larger width than for passive MTs. Tetrameric motors that crosslink polar-aligned MT pairs leads to bundle formation, which results in a narrower distribution of parallel MT displacement.

MTs in antialigned environments have a skewed velocity distribution compared to polar-aligned MTs due to sliding motor stresses. The manner by which this sliding force manifests itself is different for dimeric and tetrameric motors. Tetrameric and dimeric motors induce an average sliding velocity of 0.025 and 0.029 respectively, Table 4.1. Figure 4.7 shows that although, tetrameric motors between antialigned MTs are able to generate higher velocities, these only make up the tail of the positively skewed distribution (Table 4.1). Dimeric motors, on the other hand, have the peak of their distribution at a higher velocity than that of tetrameric motors, and the distribution is skewed in the opposite direction. This shows that the maximal relative longitudinal displacement and the resultant maximal force for tetrameric motors is higher than for dimeric motors. However, on average, antialigned MT pairs are propelled more by dimeric motors than by tetrameric motors because a larger fraction of motors crosslinking antialigned MTs are capable of inducing positive propulsion velocities.

## 4.3 Collective rotation at the boundary

So far, we have compared the overall structure and dynamics of confined MTs for dimeric and tetrameric motors. Having established that the dimeric motor system is the more dynamic of the two systems, in order to understand collective effects of motile MTs we study how motion is coordinated within the confinement by dimeric motors.

### 4.3.1 Boundary microtubules are fastest

From Fig. 4.8 we can see that the region closest to the boundary is the most dynamic. We split the confinement into three sections, as illustrated in the inset. The centers of masses of MTs at various time origins are used as reference points to spatially assign the MSD measurement. If an MT leaves its original section, we continue to track it according to its position at the time origin. We notice that for both dimeric and tetrameric motor systems, the region closest to the confining wall is the most dynamic. In regions away from the wall, MTs are either diffusive or subdiffusive because of steric effects.

Figure 4.9 shows trajectories of four especially motile probe MTs (orange, green, yellow and blue) and the environment upon which they conduct this motion. The MTs travel with higher velocities in an environment of anti-aligned MTs and show erratic motion in an environment of polar-aligned MTs. If they encounter defects at the boundary [69], such as the blue MT at  $500\tau$  in Fig. 4.9, their trajectories may change direction abruptly.

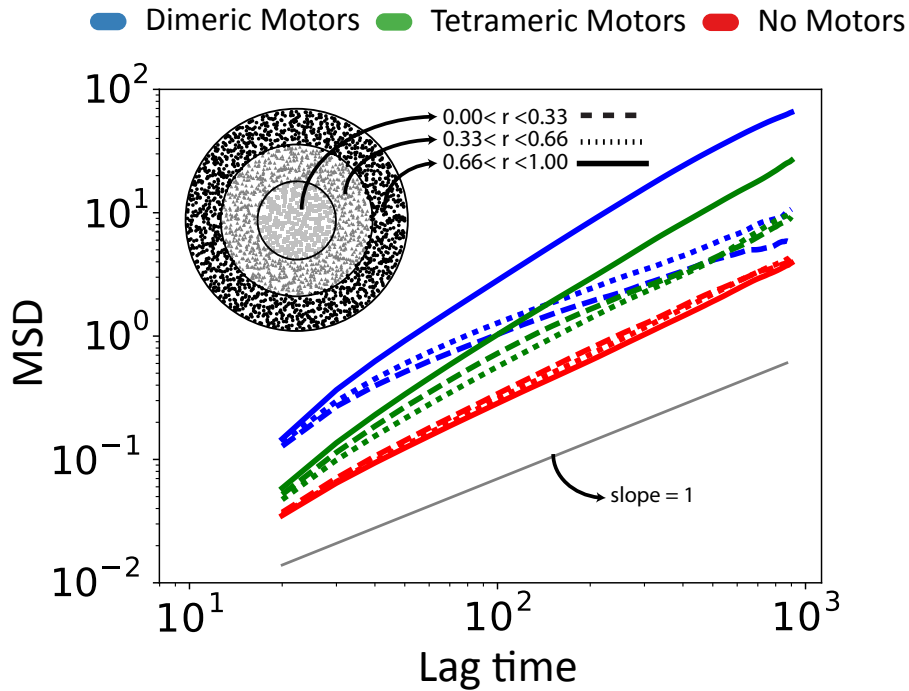


Figure 4.8: Translational mean-squared displacement (MSD) of MTs' center of masses by region.  $E_A = 0.2k_B T$  and  $N_m/N_f = 1$ . MSD is normalized using  $L^2$ . Lag time is normalised using the onset of the activity time scale,  $\tau$ . The radial distance of the MT's center of mass,  $r$  is normalised by the radius of the confinement,  $R_W$ .

### 4.3.2 Non-attractive confinement gives slower microtubules

In Fig. 4.10, we study the velocity of MTs in radial sections of the confinement. Persistent motion (as shown in Fig. 4.9) is most prevalent at the edge of the confinement for both dimeric and tetrameric motors. The parallel MT velocities are larger for MTs near the boundaries, and smaller when MTs are greater than  $0.3 R_W$  away from the boundary. Velocities at the boundary are significantly higher for dimeric motor systems than for tetrameric motor systems (Fig. 4.8). Parallel MT velocity near the boundary generally decreases with increasing MT attraction. This is due to the lack of MT activity with cohesive interactions which hinder MT-MT sliding (Fig. 4.10 inset). In both cases, we observe that MT velocities are higher than in systems without motors. Note that this analysis gives statistics over only a small number of MTs at the center, and averages over a larger number of MTs with increasing radial distance from the center.

We can attribute higher MT velocities near the boundary to a layer of immotile MTs, because having a non-attractive wall decreases parallel MT velocity for both types of motors. This is particularly the case of tetrameric motors because a non-attractive wall gives a structure of polar aligned MT bundles, and immotile MT tracks at the boundary are almost entirely absent. In this system, average parallel MT velocity is less than half that of the system with the attractive boundary. The MT velocities are closer to the system without any motors. In the case of dimeric motor systems, the effect of attraction is less, but substantial. This suggests that the immotile layer of MTs that occur due to the attractive boundary, serve as a track for the cytoplasmic MTs to slide against.

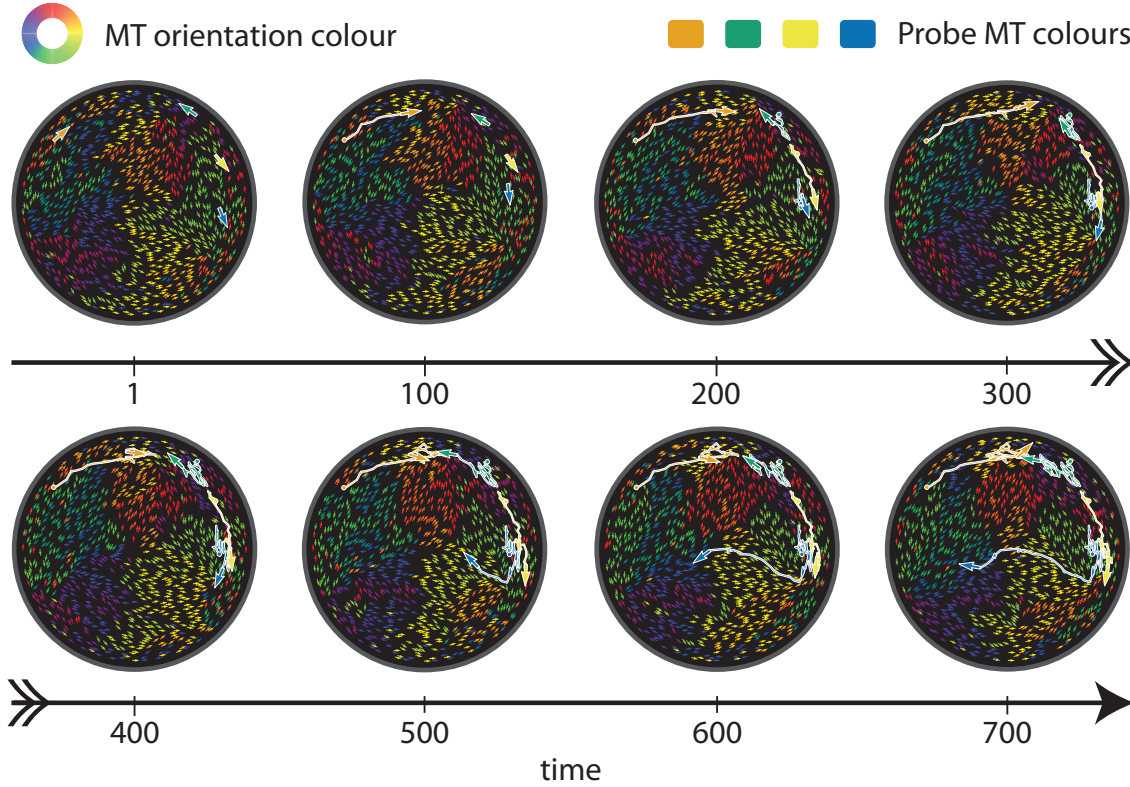


Figure 4.9: Time lapse trajectories of MTs in a dimeric motor system, with probe MTs represented with larger arrows and their trajectories are plotted in orange, green, yellow and blue. Smaller arrows represent of all other MTs. All arrows indicate the direction of vector  $\mathbf{p}$ , *i.e.*, the opposite direction of motor motion, which is generally the direction of MT propulsion. The trail left by the larger arrows correspond to the path that they have taken. In this case  $E_A = 0.2$  and  $N_m/N_f = 1$ . The time axis is normalised using,  $\tau$ .

## 4.4 Life cycle of a motor

We define motor processivity as the number of consecutive time steps that a motor remains attached without releasing the crosslinked MT pair, *i.e.*, the youngest (oldest) motors with the lowest (highest) processivity are the motors that have been attached for the shortest (longest) period of time. In our simulations, a motor that does not reach stall length will have motor-arms that each cover MT length  $L$  in  $10\tau$ .

### 4.4.1 Dimeric motors are more processive

Figure 4.11A shows that the youngest motors are the most numerous, and the number of motors decreases exponentially with processivity, *i.e.*, motors detach from MT pairs at a rate proportional to the number of surviving motors. Tetrameric motors that crosslink antialigned MTs have the fastest detachment rate and the shortest mean life time (Table 4.2 and Fig. 4.11B). The rates of detachment and mean life times in the other three cases are similar. Since the probability of motor attachment is independent of MT alignment and there are fewer antialigned MT pairs than polar-aligned MT pairs, motors between antialigned MTs are fewer than motors between polar-aligned MTs (Fig. 4.11A inset).

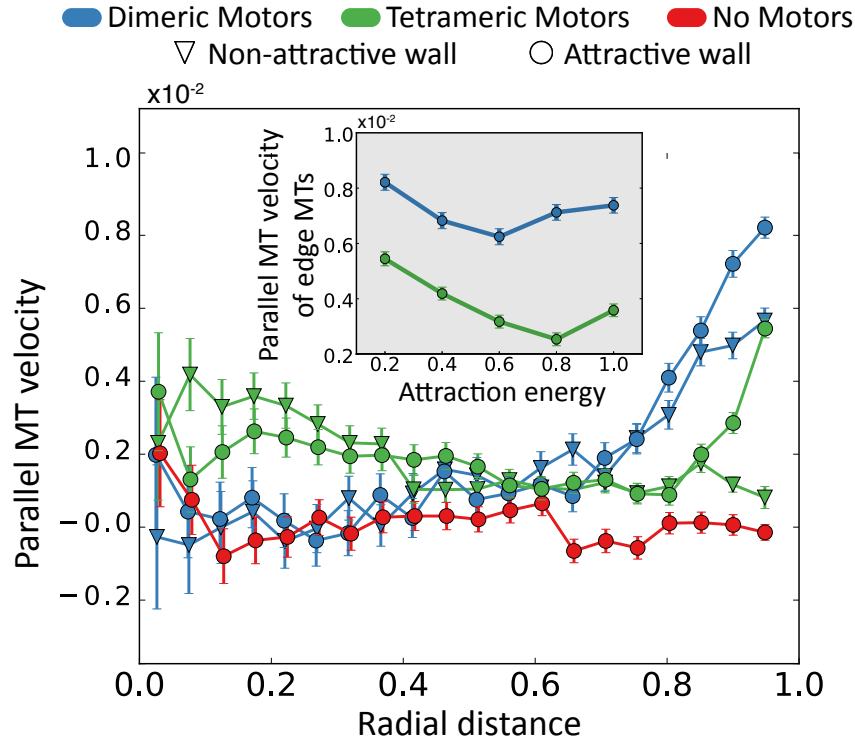


Figure 4.10: Parallel velocities of MT systems with tetrameric, dimeric and no motors as a function of radial distance for  $E_A = 0.2k_B T$  and  $N_m/N_f = 1$ , for the cases with attractive and non-attractive confining walls. Inset shows the mean velocity of the MTs closest to the confinement edge for different  $E_A$  values for  $N_m/N_f = 1$ . Velocities are normalised by  $L/\tau$ . Radial distance is normalised by confining wall radius,  $R_W$ . Attraction energy is normalised by  $k_B T$ .

Motor type	MT	Mean	Motor energy
	orientation	life time	fraction
Dimeric	Polar-aligned	2.87	0.789
	Antialigned	3.58	0.211
Tetrameric	Polar-aligned	3.05	0.936
	Antialigned	1.51	0.064

Table 4.2: Mean motor life times are obtained from fitting exponential curves to Fig. 4.11(A). Motor energy fraction is the sum of squared lengths of motors crosslinking polar-aligned (antialigned) MTs relative to all the motors in the system. Mean life time is normalised using the time scale,  $\tau$ .

At  $N_m/N_f = 1$ , half of the dimeric motors were lone motors connecting MT pairs. Of the remaining motors, 70% of the motors were in a correlated orientation, *i.e.*, with their

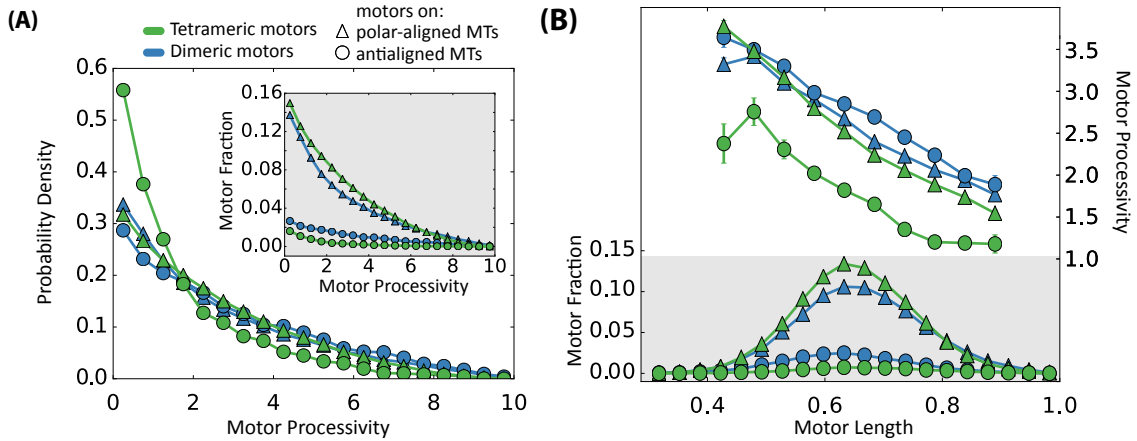


Figure 4.11: (A) Histogram of motor processivity for the four motor categories (dimeric/polar-aligned, dimeric/antialigned, tetrameric/polar-aligned and tetrameric/antialigned). Inset (grey) is the histogram before normalisation. (B) Histograms (not normalised) of motor extensions, and motor processivity as a function of motor extension. Parameters are  $E_A = 0.2$  and  $N_m/N_f = 1$ . Motor processivity is normalised using the time scale,  $\tau$ . Motor extensions are normalised using motor threshold extension,  $d_t$ .

motile (anchored) arms on the same MT.

From Fig. 4.11B we see that the average motor extensions are distributed similarly about a mean of  $0.65d_t$  for both types of motors. It also shows that the contribution of energy from the motors comes mostly from motors crosslinking polar-aligned MTs, especially for the system with tetrameric motors (Table 4.2), because motors crosslinking antialigned MT pairs are less processive, and fewer in number. We also observe that motor extension decreases linearly with processivity. The relationship between motor extension and motor processivity is similar between all motors, except for tetrameric motors that crosslink antialigned MTs.

#### 4.4.2 Effect of motor velocity on processivity

Figure 4.12 shows that increasing motor velocity decreases mean motor life time. At high motor velocities ( $v_m\tau/r_{\min} > 50$ ), tetrameric motors connecting antialigned MTs have significantly lower motor processivities than dimeric motors. This is because, at higher motor velocities, motors exceed their threshold lengths before MTs can respond to the stretched motor. Dimeric motor processivities, on the other hand, are less sensitive to motor velocity. This allows the dimeric motor system to be more dynamic due to larger sustained active stresses.

At low motor velocities ( $v_m\tau/r_{\min} = 5$ ), mean motor processivity is high. However, Fig. 4.4 shows that slow motors behave as passive cross-linkers and hinder diffusion. This suggests that a combination of high motor velocity and high motor processivity is required for fast MT dynamics.

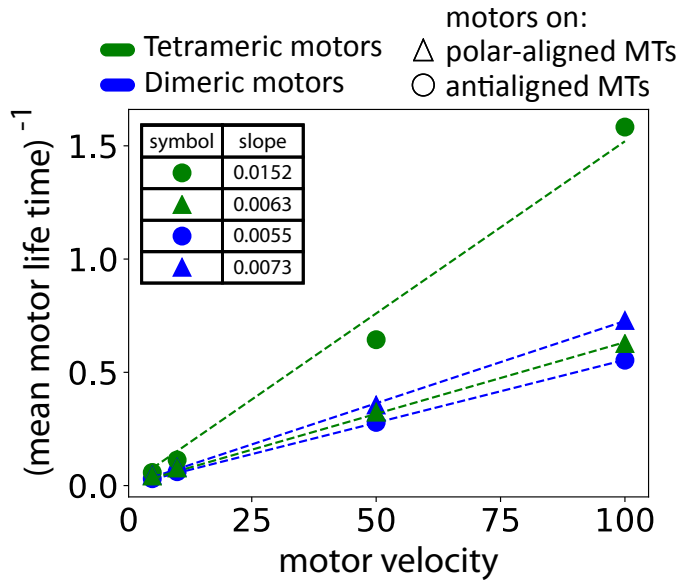


Figure 4.12: Inverse of mean motor life time as a function of motor velocity for tetrameric and dimeric motors. Mean motor life time is obtained by fitting an exponential function,  $A \exp(-t_{\text{mp}}/\lambda_{\text{mp}})$  to the histogram of motor processivity.  $t_{\text{mp}}$  and  $\lambda_{\text{mp}}$  is the motor processivity and the fitting parameter to obtain mean motor life time respectively. Mean motor life time is measured in units of  $\tau$ .  $\lambda_{\text{mp}}^{-1}$  is plotted against motor velocity, and we report the slopes of linear fits in the table. We treat motors on polar-aligned MTs and antialigned MTs separately. Motor velocity is given as  $v_{\text{m}}\tau/r_{\text{min}}$ . Area fraction of MTs is 0.74,  $R_{\text{W}}/r_{\text{min}} = 80$ ,  $\epsilon_{\text{w}} = 8k_{\text{B}}T$ ,  $E_{\text{A}} = 0.2k_{\text{B}}T$ ,  $N_{\text{m}}/N_{\text{f}} = 1$  and  $k_{\text{m}}d_{\text{t}}/f_{\text{s}} = 1$ .

## 4.5 Conclusions

We have shown that motor-mediated pairwise interactions give large-scale MT dynamics. The polarity-sorting mechanism, where motors induce cohesive interactions between polar-aligned MTs, and larger forces between antialigned MTs, have been previously observed and described in various studies [4, 5, 103]. In this study, we find that motor arm asymmetry can play a crucial role in motor mediated MT interactions. In general, our findings suggest that the dimeric motors are more effective at inducing large forces between antialigned MTs than tetrameric motors.

### 4.5.1 Effect of attractive confinement

In our simulations, the attractive wall leads to a layer of less motile, disordered MTs near the wall. This models a cortical actin cytoskeleton to which motors can crosslink and propel MTs in the bulk. *In vivo* experiments have shown that MTs are anchored to the actin cortex near the cell membrane [50]. Motors use these anchored MTs as tracks to propel cytoplasmic MTs and carry out directed streaming. In the experiments, cytoplasmic MTs were found to travel five times faster than the anchored, cortical MTs. Also, cells with kinesin mutants deficient in MT sliding resulted in a 14-fold decrease in cytoplasmic MT velocities. Relative to the MTs at the center of the confinement, we show that wall attraction, which stabilises a layer of immobile MTs at the confinement

wall, causes a three fold and 1.4-fold increase in parallel MT velocity at the confinement edge for the tetrameric and dimeric motor systems respectively (Fig. 4.10). We motivate that the overall dynamics of the system is enhanced dimeric motors, and that this is most prominent close to the edge of the confinement (Fig. 4.8).

### 4.5.2 Role of motor-arm asymmetry

By comparing dimeric motors with tetrameric motors, we have studied the role of asymmetric motor-arm velocity in propagating MT motility within confinement. The tetrameric motor model has been considered extensively in computer simulations to describe similar phenomena [4–6], but the effect of motor asymmetry has been largely ignored, despite dimeric motors being ubiquitous in nature. Apart from the role of the dimeric motor, kinesin-1, in MT-MT sliding [25, 43, 50], computer simulations that investigated force generation in one-dimensional (1-D) bundles of MTs [41] report bundle expansion only in the case of dimeric motors. Tetrameric motors, on the other hand, opposed bundle expansion. In fact, it has been shown that the regulation of axon initiation and growth can only be explained by considering the significant roles of dimeric motors, such as kinesin-1 and cytoplasmic dynein [41], on top of MT polymerisation. The extensile nature of the aligned 1-D filament bundles is reflected by the elongated clusters in our simulations.

Differences in MT motion as a result of motor asymmetry are not immediately obvious. For instance, higher sliding velocities between antialigned MTs crosslinked by tetrameric MTs, due to a higher longitudinal displacement per time step, as depicted in Fig. 1.6, may be expected. However, Fig. 4.7 shows that on average antialigned MTs crosslinked by dimeric motors slide faster, and that the higher velocities of the tetrameric motors only make the tail of a skewed parallel MT velocity distribution (Fig. 4.7 and Table 4.1). The dimeric motors, although incapable of producing as large forces as tetrameric motors, could sustain a larger force for a longer time without detaching, resulting in a more symmetric parallel MT velocity distribution with a larger absolute mean velocity (Fig. 4.11).

### 4.5.3 Dependence of dynamics on local order

We find that the dynamics of MTs is strongly dependent on the local polar order parameter, *i.e.* density of opposite-polarity MT pairs. This supports simulations of one-dimensional filament bundles cross-linked by molecular motors, where the drift rate for a given filament has been shown to be a linear function of the density of the opposite polarity filaments [42]. This further consolidates general assumptions made by polarity dependent continuum models of MTs [96], where interaction between antiparallel filaments phenomenologically leads to filament sorting. In this chapter, we identify mechanisms involved (Fig. 1.6) that contribute to the distribution of parallel MT velocities for dimeric and tetrameric motors. For dimeric motors (Fig. 4.7 blue lines), the solid line corresponds to scenarios posited in Fig. 1.6 (D and F), and the dotted line corresponds to Fig. 1.6 (C and E). Both antialigned MT mechanisms Fig. 1.6 (D and F) give an effective propulsion in the direction of MT orientation, which results in the skewed velocity distribution, where the peak is at non-zero velocity. Both polar-aligned MT mechanisms Fig. 1.6 (C and E) are impervious to the MT orientations, and result in motor-induced motion in either direction, depending on the location of the anchored arm(s). This results in a symmetric

distribution of velocities shown in Fig. 4.7 solid blue line, which has a wider distribution of velocities than both polar-aligned tetrameric motor and passive MT systems.

### 4.5.4 Relevance of results to *in vitro* experiments

In reconstituted systems of MTs *in vitro* [33], biotin-labelled kinesin motors have been conjugated using streptavidin clusters, and applied to a mixture of MTs condensed onto an oil-water interface. Based on the MT structures observed in these experiments, we hypothesise that such a system of motors can be modelled using dimeric motors. *In vitro* motility assays have shown that conventional kinesin motors are processive, *i.e.*, single molecules of kinesin move continuously along a MT for several microns [28, 29]. Biochemical experiments have confirmed that kinesin molecules hydrolyse on average 125 molecules of ATP after binding to a MT, consistent with the motor taking 125 8nm steps [27]. When such a processive motor is paired to a motor that is in the rate-limiting non-motile state [3], the stress generated between MTs will be different from that between MTs connected by a tetrameric motor, which has two fully active arms. From our system, it is clear that the asymmetry in motor-arm motion greatly aids MT activity, and the extensile sliding between MTs. This is contrary to most mechanisms posited in the literature, which bases MT-sliding descriptions on motors having symmetric arms. Hence, we propose that a model with differential motor-arm motion might be more suited to give a microscopic explanation to the extensile behaviour of MT bundles.

## Chapter 5

# Microtubule streaming in effective motor systems

The sizes of individual kinesin motors that crosslink and slide MTs are three orders of magnitude smaller than that of the cells within which they bring about large-scale dynamics. Also, there is a large disparity between the residence time of a cross-linking motor (10 seconds) [104] and the characteristic time-scale of motor-induced MT streaming or pattern formation in active gels (1 hour) [25,33,43,50]. Therefore, novel coarse-graining methods that focus on cellular-scale processes, while accurately capturing the active effects due to molecular motors are required.

As discussed in previous chapters, motors realise the polarity of MTs and - in the presence of ATP - “walk” on them unidirectionally. The presence of force dipoles at this molecular scale breaks nematic symmetry, and leads to significantly different active dynamics of MT pairs that are aligned and antialigned. However, despite actively “walking”, motors that connect aligned MTs induce relatively less sliding between adjacent MTs. They tend to hold the polar-aligned MTs together which generates an effective attraction. As demonstrated in Fig. 1.6, motors that connect antialigned MTs have arms on either MT, “walking” in opposite directions. Accommodating the stresses from the motors cause the MTs to slide away from each other, which causes large-scale flows in the cytoskeleton.

In order to capture cellular-scale dynamics induced by cytoskeletal motion in computer simulations, the approach of modelling individual motors, although done before in several studies, can prove to be unwieldy [4–6, 8, 12, 105, 106]. Although a network of MTs can be kept track of, when accessing large length and time-scales, in the context of simulations, accurately bookkeeping a bath of attached and unattached motors becomes challenging. Moreover, accurately depicting *both* motors and MTs at cellular-scale systems, although attempted before [7, 39], proves to be difficult. In order to capture cellular-level phenomena, such as organelle distribution, cytoplasmic streaming, and active cytoskeleton-induced lipid bilayer fluctuations, a minimal polarity dependent activity mechanism might suffice.

Such polarity dependent MT-MT interactions have indeed been successful in recovering experimentally relevant features of active gels, such as asters and vortices [97]. In these works, however, the aligning mechanism of motors was taken into account in a Maxwell

model of inelastic interactions between polar rods [97, 107–109]. Although these models took the orientational dynamics of MTs into account, the antialigned sliding was not considered in their anisotropic interaction kernel. Molecular motors have, however, been treated through a mean-field approach to model the buckling dynamics of non-sarcomeric MTs [110].

In our model, described in Sec. 2.3, motors are modelled as instantaneous force dipoles that crosslink MT beads based on the effective motor interaction rules. We call this the “effective motor potential”. Compared to the previous model, which account for motors explicitly, the effective motor potential removes computational overhead by neglecting explicit motor-arm positions. Furthermore, we ignore spatial variations in motor densities since the diffusion of motors can be two order of magnitudes higher than that of MTs under physiological conditions, due to their smaller size and mass [5].

In this chapter, we study MT activity due to effective motor interactions under periodic boundary conditions. In particular, we gain insights for cytoplasmic streaming by systematically varying activity and MT surface fraction. In Sec. 5.1, we qualitatively study the effect of varying the polar-aligned and antialigned effective motor probabilities on the overall structure of MTs. In Sec. 5.2, we quantify the number of MTs in polar-aligned bundles, and antialigned streams by categorising MTs based on the polarity of their local environment. In Sec. 5.3, we show trajectories of MTs, and illustrate the phenomena of collective streaming. In Sec. 5.4, we calculate the MTs’ parallel velocity, rotational diffusion, and active diffusion to compare MT advection with active Brownian particle (ABP) theory. In Sec. 5.5, we calculate skews in the histograms of MT displacements, and extract a typical time-scale for the activity. In Sec. 5.6, we extract a time-scale for MT streaming, by quantifying changes to MT local polar order. In Sec. 5.7, we calculate the displacement correlations between MT neighbours and provide predictions of photobleaching experiments to motor driven MT mixtures. In Sec. 5.8, we summarise and compare the time-scales analysed in the system, and discuss our findings in relation to other works.

## 5.1 Polar-aligned domain structures

### 5.1.1 Domains from antialigned motor potentials

Active MT sliding is driven by the effective motor potential, which is affected by both steric interactions and motor concentrations. This is similar to the explicit motor model, see Secs. 4.1.5 and 4.2. Also, similar to the case of MTs in the circular confinement we find that a perfectly sorted state is not achieved in this system. MT activity increases with surface fraction if interactions between nearby antialigned MTs is the limiting factor for active dynamics. However, at very high surface fractions, steric effects impede MT motion, and increasing surface fraction only decreases MT dynamics.

In this system, motor concentration is controlled using the polar-aligned,  $p_p$ , and antialigned,  $p_a$ , motor probabilities. The antialigned motor probability, unlike the aligned motor probability, directly affects MT advection. Structures formed due to the effective motor potential purely due to interactions between antialigned MTs are shown in Fig. 5.1.

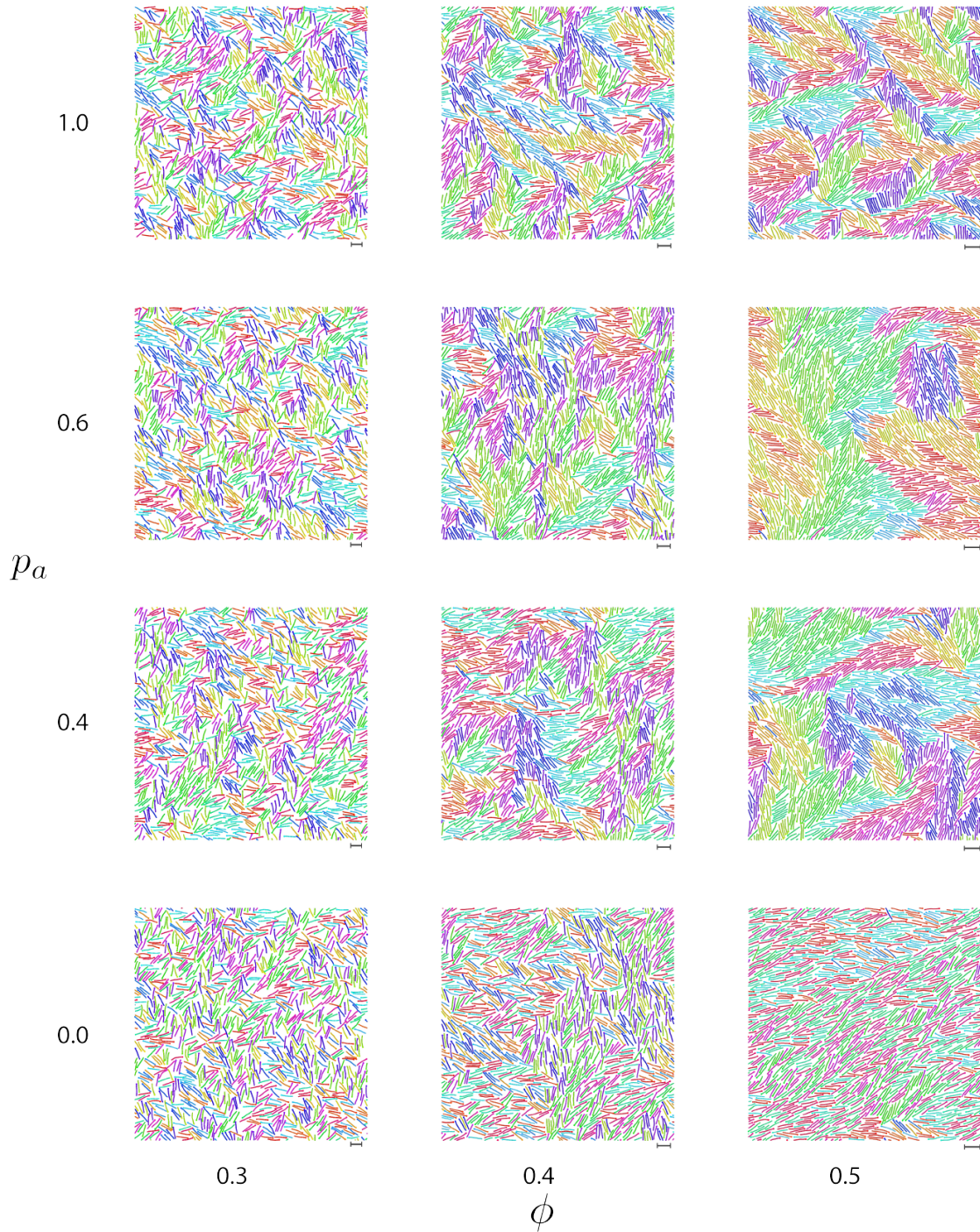


Figure 5.1: Snapshot of simulation frames at steady-state for systems with varying antialigned motor probabilities,  $0.0 < p_a \leq 1.0$ ,  $p_p = 0.0$ , and surface fractions,  $0.3 < \phi < 0.5$ . Surface fractions of MTs are varied by changing the size of the periodic box, while keeping the number of MTs constant. The scale bars that correspond to the length of a MT is indicated in the bottom right of each simulation frame. The colours represent the orientation of the polar MTs with respect to the system reference frame according to Fig. 5.2.

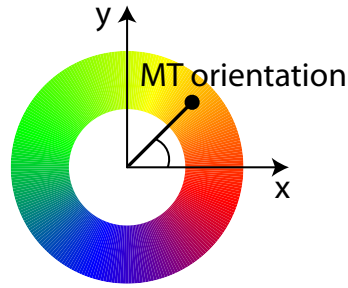


Figure 5.2: Colour legend used to represent MT orientation.

We will use the colour wheel in Fig. 5.2 to indicate the orientations of MTs for the figures in this section. Also, note that in Fig. 5.1 the surface fraction is changed by adjusting the periodic box size, while keeping the number of MTs constant. In cases without motor interactions,  $p_a = 0.0$ , at  $\phi = 0.3$ , MTs are isotropically oriented, and at  $\phi = 0.5$ , appear nematically aligned.

Figure 5.1 shows that at  $\phi = 0.3$ , the effective motor potential leads to the formation of small and highly dynamic polar-aligned domains. There is no appreciable difference in the systems' structures due to increasing antialigned motor probability at  $\phi = 0.3$ . MTs tend to enter and leave these polar-aligned domains continually throughout the simulation due to the high probability of interaction with antialigned MTs. The antialigned MTs tend to break polar-aligned bundles and transport them away to other polar-aligned locations.

At  $\phi = 0.4$  and  $\phi = 0.5$ , the size of polar-aligned domains increases compared to  $\phi = 0.3$ . The domain sizes decrease with increasing  $p_a$ . We find domains spanning the entire simulation box at  $0.2 \leq p_a \leq 0.6$  and at  $\phi = 0.5$ . This indicates that activity and MT streaming break apart large polar-aligned domains. At high densities, especially when passive MT systems form a nematic state, the ground state of the system for all MTs is polar-aligned. In this state antialigned MT interaction and MT activity is not possible. However, the ground state is unstable to perturbations from antialigned MT interactions at high  $p_a$  values. At lower  $p_a$  values, antialigned MT sliding still occurs, giving rise to polar-aligned domains. These domains are relatively stable for low activity because antialigned MT interactions are less prone to large-scale streaming.

### 5.1.2 Effect of aligned motor potentials

The implementation of the aligned motor potential according to Sec. 2.3 assumes that motors crosslinking polar-aligned MTs only cause them to attract to each other, and that this motor mechanism does provide relative sliding between them. This assumption is valid for tetrameric motors, *i.e.*, both motor-arms walk at same speeds on both crosslinked MTs. In order to accommodate active stresses from motors, MT pairs relax quickly compared to the rate at which motors walk and stretch. However, this assumption breaks down if either the motors are dimeric [39], or if the probability of motor-arm walking is highly stochastic [42], leading to significant asymmetry in motor-arm motion.

Structures formed due to a combination of antialigned and aligned motor potentials are shown in Fig. 5.3 at a surface fraction of  $\phi = 0.3$ . Increasing  $p_p$  leads to polar-aligned bundling of MTs, and slower dynamics. We observe slower dynamics because there are

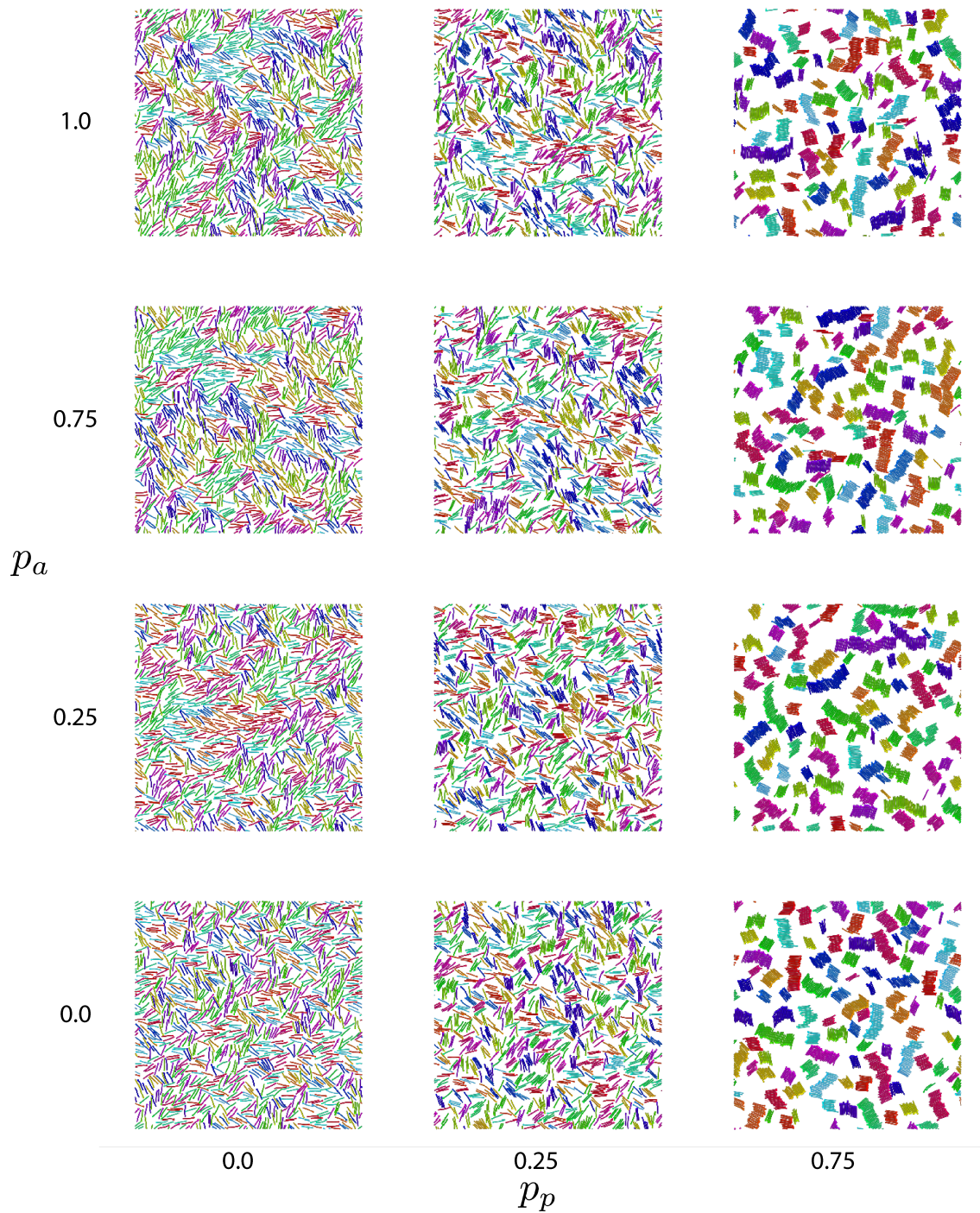


Figure 5.3: Snapshots of simulation frames at steady-state for systems with varying aligned,  $0.0 < p_p \leq 0.75$ , and antialigned motor probabilities,  $0.0 < p_a \leq 1.0$ . For all systems  $\phi = 0.3$ . Aligned motor probabilities higher than those shown in the phase diagram gave similar results as for  $p_p = 0.75$ . The colours represent the orientation of the polar MTs with respect to the system reference frame according to Fig. 5.2.

fewer antialigned MT interfaces that lead to activity. The large bundles, bound together by the aligned motor potential, diffuse slowly compared to isolated MTs.

High  $p_a$  values are ineffective in breaking up polar-aligned bundles because both antialigned and polar-aligned motors have the same spring constant and the polar-aligned MT bundles have more interacting beads compared to antialigned MTs. This is because antialigned motors lead to MT propulsion, and the interaction between adjacent MTs is transient. The aligned motor potential acts as a cohesive interaction, and leads to stable bundles. As a result, we observe similar structures for all  $p_a$  values for a given  $p_p$  value (greater than 0), due to the stability of the polar-aligned bundles.

In this model, it turned out to be difficult to bring about MT advection due to polar-aligned motor effects. In order to achieve the highest MT advection, after demonstrating the effect of the aligned motor potential, we set  $p_p = 0$  in the following sections.

## 5.2 Local polar order

To quantify the number of MTs in polar-aligned bundles, and antialigned streams, we use the technique described in Sec. 3.6. This allows us to investigate the extent of bundling as a function of antialigned motor probability,  $p_a$ , and surface fraction,  $\phi$ . Also, it helps to link the MT's local environment to its velocity.

Using the local polar order parameter,  $\psi_i$ , we distinguish MTs based on their orientation relative to their local environment. As shown in Fig. 5.4, all MTs in the system are separated into three fractions based on their local environment:

1. Fraction of MTs in antialigned environments,  $\psi_i \leq -0.5$ , given by  $n_A$ ,
2. fraction of MTs in mixed environments,  $-0.5 < \psi_i \leq 0.5$ , given by  $n_M$ ,
3. and fraction of MTs in polar-aligned environments,  $0.5 < \psi_i$ , given by  $n_P$ .

Those MTs which are isolated, and are away from neighbouring MTs are categorised as being in a mixed environment. However, such instances are rare even at the lowest surface fraction that we studied,  $\phi = 0.2$ .

Figure 5.4 gives examples of MTs in each environment category. MTs in mixed environments with  $\psi_i \approx 0$  can be either perpendicularly oriented with respect to their neighbouring MTs, or in a sparse environment without neighbours, or have neighbours which are both polar-aligned and antialigned. The former two instances are more likely at lower surface fractions. At higher surface fractions steric interactions and nematic alignment make the former two instances unlikely. We can write

$$n_A + n_M + n_P = 1, \tag{5.1}$$

since each group of MTs is normalised by the total number of MTs in the system,  $N$ .

Figure 5.5 quantifies the polar structure of the systems described in Fig. 5.1. At the lowest density,  $\phi = 0.2$ , the largest population of MTs are  $-0.5 < \psi_i \leq 0.5$ . This population of MTs that are perpendicularly oriented with respect to their environment give a spike at  $\psi_i = 0.0$  in Fig. 5.5. The spikes are more pronounced for  $\phi = 0.2$  and  $\phi = 0.3$  compared to other surface fractions. They are formed because the orientations on either side of the peak,  $\psi_i > 0.0$  and  $\psi_i < 0.0$ , are unfavourable for the MT pairs. When

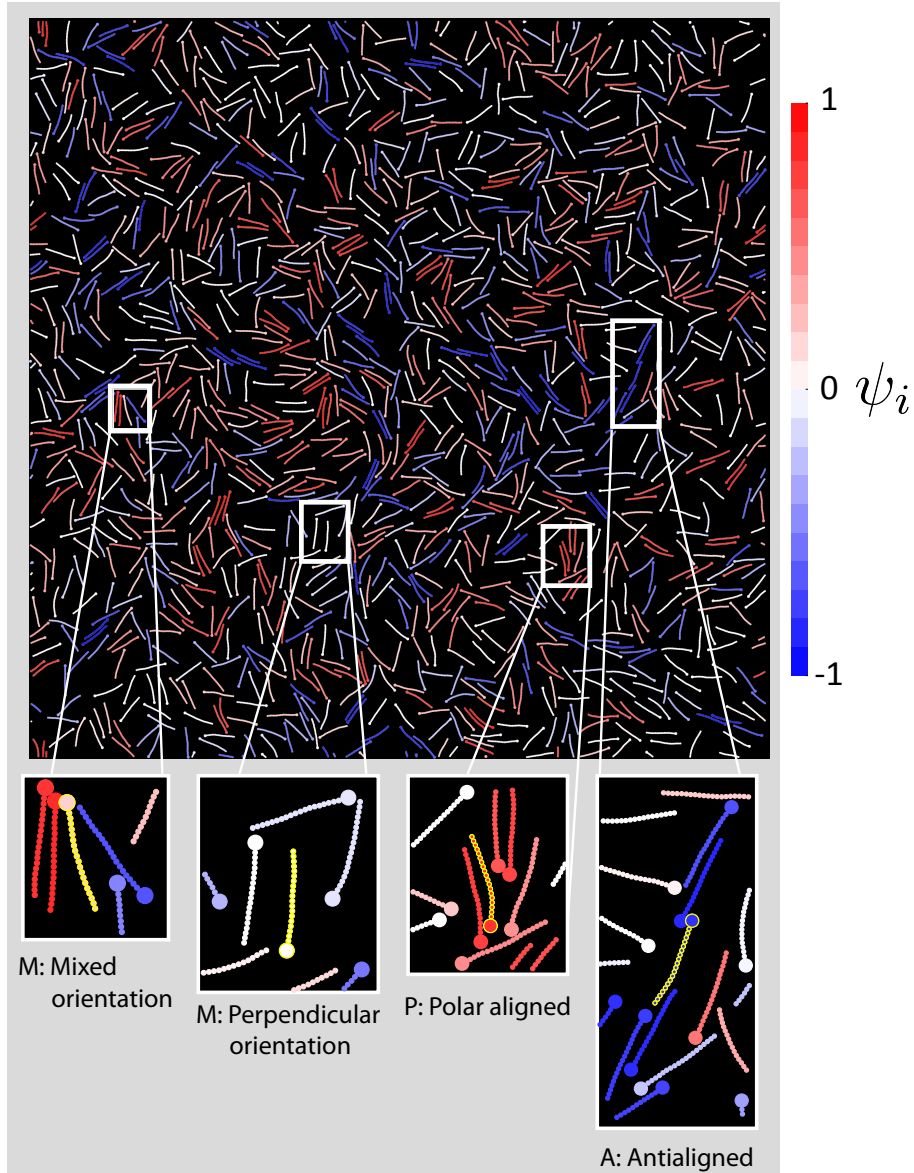


Figure 5.4: MTs coloured based on their local polar order,  $\psi_i$ , for  $p_a = 1.0$ ,  $\phi = 1.0$ . The colour corresponding to  $-1 < \psi_i < 1$  is given on the right. Zoomed in illustrations of MTs show examples of MTs in the three  $\psi_i$  categories distinguished in Fig. 5.5. The MT in question is highlighted in yellow in the zoomed in graphics. (M)  $\psi_i \approx 0$  values can occur either when MTs are perpendicularly oriented with respect to its surrounding or when MTs have neighbours which are both polar-aligned and antialigned. (P)  $\psi_i > 0.5$  occurs when MTs have neighbours which are mostly polar-aligned. (A)  $\psi_i < -0.5$  occurs when MTs have neighbours which are mostly antialigned.

$\psi_i < 0.0$ , MT pairs actively slide away from each other due to the effective motor potential. When  $\psi_i > 0.0$ , the MTs form a polar bundle, which is entropically unfavourable, *i.e.*, there are no forces to keep MT pairs bound together when  $p_p = 0.0$ , and thermal fluctuations rotate them away from aligned configurations. However, for  $\phi = 0.2$  and  $\phi = 0.3$ , we observe a pronounced difference in probability density between the two sides

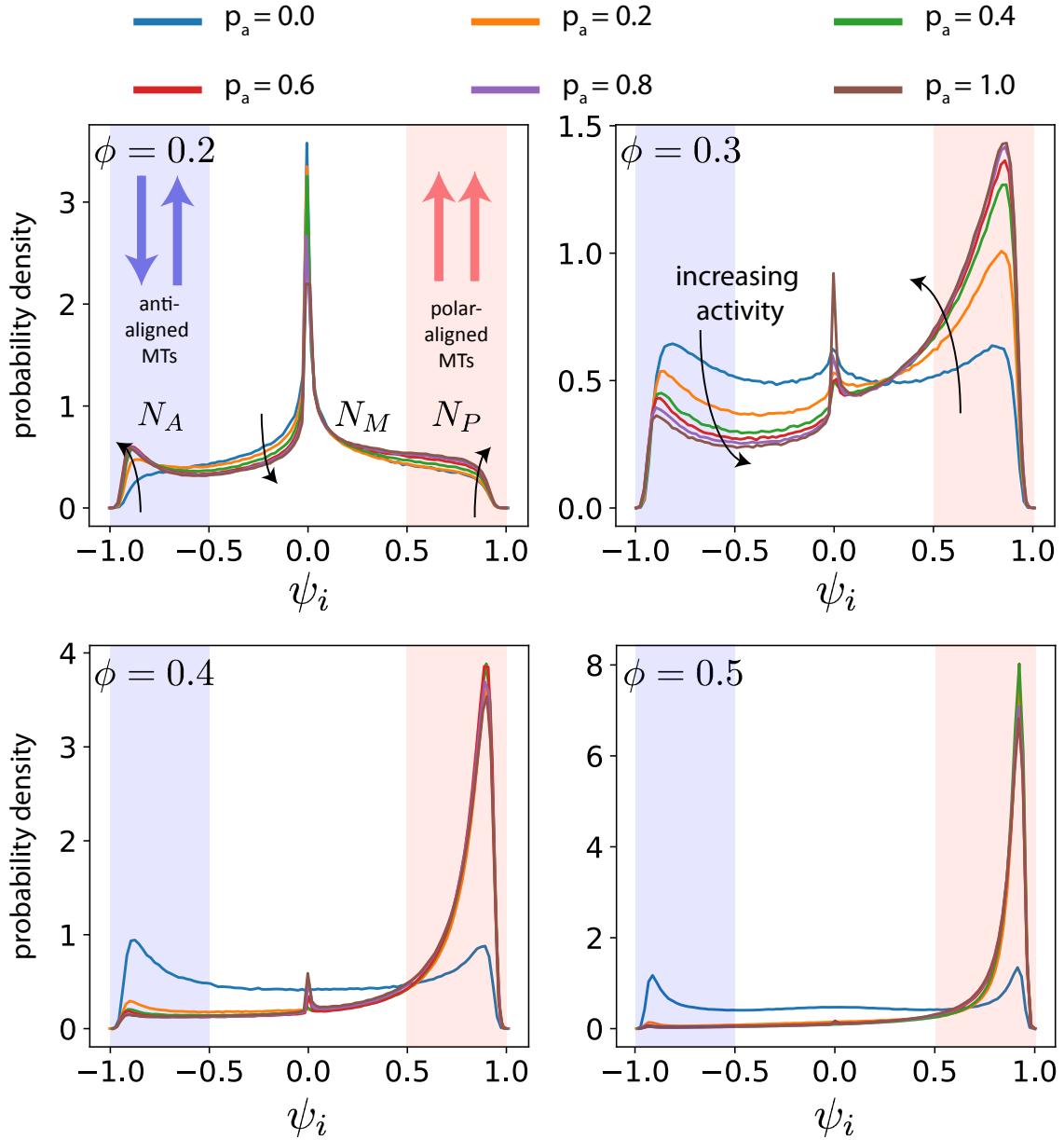


Figure 5.5: Probability densities of MTs' local polar order as a function of  $p_a$  and  $\phi$ . The arrows are guides, which indicate the directions in which activity increases. In the following sections MTs are distinguished based on their relative orientation to their local environment. *A*, *M* and *P* indicate MTs that have local polar order corresponding to  $\psi_i \leq -0.5$  (green),  $-0.5 < \psi_i < 0.5$  (white),  $\psi_i \geq 0.5$  (blue), respectively.  $n_A$ ,  $n_m$  and  $n_P$  are the number of MTs which are in antialigned, perpendicular and polar-aligned environments respectively. Note that the scale of the ordinate axis is different for each surface fraction.

of  $\psi_i = 0.0$ . The markedly smaller distribution on the left of  $\psi_i = 0.0$  suggests that these orientations are energetically more unfavourable than the entropic effect that drives MTs to be isotropic at low surface fractions.

In Fig. 5.6, we quantify the ratios of (A) antialigned to (P) polar-aligned MTs, and

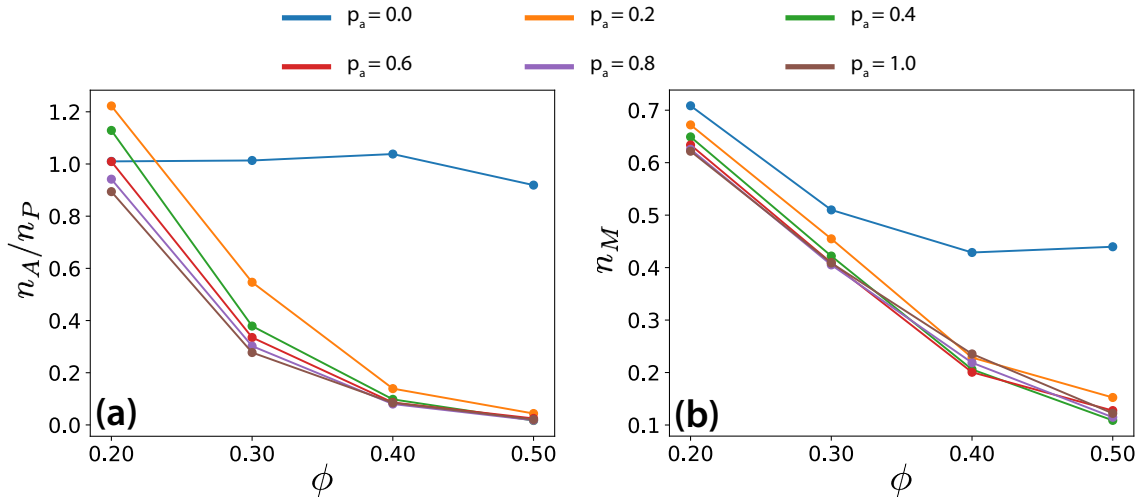


Figure 5.6: Ratios of MT populations in (a) antialigned to polar-aligned environments, and (b) perpendicular environments to total number of MTs, for different surface fractions and  $p_a$ .

of (M) mixed to total MTs. Due to the lack of active MT sliding in passive systems, we see a symmetric distribution of  $\psi_i$  values on either side of  $\psi_i = 0$  in Fig. 5.5. This leads to  $n_A/n_P = 1$  for all surface fractions shown in Fig. 5.6(a). For systems, which undergo antialigned MT sliding,  $n_A/n_P$  decreases with increasing surface fraction for all  $p_a$  values. This corresponds to the increase in size of the polar-aligned clusters with surface fractions observed in Fig. 5.1. Also, higher  $p_a$  values lead to larger  $n_A/n_P$ , and this difference in  $n_A/n_P$  decreases with increasing surface fraction. This indicates that at high surface fractions,  $n_A/n_P$  is similar. However, Fig. 5.1 shows that the size of polar-aligned domains decreases with activity at  $\phi = 0.5$ . The ratio  $n_A/n_P$  is a good indicator for the length of antialigned MT interface in the system, which is linked to the overall polar-aligned domain size. The decrease in  $n_m$ , for the passive system in Fig. 5.6(b) is due to the isotropic-nematic phase transition. In general, we see a similar decrease in  $n_m$  for all active systems. This decrease in  $n_m$  in active systems is significantly lower than that observed in passive systems.

Figure 5.7 shows the mean local polar order of MTs,  $\langle\psi_\infty\rangle$ , for various  $\phi$  and  $p_a$ . When the system is passive,  $p_a = 0.0$ , there is no activity, and both polar-aligned and antialigned orientations are equally likely. Since at low surface fractions  $\phi = 0.2$ ,  $\langle\psi_\infty\rangle \approx 0$ , for all  $p_a$ , it appears that the effective motor force and the MTs' steric effects, are both required for polar-aligned domain formation. The effective motor force is dominant at intermediate surface fractions,  $\phi = 0.3$ , where increasing  $p_a$  results in an increase in polar order. However, at higher surface fractions,  $p_a$  does not have any effect on  $\langle\psi_\infty\rangle$ , and the MT surface fraction determines polar-aligned domain formation.

### 5.3 Microtubule Streaming

Streaming occurs when multiple MTs collectively migrate, tracing the same path coherently over multiple time frames. In order to understand MT streaming arising from the

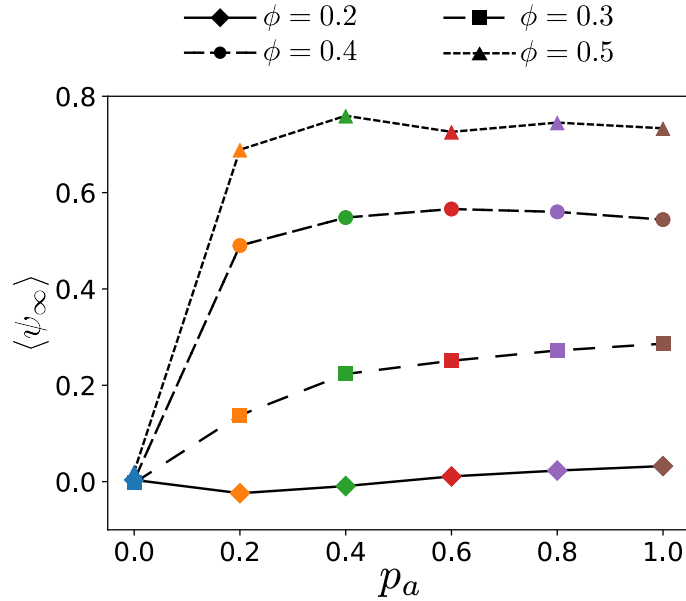


Figure 5.7: Mean local polar order of MTs at long times,  $\langle \psi_\infty \rangle$ , for various  $\phi$  and  $p_a$ .

effective motor potential, we need to track the trajectories of multiple MTs over a time window. Figure 5.8 shows trajectories of MT centers of mass for a time window of  $1.2\tau_R$  for the three local polar order categories. To generate the trajectories, we connect the center of mass positions of MTs with line segments, depending on which local polar order category they exhibit during this time window.

For example, a MT which is moving in an antialigned environment for  $0.5\tau_R$ , then moves to a mixed environment for  $0.1\tau_R$ , and continues to be propelled in an antialigned environment for  $0.6\tau_R$ , will be represented by two broken line segments in the antialigned trajectory diagram. The  $0.1\tau_R$  time segment MT trajectory missing in the antialigned diagram will be represented in the mixed environment trajectory diagram. Plotting the trajectories together in the same diagram shows how MTs cooperate to form streams.

For  $p_a = 0.0$  the antialigned and polar-aligned categories are identical, because there is no MT sliding in the absence of the motor potential. Hence, the diagrams for both categories exhibit similar trajectories. With increasing  $p_a$ , the trajectories in the antialigned diagrams in Fig. 5.8 become more contiguous and the streams become more coherent. For  $p_a = 1.0$  the trajectories of multiple MTs form long streams, that span the entire simulation box.

Polar-aligned and mixed trajectories are similar for all active cases, although we see infrequent occurrences of contiguous, elongated trajectories in the mixed environments. Elongated propulsion trajectories for the polar-aligned system are not observed.

Figure 5.9 shows that MT streaming increases with MT surface fraction for  $p_a = 1.0$  for  $\phi < 0.4$ . For low  $\phi$ , antialigned MTs exhibit short bursts of activity, giving a fragmented trajectory diagram. For higher  $\phi$ , a smaller fraction of MTs are in antialigned environments, but the coherence of the streams increases, and the trajectory fragments increase in length. For  $\phi = 0.5$ , streaming has decreased substantially, and only a few antialigned MTs are propelled over long distances continuously during this time window.

The diagram for the mixed category shows no clear structure for  $\phi = 0.2$ . However,

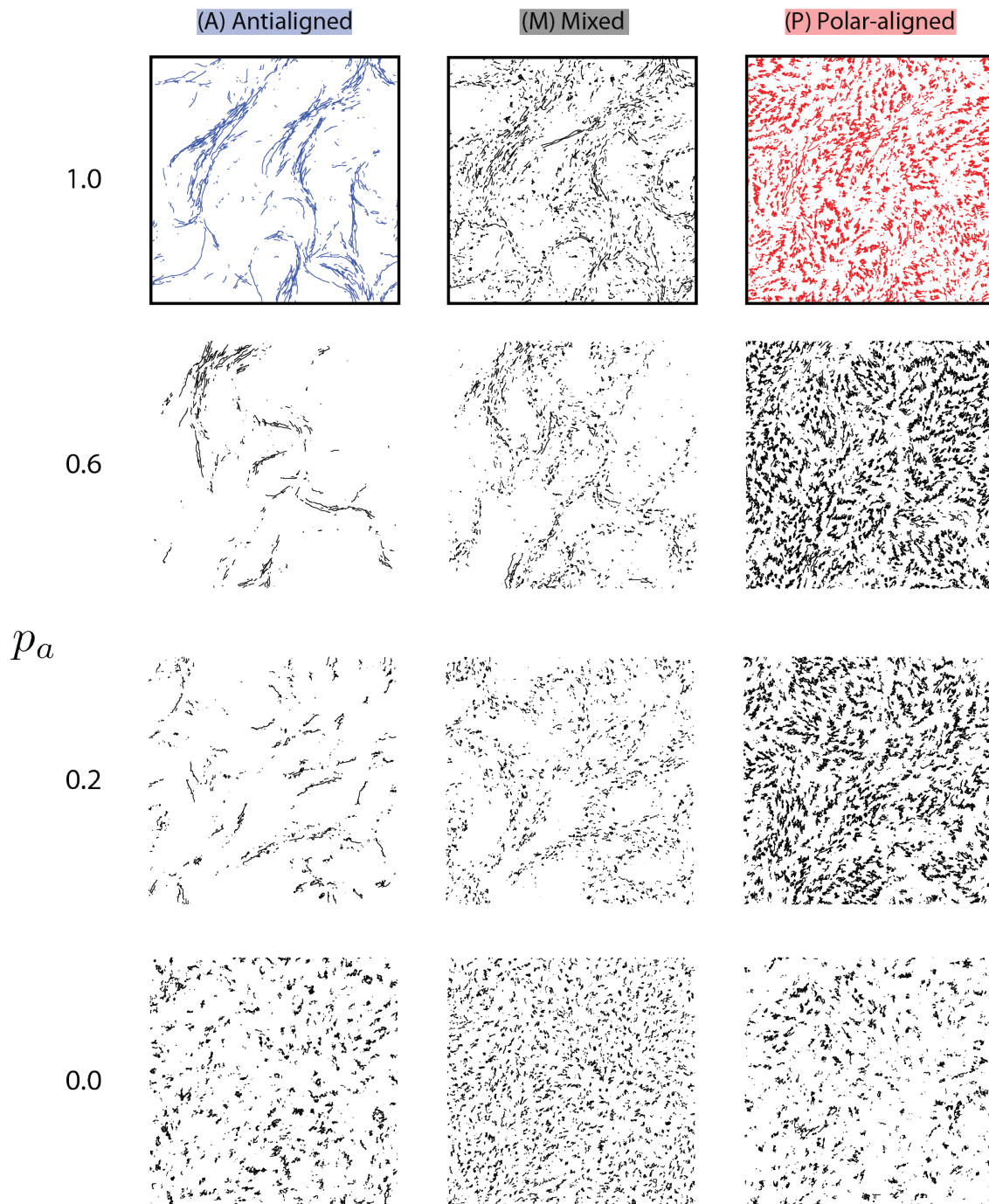


Figure 5.8: Trajectories of MTs within a time window of  $1.2\tau_R$  separated based on the antialigned, polar-aligned and mixed local polar order categories, for different  $p_a$ , for  $\phi = 0.4$ . The  $p_a = 1.0$  case is highlighted because it is used as the maximum streaming instance in Fig. 5.9.

MTs in mixed orientations feed MTs into the antialigned streams at higher MT surface fractions and the diagrams indicate the general stream structure. Due to the prevalence of polar-aligned bundles at higher surface fractions, the trajectory diagrams exhibit the order observed between bundles, compare Figs. 5.1 and 5.9 for  $\phi = 0.5$  and  $p_a = 1.0$ .

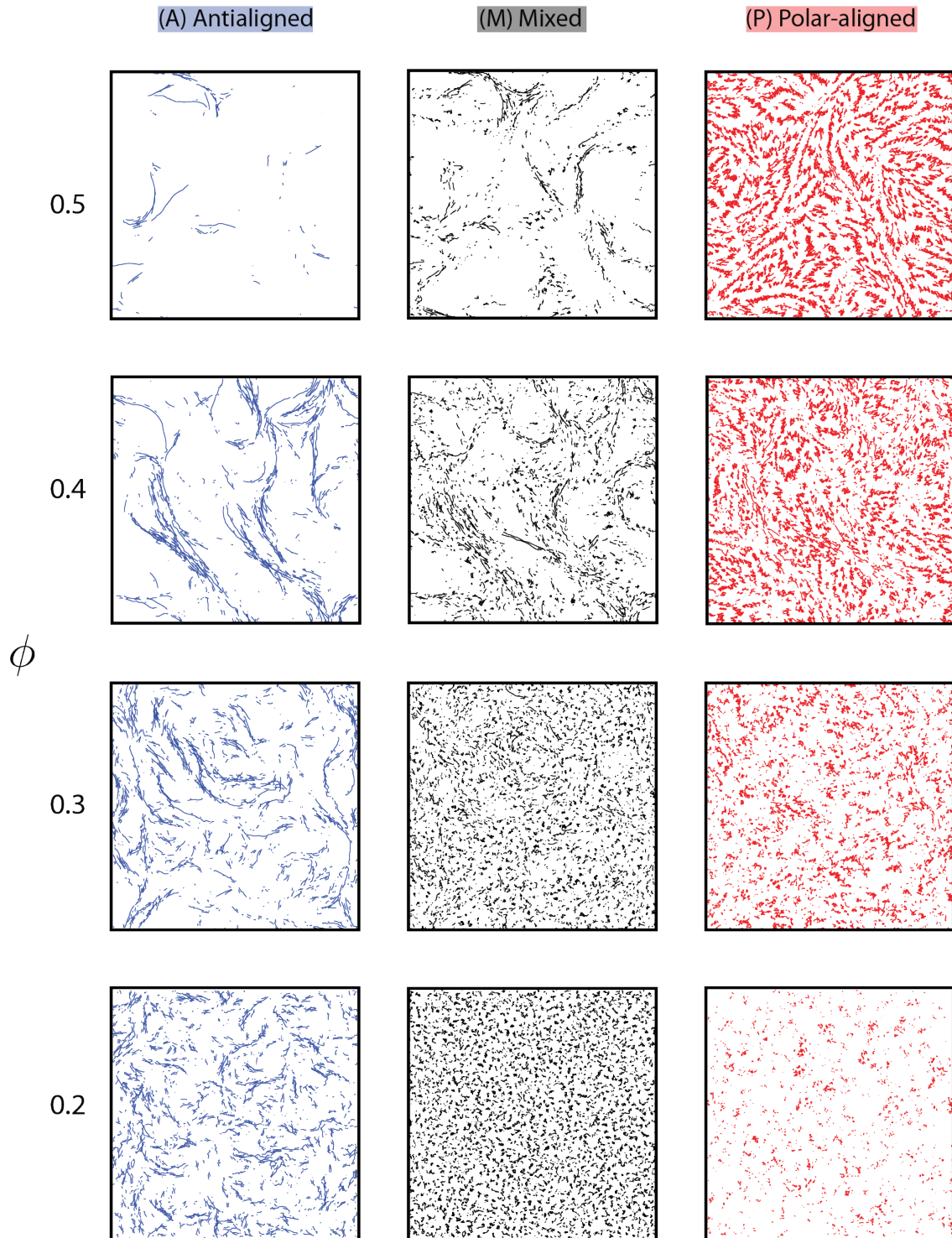


Figure 5.9: Trajectories of MTs within a time window of  $1.2 \tau_R$  separated based on the antialigned, polar-aligned and mixed local polar order categories, for  $p_a = 1.0$ , for various  $\phi$ .

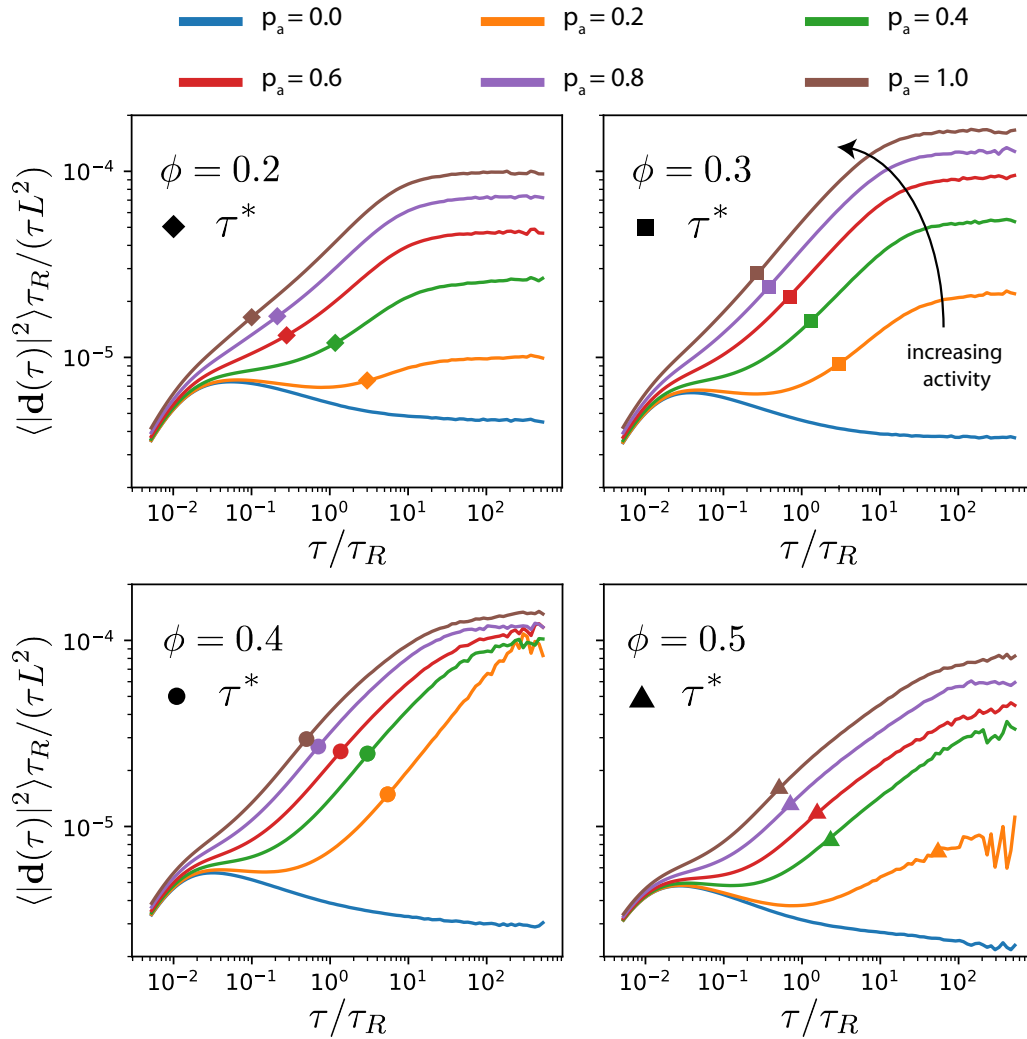


Figure 5.10: Translational MSD/Lag time for various activities,  $p_a$ , and surface fractions,  $\phi$ . MSD is normalised using  $L^2/\tau_R$ , and lag time,  $\tau$ , is normalised using  $\tau_R$ . The symbols on the plots indicate the time-scale at which parallel velocity is maximally skewed due to active forces, see Sec. 5.5.

## 5.4 Polarity-driven active motion

### 5.4.1 Mean-squared displacement

In order to quantify the velocities of MTs in different time regimes, we use their MSDs defined in Eq. 4.1. Here, instead of using the same characteristic activity time-scale for all simulations, as done in Chapter 4,<sup>1</sup> we study the changes to this time-scale with MT surface fraction,  $\phi$ , and control activity in the system using  $p_a$ .

The displacement vector of the center of mass of MT  $i$  over a lag time  $\tau$  can be written as

<sup>1</sup>Note that notations used within this chapter are consistent only with findings within this chapter.  $\tau$  used here is not the same as the characteristic lag times used in Chapter 4.

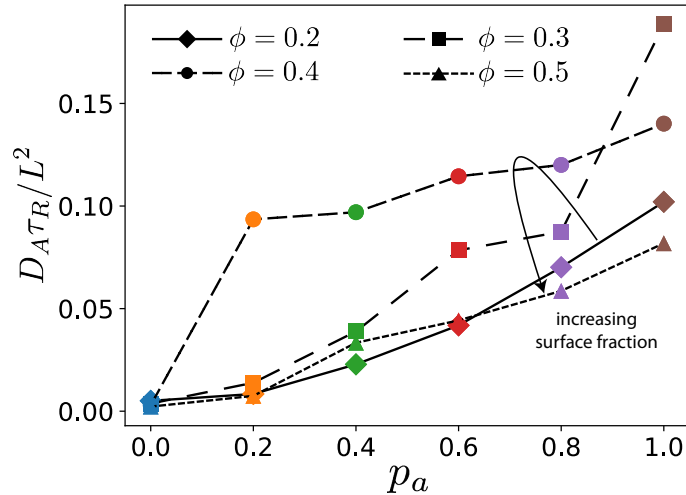


Figure 5.11: Active diffusion constant,  $D_A$ , plotted for different  $p_a$  and  $\phi$ .  $D_A$  is calculated by fitting  $4D_A\tau$  to the long-time active diffusive regime of the MSD, see Fig. 5.10.

$$\mathbf{d}_i(t, \tau) = \mathbf{r}_i(t + \tau) - \mathbf{r}_i(t), \quad (5.2)$$

where  $\mathbf{r}_i(\tau)$  is the vector indicating the center of mass of MT  $i$  at time  $\tau$ .

Figure 5.10 shows  $\text{MSD}/\tau$  for various values of  $p_a$  and  $\phi$ . In all active cases,  $p_a > 0$ , there are four different regimes of motion. Unlike in Chapters 3 and 4, in this system, we integrate the Langevin equation. Since the exponent of the MSD is unity in the diffusive regime, the curves in Fig. 5.10 must be horizontal when particles are diffusive. For all surface fractions, we observe the diffusive regime when the MT velocity is dissipated by the environment for  $10^{-2} < \tau/\tau_R < 10^{-1}$ . For the active cases, the intermediate time-scale,  $10^{-1} < \tau/\tau_R < 10^1$ , gives the active regime where MTs move such that the slope of  $\text{MSD}/\tau > 1$ .

#### 5.4.2 Active diffusion

Comparing the MSDs for the surface fractions of  $\phi = 0.2$  and  $\phi = 0.3$ , Fig. 5.10 shows that there is an increase in MT displacement between systems with same  $p_a$  for increasing  $\phi$ . This is because at higher surface fractions MTs are more likely to find antialigned MTs against which they can propel themselves. However, at larger surface fractions steric effects also impede motion. For  $\phi = 0.4$  and  $\phi = 0.5$ , the MT displacement decreases in systems with same  $p_a$  for increasing  $\phi$ .

For passive systems ( $p_a = 0$ ) where there are no active forces that induce ballistic motion,  $\text{MSD}/\tau$  peaks in the short-time diffusive regime, and decreases at larger lag time because steric effects impede free diffusion. With increasing MT surface fraction, steric effects become more pronounced, and  $\text{MSD}/\tau$  decreases. This manifests as a larger deviation from the MSDs of single filaments, see Fig. A.1.

At the largest time-scale, the active system behaves in a diffusive manner, where  $\text{MSD}/\tau$  plateaus (Fig. 5.10). We calculate  $D_A$  by fitting  $4D_A\tau$  to the long-time active diffusive regime of the MSD in Fig. 5.11. For a given surface fraction, the active diffusion

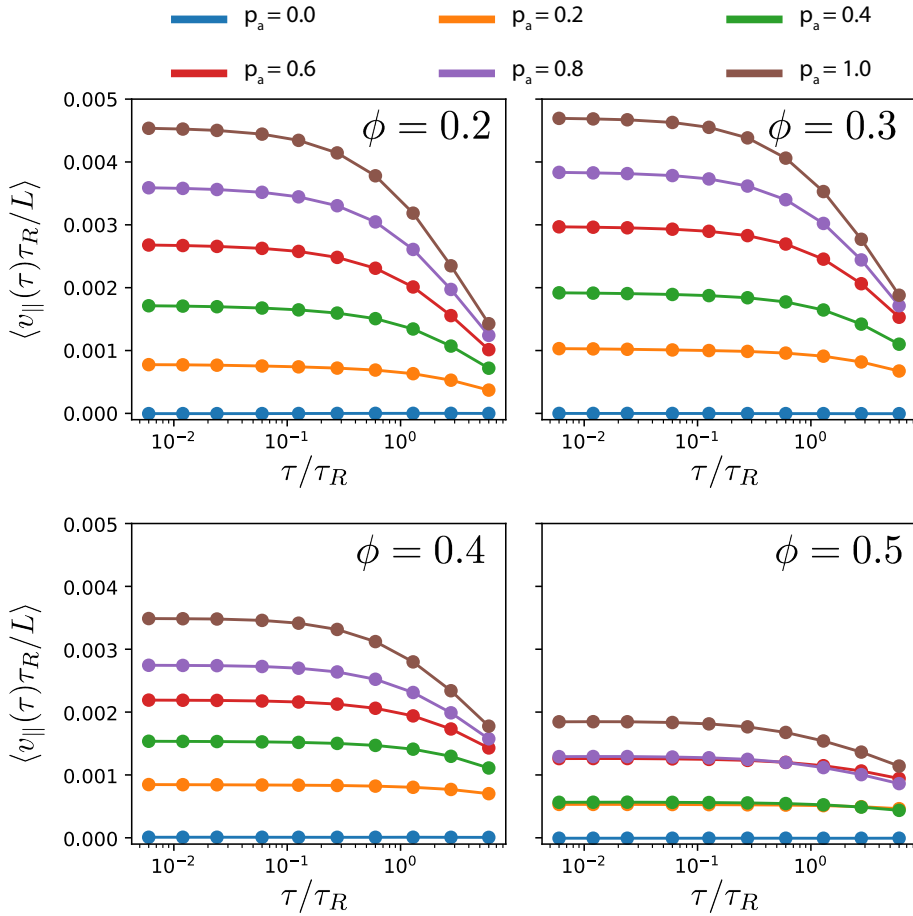


Figure 5.12: Parallel velocity computed from displacements for different lag times.  $v_{\parallel}$  is calculated by extrapolating parallel velocity to  $\tau \rightarrow 0$ .

increases with increasing  $p_a$ . For  $p_a \leq 0.8$ ,  $D_A$  is maximal for  $\phi = 0.4$ , and for  $p_a = 1.0$ ,  $D_A$  is maximal for  $\phi = 0.3$ , before decreasing at higher surface fractions.

### 5.4.3 Parallel velocity and rotational diffusion

Since motor-driven sliding propels MTs predominantly along their orientation vector  $\mathbf{p}$ , in order to quantify the activity of MTs due to motors, we calculate the parallel velocity of MTs. We can write the mean parallel velocity of a system using

$$\langle v_{\parallel}(\tau) \rangle = \langle \mathbf{d}(\tau) \cdot \mathbf{p}(0) / \tau \rangle, \quad (5.3)$$

where  $\mathbf{p}(0)$  is the orientation of the MT at an arbitrary time origin. The time  $\tau$  is measured respective to this time origin. The mean is taken over various time origins for a given  $\tau$ . For small  $\tau$  the displacements of MTs are parallel to the initial MT orientation.

Figure 5.12 shows that the parallel velocity decreases with increasing  $\tau$ , which indicates that the orientations of the MTs deviate from  $\mathbf{p}(0)$ . The direction of MT motion typically persists in the direction of initial MT orientation for about  $\tau_R$ , the rotational diffusion time for a single MT. The displacement averaged over all MTs increases with  $p_a$ , even though only a small fraction of MTs experience the antialigned motor potential. The deviation

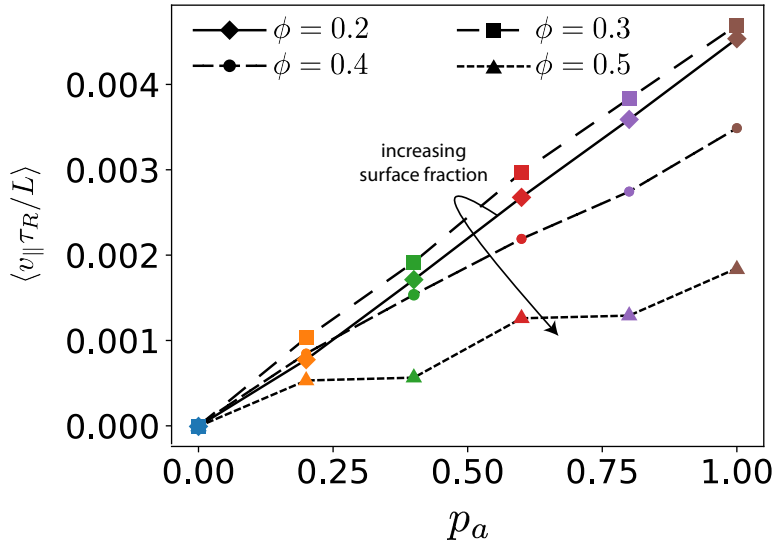


Figure 5.13: Parallel velocity,  $v_{\parallel}$ , calculated by extrapolating the curves in Fig. 5.12 to  $\tau \rightarrow 0$ .

of the displacement from the initial orientation is faster at lower densities, suggesting a lack of streaming in these regimes.

Figure 5.13 shows the parallel velocity,  $v_{\parallel}$ , averaged over MTs, obtained from extrapolating  $\tau \rightarrow 0$  from the values obtained from Fig. 5.12.<sup>2</sup> The parallel velocity of MTs,  $v_{\parallel}$ , is linear in  $p_a$ , giving us a good control of the activity in the system.

The parallel velocity,  $v_{\parallel}$ , peaks at  $\phi = 0.3$ . This suggests that availability of antialigned MT interactions limit MT activity for  $\phi = 0.3$ . For  $\phi > 0.3$ , the activity is limited by steric interactions. Nevertheless, the slower deviation of MTs from their initial orientation for Fig. 5.12, suggests that MTs are more likely to stream at higher densities. The increase of  $v_{\parallel}$  with  $p_a$  is similar in all cases except for  $\phi = 0.5$ , where differences in  $v_{\parallel}(0)$  for varying  $p_a$  are small due to the substantial effect of steric interactions.

Figure 5.14 shows the average time taken by MTs to rotate away from their initial orientation,  $\mathbf{p}(0)$ , for different values of  $p_a$  and  $\phi$ . For small  $\tau$ , MTs remain close to their original orientation, and  $\langle \mathbf{p}(\tau) \cdot \mathbf{p}(0) \rangle \rightarrow 1$ . For larger  $\tau$ , MTs rotate away from this orientation, and on average  $\langle \mathbf{p}(\tau) \cdot \mathbf{p}(0) \rangle \rightarrow 0$ . For all systems that we simulated, the orientational autocorrelation time for dense active systems is longer than the single-MT orientational autocorrelation time in dilute systems. This is because in all those cases, MT rotation is impeded by steric interactions.

By fitting an exponential function to the data shown in Fig. 5.14,

$$\langle \mathbf{p}(\tau) \cdot \mathbf{p}(0) \rangle = e^{-D_r \tau}, \quad (5.4)$$

we obtain the transition time to long-time diffusive behaviour,  $\tau_r = D_r^{-1}$ .

<sup>2</sup>Parallel velocity is typically linearly related to the Péclet number, which is the ratio of active forces to thermal forces in the system (See Sec. 2.1.4). Here, we refrain from calling this a Péclet number because there are different populations of MTs in the system, which are active only if in contact with an antialigned MT environment. Thus, a Péclet number should be calculated only for MTs that transiently undergo motor propulsion. An averaged velocity across all MTs will spuriously decrease this Péclet number due to the presence of MTs in aligned environments.

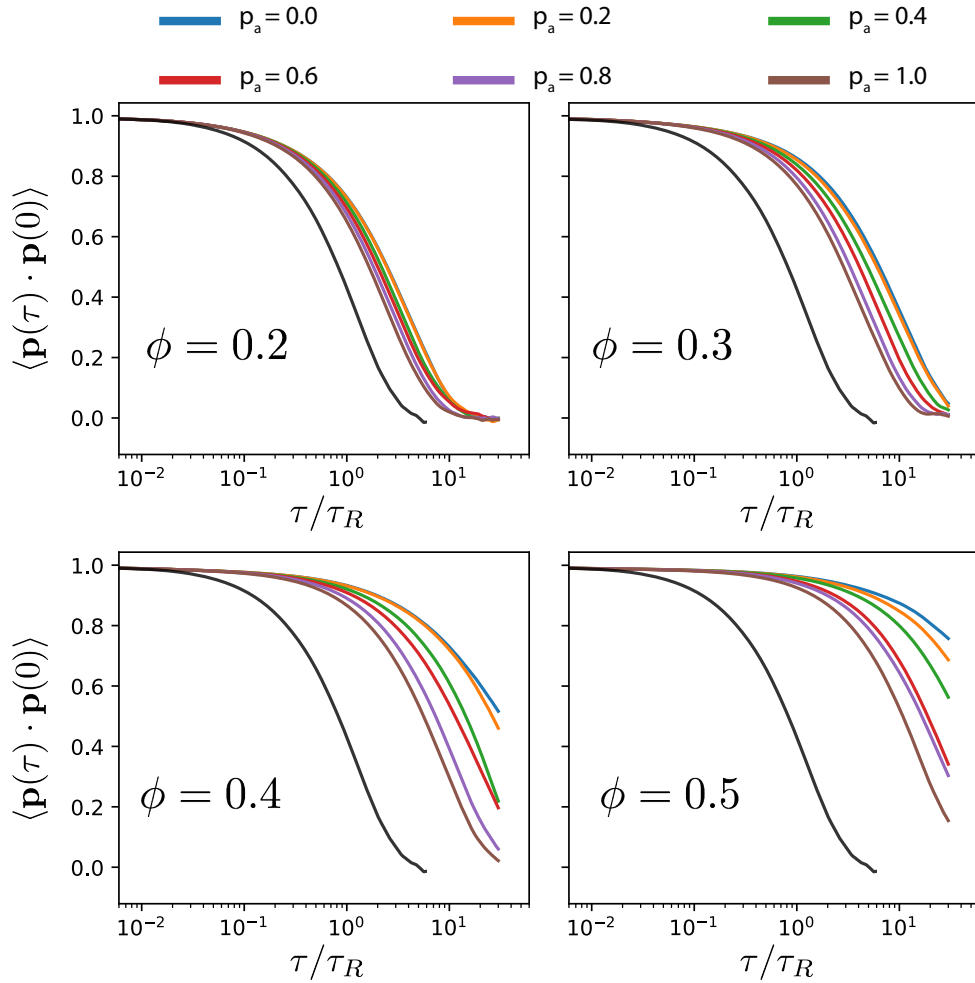


Figure 5.14: MT orientational autocorrelation function for different antialigned motor probabilities,  $p_a$ , and surface fractions,  $\phi$ . The colours of the curves represent different  $p_a$  values. The black curve in all plots represents results obtained for a single (passive) MT. The rotational diffusion time  $D_r^{-1} = \tau_R$  is obtained from fitting an exponential function,  $e^{-D_r\tau}$ . The single MT orientational autocorrelation time,  $\tau_R$ , is used to normalise time. See Fig. A.2 for larger lag times than shown here.

Figure 5.15 shows  $\tau_r$  for various  $p_a$ . For passive systems ( $p_a = 0$ ),  $D_r$  decreases with surface fraction. For active systems,  $\tau_r$  decreases with increasing  $p_a$  and with decreasing  $\phi$ . In the nematic state for  $\phi = 0.4$  (Fig. 5.1), MTs are no longer able to rotate freely as they are able to in the isotropic case.

The decrease of  $\tau_r$  with increasing  $p_a$  is pronounced at higher MT surface fractions. Comparing the structures in Fig. 5.1 to these results suggests that higher values of  $D_r$ , or smaller orientational autocorrelation times, correspond to smaller domain sizes. In larger domains, the streams appear as interfaces between polar-ordered domains and antialigned MTs, at larger length scales. The streams extend in the same direction over larger lengths, for longer times, and MTs do not rotate away from their initial orientation as quickly. Also, MTs that are trapped in aligned MT bundles are less likely to exit their environments and their rotational diffusion is smaller for higher  $\phi$  and lower  $p_a$ .

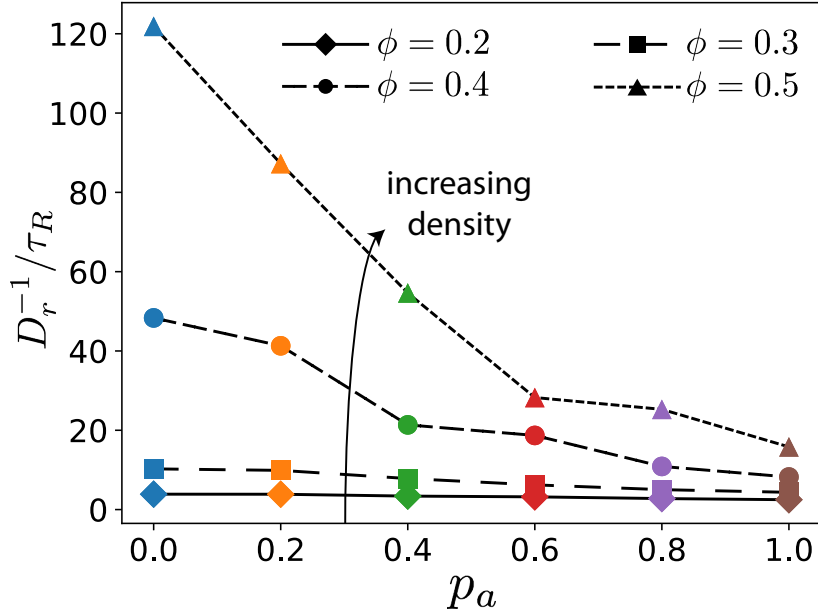


Figure 5.15: MTs' average transition time to long-time diffusive behaviour. This is calculated by fitting an exponential to Fig. 5.14, and computing the decay constant, which is also the transition time,  $\tau_r$ , and the inverse of rotational diffusion,  $D_r$ . Time is normalised in this system using,  $\tau_R$ , the rotational diffusion of a single passive MT, shown in Fig. 5.14.

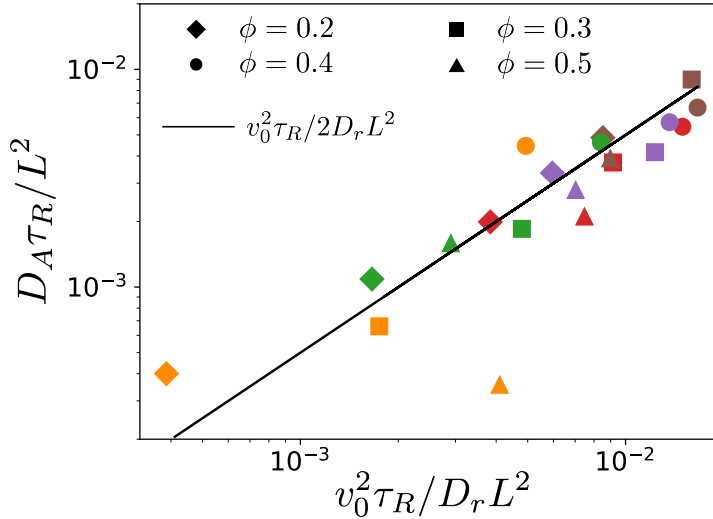


Figure 5.16: Active diffusion coefficient,  $D_A$  vs. the ratio of squared parallel velocity and rotational diffusion,  $v_0^2/D_r$ . The colours indicate MT surface fractions. The diffusion coefficient scales as  $D_A \sim 0.5 v_0^2/D_r$ , as predicted for active Brownian particles.

The active diffusion constant obtained for different MT surface fraction obeys Eq. 2.29.

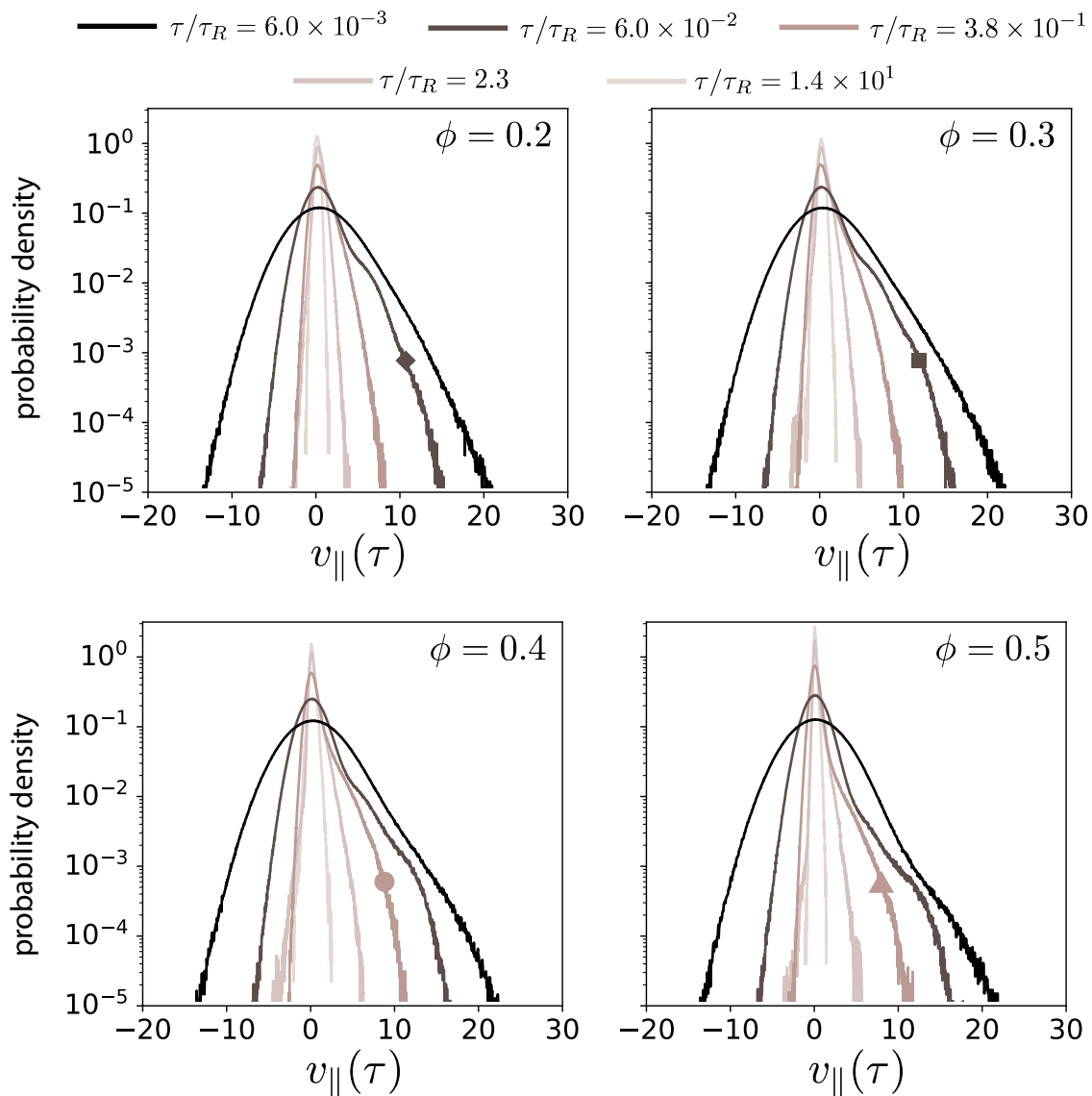


Figure 5.17: Histogram of  $v_{\parallel}$  for various surface fractions and five lag times. The darkness of the curve represents the lag time used to measure the parallel velocity. The darkest-coloured curve represents the parallel velocity obtained for the shortest lag time, and the lightest-coloured curve is obtained from the longest lag time. The symbols on the curves indicate the curves which are most skewed for various values of  $\phi$ .

At long times,

$$\langle |\mathbf{r}(t) - \mathbf{r}(0)|^2 \rangle \approx 4Dt + \frac{2v_0^2}{D_r}t \equiv 4D_A t. \quad (5.5)$$

If the passive diffusion constant,  $D$ , is much smaller than  $v_0^2/D_r$ , we expect,

$$D_A = \frac{v_0^2}{2D_r}. \quad (5.6)$$

In Fig. 5.16, we plot  $D_A$  as function of  $v_0^2/D_r$ , and find that it follows the active Brownian particle relationship predicted in Eq. 5.6. We find that systems with the lowest activity,  $p_a = 0.2$ , do not fit this relationship well for most MT surface fractions.

## 5.5 Asymmetries in parallel velocity distributions

Displacements and velocities are dependent on the lag time upon which the measurements are taken. Diffusive and active displacements manifest in different time regimes as seen in Fig. 5.10. In order to characterise the effect of  $p_a$ , for instance, it is important to specify the lag time,  $\tau$ , that has been used to evaluate the data.

### 5.5.1 Time-scale of maximum skew

Figure 5.17 shows the histogram of  $v_{\parallel}$  for various lag times and  $\phi$  for  $p_a = 1.0$ . At short lag times, MT displacement is correlated with the MT's initial orientation vector, giving large values for  $v_{\parallel}$ . Here, the distribution is also symmetric, because thermal forces dominate. With increasing lag time, due to both activity and thermal forces, the MT orientations deviate from their initial orientations. The effect of activity is reflected by the asymmetry of  $v_{\parallel}$ . Although larger time-scales lead to smaller  $v_{\parallel}$ , we notice that the distributions extend less to negative  $v_{\parallel}$  than to positive  $v_{\parallel}$ . In quantifying asymmetry (third moment) in these distributions, we identify the time-scale at which active motion in each system is strongest.

If we make a set of observations,  $x_i, i \in [1, n]$  and define the mean of these observations to be  $\bar{x}$ , we can take moments of the distribution to characterise it in more detail. Namely, the  $r^{\text{th}}$  moment about the mean of such a distribution is

$$m_r = \frac{1}{n} \sum_{i=1}^n (x_i - \bar{x})^r. \quad (5.7)$$

The skew of this distribution is

$$\alpha_3 = \frac{m_3}{m_2^{3/2}}. \quad (5.8)$$

Larger absolute values of  $\alpha_3$  indicate more asymmetry in the distribution of the observations. Note that we can perform this calculation regardless of how the observations are distributed, Gaussian or otherwise.

Figure 5.18 shows the skews of  $v_{\parallel}(\tau)$  distributions (Fig. 5.17) as functions of lag times,  $\tau$ . The lag time for the distribution with maximal skew is defined as  $\tau^*$ , and is marked with different symbols in Fig. 5.10;  $\tau^*$  is a good indicator for the active time-scale, because it appears consistently for all MT surface fractions and activities in the middle of the ballistic regime of the MSD. For passive MTs, the asymmetry vanishes for all surface fractions, because passive velocity distributions are due to stochastic forces only, and thus symmetric for all lag times.

Figure 5.18 shows that the asymmetry of the  $v_{\parallel}$  distribution is small at short lag-times,  $\tau < \tau^*$ , because of the dominance of thermal forces, which makes the distribution symmetric. At  $\tau = \tau^*$  the skew is maximal, and we use this time-scale to characterise active displacements. For  $\tau > \tau^*$  the  $v_{\parallel}$  probability distribution becomes increasingly symmetric, since the orientations of MTs deviate from the direction of  $\mathbf{p}(0)$ , such that  $\mathbf{d}(\tau) \cdot \mathbf{p}(0)$  is small. The distributions of  $v_{\parallel}(\tau^*)$  become increasingly asymmetric with increasing  $p_a$ , because larger active forces drive MTs further; the dependence of the asymmetry of  $v_{\parallel}(\tau^*)$  on  $p_a$  increases with increasing MT surface fraction.

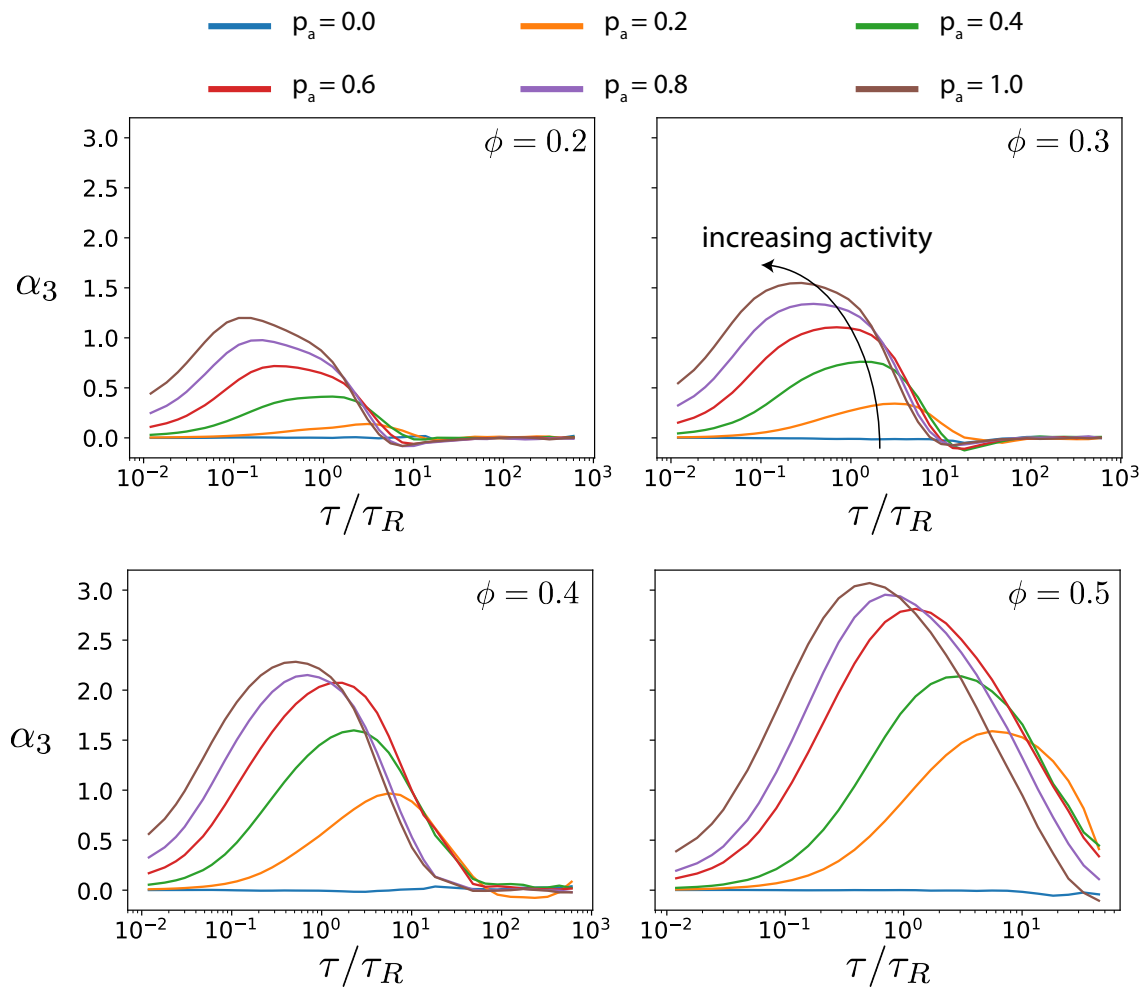


Figure 5.18: Skews,  $\alpha_3$ , of  $v_{\parallel}$  (Fig. 5.17) computed as a function of lag times for different  $p_a$  and  $\phi$ . The probability distributions that correspond to the maximal skew are shown in Fig. 5.17 together with distributions for few other lag times. The ordinate scale is the same for comparison of overall skew between different MT surface fractions.

The slopes of  $\alpha_3$  in Fig. 5.18 is similar for the same  $p_a$  values for different  $\phi$ , but  $\tau^*$  increases with increasing  $\phi$ . We plot  $\tau^*$  as a function of various  $p_a$  and  $\phi$  in Fig. 5.19, and find that  $\tau^*$  exponentially decreases with increasing  $p_a$ , for all  $\phi$ . Also,  $\tau^*$  generally increases with  $\phi$ .

### 5.5.2 Microtubule dynamics at active timescale

Figure 5.20 shows probability densities of  $v_{\parallel}(\tau^*)$  for various  $\phi$  and  $p_a$ . This is the parallel velocity distribution, for each parameter combination, which is most representative of that induced by the effective motor potential. For all surface fractions, motor activity makes the  $v_{\parallel}(\tau^*)$  distribution wider. This widening of the distribution becomes less pronounced with increasing  $\phi$ . The shifting of the negative arm of the  $v_{\parallel}$  distribution ( $v_{\parallel}(\tau^*) < 0$ ) in the negative direction with increasing  $p_a$  is because  $\tau^*$  decreases simultaneously. Figure 5.17 shows that with increasing  $\tau$ , the negative arm of the distribution approaches 0 because of the deviation of MT orientation from  $\mathbf{p}(0)$  due to rotational diffusion. Thermal

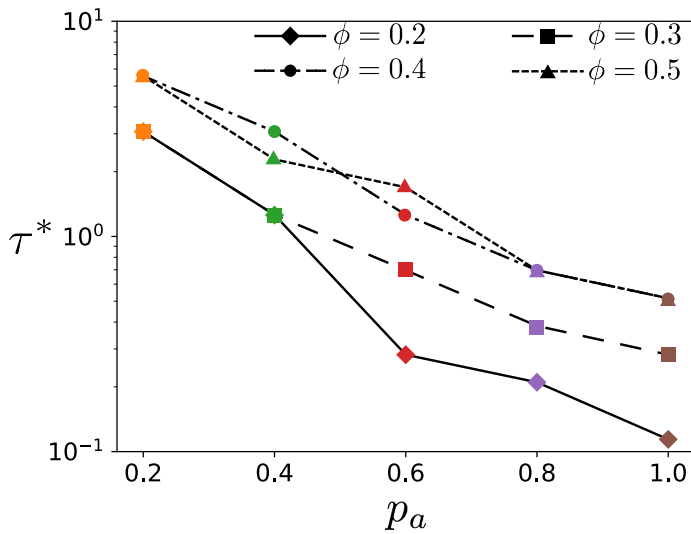


Figure 5.19: Lag time at which maximal skew is observed in the  $v_{\parallel}(\tau)$  distribution (Fig. 5.18). The ordinate axis is log-scaled to show that  $\tau^*$  is exponentially decreasing with  $p_a$ .

forces also affect the positive arm ( $v_{\parallel}(\tau^*) > 0$ ) in the same way, but increasing  $p_a$  has a larger effect on the positive arm of the distribution than on the negative arm. Namely, for all  $\phi$ , we observe that the positive arms are shifting more with  $p_a$  than the negative arms. This is particularly evident for  $\phi = 0.4$  and  $0.5$ , where there are only small differences in the negative arm, but the difference in the positive arm is pronounced due to changes in  $p_a$ .

To understand the polarity of the environment under which MTs undergo large parallel displacements, we perform an analysis similar to that in Fig. 4.6. The relationship between  $v_{\parallel}(\tau^*)$  and  $\psi_i$ , shows that the largest parallel velocities occur in antialigned environments with  $-1.0 < \psi_i < -0.8$ . In less polar environments with  $-0.8 < \psi_i < 0$ ,  $v_{\parallel}(\tau^*)$  decreases linearly with  $\psi_i$ . The number of interacting antialigned MT bead pairs decreases as  $\psi_i$  approaches 0, leading to smaller MT velocities.

When  $\psi_i$  transitions from negative to positive (antialigned to polar-aligned), for low surface fractions, we observe a sharp decrease in  $v_{\parallel}(\tau^*)$ , as predicted from Fig. 5.5. This is because the antialigned motor potential only affects MT pairs which are in antialigned orientations, and there is a discontinuous difference in MT velocity, when it is in a perpendicular orientation with its surrounding. For large surface fractions,  $\psi_i \approx 0$  represents mixed orientations, where MTs are surrounded by equal numbers of antialigned and polar-aligned MTs, and MTs are not necessarily perpendicularly oriented, since this is unfavourable due to steric interactions. This causes the jump in  $v_{\parallel}(\tau^*)$  to decrease.

The parallel velocity,  $v_{\parallel}(\tau^*)$ , increases with increasing  $p_a$  for all MT surface fractions. For  $\phi = 0.2$ ,  $\psi_i > 0$ , this effect is less pronounced because this regime contains slowly diffusing polar-aligned MTs, which are unaffected by the antialigned effective motor potential. The local polar order parameter in higher surface fractions represents an environment where MTs are in mixed orientations, polar-aligned and antialigned with respect to the MT in question. The increase in  $v_{\parallel}(\tau^*)$  for  $\psi_i > 0$ , indicates that po-

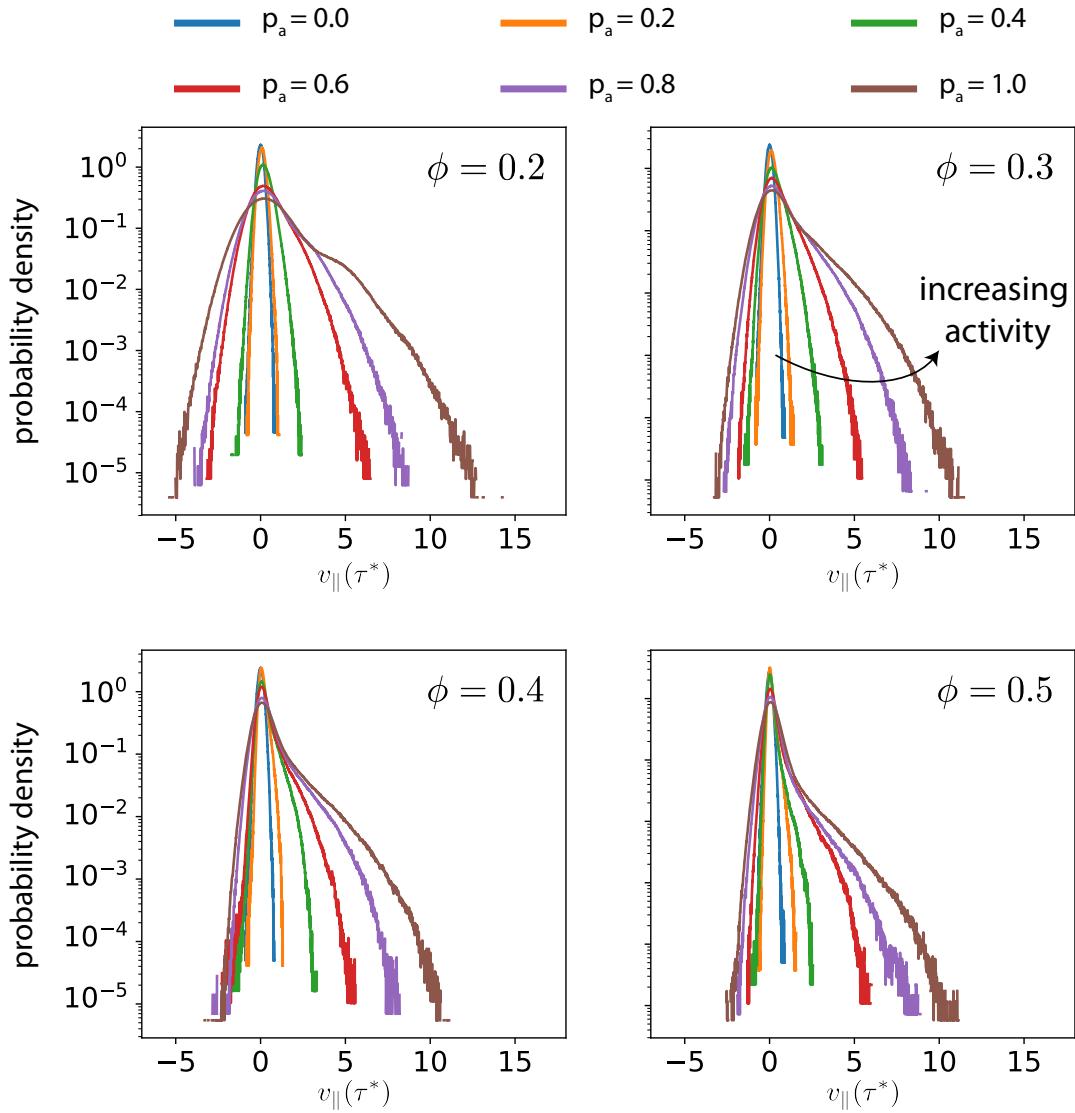


Figure 5.20: Histogram of  $v_{\parallel}(\tau^*)$  for various  $p_a$  and  $\phi$ . This indicates the structure of the velocity distribution when the skew is maximal. The ordinate axis is log scaled to show the deviation of the distribution from a Gaussian, which would appear as a symmetric inverted parabola.

lar aligned MTs' are affected by  $p_a$  even though they are surrounded predominantly by polar-aligned MTs.

The  $v_{\parallel}(\tau^*)$  peaks appearing for antialigned MTs for different  $\phi$  and  $p_a$  in Fig. 5.21, is shown in Fig. 5.22. Interestingly, the maximum parallel velocities of antialigned MTs,  $v_{\parallel,A}(\tau^*)$ , are similar regardless of the surface fractions. Also,  $v_{\parallel,A}(\tau^*)$ , similar to  $v_{\parallel}(0)$ , is linearly increasing with increasing  $p_a$ .

### 5.5.3 Microtubule dynamics in different regions

Since the velocities described in Fig. 5.20 are averaged over all the MTs in the system, it is difficult to pinpoint the origin of the asymmetry in  $v_{\parallel}(\tau^*)$  distributions. Using the

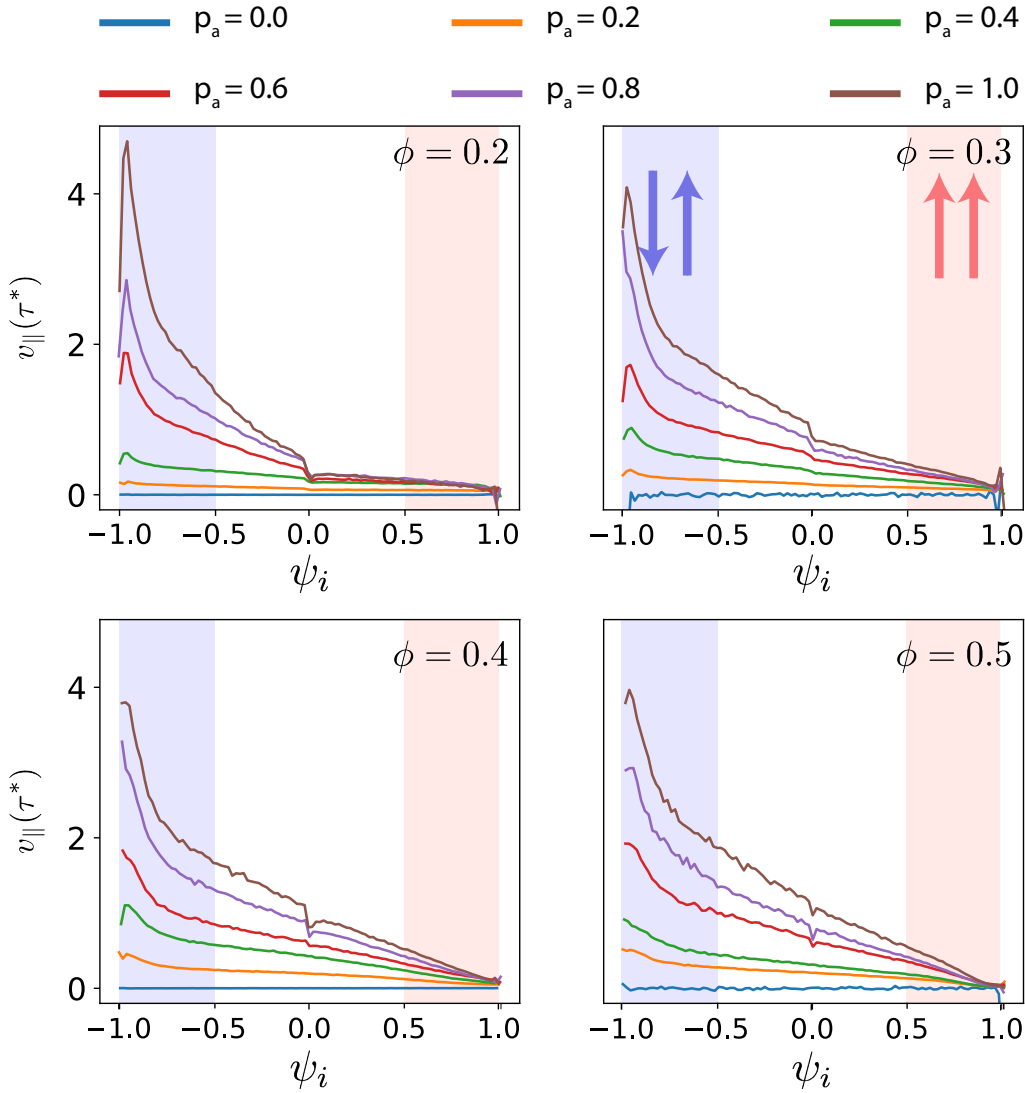


Figure 5.21: Parallel velocities of MTs,  $v_{\parallel}(\tau^*)$ , as a function of their local polar order,  $\psi_i$ , for various activities and MT surface fractions. MTs in antialigned and polar-aligned environments are highlighted in blue and red respectively.

local polar order parameter, we are able to analyse the dynamics of MTs in more detail based on their environments.

Figure 5.23 decomposes  $v_{\parallel}(\tau^*)$  distributions, shown in Fig. 5.20, for  $\phi = 0.3$ , into MTs in three environments described in Fig. 5.4. This analysis is similar to that described in Sec. 3.6. For both,  $p_a = 0.2$  and  $p_a = 1.0$ , the highest values of  $v_{\parallel}(\tau^*)$  occurs due to the MTs in antialigned environments, shown in Fig. 5.22. However, in Fig. 5.22 we only have the means of the  $v_{\parallel}(\tau^*)$  values for any given  $\psi_i$ . The distribution of  $v_{\parallel}(\tau^*)$  highlights the manner in which activity manifests in the effective motor system.

In Fig. 5.23(a) and (b), we compute the probability density of  $v_{\parallel}(\tau^*)$ , for  $p_a = 0.2$  and 1.0, respectively. It shows that the  $v_{\parallel}(\tau^*)$  distributions are symmetric and asymmetric for  $p_a = 0.2$  and  $p_a = 1.0$ , respectively, for MTs in all three environments. However, the asymmetry due to MTs in antialigned environments is significantly more pronounced

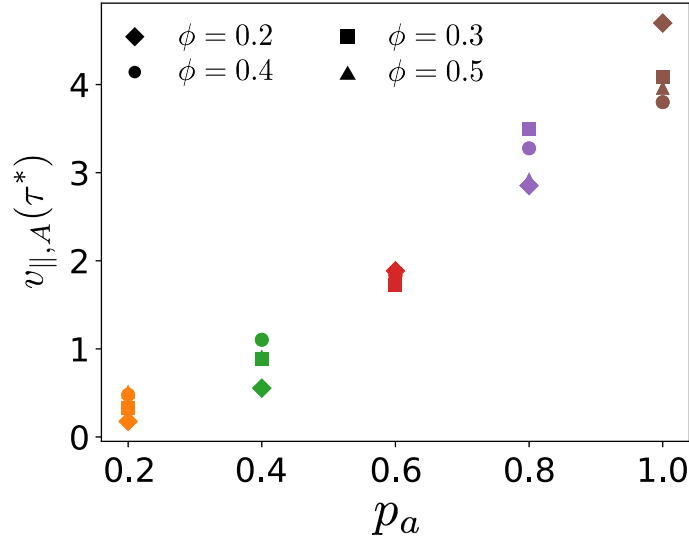


Figure 5.22: Maximum parallel velocity of MT,  $v_{||,A}(\tau^*)$ , as a function of  $p_a$  for different surface fractions. These are the maximum velocity peaks seen in Fig. 5.21

compared to MTs in polar-aligned and mixed environments. This shows that the active velocity in the case of  $p_a = 0.2$  is due to an overall shift of the  $v_{||}(\tau^*)$  peak, due to MTs in mixed and antialigned environments. For  $p_a = 1.0$ , the active velocity is due to the asymmetry of  $v_{||,M}(\tau^*)$  for MTs in mixed environments, and the asymmetry and the positive peak position of  $v_{||,A}(\tau^*)$  for MTs in antialigned environments.

In order to compare the  $v_{||}(\tau^*)$  distributions for various activities and surface fractions, we compute the first three moments of the distribution and plot that as a function of  $\phi$  and  $p_a$ . In order to construct the skewed normal distributions to fit the data, we first write the standard normal probability density function,

$$\Phi(x) = \frac{1}{\sqrt{2\pi}} e^{-\frac{1}{2}x^2}. \quad (5.9)$$

By stretching the domain by a factor,  $\xi$ , and shifting the  $x$ -axis by  $\omega$  we have the general form of the normal distribution,

$$f(x|\xi, \omega) = \frac{1}{\sigma} \Phi\left(\frac{x - \omega}{\xi}\right). \quad (5.10)$$

When the skew of the distribution is 0,  $\omega$  and  $\xi$  are the standard deviation, and the mean of the normal distribution, respectively. The cumulative distribution function is given by,

$$\Psi(x) = \int_{-\infty}^x dt \Phi(t) = \frac{1}{2} \left( 1 + \operatorname{erf}\left(\frac{x}{\sqrt{2}}\right) \right), \quad (5.11)$$

where erf is the error function. The probability density function of the skew-normal distribution with skew parameter  $\alpha$  is the product of the normal distribution with the cumulative distribution,

$$f_s(x|\xi, \omega, \alpha) = \frac{2}{\omega} \Phi\left(\frac{x - \xi}{\omega}\right) \Psi\left(\alpha \left(\frac{x - \xi}{\omega}\right)\right). \quad (5.12)$$

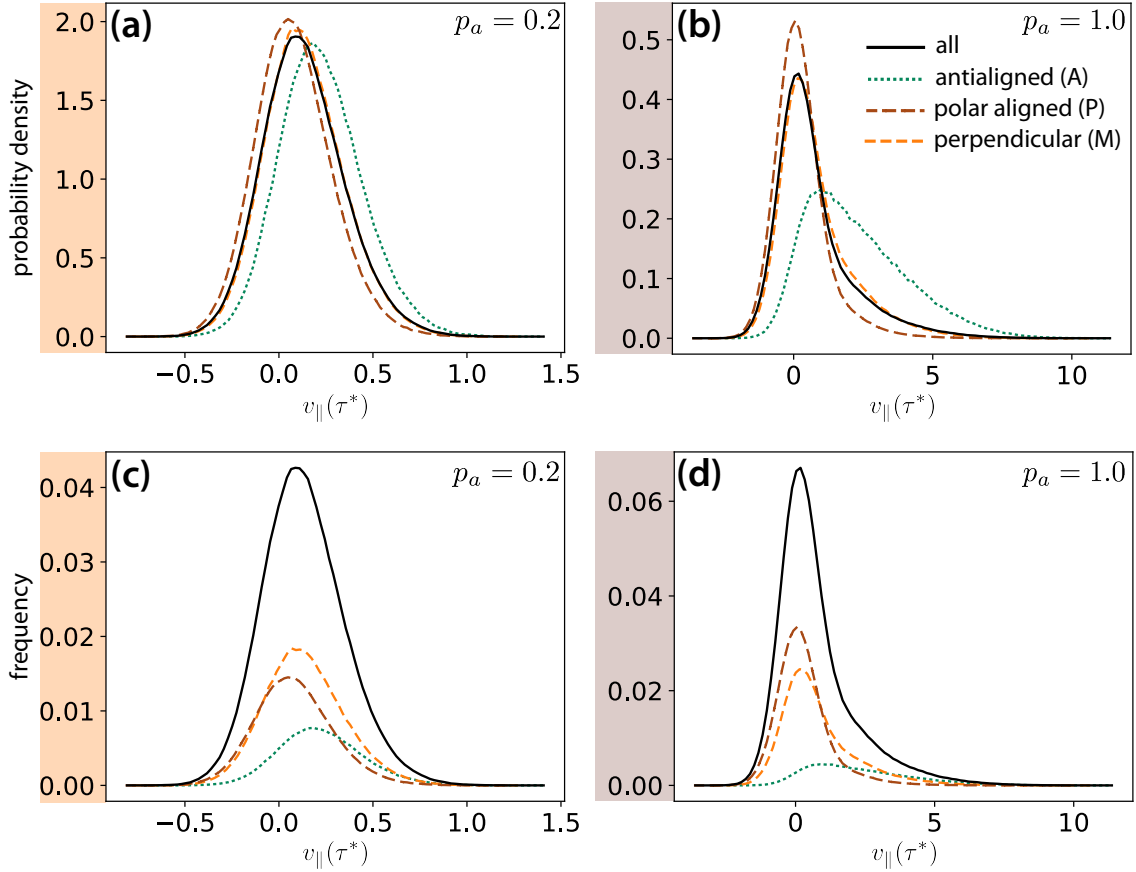


Figure 5.23: MT parallel velocity  $v_{\parallel}(\tau^*)$  distributions, for  $\phi = 0.3$ , decomposed based on MT environments (A, M, P) determined by their local polar order parameter,  $\psi_i$ , see Fig. 5.5. (a) and (b) show probability density histograms of  $v_{\parallel}(\tau^*)$  for  $p_a = 0.2$  and 1.0, respectively. (c) and (d) show frequencies of occurrence of  $v_{\parallel}(\tau^*)$  for  $p_a = 0.2$  and 1.0, respectively. The sum of the decomposed curves in (c) and (d) gives the solid curve shown.

In Fig. 5.24(a), (b) and (c) we use,  $\xi$ ,  $\omega$  and  $\alpha$  as fitting parameters to fit Eq. 5.12 to the  $v_{\parallel,A}(\tau^*)$  distributions. In order to compute the moments, we use the following relationships for mean,

$$\mu = \xi + \omega\delta\sqrt{\frac{2}{\pi}}, \quad (5.13)$$

variance,

$$\sigma^2 = \omega^2 \left(1 - \frac{2\delta^2}{\pi}\right), \quad (5.14)$$

and skew,

$$\alpha_3 = \frac{(4 - \pi) \left(\delta\sqrt{2/\pi}\right)^2}{2(1 - 2\delta^2/\pi)^{3/2}}, \quad (5.15)$$

where,

$$\delta = \frac{\alpha}{\sqrt{1 + \alpha^2}}. \quad (5.16)$$

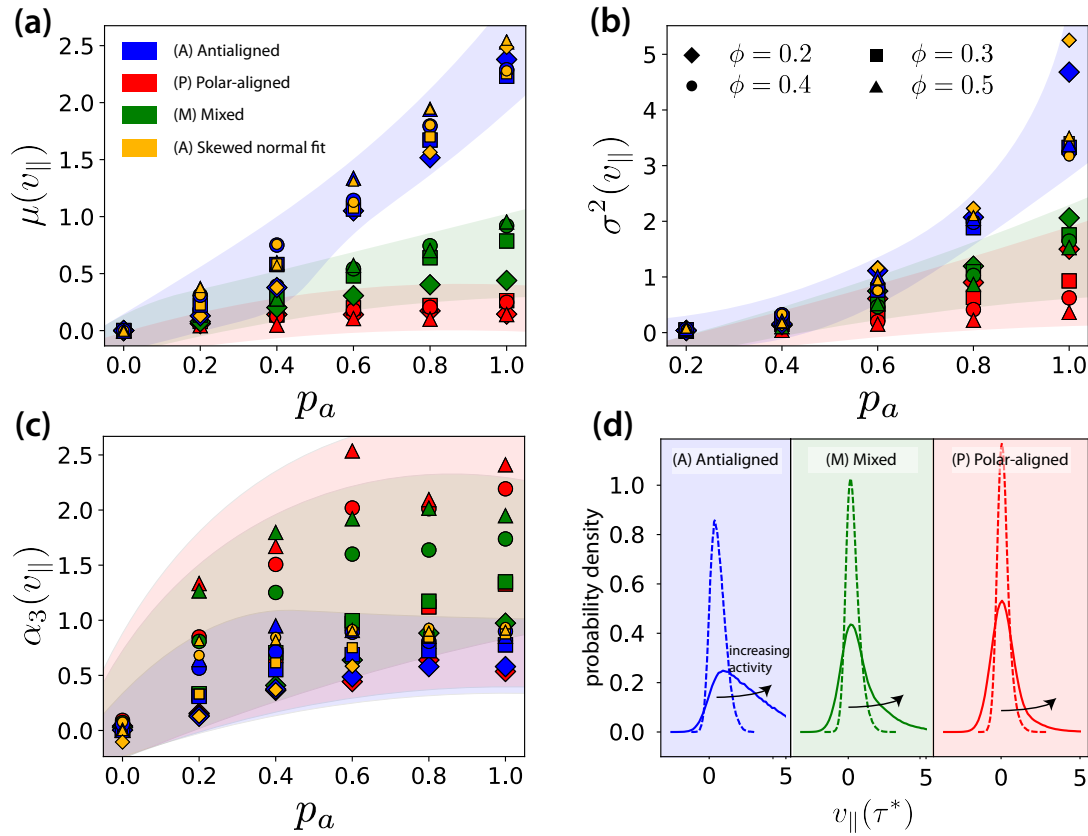


Figure 5.24: First three moments, **(a)** mean, **(b)** variance, **(c)** skew of  $v_{\parallel}(\tau^*)$  distribution for MTs in (A) antialigned ( $\psi_i < -0.5$ , blue), (P) polar-aligned ( $\psi_i > 0.5$ , red), and (M) mixed ( $|\psi_i| \leq 0.5$ , green) environments, for different  $\phi$  and  $p_a$ . The blue, red and green markers indicate moment calculated from raw data. The yellow markers are obtained from calculating moments from fits to  $v_{\parallel,A}(\tau^*)$ , antialigned MT parallel velocity. **(d)** Example of differences in structures of  $v_{\parallel}(\tau^*)$  distributions due to increasing activity from  $p_a = 0.4$  (dotted line) to  $p_a = 1.0$  (solid line) for  $\phi = 0.3$ , for A, P and M categories of MT environment.

This gives good agreement with the calculation of moments from raw parallel velocity data, using Eq. 5.7, see Fig. 5.24(a), (b) and (c). Since the mixed and polar-aligned MTs' velocity distributions,  $v_{\parallel,M}(\tau^*)$  and  $v_{\parallel,P}(\tau^*)$ , are affected by both motor forces and steric interactions, they cannot be well described by a skewed normal distributions. Figure 5.24(d) shows the differences in distributions of  $v_{\parallel}(\tau^*)$  due to increasing motor activity at  $\phi = 0.3$ . We quantify these differences, by computing moments of the  $v_{\parallel}(\tau^*)$  distributions for varying  $\phi$  and  $p_a$ , for the three categories of MT environments.

Figure 5.24(a) shows that the mean  $\mu(v_{\parallel,A}(\tau^*))$  increases much faster than  $\mu(v_{\parallel,P}(\tau^*))$  and  $\mu(v_{\parallel,M}(\tau^*))$ . This is identical to the information presented in Fig. 5.21, which shows that antialigned MTs displace the fastest. This also shows that the polar-aligned MTs are propelled the slowest, and a non-zero  $\mu(v_{\parallel,P}(\tau^*))$  is likely due to bulk forces due to activity in the system, *i.e.*, dragging of polar-aligned MTs due to streaming of antialigned MTs, via the friction between MTs, and collision of fast moving antialigned MTs onto slower polar-aligned clusters. A non-zero  $\mu(v_{\parallel,P}(\tau^*))$  can also be because the environment of

polar-aligned MTs could become antialigned in the time when the measurement is taken. These effects, however, are small compared to the activity in antialigned MTs.

Figure 5.24(b) shows that in general, the variance of  $v_{\parallel}(\tau^*)$  increases both with  $\psi_i$  and  $p_a$ , and decreases with  $\phi$ . The variance of  $v_{\parallel}(\tau^*)$  is highest for MTs in antialigned environments for all activities. This is also the category of MTs whose  $\sigma^2(v_{\parallel})$  increases the fastest with  $p_a$ . The  $\sigma^2(v_{\parallel,A}(\tau^*))$  increases with  $p_a$ , because more MTs access higher velocities due to the effective motor potential, which is also shown in the difference between Fig. 5.23(a) and (b).  $\sigma^2(v_{\parallel}(\tau^*))$  decreases with  $\phi$  because at higher surface fractions, MTs are more likely to be impeded to access a larger spread of velocities. Their velocities are dictated by the velocities of MTs around them.

Figure 5.24(c) shows that the skew of  $v_{\parallel}(\tau^*)$  for MTs increases with activity. Also MTs in antialigned environment have a smaller  $\alpha_3(v_{\parallel}(\tau^*))$  than that of MTs in polar-aligned and mixed environments. This is because parallel velocities of antialigned MTs have peaks which are centred at  $v_{\parallel}(\tau^*) > 0$ . For MTs in mixed and polar-aligned environments, the asymmetry represents the ratio of their velocities due to passive motion (which is symmetric) and their response to friction with active MTs. In general, we see that  $\alpha_3(v_{\parallel}(\tau^*))$  increases with  $\phi$ . This further suggests that the source of positive  $\mu(v_{\parallel,P})$  and large  $\alpha_3(v_{\parallel,P}(\tau^*))$  are friction forces, driven by highly motile, antialigned MTs.

## 5.6 Time-scale of microtubule streaming

So far, we have used  $\psi_i$  to distinguish the environments that affect MT displacements. By tracking changes in  $\psi_i$ , we can measure the time that MTs spend in antialigned and polar-aligned environments, and how this is affected by  $p_a$  and  $\phi$ .

The change in local polar order for MT  $i$  is

$$\Delta\psi_i(\tau) = \psi_{i,0} - \psi_i(\tau), \quad (5.17)$$

where  $\psi_{i,0} = \psi_i(\tau = 0)$ . As before, we indicate MTs starting in antialigned, mixed and polar-aligned environments using the  $A$ ,  $M$  and  $P$  subscripts, respectively. Figure 5.25(a) shows  $\langle\psi_{i,A}(\tau)\rangle$  and  $\langle\psi_{i,P}(\tau)\rangle$  for  $p_a = 1.0$  and  $p_a = 0.0$ . In both cases, we find that  $\langle\psi_{i,A}(\tau)\rangle$  increases with time, indicating antialigned MTs leaving their antialigned environments, and  $\langle\psi_{i,P}(\tau)\rangle$  decreases with time, indicating polar-aligned MTs leaving their polar-aligned environments. At long times,  $\psi_{i,A}$  and  $\psi_{i,P}$  converges to the long-time mean  $\langle\psi_{i,\infty}\rangle = 0$  for passive systems, and to  $\langle\psi_{i,\infty}(\tau)\rangle > 0$  for active systems. The time-scale for relaxing of  $\langle\psi_i\rangle$  to the equilibrium value is as expected, shorter for the active than for the passive system.

In order to quantify the change in  $\langle\psi_i\rangle$ , we construct

$$Q(\tau) = 1 - \frac{\langle\Delta\psi_i(\tau)\rangle}{\langle\psi_{i,0}\rangle - \langle\psi_{i,\infty}\rangle}, \quad (5.18)$$

and estimate the correlation time,  $\tau_{\frac{1}{2}Q}$ , by the time for  $Q$  to decay to  $0.5Q(\tau = 0)$ , in Figs. 5.25 (c) and (d). Interestingly, we find  $\tau_{\frac{1}{2}Q,A} = \tau_{\frac{1}{2}Q,P}$ . For MTs that begin in an antialigned environment at  $\tau = 0$ ,  $\tau_{\frac{1}{2}Q}$  gives an estimate of how long MTs spend in streams. Figure 5.25 (b) shows that  $\tau_{\frac{1}{2}Q,A}$  decreases exponentially with  $p_a$  and increases

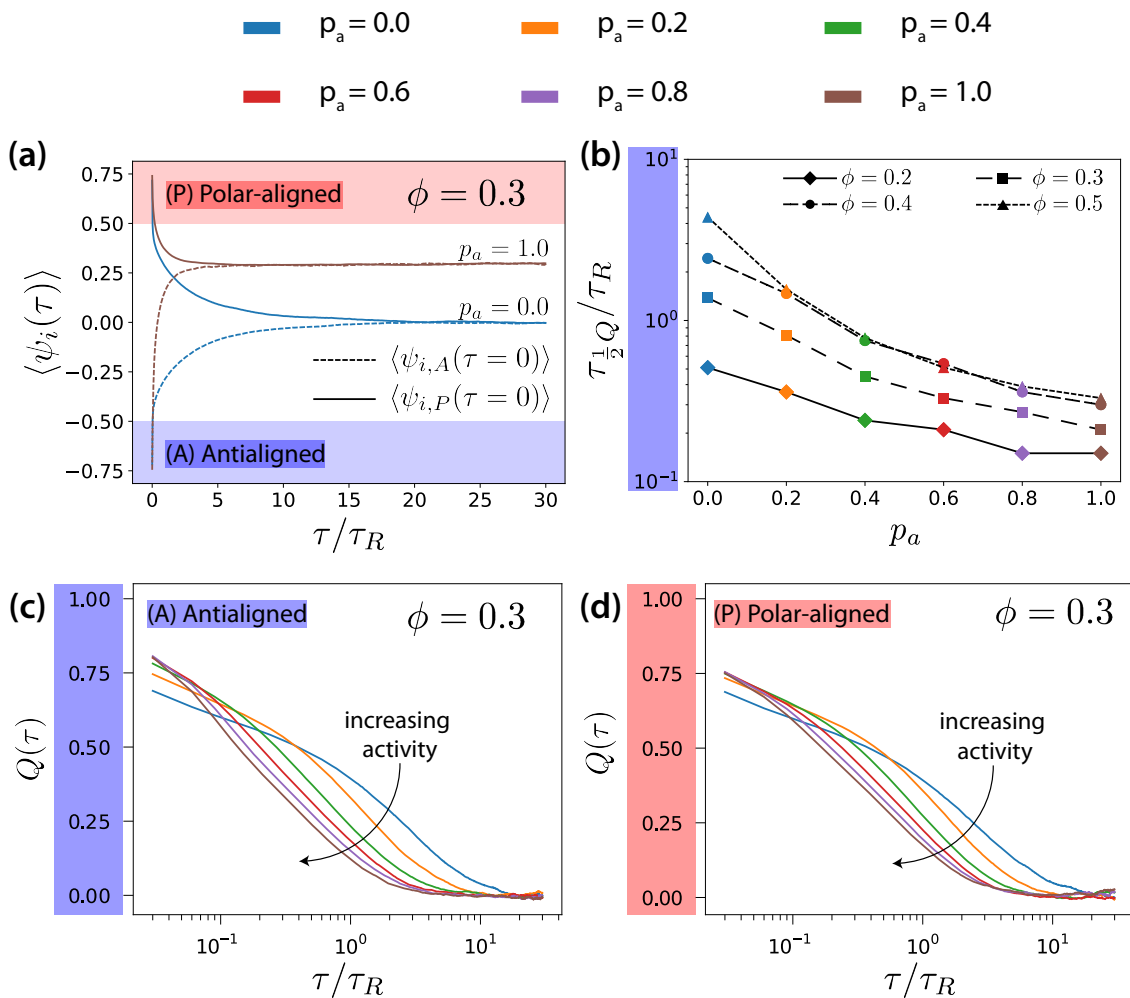


Figure 5.25: (a) Mean local polar order  $\langle \psi_i(\tau) \rangle$  for  $p_a = 0.0$  and  $p_a = 1.0$  at  $\phi = 0.3$ , for MTs starting from antialigned (dotted line) and aligned (solid line) environments. (b) Relaxation time for the polar order parameter,  $\tau_{1/2 Q}$  for various  $p_a$  and  $\phi$ , estimated by the time for  $Q$  to decrease to  $0.5Q(\tau = 0)$ , see (c) and Eq. 5.18. (c), (d)  $Q(\tau)$  for  $\phi = 0.3$  for various  $p_a$ . Plots of  $Q(\tau)$  for other surface fractions are provided in Fig. A.3.

with  $\phi$ . However, there is no difference in  $\tau_{1/2 Q, A}$  between the MT surface fractions  $\phi = 0.4$  and  $\phi = 0.5$ . At steady-state, the rates at which MTs change their environments between  $A$  and  $P$  are identical. An analysis of how  $\langle \psi_{i, \infty} \rangle$  changes with  $\phi$  and  $p_a$  is shown in Fig. 5.7.

## 5.7 Time-scale of collective effects

The observables discussed in the previous subsections characterise individual MTs. They only take collective effects into consideration indirectly, *e.g.*, via the non-vanishing asymmetry of the  $v_{\parallel}$  distribution for polar-aligned MTs.

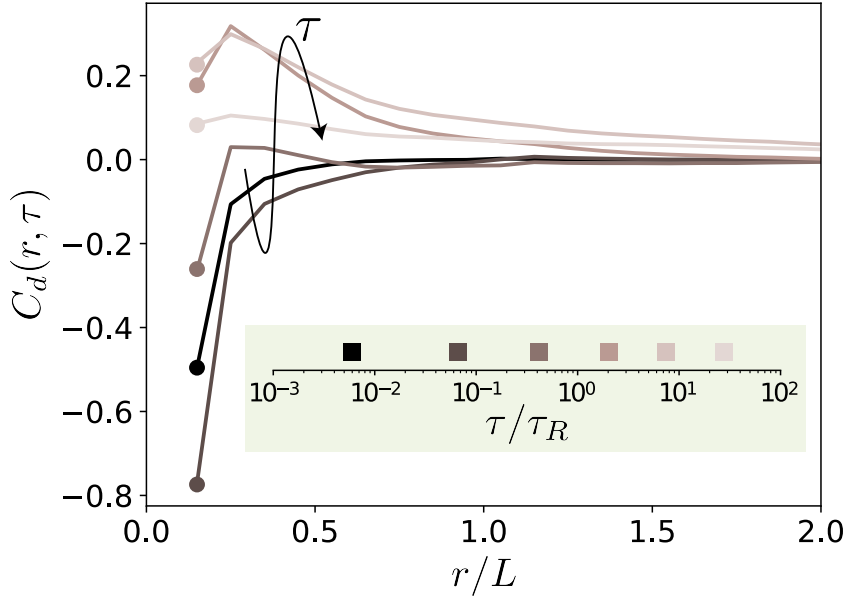


Figure 5.26: Spatio-temporal correlation function for  $\phi = 0.3$  and  $p_a = 1.0$ , for some selected lag times. The arrow and the colours of the curves indicate increasing lag time. The lag times are picked from a logarithmic scale.

### 5.7.1 Neighbour displacement correlation function

To directly characterise, and quantify time-scales of antialigned MT motion and collective streaming, we construct the spatio-temporal displacement correlation function [111, 112],

$$C_d(r, \tau) = \frac{\langle \sum_{i, i \neq j} \mathbf{d}_i \cdot \mathbf{d}_j \delta(r - |\mathbf{r}_i - \mathbf{r}_j|) \rangle_t}{c_0 \langle \sum_{i, i \neq j} \delta(r - |\mathbf{r}_i - \mathbf{r}_j|) \rangle_t}, \quad (5.19)$$

where  $\mathbf{d}_i(t, \tau)$  is the displacement vector defined in Eq. 5.2, and  $c_0 = \langle \sum_i \mathbf{d}_i^2 / N \rangle_\tau$  is used for normalisation. In the limit  $\tau \rightarrow 0$ ,  $C_d$  is the equal-time spatial velocity correlation function [112].

Figure 5.26 shows displacement correlation functions for  $\phi = 0.3$  and  $p_a = 1.0$ . In general, at short times and distances, we find negative displacement correlations due to the effective motor potential, which selectively displaces neighbouring antialigned MTs. These negative correlations decay rapidly in space, and do not contribute substantially for  $r/L = 1$ . Intermediate lag times show positive displacement correlations with a slower spatial decay, and long lag times show no correlations. In order to study these rich displacement correlations systematically, we disregard the decay of the correlations in space, and introduce a neighbour displacement correlation,  $N_d = C(r \rightarrow \sigma/L, \tau)$ . We identify neighbouring MTs at an arbitrary  $t$ , and calculate the displacement correlations between time  $t$  and time  $t + \tau$ , regardless of how far away the two MTs may be at  $t + \tau$ .

Figure 5.27 shows neighbour displacement correlation functions for various  $\phi$  and  $p_a$ . Firstly, for passive systems, for all surface fractions,  $N_d$  is positive but considerably weak compared to  $N_d$  of active systems. The small positive correlation is due to steric interaction, and friction due to the roughness of MTs (made up of overlapping beads). This causes MTs to move in the same direction over short distances. For active systems, Fig. 5.27 illustrates that the temporal dependence,  $N_d(\tau)$ , can be split into three regimes:

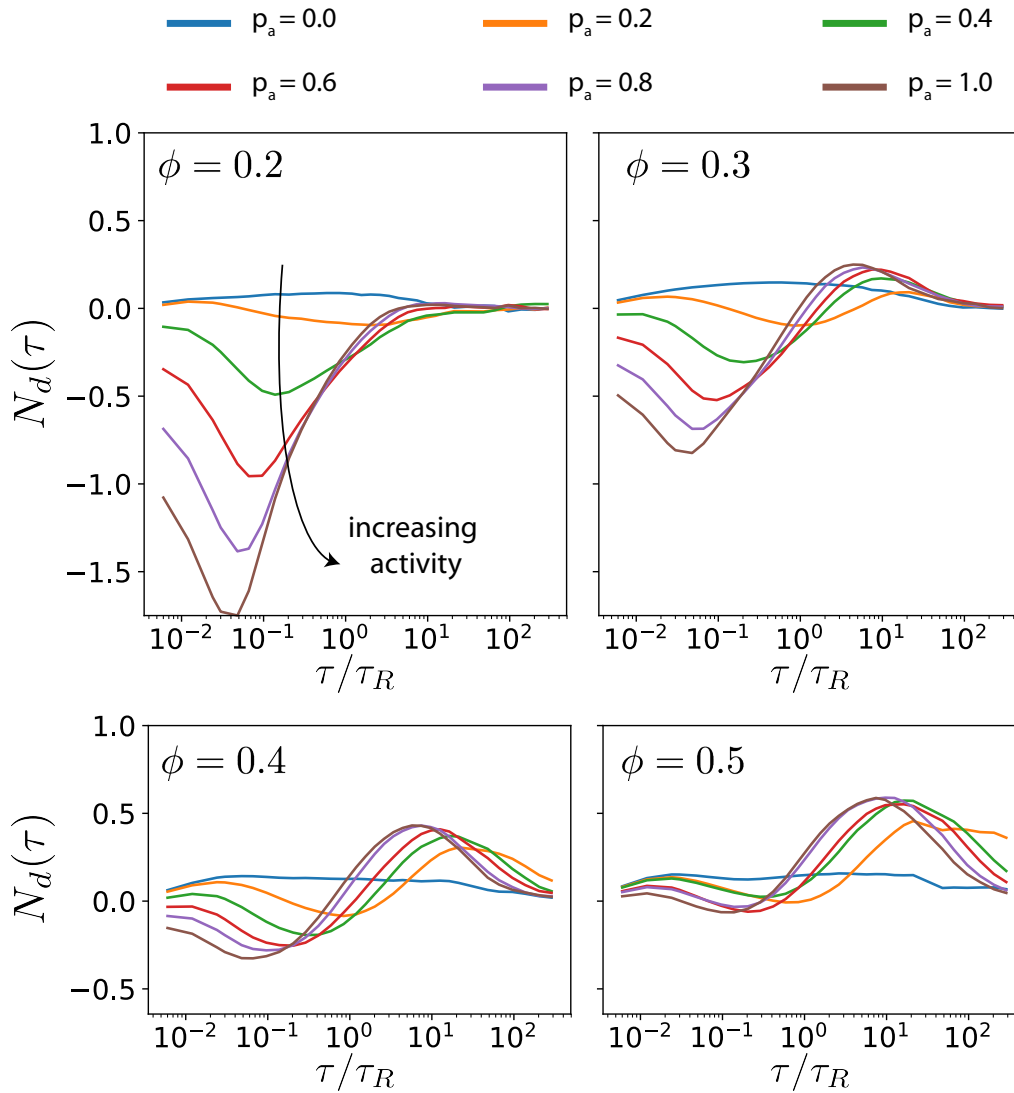


Figure 5.27: Neighbour displacement correlation function,  $N_d(\tau)$  for different  $\phi$  and  $p_a$ .  $N_d(\tau)$  is obtained from the value of  $C_d$  in Fig. 5.26 for the smallest value of  $r/L$ . The time at which the minimum and maximum of  $N_d(\tau)$  occurs are  $\tau_{N,\min}$  and  $\tau_{N,\max}$  respectively.

1. In the short-time regime,  $\tau/\tau_R \sim 10^{-1}$ , the effective motor potential propels neighbouring antialigned MTs away from each other and  $N_d$  is negative. This is aided by higher  $p_a$  but hindered by higher  $\phi$ , which opposes active motion sterically. The time-scale at which the minima occur represents when MTs are propelled because of effective motor interactions, due to presence of the antialigned neighbours. We call this time-scale  $\tau_{N,\min}$ .
2. In the intermediate-time regime,  $10^{-1} < \tau/\tau_R < 10^1$ , we observe a positive neighbour displacement correlation. This is altogether absent at low surface fractions,  $\phi = 0.2$ , but the positive correlations increases with increasing  $\phi$ . It suggests that neighbouring MTs in a particular stream (likely polar-aligned) travel in the same direction. These polar-aligned MTs will collectively migrate in the same direction,

since they are in a similarly antialigned environment. Correlations in their motion can only manifest at longer lag times, since at short lag times, the correlation contribution will be dominated by fast-moving antialigned MTs. We denote the lag time for the maximum of  $N_d$ , when collective migration occurs,  $\tau_{N,\max}$ .

3. At the long-time regime,  $\tau/\tau_R > 10^2$ , MTs lose memory of their neighbours and the correlations decay to 0.

### 5.7.2 Predictions of photobleaching microtubule mixtures

In order to show that positive neighbour displacement correlations observed in the intermediate time regime are due to collective migration of similarly oriented MTs, we simulate the results of a photobleaching experiment [5]. In experiments, this is similar to a high-intensity laser beam inactivating the fluorescent molecules in a circular region [113]. The time evolution of the distribution of the light-inactivated regions gives clues about the underlying mechanisms which mediate this motion.

Figure 5.28(a) illustrates that we expect little or no MT sliding to occur in a polar-aligned region, and the photobleached area maintains its shape. In Fig. 5.28(b), however, the photobleached area is antialigned and we expect antialigned MT sliding to cause the photobleached spot to separate into two regions [5]. In our simulations we perform a similar experiment, where instead of inactivating regions to inhibit fluorescence, we selectively fluoresce MT beads within a certain region. We then track their locations for  $t = \tau_{N,\max}$  and investigate their displacements. In Fig. 5.28(c), for  $\phi = 0.4$ ,  $p_a = 1.0$ , we visualise a four rod length radius circular area. MTs move in response to the effective motor potential, and form streams.

In order to investigate the collective motion at  $\tau_{N,\max}$  described in the previous section, we visualise a smaller circular area with a radius of  $2.5L$ , in Fig. 5.29. We perform this experiment on systems with  $\phi$  which show the peak at  $\tau_{N,\max}$  in Fig. 5.27,  $\phi = 0.3, 0.4, 0.5$ . Figure 5.29 shows that the coherence of MT streaming increases with  $\phi$ . Although for  $\phi = 0.3$  we see some instances of similarly oriented MTs displacing in the same direction, the displacements are isotropic compared to higher  $\phi$ . For  $\phi = 0.4$  and  $0.5$ , we observe long streams of MTs, composed of similarly oriented (coloured) MTs. This confirms that the height of the peaks in Fig. 5.27 represents the coherent motion of MT neighbours with similar orientations. A taller peak indicates higher coherence, where similarly oriented MTs displace along the same stream in the same direction, since they are propelled by an environment of similarly antialigned MT neighbours.

## 5.8 Conclusions

### 5.8.1 Summary of time-scales

We have shown that dipolar effective motor forces that drive antialigned MT pairs are sufficient to bring about MT streams which are perpetually created and annihilated. In other works which use a similar coarse-graining technique, the focus has been on understanding and capturing biologically relevant cytoskeletal structures due to the alignment

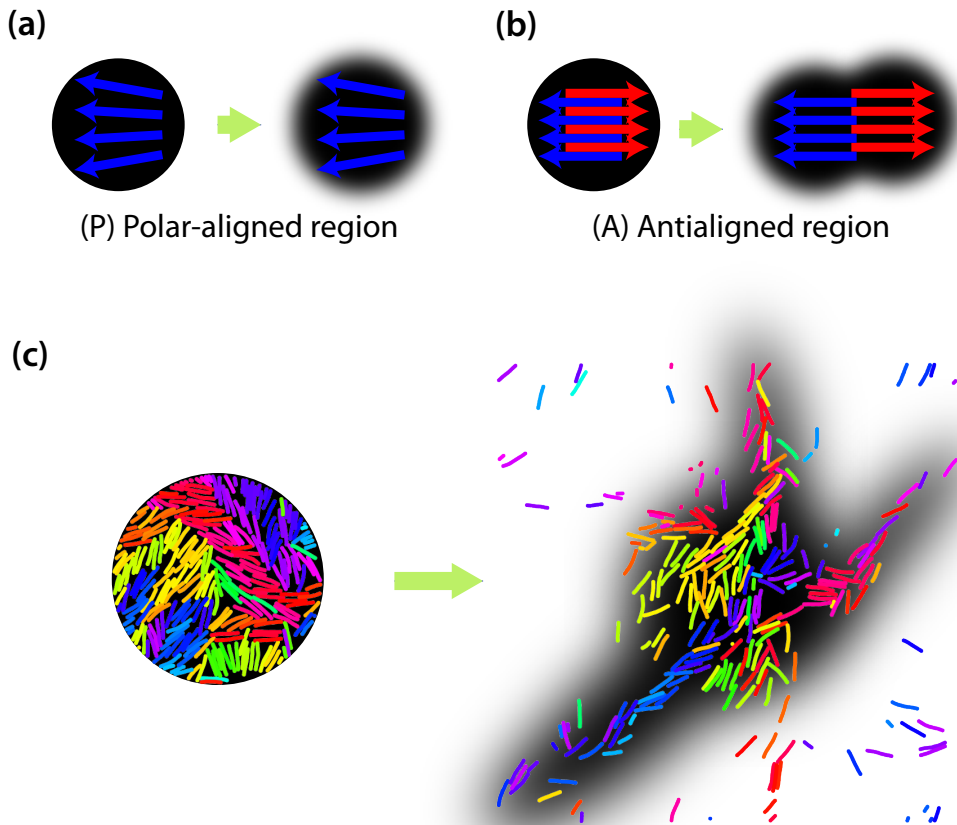


Figure 5.28: Illustrations of a photobleaching experiment, where bleaching is performed on a region which is (a) polar-aligned, (b) antialigned. Blue and red colours are used to distinguish between the MTs oriented in left and right directions. (c) Prediction of a photobleaching experiment on a mixture of MTs obtained for simulation with  $\phi = 0.4$  and  $p_a = 1.0$ . MTs (right) retain the orientation colour from when they were tagged (left). The black shadow illustrates our prediction for an equivalent photobleaching experiment. The green arrow represents the passage of time, showing how the MTs have dispersed upon photobleaching.

mechanism by motors [97, 107]. Here, for the first time, we have decomposed the time-scales of activity that bring about system-scale ordering and streaming, for an effective motor system.

By varying the surface fraction and antialigned motor probability, we study the length, lifetime and coherence of MT streams. We find that the streaming process can be decomposed into six consecutive processes which occur at distinct time-scales. These processes and the associated time-scales are provided in chronological order in Table 5.1.

From Fig. 5.30(a), we observe that the chronology of events listed in Table 5.1 holds for almost all simulations. Furthermore, the time intervals between these processes are functions of both MT surface fraction and activity. This is because the advent and extent of streaming depends on these variables, as seen in Figs. 5.8 and 5.9.

In general, we find that all processes become slower and shift to longer times, with

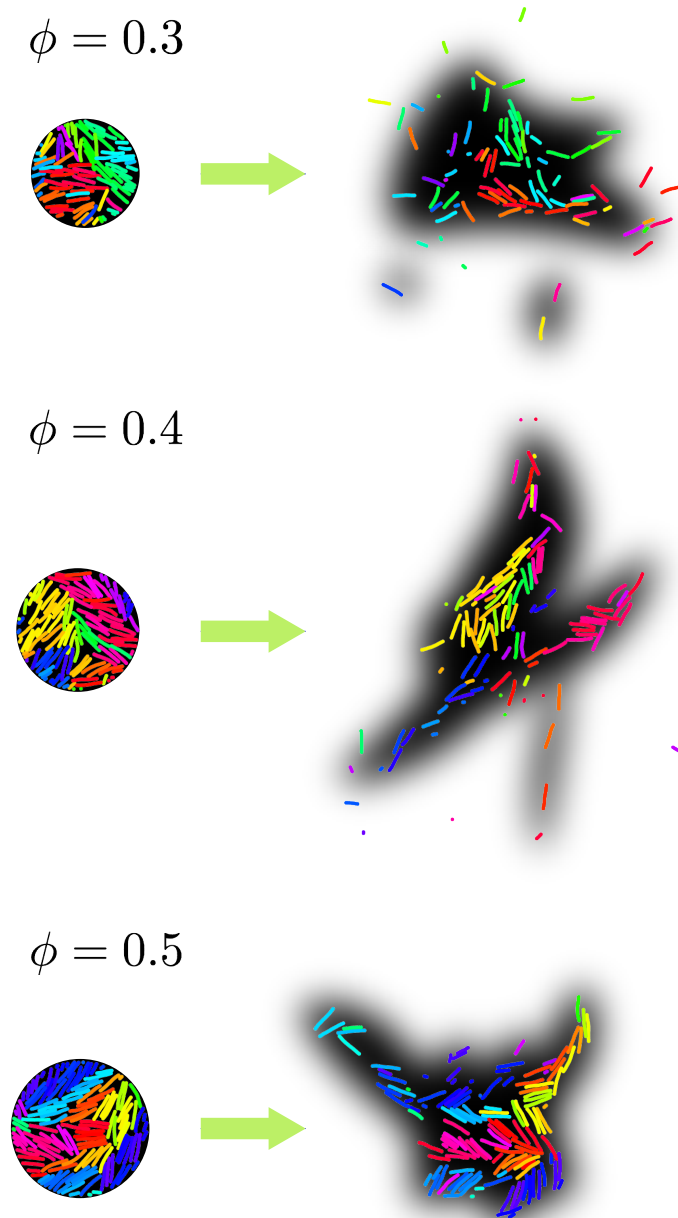


Figure 5.29: Predictions for a photobleaching experiment with  $\phi = 0.3, 0.4$  and  $0.5$ . MTs (right) retain the orientation colour from when they were tagged (left). The black shadow illustrates our prediction for an equivalent photobleaching experiment.

decreasing activity, and with increasing surface fraction. Figure 5.30(b) indicates that the velocities decrease with time-scales for the events. This shows that activity is propagated at the  $\tau_{N,\min}$  time-scale, and is dissipated at the  $\tau_r$  time-scale. Although MTs undergo coherent streaming at higher  $\phi$ , we find that these are also systems where MT velocity is relatively low, due to MT motion being inhibited by steric interactions.

	Symbols	time-scale ( $\tau_R$ )	Derivation
Diffusion	$\tau_D$	$\tau < 10^{-1}$	Slope of MSD $\approx 1$
Antialigned propulsion	$\tau_{N,\min}$	$\tau \approx 10^{-1}$	Minimum of $N_d$
Streaming	$\tau_{\frac{1}{2}Q}$	$10^{-1} < \tau < 10^0$	$\langle \psi_i \rangle$ decay time
Maximal skew	$\tau^*$	$10^0 < \tau < 10^1$	Maximum skew of $\mathbf{p}_0 \cdot \mathbf{d}$
Collective migration	$\tau_{N,\max}$	$\tau \approx 10^1$	Maximum of $N_d$
Rotation	$\tau_r$	$\tau > 10^1$	Orientational correlation time

Table 5.1: Table of time-scales involved in MT dynamics. The time-scales reported are approximate values for various  $p_a$  and  $\phi$ .

### 5.8.2 Dynamics

The exponent of the MSD in the active regime, for highly active systems at intermediate lag times is approximately 1.6. This is less than the theoretically predicted value, 2, for active Brownian particles [114]. Also, simulations for semiflexible chains that neglect steric interactions in two dimensions observed a  $\delta t^2$  dependence in MSD [106]. This suggests that the activity occurs in our simulations with a smaller exponent due to MT motion which is hindered by steric interactions.

In active systems, thermal and active fluctuations can affect the motion of particles. At long lag times, in our system, these fluctuations cause MTs to deviate from their initial orientations, and give  $\text{MSD} \propto \delta t$ . This regime is called the active diffusion regime [114]. On top of describing the MSD of active particles, such as point particles, spheres and stiff rods, it has been shown that Eq. 2.29 can also describe self-propelled semiflexible filaments [80]. In Fig. 5.16, we show that the active Brownian particle model can also describe the motion of the center of masses of MTs propelled by the effective motor potential.

### 5.8.3 Effective motor models

Various works have strived to circumvent the short time-scales, and length-scales involved in cytoskeletal dynamics such as the diffusion and active motion of individual motors in two dimensions [96, 97, 107–110, 115, 116]. For example, the phenomenological flux-force model used to describe the motion of MTs in one dimension, which occur due to the orientation of neighbouring MTs is described in Sec. 2.3.1 [95, 117].

Existing, two dimensional models, on the other hand, captured only the aligning mechanism of motors [97, 107–109]. In these simulations, MTs are modelled as stiff polar rods of equal length. The motors are taken into account using a Maxwellian model of

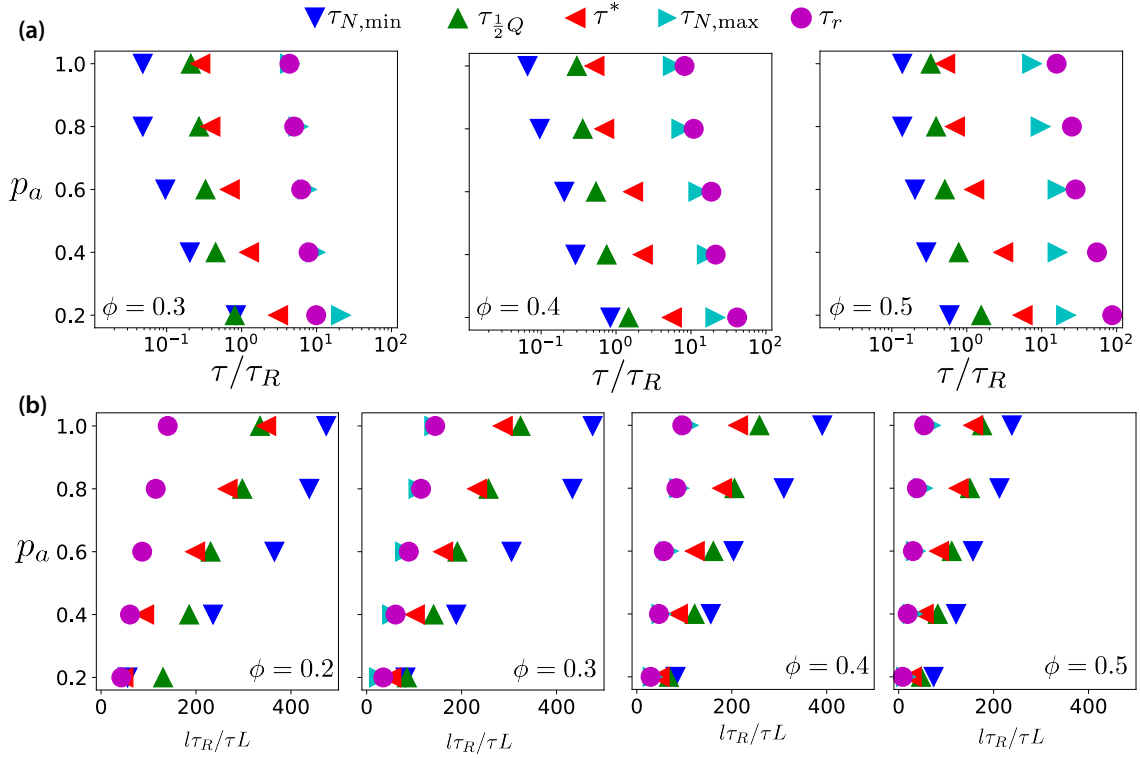


Figure 5.30: (a) Chronology of events from antialigned MT propulsion to MT rotation (left to right) which make up the streaming process, for various surface fractions and activities. We do not show  $\phi = 0.2$ , because there is no evidence of streaming in these systems, and the chronology of events are not consistent with those observed for higher surface fractions. (b) Velocity of MTs for each event, for various surface fractions and activities.  $l$  is the average distance traversed by the MT in the time span plotted in (a).

inelastic interactions between polar rods. These probabilistic collision rules result in the alignment of rods and an alignment event decreases the angular difference in their orientation by 25%. Although, these models captured the self-organization of MT-motor mixtures into stable patterns of vortices, asters and smectic bundles, the collision rule does not reproduce the sliding of antialigned MTs described in Fig. 1.6. Since, the sliding of antialigned MTs due to kinesin motors has been identified as a key ingredient for cytoplasmic advection in *in vivo* experiments [25, 50, 118], an effective motor potential, such as the one introduced in this chapter, which slides antialigned MTs, becomes relevant.

#### 5.8.4 Polar ordering with antialigned motor potential

The antialigned motor potential leads to MT propulsion when MT pairs are antialigned. We therefore find polar-aligned bundles with an interface of antialigned MTs as shown in Fig. 5.1. Similar smectic ordered, layered bundles were observed for high motor concentrations in simulations due to microscopic interaction laws which result in the MT-MT alignment interactions [97], which have also been analytically predicted [107, 108]. We reproduce these structures, not only because antialigned interfaces are constantly annihilated (and created), but also because the steric interactions induce nematic ordering,

which are neglected in other works [97,107,108]. However, the asters, and vortices, which result from the alignment mechanism, have not been observed using our effective motor potential.

### 5.8.5 Asymmetric displacements in polar particles

Analysis techniques used in this work are similar to those used in experiments for anisotropic vibrated rods [119]. Although the implications of our work are distinct from those of self-propelled particles, we observe that active forces in polar particles give characteristically asymmetric displacement distributions. When studied over a range of time intervals, similar to anisotropic vibrated rods, we observe that the skew of the displacement distributions increases towards the direction of propulsion with increasing lag times (Sec. 5.5). We predict that the skew of the displacement distributions will similarly vanish in experiments for longer lag times. Furthermore, it was found that the probability distribution function for vibrated rods in the parallel direction has a mean which is also shifted from zero, and that this shift grows as the vibration frequency is increased. Although this is similar to the findings in our system, for longer lag times, we see a shift of the distribution towards the center for the negative arm (passive arm). For vibrated rods, however, the distribution widens for both arms. Since in our simulations the widening of the positive arm is more than that of the left, this manifests in skews which follow a similar trend with lag time and activity.

Even though the mechanism of activity implemented in the vibrated rod system is different, we predict that the activity due to the vibration might also manifest in the displacement asymmetry for the smallest lag times, as was observed in our simulations, ( $\tau/\tau_R = 10^{-2}$  in Fig. 5.17 and 5.18).

### 5.8.6 Cytoplasmic streaming in *Drosophila*

Using Particle Image Velocimetry (PIV) in *Drosophila* cells, the probability distribution function of fluid speeds were calculated for wild type oocytes and those lacking *pat1*, a protein required for kinesin heavy chain to maximise its motility [43]. Although, both these distributions show clear peaks and long tails, the mean speed of the system that lacked the *pat1* protein was slower, and had a smaller tail than the wild type. This is similar to our findings in our simulations shown in Fig. 5.17, with varying  $p_a$ . Unlike in our simulations, where the velocity peak was at 0, results from the PIV showed velocity peaks close to 10nm/s.

It was suggested that the long tails in the velocity distribution of the cytosol can reflect a combination of an underlying distribution of motor speeds, and a complex MT network geometry. From our simulations, we show that neither a complex three dimensional cytoskeletal geometry nor a combination of different motor speeds are required to reproduce cytoskeletal velocity distributions with long tails.

MT advection was also analysed by performing photoconversion in interphase *Drosophila* S2 cells, where MTs were observed to buckle and loop [25]. MT motion was visualised by photoconverting a circular region within the cell. These MTs were observed over a 7 minute period, during which time, 36% of the MTs were determined to be motile. It

was observed that MTs spent most of the time not moving, but underwent abrupt long-distance streaming. They were found to achieve velocities up to  $13 \mu\text{m}/\text{min}$ , during these bursts of active motion.

These observations are similar to those in our simulations where MTs spend most of their times in stable polar-aligned bundles, but when in contact with an antialigned stream, coherently stream over large distances, as shown in Fig. 5.8. We observe a similar 36% motile MT fraction if  $\phi = 0.3$ . In Fig. 5.29, for this surface fraction, we find qualitative agreement between our FRAP predictions and the experiments [25]. Due to the polarity sorting of MTs, a similar FRAP result was also predicted in simulations in the literature [5], but the time-scale of collective migration was not predicted.

### 5.8.7 Collective effects

For all streaming systems, our simulations show collective migration of MTs at  $\tau_{N,\text{max}}$ , Fig. 5.27. Using the FRAP visualisation in Fig. 5.29 we confirmed that the peak in  $N_d$  was due to the migration of similarly oriented neighbouring MTs together in the same stream. This leads to elongated MT stream patterns similar to those observed in experiments [25].

Moreover, we have shown that the spatio-temporal correlation function, in Fig. 5.26, is a function of lag time. For motor-driven systems, which slide antialigned MTs away from each other, we predict a negative  $C_d$  for short length scales at  $\tau_{N,\text{min}}$ . In experiments positive flow correlations have been found in streaming systems [43]. Since we observe a similar spatio-temporal correlation in the time-scale corresponding to collective migration, we posit that the experimental findings have the underlying migration mechanism proposed in our work at  $\tau_{N,\text{max}}$ . This approach gives a direct handle over comparing time-scales between the experiments and simulations. By comparing the spatial decay of displacement correlations, we can also link the lengths between the experiment and the simulation [97].

# Chapter 6

## Conclusions

We have investigated the dynamics of MT-motor mixtures in confinement and in bulk using computational tools, coupled with analysis methods from statistical physics. For the confined system, we systematically studied the difference between dimeric and tetrameric motors on MT structure and their collective dynamics. By introducing an effective motor potential for a bulk MT system, we captured active events that are found to occur in chronological order across a large span of time scales.

We summarise the key results, categorising them into those obtained using explicit motors, Sec. 6.1, and the effective motor potential, Sec. 6.2. In Sec. 6.3 we provide an outlook for open questions, which can extend the presented investigation.

### 6.1 Confined filaments driven by explicit motors

We have studied first a model in which motors are described explicitly as they walk and slide confined, stiff MTs. The novel aspects of this model are:

- (a) A comparison between tetrameric and dimeric motors is introduced in the context of their effect on sliding confined MTs. Tetrameric motors have motor-arms which walk on both crosslinked MTs, whereas dimeric motors have motor-arms that walk on only one crosslinked MT and the other arm remains anchored.
- (b) In order to highlight the asymmetry of the motor-arms, we choose a constant active motor-arm speed, *i.e.*, if a motor-arm is motile, it always moves in the direction of MT polarity. The motor detaches if the motor extension is larger than the motor threshold length, or if the motor-arm reaches the end of the MT.
- (c) The confinement is attractive, which traps a layer of immotile MTs. Motors use these MTs as tracks to slide MTs in the bulk.
- (d) MTs interact via an excluded volume interaction potential with an adjustable overlap energy, which allows them to cross over each other. Simultaneously, the potential has an attractive well to mimic depletion interactions that promote MT cohesion, and motor binding.

### 6.1.1 Microtubule structures in confinements

In Chapter 3, we give a qualitative description of MT structures when parameters controlling cytoskeletal filament dynamics are changed. The key results are:

- (a) MT-MT attraction leads to bundle formation. At low attractions, the structures formed are shown to be qualitatively similar to those observed in other simulations and experiments [57, 68].
- (b) Tetrameric motors give polar-aligned bundles, similar to simulations of MTs connected by static crosslinkers in bulk [4]. These bundles are also more pronounced at higher MT-MT attraction.
- (c) Dimeric motors give large polar-aligned domains. The domain sizes are not affected by the confinement size. At low surface fractions, these structures are isotropic for both motors. For high surface fractions, multiple dynamic  $+1/2$  topological defects are observed for the dimeric motors.
- (d) Polarity sorting occurs even at the lowest motor concentrations for both type of motors. Altering the motor spring constant, or the motor velocity does not change the overall structure for systems driven by either type of motor.
- (e) The ordering time to form large-scale structures is faster in tetrameric motor systems than dimeric motor systems. Also, the tetrameric motor systems are more polar-aligned than the dimeric motor systems.

### 6.1.2 Confined microtubules driven by explicit motors

In Chapter 4, we quantitatively describe the dynamical properties of the perpetually dynamic, confined MT network. The key results are:

- (a) Using the mean squared displacement of MTs, we categorise the time-scales into diffusive, and active regimes. The MSD plateaus after the active regime, once MTs reach the confinement radius. For the time-scales simulated, MTs driven by tetrameric motors have MSDs that do not reach the confinement radius. Also, the MSDs show that the dimeric motor systems are significantly more dynamic than the tetrameric motor systems.
- (b) MTs in antialigned environments are significantly faster than polar-aligned MTs, due to the motor-induced MT-MT sliding. For the same antialigned configurations, dimeric motors slide MTs faster than tetrameric motors, even though they only have one active arm.
- (c) These antialigned MTs have a skewed velocity distribution due to motor-induced sliding. Tetrameric motors that crosslink antialigned MTs are able to generate higher velocities that only make up the tail of the positively skewed distribution. Dimeric motors have the peak of their distribution at a higher velocity than that of tetrameric motors, and the distribution is skewed in the opposite direction. The relative longitudinal displacement and the resulting maximal force for tetrameric motors is higher than for dimeric motors.

- (d) The region near the attractive confining boundary is the most dynamic. A non-attractive boundary results in a significant decrease in the parallel velocity of this dynamic layer.
- (e) The number of motors decreases exponentially with processivity. Tetrameric motors have the fastest detachment rate and the shortest mean life time.

## 6.2 Bulk microtubules driven by effective motors

Modelling individual motors, and capturing cellular-scale phenomena at the same time is unwieldy for large system sizes. Based on our findings from modelling explicit motors, we introduce a model for an effective motor potential. In this model, only MT pairs which are antialigned can slide actively with respect to each other. The system is active at steady state because active and thermal fluctuations perpetuates antialigned interfaces preventing complete polarity sorting.

As there are no real motors in the system, we construct an antialigned motor probability,  $p_a$ , to control the activity in the system. We show that  $p_a$  is a linear function of the parallel velocity. We vary the MT surface fraction,  $\phi$ , and  $p_a$ , to study their effects on MT structure and dynamics under periodic boundary conditions. The key results are:

- (a) The antialigned effective motor potential gives rise to large polar-aligned domains, similar to that observed in the confined dimeric motor systems. The domain size increases with surface fraction, and decreases with  $p_a$ . The aligned effective motor potential, on the other hand, slows down the dynamics, and gives rise to polar-aligned bundles, similar to those observed in the confined tetrameric motor system.
- (b) The MSD shows three regimes of motion: diffusive (small time scale), active (intermediate time scale, ballistic MT motion) and active diffusive (largest time scale, diffusive MT motion). Calculating the active diffusion constant shows that the effective motor system exhibits long-time-scale activity similar to the larger class of active Brownian particles.
- (c) Due to motor activity, the MTs' parallel velocity distributions are skewed in the positive direction. The extent of the skew changes with the time-scale chosen to measure velocity. There is a peak in the skew at a time  $\tau^*$ , which decreases exponentially with activity, for all surface fractions. Also,  $\tau^*$  occurs at the middle of the ballistic time-regime in the MSD curves.
- (d) The collective effects of MT motion are characterised by the displacement correlation function,  $C_d(r, \tau)$ , and the neighbour displacement correlation function,  $N_d$ . For active systems, the temporal dependence of  $N_d$  indicates that MT motion can be split into three time-regimes:
  - MT-MT antialigned sliding time-regime,  $\tau_{N,\min}$ , where MTs are propelled away from each other.
  - Collective migration time-regime,  $\tau_{N,\max}$ , where neighbouring MTs in a particular stream travel together in the same direction since they share a similar local polar order.

- Decorrelation time-regime, where MTs lose memory of their neighbours and correlations vanish.
- (e) The overall MT dynamics can be ordered chronologically in the following manner: (1) MT diffusion, (2) antialigned MT propulsion, (3) streaming, (4) collective migration, (5) MT rotation from initial orientation. The active time-regime,  $\tau^*$ , occurs between streaming and collective migration. The coherence and persistence of MT streaming increases with  $p_a$ . We observe the longest streams for  $\phi = 0.3$  and  $0.4$ .
- (f) We predict photobleaching results, and show that elongated MT streams can be observed at higher surface fractions. At low surface fractions, MTs are displaced more isotropically.

### 6.3 Outlook

The MT-motor model employed here to investigate the relation between biological phenomena and cytoskeletal organisation are minimalistic. They have, nevertheless, proven to be useful in capturing aspects of complex phenomenology observed in experiments. In doing so, we have provided clues about the fundamental mechanisms that have evolved in nature to bring about specific cytoskeletal structures and dynamics.

However, modelling a biological cell, or preparing functional microscopic structures, requires not only a good understanding of the underlying mechanisms, but also an inclusion of complex and non-trivial details of biological molecules and materials. Additional features that can be built into the phenomenological model to capture higher levels of complexity are highlighted here:

- In all cases presented, we assume that the distribution of motors is uniform in the solvent, *i.e.*, the time scale of motor diffusion in the solvent is much faster than the time scale of motor walking, and MT dynamics. In cells, motors are synthesised in specific organelles and regions. When capturing long-time-scale phenomena, one must take the concentration and flux of motors into consideration. For instance, it would be instructive to study MT motion due to a concentration gradient of motors in solvent.
- Cells are enclosed by a flexible lipid bilayer membrane. For simplicity, we have assumed that the confinement is rigid and non-motile. It would be interesting to study the shapes of a semi-flexible ring which can encompass the MT-motor mixture. Also, one can study the motility patterns of these flexible membranes that encloses the MTs that interact via motors.
- We have assumed the motor velocity to be a constant to emphasise the motor-arm asymmetry. Since the asymmetry of the motor-arm brings about a substantial difference in the resulting MT structure, it would be interesting to study the effect of a linear-force velocity dependence for motor walking, and to make the motor-arms asymmetric in this context.

- We have established a viable model for MT streaming using the effective motor potential. Since substantial computational overhead could be removed by omitting the simulation of explicit motors, it is now possible to study the system for a substantially larger simulation box, and to enclose the mixture in a circular confinement.
- The length of MTs in our simulations were always held constant. Under physiological conditions, MTs are subject to assembly and disassembly phases. Modelling the polymerisation dynamics of MTs, as explained in Sec. 1.1.2, on top of motor-induced MT sliding, would be a step towards capturing physiological phenomena.
- The effect of semiflexibility of motor-driven filaments in the context of both explicit and effective motors remains an important open question.

# Appendix A

## Supplementary Figures

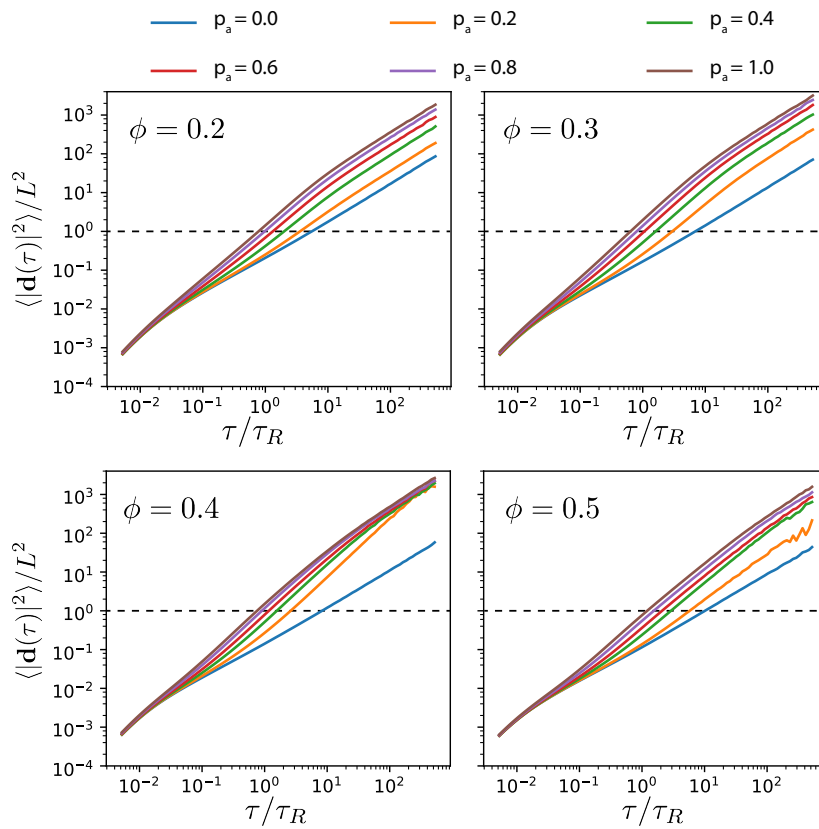


Figure A.1: MSD of MTs for different densities and activities in the effective motor systems.

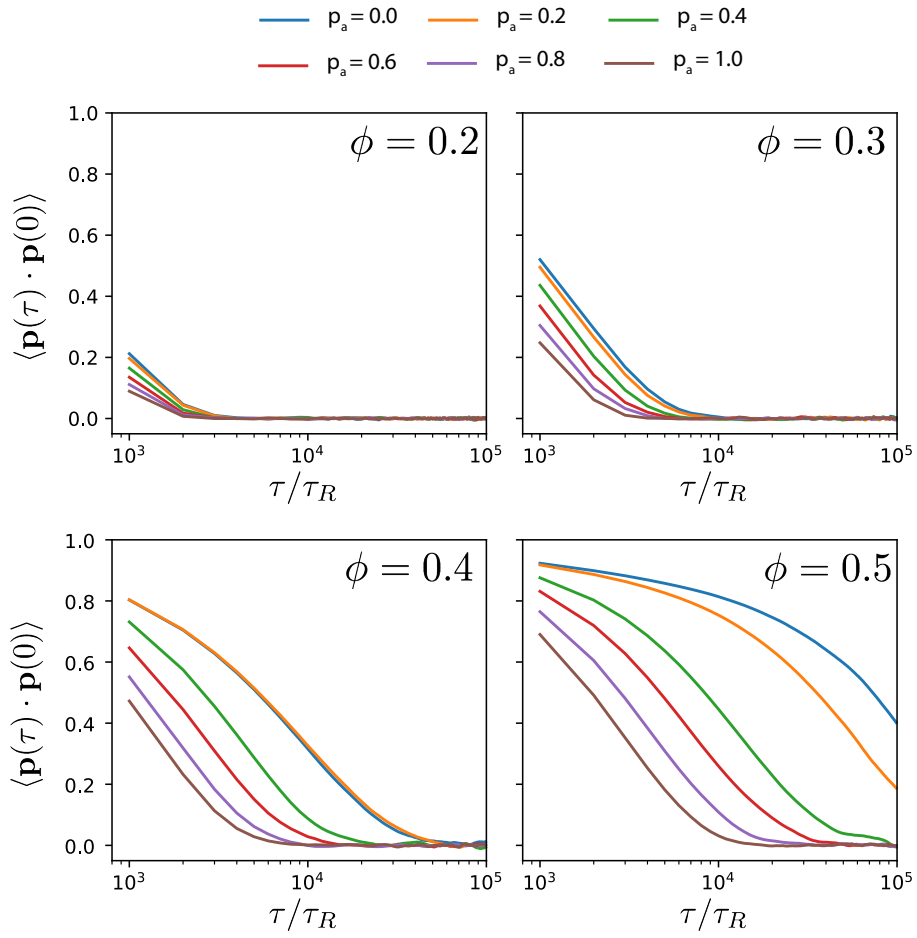


Figure A.2: Long-time rotational correlations for different densities and activities in the effective motor systems.

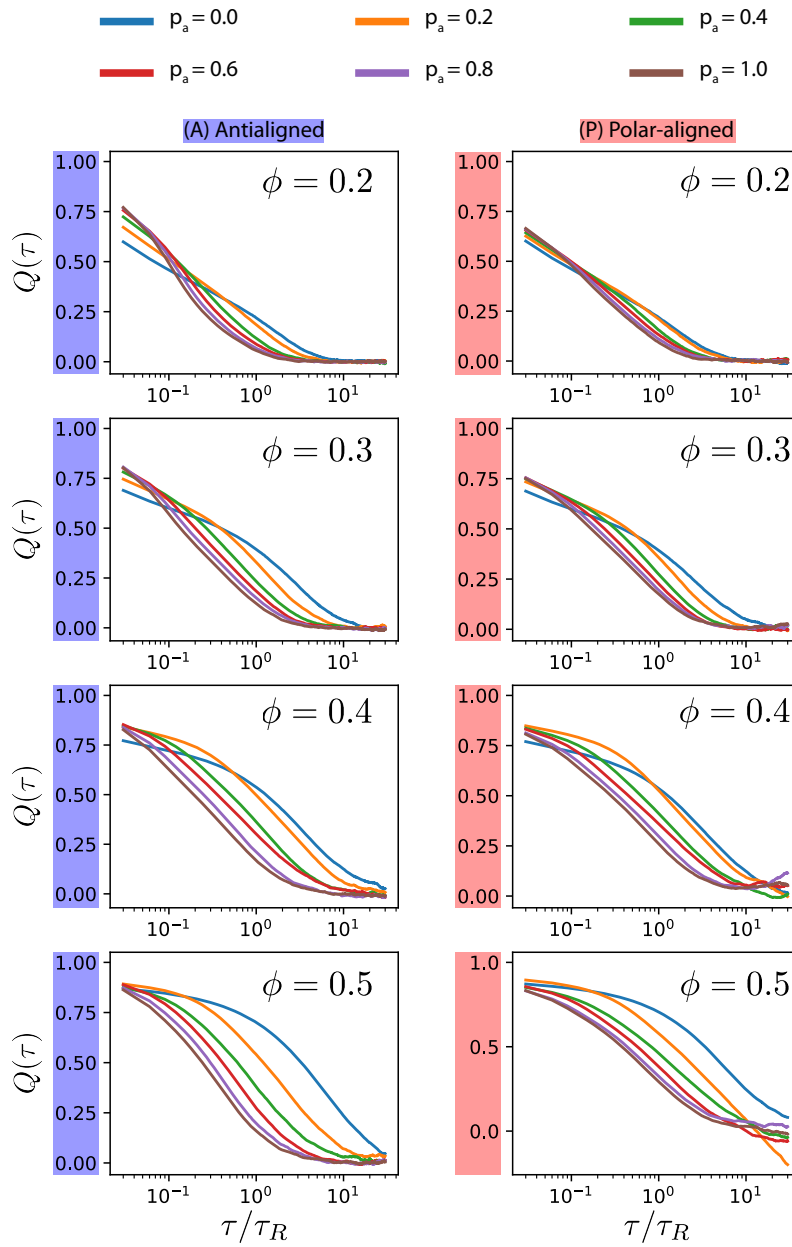


Figure A.3: Local polar order correlations for MTs that are initially antialigned and polar aligned for different densities in the effective motor system.

## Appendix B

# Time correlation algorithms

In molecular dynamics simulations, one of two approaches can be used to calculate the time correlations of particles, such as mean squared displacements.

- Final output method: This method is easier to implement, has no computational overhead, requires analysis of simulation output, but requires a larger output from the simulation, and is unsuitable to resolve small time scales.
- *On the fly* method: Although this method is harder to implement and requires a small computational overhead, it can capture time resolutions as small as the simulation time-step, and if implemented appropriately can give uncorrelated data for the calculation of the second moment of a given distribution (e.g. standard deviation of displacements).

Although these techniques can be adapted to accommodate any time correlation calculation, we will use the example of the mean squared displacement to describe the algorithm.

### B.1 Final output method

Assuming that we perform the simulations for  $T$  integration time steps, and we save the data every  $t$  steps, we will have  $F = T/t$  number of data frames, where  $F$  is the quotient of  $T/t$ . The pseudocode for the method is:

- Prepare a list of lag times, e.g.,  $[1, 2, 3, \dots, d, \dots, D]$ , called *lags*.
- Allocate a corresponding array of zeroes of length  $D$ , called *sums*.
- Allocate another array of length  $D$ , called *divs*.
- Iterate through the data frames from the simulation output, with some index,  $i$ :
  - Iterate through *lags*:
    - \* If  $i + d > D$ , break the loop and go to the next lag time
    - \* Perform the MSD calculation,  $(x_i - x_{i+d})^2$
    - \* Add it to  $d^{\text{th}}$  element of *sums*:  $\text{sums}[d]$
    - \* Add 1 to  $d^{\text{th}}$  element of *divs*:  $\text{divs}[d]$

- Divide every element in *sums*, with the corresponding element in *divs*, to obtain the *mean* of the squared displacements.

Plotting *sums* against *lags* in log-log scale gives the familiar MSD plot. Note that the x-axis must be appropriately scaled with *t*, in order to obtain time in simulation time units, instead of units of output frame rate.

If the data for multiple particles is stored in a three dimensional array, *xi*, such that the first axis is the data frame index, second axis is the dimensional index (*x, y* for 2-D), and the third axis is the particle index, the procedure can be written in Python, for multiple particles in the following manner:

```
import numpy as np

lags = np.zeros(D)
msd = np.zeros(D)

for d in range(1, D):
    lags[d] = d
    msd[d] = np.mean(np.mean(\
        (xi[d:,0,:] - xi[: -d,0,:])**2 + \
        (xi[d:,1,:] - xi[: -d,1,:])**2, axis=1))
```

The smallest resolution that can be achieved in this method is *t*. In order to obtain smaller resolutions, *t* needs to be decreased, which increases  $F = T/t$ . For numerous particles, this becomes tedious, and in some cases infeasible due to storage and processing reasons.

## B.2 On the fly method

The alternate method must be performed on the fly, which means, the calculation must be embedded in the molecular dynamics algorithm, after the integration step, and must be carried out when the simulation is running.

- Prepare a list of (roughly) log spaced lag times of length *D*, called *lags*. *lags* is a  $[1 \times D]$  array.
- Allocate an array of reference positions for each particle in lag time, called *refs*. *refs* is a  $[D \times N \times 2]$  array. The last index, 2, is for a 2-D system.
- Allocate an array of zeroes of length *D*, called *sums*. *sums* is a  $[1 \times D]$  array.
- Allocate another array of length *D*, called *divs*. *divs* is a  $[1 \times D]$  array.
- Anytime the simulation timestep can be exactly divided by any element in *lags*, we do the following:
  - Update and overwrite the reference position of the particles, *refs*.
  - Subtract (and square) the current position of the particles with the reference position of that lag time,  $(x_i - refs[d])^2$

- Add it to  $d^{\text{th}}$  element of *sums*:  $sums[d]$
- Add 1 to  $d^{\text{th}}$  element of *divs*:  $divs[d]$
- Divide every element in *sums*, with the corresponding element in *divs*, to obtain the mean of the squared displacements.

We can now plot these values on log-log scale. This method can be easily added to the LAMMPS source code, so as to achieve the smallest resolution necessary for MSDs.

## Appendix C

# Non-equilibrium as a violation of detailed balance

At equilibrium, the rates of transition into and out of a system's microstate is balanced. This is to say that the system obeys detailed balance, where *each* elementary process is equilibrated by its reverse process. Systems that obey detailed balance have transition rates between any two microstates that are *pairwise balanced*, Fig. C.1A. At equilibrium, in the entire phase space, composed of many such microstates, there cannot exist any pair of states which have a net flux of transitions between them [120].

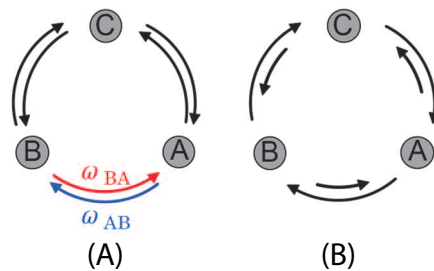


Figure C.1: (A) For detailed balance to be satisfied, transitions between microscopic states must be pairwise-balanced. (B) A system can break detailed balance, exhibit non-equilibrium behaviour and still be at steady state if there is a flux loop in phase space. Image is adapted from Battle *et al.* [121].

Almost all systems found in nature, however, are not in equilibrium, and detailed balance is violated at a molecular-scale [6, 48, 50, 122]. Such processes are characterised by the directed fluxes through chemical states. For instance, metabolic and enzymatic processes drive closed-loop fluxes through the system's chemical states, Fig. C.1B [121]. Quantifying the extent to which a system breaks detailed balance is useful, because this characterises the extent to which it deviates from equilibrium [123].

## Appendix D

# Benchmarking of effective motor system

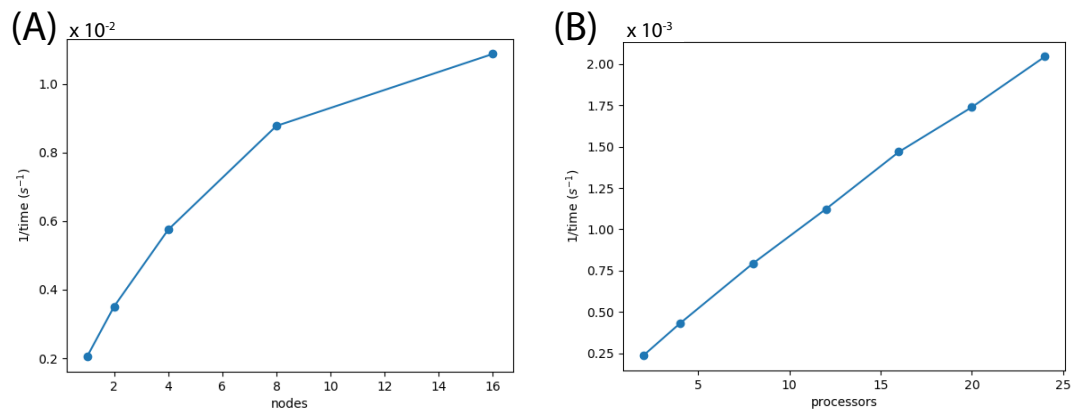


Figure D.1: Scaling of simulation time with number of nodes and processors for the effective motor system using LAMMPS [94], on JURECA supercomputer. Simulations performed using (A) 1 node and multiple processors, and (B) multiple nodes with 24 processors per node.

# Bibliography

- [1] P. Mitchell, *Chemiosmotic coupling in oxidative and photosynthetic phosphorylation*, Biol. Rev. Camb. Philos. Soc. **41**, 445 (1966).
- [2] B. Alberts et al., *Molecular Biology of the Cell 5th edition*, Garland Science, New York, 2007.
- [3] J. Howard, *Mechanics of motor proteins and the cytoskeleton*, Sinauer Associates Sunderland, Massachusetts, 2001.
- [4] R. Blackwell et al., *Microscopic origins of anisotropic active stress in motor-driven nematic liquid crystals*, Soft Matter **12**, 2676 (2016).
- [5] T. Gao, R. Blackwell, M. A. Glaser, M. D. Betterton, and M. J. Shelley, *Multiscale Polar Theory of Microtubule and Motor-Protein Assemblies*, Phys. Rev. Lett. **114**, 048101 (2015).
- [6] D. A. Head, W. J. Briels, and G. Gompper, *Nonequilibrium structure and dynamics in a microscopic model of thin-film active gels*, Phys. Rev. E **3**, 032705 (2014).
- [7] D. A. Head, W. J. Briels, and G. Gompper, *Spindles and active vortices in a model of confined filament-motor mixtures*, BMC Biophys. **4**, 18 (2011).
- [8] P. Ronceray, C. P. Broedersz, and M. Lenz, *Fiber networks amplify active stress*, Proc. Natl. Acad. Sci. U.S.A. **113**, 2827 (2016).
- [9] M. C. Marchetti et al., *Hydrodynamics of soft active matter*, Rev. Mod. Phys. **85**, 1143 (2013).
- [10] F. Jülicher, A. Ajdari, and J. Prost, *Modeling molecular motors*, Rev. Mod. Phys. **69**, 1269 (1997).
- [11] J. Prost, F. Jülicher, and J.-F. Joanny, *Active gel physics*, Nat. Phys. **11**, 111 (2015).
- [12] T. Hiraiwa and G. Salbreux, *Role of turn-over in active stress generation in a filament network*, Phys. Rev. Lett. **116**, 188101 (2016).
- [13] K. H. Downing and E. Nogales, *Tubulin and microtubule structure*, Curr. Opin. Cell Biol. **10**, 16 (1998).
- [14] R. H. Wade and A. A. Hyman, *Microtubule structure and dynamics*, Curr. Opin. Cell Biol. **9**, 12 (1997).

- 
- [15] H. Flyvbjerg, T. E. Holy, and S. Leibler, *Stochastic dynamics of microtubules: a model for caps and catastrophes*, Phys. Rev. Lett. **73**, 2372 (1994).
- [16] D. Chrétien and R. H. Wade, *New data on the microtubule surface lattice*, Biol. Cell **71**, 161 (1991).
- [17] S. A. Wainwright, *Mechanical design in organisms*, Princeton University Press, 1982.
- [18] S. Heins et al., *The rod domain of NF-L determines neurofilament architecture, whereas the end domains specify filament assembly and network formation.*, J. Cell Biol. **123**, 1517 (1993).
- [19] M. Baus, L. F. Rull, and J.-P. Ryckaert, *Observation, prediction and simulation of phase transitions in complex fluids*, volume 460, Springer Science & Business Media, 2012.
- [20] R. D. Vale and R. A. Milligan, *The way things move: looking under the hood of molecular motor proteins*, Science **288**, 88 (2000).
- [21] R. Urrutia, M. A. McNiven, J. P. Albanesi, D. B. Murphy, and B. Kachar, *Purified kinesin promotes vesicle motility and induces active sliding between microtubules in vitro*, Proc. Natl. Acad. Sci. U.S.A. **88**, 6701 (1991).
- [22] A. Straube, G. Hause, G. Fink, and G. Steinberg, *Conventional kinesin mediates microtubule-microtubule interactions in vivo*, Mol. Biol. Cell **17**, 907 (2006).
- [23] M. E. Tanenbaum, R. D. Vale, and R. J. McKenny, *Cytoplasmic dynein crosslinks and slides anti-parallel microtubules using its two motor domains*, Elife **2**, 1 (2013).
- [24] L. Wordeman, *How kinesin motor proteins drive mitotic spindle function: Lessons from molecular assays*, in *Seminars in cell and developmental biology*, volume 21, pages 260–268, Elsevier, 2010.
- [25] A. L. Jolly et al., *Kinesin-1 heavy chain mediates microtubule sliding to drive changes in cell shape*, Proc. Natl. Acad. Sci. U.S.A. **107**, 12151 (2010).
- [26] R. D. Vale, T. S. Reese, and M. P. Sheetz, *Identification of a novel force-generating protein, kinesin, involved in microtubule-based motility*, Cell **42**, 39 (1985).
- [27] D. D. Hackney, *Highly processive microtubule-stimulated ATP hydrolysis by dimeric kinesin head domains*, Nature **377**, 448 (1995).
- [28] J. Howard, A. J. Hudspeth, and R. D. Vale, *Movement of microtubules by single kinesin molecules*, Nature **342**, 154 (1989).
- [29] S. M. Block, L. S. B. Goldstein, and B. J. Schnapp, *Bead movement by single kinesin molecules studied with optical tweezers*, Nature **348**, 348 (1990).
- [30] R. D. Astumian, *Microscopic reversibility as the organizing principle of molecular machines*, Nat. Nanotechnol. **7**, 684 (2012).

## BIBLIOGRAPHY

---

- [31] F. Jülicher, *Force and motion generation of molecular motors: A generic description*, pages 46–74, Springer Berlin Heidelberg, Berlin, Heidelberg, 1999.
- [32] T. Sanchez, T. D. Chen, S. J. Decamp, M. Heymann, and Z. Dogic, *Spontaneous motion in hierarchically assembled active matter*, *Nature* **491**, 431 (2012).
- [33] S. J. Decamp, G. S. Redner, A. Baskaran, M. F. Hagan, and Z. Dogic, *Orientational order of motile defects in active nematics*, *Nat. Mater.* **14**, 1110 (2015).
- [34] I. M. Palacios and D. S. Johnston, *Kinesin light chain-independent function of the Kinesin heavy chain in cytoplasmic streaming and posterior localisation in the *Drosophila oocyte.**, *Development* **129**, 5473 (2002).
- [35] M. Braun, D. R. Drummond, R. A. Cross, and A. D. McAinsh, *The kinesin-14 *Klp2* organizes microtubules into parallel bundles by an ATP-dependent sorting mechanism.*, *Nat. Cell Biol.* **11**, 724 (2009).
- [36] M. Schliwa, editor, *Molecular Motors*, Wiley-VCH, Weinheim, 2003.
- [37] C. Hentrich and T. Surrey, *Microtubule organization by the antagonistic mitotic motors kinesin-5 and kinesin-14*, *J. Cell Biol.* **189**, 465 (2010).
- [38] S. M. van den Wildenberg et al., *The Homotetrameric Kinesin-5, *KLP61F*, Preferentially Crosslinks Microtubules into Antiparallel Orientations*, *Curr. Biol.* **18**, 1860 (2008).
- [39] A. Ravichandran, G. A. Vliegenthart, G. Saggiorato, T. Auth, and G. Gompper, *Enhanced Dynamics of Confined Cytoskeletal Filaments Driven by Asymmetric Motors*, *Biophys. J.* **113**, 1121 (2017).
- [40] G. Arpağ, S. Shastry, W. O. Hancock, and E. Tüzel, *Transport by populations of fast and slow kinesins uncovers novel family-dependent motor characteristics important for in vivo function*, *Biophys. J.* **107**, 1896 (2014).
- [41] M. Jakobs, K. Franze, and A. Zemel, *Force Generation by Molecular-Motor-Powered Microtubule Bundles; Implications for Neuronal Polarization and Growth*, *Front. Cell. Neurosci.* **9**, 1 (2015).
- [42] A. Zemel and A. Mogilner, *Motor-induced sliding of microtubule and actin bundles*, *Phys. Chem. Chem. Phys.* **24**, 4821 (2009).
- [43] S. Ganguly, L. S. Williams, I. M. Palacios, and R. E. Goldstein, *Cytoplasmic streaming in *Drosophila oocytes* varies with kinesin activity and correlates with the microtubule cytoskeleton architecture*, *Proc. Natl. Acad. Sci. U.S.A.* **109**, 15109 (2012).
- [44] J. Verchot-Lubicz and R. E. Goldstein, *Cytoplasmic streaming enables the distribution of molecules and vesicles in large plant cells*, *Protoplasma* **240**, 99 (2010).
- [45] T. Shimmen, *The sliding theory of cytoplasmic streaming: fifty years of progress*, *J. Plant Res.* **120**, 31 (2007).

- [46] R. E. Goldstein and J.-W. van de Meent, *A physical perspective on cytoplasmic streaming*, *Interface Focus* **5**, 20150030 (2015).
- [47] H. Gutzeit, *The role of microtubules in the differentiation of ovarian follicles during vitellogenesis in Drosophila*, *Roux Arch. Dev. Biol.* **195**, 173 (1986).
- [48] W. E. Theurkauf, *Microtubules and cytoplasm organization during Drosophila oogenesis*, *Dev. Biol.* **165**, 352 (1994).
- [49] L. R. Serbus, B.-J. Cha, W. E. Theurkauf, and W. M. Saxton, *Dynein and the actin cytoskeleton control kinesin-driven cytoplasmic streaming in Drosophila oocytes.*, *Development* **132**, 3743 (2005).
- [50] W. Lu, M. Winding, M. Lakonishok, J. Wildonger, and V. I. Gelfand, *Microtubule–microtubule sliding by kinesin-1 is essential for normal cytoplasmic streaming in Drosophila oocytes*, *Proc. Natl. Acad. Sci. U.S.A.* **113**, E4995 (2016).
- [51] N. Suetsugu et al., *Two kinesin-like proteins mediate actin-based chloroplast movement in Arabidopsis thaliana*, *Proc. Natl. Acad. Sci. U.S.A.* **107**, 8860 (2010).
- [52] K. Yi et al., *Dynamic maintenance of asymmetric meiotic spindle position through Arp2/3 complex-driven cytoplasmic streaming in mouse oocytes*, *Nat. Cell Biol.* **13**, 1252 (2011).
- [53] B. Kachar, *Direct visualization of organelle movement along actin filaments dissociated from characean algae*, *Science* **227**, 1355 (1985).
- [54] R. E. Goldstein, I. Tuval, and J.-W. van de Meent, *Microfluidics of cytoplasmic streaming and its implications for intracellular transport*, *Proc. Natl. Acad. Sci. U.S.A.* **105**, 3663 (2008).
- [55] C. E. Monteith et al., *A Mechanism for Cytoplasmic Streaming: Kinesin-Driven Alignment of Microtubules and Fast Fluid Flows.*, *Biophys. J.* **110**, 2053 (2016).
- [56] J. R. Ellis, *Macromolecular crowding: obvious but underappreciated*, *Trends Biochem. Sci.* **26**, 597 (2001).
- [57] M. S. de Silva et al., *Self-organized patterns of actin filaments in cell-sized confinement*, *Soft Matter* **7**, 10631 (2011).
- [58] M. Gonzalez-Pinto, F. Borondo, Y. Martinez-Raton, and E. Velasco, *Clustering in vibrated monolayers of granular rods*, *Soft Matter* **13**, 2571 (2017).
- [59] M. Théry et al., *The extracellular matrix guides the orientation of the cell division axis*, *Nat. Cell Biol.* **7**, 947 (2005).
- [60] J. Fink et al., *External forces control mitotic spindle positioning*, *Nat. Cell Biol.* **13**, 771 (2011).
- [61] M. Versaevel, T. Grevesse, and S. Gabriele, *Spatial coordination between cell and nuclear shape within micropatterned endothelial cells*, *Nat. Commun.* **3**, 671 (2012).

## BIBLIOGRAPHY

---

- [62] A. B. Verkhovsky et al., *Orientational order of the lamellipodial actin network as demonstrated in living motile cells*, Mol. Biol. Cell **14**, 4667 (2003).
- [63] F. Hilitski et al., *Measuring Cohesion between Macromolecular Filaments One Pair at a Time: Depletion-Induced Microtubule Bundling*, Phys. Rev. Lett. **114** (2015).
- [64] F. J. Nédélec, T. Surrey, A. C. Maggs, and S. Leibler, *Self-organization of microtubules and motors*, Nature **389**, 305 (1997).
- [65] F. C. Keber et al., *Topology and dynamics of active nematic vesicles*, Science **345**, 1135 (2014).
- [66] J. Toner and Y. Tu, *Flocks, herds, and schools: A quantitative theory of flocking*, Phys. Rev. E **58**, 4828 (1998).
- [67] T. Vicsek, A. Czirók, E. Ben-Jacob, I. Cohen, and O. Shochet, *Novel type of phase transition in a system of self-driven particles*, Phys. Rev. Lett. **75**, 1226 (1995).
- [68] J. Z. Y. Chen, *Structure of two-dimensional rods confined by a line boundary*, Soft Matter **9**, 10921 (2013).
- [69] L. Giomi, M. J. Bowick, P. Mishra, R. Sknepnek, and M. C. Marchetti, *Defect dynamics in active nematics*, Phil. Trans. R. Soc. A **372** (2014).
- [70] S. P. Thampi, R. Golestanian, and J. M. Yeomans, *Velocity correlations in an active nematic*, Phys. Rev. Lett. **111**, 118101 (2013).
- [71] L. Onsager, *The effects of shape on the interaction of colloidal particles*, Ann. N. Y. Acad. Sci. **51**, 627 (1949).
- [72] T. Odijk, *Theory of lyotropic polymer liquid crystals*, Macromolecules **19**, 2313 (1986).
- [73] T. Sanchez, D. T. N. Chen, S. J. Decamp, M. Heymann, and Z. Dogic, *Spontaneous motion in hierarchically assembled active matter*, arXiv:1301.1122 [cond-mat.soft] (2012).
- [74] V. Schaller, C. Weber, C. Semmrich, E. Frey, and A. R. Bausch, *Polar patterns of driven filaments*, Nature **467**, 73 (2010).
- [75] R. Suzuki, C. A. Weber, E. Frey, and A. R. Bausch, *Polar pattern formation in driven filament systems requires non-binary particle collisions*, Nat. Phys. **11**, 839 (2015).
- [76] R. Zwanzig, *Nonequilibrium statistical mechanics*, Oxford University Press, 2001.
- [77] M. Doi and S. F. Edwards, *The theory of polymer dynamics*, volume 73, oxford university press, 1988.
- [78] J. G. Kirkwood, *The general theory of irreversible processes in solutions of macromolecules*, J. Polym. Sci. **12**, 1 (1954).

- 
- [79] J. Elgeti, M. Cates, and D. Marenduzzo, *Defect hydrodynamics in 2D polar active fluids*, *Soft Matter* **7**, 3177 (2011).
- [80] R. E. Isele-Holder, J. Elgeti, and G. Gompper, *Self-propelled worm-like filaments: spontaneous spiral formation, structure, and dynamics*, *Soft Matter* **11**, 7181 (2015).
- [81] J. Gay and B. Berne, *Modification of the overlap potential to mimic a linear site-site potential*, *J. Chem. Phys.* **74**, 3316 (1981).
- [82] R. A. Persson, *Note: Modification of the Gay-Berne potential for improved accuracy and speed*, *J. Chem. Phys.* **136**, 226101 (2012).
- [83] M. Abkenar, K. Marx, T. Auth, and G. Gompper, *Collective behavior of penetrable self-propelled rods in two dimensions*, *Phys. Rev. E* **88**, 062314 (2013).
- [84] M. E. Fisher and D. Ruelle, *The stability of many-particle systems*, *J. Math. Phys.* **7**, 260 (1966).
- [85] M. Zacharias, T. P. Straatsma, and J. A. McCammon, *Separation-shifted scaling, a new scaling method for Lennard-Jones interactions in thermodynamic integration*, *J. Chem. Phys.* **100**, 9025 (1994).
- [86] J. Happel and H. Brenner, *Low Reynolds number hydrodynamics*, volume 1, Martinus Nijhoff Publishers, Hague, Netherlands, 1983.
- [87] H. Löwen, *Brownian dynamics of hard spherocylinders*, *Phys. Rev. E* **50**, 1232 (1994).
- [88] Y.-G. Tao, W. K. den Otter, J. T. Padding, J. K. Dhont, and W. J. Briels, *Brownian dynamics simulations of the self and collective rotational diffusion coefficients of rigid long thin rods*, *J. Chem. Phys.* **122**, 244903 (2005).
- [89] D. Wirtz, *Particle-tracking microrheology of living cells: principles and applications.*, *Annu. Rev. Biophys* **38**, 301 (2009).
- [90] S. T. Brady, K. K. Pfister, and G. S. Bloom, *A monoclonal antibody against kinesin inhibits both anterograde and retrograde fast axonal transport in squid axoplasm.*, *Proc. Natl. Acad. Sci. U.S.A.* **87**, 1061 (1990).
- [91] I. Crevel, N. Carter, M. Schliwa, and R. Cross, *Coupled chemical and mechanical reaction steps in a processive *Neurospora* kinesin*, *EMBO J* **18**, 5863 (1999).
- [92] C. M. Coppin, J. T. Finer, J. A. Spudich, and R. D. Vale, *Measurement of the isometric force exerted by a single kinesin molecule.*, *Biophys. J.* **68**, 242S (1995).
- [93] G. L. Lukacs et al., *Size-dependent DNA mobility in cytoplasm and nucleus*, *J. Biol. Chem.* **275**, 1625 (2000).
- [94] S. Plimpton, *Fast parallel algorithms for short-range molecular dynamics*, *J. Comput. Phys.* **117**, 1 (1995).

## BIBLIOGRAPHY

---

- [95] K. Kruse, J. F. Joanny, F. Jülicher, J. Prost, and K. Sekimoto, *Asters, Vortices, and Rotating Spirals in Active Gels of Polar Filaments*, Phys. Rev. Lett. **92**, 078101 (2004).
- [96] K. Kruse and F. Jülicher, *Actively contracting bundles of polar filaments*, Phys. Rev. Lett. **85**, 1778 (2000).
- [97] Z. Jia, D. Karpeev, I. S. Aranson, and P. W. Bates, *Simulation studies of self-organization of microtubules and molecular motors*, Phys. Rev. E **77**, 051905 (2008).
- [98] R. E. Isele-Holder, J. Jäger, G. Saggiorato, J. Elgeti, and G. Gompper, *Dynamics of self-propelled filaments pushing a load*, Soft matter **12**, 8495 (2016).
- [99] J. D. Weeks, D. Chandler, and H. C. Andersen, *Role of repulsive forces in determining the equilibrium structure of simple liquids*, The Journal of chemical physics **54**, 5237 (1971).
- [100] M. A. Bates and D. Frenkel, *Phase behavior of two-dimensional hard rod fluids*, J. Chem. Phys. **112**, 10034 (2000).
- [101] P. Bolhuis and D. Frenkel, *Tracing the phase boundaries of hard spherocylinders*, J. Chem. Phys. **106**, 666 (1997).
- [102] S. C. McGrother, D. C. Williamson, and G. Jackson, *A re-examination of the phase diagram of hard spherocylinders*, J. Chem. Phys. **104**, 6755 (1996).
- [103] D. A. Head, G. Gompper, and W. J. Briels, *Microscopic basis for pattern formation and anomalous transport in two-dimensional active gels*, Soft Matter **7**, 3116 (2011).
- [104] E. Toprak, A. Yildiz, M. T. Hoffman, S. S. Rosenfeld, and P. R. Selvin, *Why kinesin is so processive*, Proc. Natl. Acad. Sci. U.S.A. **106**, 12717 (2009).
- [105] D. Mizuno, C. Tardin, C. F. Schmidt, and F. C. MacKintosh, *Nonequilibrium mechanics of active cytoskeletal networks*, Science **315**, 370 (2007).
- [106] S. L. Freedman, S. Banerjee, G. M. Hocky, and A. R. Dinner, *A versatile framework for simulating the dynamic mechanical structure of cytoskeletal networks*, Biophys. J. **113**, 448 (2017).
- [107] I. S. Aranson and L. S. Tsimring, *Pattern formation of microtubules and motors: inelastic interaction of polar rods*, Phys. Rev. E **71**, 050901 (2005).
- [108] I. S. Aranson and L. S. Tsimring, *Theory of self-assembly of microtubules and motors*, Phys. Rev. E **74**, 031915 (2006).
- [109] S. Swaminathan, F. Ziebert, I. Aranson, and D. Karpeev, *Patterns and intrinsic fluctuations in semi-dilute motor-filament systems*, EPL **90**, 28001 (2010).
- [110] A. Córdoba, J. D. Schieber, and T. Indei, *The role of filament length, finite-extensibility and motor force dispersity in stress relaxation and buckling mechanisms in non-sarcomeric active gels*, Soft Matter **11**, 38 (2015).

- 
- [111] B. Doliwa and A. Heuer, *Cooperativity and spatial correlations near the glass transition: Computer simulation results for hard spheres and disks*, Phys. Rev. E **61**, 6898 (2000).
- [112] A. Wysocki, R. G. Winkler, and G. Gompper, *Cooperative motion of active Brownian spheres in three-dimensional dense suspensions*, Europhys. Lett. **105**, 48004 (2014).
- [113] D. Axelrod, D. Koppel, J. Schlessinger, E. Elson, and W. W. Webb, *Mobility measurement by analysis of fluorescence photobleaching recovery kinetics*, Biophys. J. **16**, 1055 (1976).
- [114] J. Elgeti, R. G. Winkler, and G. Gompper, *Physics of microswimmers—single particle motion and collective behavior: a review*, Rep. Prog. Phys **78**, 056601 (2015).
- [115] K. Kruse, J.-F. Joanny, F. Jülicher, J. Prost, and K. Sekimoto, *Generic theory of active polar gels: a paradigm for cytoskeletal dynamics*, Eur. Phys. J. E **16**, 5 (2005).
- [116] G. Salbreux, J. Prost, and J.-F. Joanny, *Hydrodynamics of cellular cortical flows and the formation of contractile rings*, Phys. Rev. Lett. **103**, 058102 (2009).
- [117] K. Kruse, S. Camalet, and F. Jülicher, *Self-propagating patterns in active filament bundles*, Phys. Rev. Lett. **87**, 138101 (2001).
- [118] M. Winding, M. T. Kelliher, W. Lu, J. Wildonger, and V. I. Gelfand, *Role of kinesin-1-based microtubule sliding in Drosophila nervous system development*, Proc. Natl. Acad. Sci. U.S.A. **113**, E4985 (2016).
- [119] A. Kudrolli, G. Lumay, D. Volfson, and L. S. Tsimring, *Swarming and swirling in self-propelled polar granular rods*, Phys. Rev. Lett. **100**, 058001 (2008).
- [120] T. L. Hill, *Statistical Mechanics: Principles and Selected Applications*, Dover Publications Inc., New York, 1987.
- [121] C. Battle et al., *Broken detailed balance at mesoscopic scales in active biological systems*, Science **352**, 604 (2016).
- [122] G. H. Koenderink et al., *An active biopolymer network controlled by molecular motors*, Proc. Natl. Acad. Sci. U.S.A. **106**, 15192 (2009).
- [123] V. Mustonen and M. Lässig, *From fitness landscapes to seascapes: non-equilibrium dynamics of selection and adaptation*, Trends Genet. **25**, 111 (2009).



## Acknowledgements

This thesis is dedicated to my best friend, my mother. I attribute my successes to her superhuman abilities to encourage, support, love and carry me through the seemingly insurmountable challenges that I have faced in this thesis and in life.

I would like to thank my thesis committee for their patience and consideration: Prof. Dr. Gerhard Gompper, Prof. Dr. Tobias Bollenbach, and Prof. Dr. Thomas Michely.

It is impossible for me to find enough words of gratitude for my mentors, Dr. Gerrit Vliegenthart and Dr. Thorsten Auth, who have undeniably influenced the way I think. Without them, I cannot consider myself a scientist, today. Not only have they mentored me as their student, but often, I have felt that they were my friends. Gerrit, thank you for your ever-open office door, that received many nervous questions about whether I was doing things correctly. I have always greatly admired your dedication to scientific accuracy and patience to check and recheck every calculation. Despite your high standards for science, I have found your friendly and jovial nature a great blessing in my PhD.

Thorsten, thank you for your patience in charting time for our discussions even at obscure times of the day and on weekends. In three years, my inability to recall a single instance for when you turned me away when I came to discuss, speaks volumes about your dedication to mentoring and scientific curiosity. Thank you very much for your specific, critical and constructive feedback on everything that I put my name on. Thank you also for all your encouragement, and ensuring that I was maintained focussed on my targets.

I think it is because of Prof. Dr. Gerhard Gompper that I am fond of the German tradition of calling my advisor: thesis father. Gerhard, I am amazed by the manner in which you conduct science, and consider myself very lucky to have been under your advisement. I will always fondly remember your patience and willingness to talk through my unchecked enthusiasm in science. Despite your endless commitments and responsibilities, I am astonished by your astuteness, and attention to detail. Even though I might have pondered over a problem for weeks on end, I cannot forget the manner in which you look at the same problem for the first time, and always bring new insight.

From the beginning, in Jülich, I was graced with the company of my close friend, Özer Duman. Özer, I will sorely miss your company at work, and at home as a flatmate. Your unwavering support and motivation in science and life has been the bedrock for all my successes here. Amongst those successes, I will proudly include the undeniable fact that I made a dear friend for life. I owe you far too much for me to thank you enough.

Although the real work always happened within the office, it would have been terribly uninspiring if not for the enthusiastic scientific discussions that was abundantly available in the corridors of ICS-2. With Masoud Hoore, I toyed around with some ideas for the effective motor project in the train rides to our classes. These led to a wonderful collaboration, and almost half of the results presented in this thesis. Masoud, you have made my days at work cheerful with your smile and gregarious conversations. I have found your shrewdness in attacking gnarly problems in physics greatly inspiring.

With my compatriots, Thomas, Shiba and Clara, I have never had a moment of embarrassment clarifying my shortcomings in vector algebra, high school geometry and occasionally more advanced molecular dynamics! I am very grateful for your patience in accommodating no small amount of my incessant rants and annoyances over the banalities

that plagued my research as an engineer studying theoretical physics. I am also thankful to Thomas and Clara for reading through my thesis, and pointing out those small, yet, embarrassing errors, which would have gone unnoticed without your astuteness.

Guglielmo, and Sabya, were my academic elders who supported me intellectually during the brief overlap of our PhDs. Guglielmo, I've found you to be a source of great inspiration and creativity. I will always remember you for your sharpness, for there has never been a time when you took a minute too long to comprehend my tedious ramble of needlessly convoluted concepts. I only hope to be involved in more fruitful scientific (and robotic) collaborations with you in the future.

I started science because of Dr. Dilip Asthagiri. Sir, your unrelenting faith in my abilities is what brought me here. I am eternally grateful for your mentorship and advice in nearly every important step that I take in my life.

My chapter in science would not be complete without my time in Philadelphia. Rick, Ram and Ryan, I would not be using Python without you guys. Ram, I am very grateful for your warmth and support through science and life. Along with Sumedh and Rohini, you made even my difficult times in UPenn very pleasant and memorable. Thank you, Nate and Sarah, my dear friends and flatmates for starting this journey in science with me.

Luca and Aitor, my flatmates in Jülich - thank you for putting up with me and giving me a home away from home. Varun - for being a cheerful, jolly and ever-reliable friend. Karandeep Singh - for knowing how to throw a great party. Alisa, Mythreyi and Ganesh - for always only being a phone call away.

I am very grateful for the Otto Bayer Fellowship program, which partly funded my PhD, and the Jülich Supercomputing Center staff who have helped me greatly in using JURECA. I also owe a great debt of gratitude to all the open-source developers. Thanks to all those strangers (and Linus Torvalds) who unwittingly unite by the idea of open content and collaboration. GNU/Linux, L<sup>A</sup>T<sub>E</sub>X, NumPy and Matplotlib - without whom all of this would have been much harder and less colourful. Thank you James McAlister, Nico Muhly, Bryce Dessner and Sufjan Stevens for Planetarium; the album which I played endlessly throughout the thesis writing.

None of this would have been possible without the rest of my family: My father, brother, and Chocku mama who have been there with me every day.

Finally, my dearest Claire - thank you for all your love, and support.

Ich versichere, daß ich die von mir vorgelegte Dissertation selbständig angefertigt, die benutzten Quellen und Hilfsmittel vollständig angegeben und die Stellen der Arbeit — einschließlich Tabellen, Karten und Abbildungen —, die anderen Werken im Wortlaut oder dem Sinn nach entnommen sind, in jedem Einzelfall als Entlehnung kenntlich gemacht habe; daß diese Dissertation noch keiner anderen Fakultät oder Universität zur Prüfung vorgelegen hat; daß sie — abgesehen unten angegebenen Teilpublikationen — noch nicht veröffentlicht worden ist sowie, daß ich eine solche Veröffentlichung vor Abschluß des Promotionsverfahrens nicht vornehmen werde. Die Bestimmungen der Promotionsordnung sind mir bekannt. Die von mir vorgelegte Dissertation ist von Professor Gompper betreut worden.

1. A. Ravichandran, G. A. Vliegthart, G. Saggiorato, T. Auth, G. Gompper  
Enhanced dynamics of confined cytoskeletal filaments driven by asymmetric motors  
Biophys. J. **113**(5), 1121-1132 (2017)

Jülich, den 14. Nov 2017





**Arvind Ravichandran**

Address	Eschenweg 15, Jülich 52428, Deutschland
Date of birth	26 Feb 1990
Place of birth	Mumbai
Nationality	Indian
<b>1997 – 2002</b>	<b>Primary school</b> Princess Elizabeth Primary School Singapore
<b>2003 – 2006</b>	<b>Secondary school</b> St. Joseph's Institution Singapore
<b>2007 – 2008</b>	<b>Pre-university</b> Raffles Junior College Singapore
<b>2009 – 2012</b>	<b>BS in Chemical Biomolecular Engineering</b> Johns Hopkins University Baltimore, MD, USA
<b>2012 – 2014</b>	<b>MS in Chemical Biomolecular Engineering</b> University of Pennsylvania Philadelphia, PA, USA
<b>from Aug 2014</b>	<b>PhD in Physics</b> Forschungszentrum Jülich (Universität zu Köln)

Jülich, den 14. November 2017